The Atlantic Inflow: atmosphere-land-ocean interaction at the south-western edge of the Saharan heat low

Der „Atlantic Inflow“: Atmosphäre-Land-See Wechselwirkung am südwestlichen Rand des Sahara-Hitzetiefs

Diplomarbeit im Fach Meteorologie
vorgelegt von

Christian Grams

18. März 2008

Referent: Prof. Dr. Sarah Jones
Korreferent: Prof. Dr. Klaus Dieter Beheng

Karlsruhe Institute of Technology
Institut für Meteorologie und Klimaforschung
Universität Karlsruhe / Forschungszentrum Karlsruhe

Contents

Überblick

Die vorliegende Arbeit entstand unter der gemeinsamen Betreuung von Prof. Dr. Sarah Jones, Institut für Meteorologie und Klimatologie, Universität Karlsruhe (TH) und Dr. Douglas Parker, Institute for Atmospheric Science, University of Leeds, United Kingdom. Sie wurde in englischer Sprache verfasst, damit die Kollegen in Leeds die abgeschlossene Arbeit ebenfalls lesen können. Im Folgenden sollen die wichtigsten Ergebnisse in deutscher Sprache vorgestellt werden.

Das Sahara-Hitzetief ist ein bedeutendes Element des Westafrikanischen Monsunsystems. Die hohe Sonneneinstrahlung über der Sahara führt tagsüber zu einem starken Aufheizen der Erdoberfläche und der unteren Luftschichten. Dies ist verbunden mit starker trockener Konvektion, die einen horizontalen Austausch verhindert. Dadurch entsteht ein flaches Tiefdruckgebiet, dessen tiefster Luftdruck am Abend erreicht wird. Als Reaktion auf den Druckgradienten nimmt nachts, wenn die Turbulenz aufgrund der fehlenden Einstrahlung verschwindet, die Strömung in das Tiefdruckgebiet zu, der Luftdruck steigt. Durch diesen charakteristischen Tagesgang beeinflusst das Sahara-Hitzetief die nächtliche Advektion der feucht-kühlen Monsunluft in die Sahelzone (Parker et al. 2005). Die nördliche Grenze der Monsunströmung ist durch einen starken zonalen Feuchtegradienten sowie von Konvergenz des Südwestmonsuns und des Nordostpassats, auch Harmattan genannt, gekennzeichnet. Man bezeichnet diese Grenze innertropische Front. Das Sahara-Hitzetief steuert weiter das Einsetzen des Sommermonsuns, das durch eine abrupte nordwärtige Verlagerung der innertropischen Front gekennzeichnet ist (Sultan and Janicot 2003b,a; Ramel et al. 2006; Hagos and Cook 2007). Die hochreichende trockene Konvektion in der Hitzetiefregion leistet einen entscheidenden Beitrag zur Erhaltung des afrikanischen Oststrahlstroms, eines zonalen Starkwindbandes in ca. 3-4 km Höhe über dem tropischen Nordafrika und Nordatlantik (5°N-15°N) (Thorncroft and Blackburn 1999).

Seit Mitte der 1970er Jahre stellte sich in der Sahelzone ein trockeneres Klimaregime ein. Dies hatte teils verheerende Auswirkungen auf die agrarisch geprägte und niederschlagsabhängige Wirtschaft Westafrikas. Ein besseres Verständnis des Westafrikanischen Monsuns ist Grundvoraussetzung für die korrekte Darstellung und Vorhersage des Monsunsystems in numerischen Modellen sowie für die Abschätzung zukünftiger Entwicklungen. Nur so ist es den Gesellschaften Westafrikas möglich, sich den natürlich verfügbaren Ressourcen anzupassen. Dies ist Anliegen des internationalen Forschungsprogramms „Afrikanischer Monsun Multidisziplinäre Analysen“ (AMMA)[1] zu welchem diese Arbeit beiträgt.

In der vorliegenden Arbeit wird die meteorologische Situation am südwestlichen Rand des Sahara-Hitzetiefs untersucht. In dieser Region finden Wechselwirkungen zwischen dem Hitzetief im Norden und Osten, einer vom Atlantik beeinflussten Atmosphäre im Westen und der Monsunströmung im Süden statt. Dabei ist das numerische Wettervorhersagemodell COSMO des Deutschen Wetterdienstes (Doms and Schättler 2002) das wichtigste

[1] `http://www.amma-eu.org`

Hilfmittel. COSMO ist ein nicht-hydrostatisches regionales Wettervorhersagemodell, das speziell für die Anwendung auf der meso-β (5 km - 50 km) und meso-γ (500 m - 5 km) Ebene entwickelt wurde. Weiter steht ein umfangreicher Datensatz der Flugzeugmesskampagne GERBILS zur Verfügung. Die Modelldaten wurden zunächst mit Hilfe der Flugzeugmessungen validiert und anschließend für genauere Untersuchung mesoskaliger Phänomene verwendet. Dabei entdeckten wir den „Atlantic Inflow“ im Westen Mauretaniens. Die Analyse des „Atlantic Inflow“ ist Hauptgegenstand im zweiten Teil der Arbeit.

Im Unified Model des britischen Wetterdienstes UK Met Office zeigten sich Diskrepanzen zwischen modellierter und gemessener Strahlung über dem südlichen Sahara-Hitzetief (Abb. 3.1, S. 26) (Haywood et al. 2005, 2007). Diese werden auf eine mangelhafte Repräsentation von Staub- und Oberflächeneigenschaften im Modell zurückgeführt. Daher ist es nötig, den Einfluss dieser Parameter auf die Strahlungsbilanz der Erdoberfläche und am Oberrand der Atmosphäre besser zu verstehen. Flugzeuggestützte Messungen eignen sich gut um hierfür einen entsprechenden Datensatz zu gewinnen. Daher führte das UK Met Office Ende Juni 2007 die Flugzeugmesskampagne GERBILS (GERB Intercomparison of Longwave and Shortwave radiation) in Westafrika durch (Haywood et al. 2007). Vom 18. bis 29. Juni 2007 wurden sechs Messflüge zwischen Niamey, Niger, und Nouakchott, Mauretanien, durchgeführt. Die geplante Flugstrecke verlief entlang 18°N und damit genau über dem südwestlichen Bereich des Sahara-Hitzetiefs (Abb. 2.1, S. 21 und Abb. 3.2, S. 27). Während der GERBILS-Kampagne erstellten wir zweimal täglich mit COSMO eine räumlich hochaufgelöste operationelle Wettervorhersage (Grams 2007). Die COSMO-Vorhersagen halfen z.T. entscheidend bei der Planung der exakten Flugroute. Darüberhinaus konnten von COSMO vorhergesagte Strukturen gezielt durch entsprechend positionierte Dropsondenabwürfe vermessen werden. So wurden die Flugzeug- und Dropsondenmessungen hinsichtlich einer COSMO-Modellvalidierung optimiert.

Die interessanteste der gefundenen Strukturen war eine barokline Zone, die im Vertikalschnitt potentieller Temperatur entlang 18°N am 24. Juni 2007 auffiel (Abb. 4.3, S. 37). Die barokline Zone trennt die trocken-heiße, neutral geschichtete Sahara-Grenzschicht von einer atlantisch beeinflussten, leicht stabil geschichteten Atmosphäre im Westen. Die detaillierte Modellvalidierung zeigt, dass COSMO die thermodynamische Struktur und die Verteilung spezifischer Feuchte sehr gut wiedergibt (siehe z.B. Abb. 4.8, S. 42, Abb. 4.17, S. 51 und Abb. 4.18, S. 53). Dies rechtfertigt die Nutzung der COSMO-Vorhersagen für eine genauere Untersuchung der räumlichen und zeitlichen Variabilität der baroklinen Zone. Dabei wurde der „Atlantic Inflow“ entdeckt (Abb. 5.1, S. 62).

Der „Atlantic Inflow“ ist ein Land-See-Wind-System an der mauretanischen Küste, welches sich abends in eine See-Wind-Front umwandelt und landeinwärts vordringt. Der „Atlantic Inflow“ trat fast an jedem Tag der GERBILS-Kampagne in den COSMO-Vorhersagen auf. Die mauretanische Küstenregion ist von einem starken meridionalen Temperaturgradienten geprägt. Aufgrund des kalten Kanarenstroms und des schwachen Aufsteigens von Tiefenwasser ist der Atlantik vor der mauretanischen Küste relativ kalt (22°C Wassertemperatur). Dagegen heizt sich die Landoberfläche des wüstenhaften Landesinneren tagsüber auf über 45°C auf (vgl. Abb. 5.2, S. 63). Dies führt zu einem starken sensiblen Wärmestrom und einer starken turbulenten Durchmischung. Es entwickelt sich eine ca. 2 km mächtige neutral geschichtete konvektive Grenzschicht (Abb. 5.19, S. 80). Eine Küstenebene erstreckt sich von ca. 20°N bis nach Senegal im Süden und von der Küste

bei 16°N 400 km landeinwärts. Diese äußerst flache Orographie prägt den Westen Mauretaniens (Abb. 3.2, S. 27). Das in Nord-Süd-Richtung verlaufende Tagant-Plateau stellt mit einem steilen Anstieg von ca. 100 m ü. NN auf 400-600 m ü. NN bei 12°W das erste orographische Hindernis östlich der Küstenlinie dar. Nördlich von ca. 20°N ist die Küstenebene auf einen schmalen Streifen begrenzt.

Für ein besseres Verständnis des „Atlantic Inflow“ wurde der Programmcode des COSMO-Modells so angepasst, dass die einzelnen Terme der Temperatur- und Wasserdampftendenzgleichung als Ausgabegröße zur Verfügung stehen. Damit wurde der Beitrag jedes physikalischen Prozesses (horizontale und vertikale Advektion, Strahlung, Turbulenz, Phasenumwandlung sowie numerische Filter) zur Temperatur- und Feuchtetendenz ersichtlich.

Der „Atlantic Inflow“ ist auf verschiedene Arten nachweisbar: 1.) Die Darstellung einer meteorologischen Größe - wie Temperatur, Feuchte oder Wind - über die Zeit und Höhe macht den „Atlantic Inflow“ an einem festen Ort erkennbar. Die Passage der mit dem „Atlantic Inflow“ verbundenen Front zeigt sich unterhalb von 950 hPa durch eine starke Abkühlung (5 K in 1h), ein starkes Ansteigen der zonalen Windkomponente (von ca. 2 m/s auf über 10 m/s) und, abhängig von der synoptischen Situation, durch einen Anstieg der spezifischen Feuchte (Abb. 5.6, S. 69). Hinter der Front sorgt die Advektion kühler maritimer Luft für ein weiteres Abkühlen und für eine starke Stabilisierung in den unteren Schichten (Abb. 5.8, S. 71). 2.) Der Gradient potentieller Temperatur zeigt die horizontale Ausdehnung des „Atlantic Inflow“ an (Abb. 5.14, S. 76). Jeden Tag entwickelt sich entlang der Küste in den Mittagsstunden ein starker Gradient potentieller Temperatur. Diese Küstenfront bleibt bis in den späten Nachmittag stationär. Dabei wächst der Temperaturkontrast weiter an. Ab ca. 17 UTC beginnt die Front langsam landeinwärts vorzudringen. Um 19 UTC erreicht sie ihre endgültige Propagationsgeschwindigkeit von ca. 10 m/s und wandert in den folgenden Stunden ca. 400 km landeinwärts. Am Fuß des Tagant-Plateaus löst sich die Front schließlich auf (Abb. 5.14, S. 76). Es hat sich gezeigt, dass der „Atlantic Inflow“ zwischen 17°N und 19°N am besten ausgebildet ist. 3.) Die vertikale Ausprägung des „Atlantic Inflow“ wird in Vertikalschnitten entlang 18°N deutlich. Im Vertikalschnitt potentieller Temperatur trennt die Küstenfront die gut durchmischte Grenzschicht über dem Landesinneren im Osten von der stark stabil geschichteten Atmosphäre über dem Atlantischen Ozean (Abb. 5.6, S. 69). Dicht gedrängte Isentropen unterhalb von 900 hPa sowie ein Aufwölben der Isentropen darüber kennzeichnen die Front. Der wellenförmige Verlauf der Isentropen über der Küstenfront deutet das Auslösen einer Schwerewelle an (Abb. 5.21, S. 83). Diese wandert zwischen 900 hPa und 300 hPa, entgegen dem östlichen Grundstrom der mittleren Atmosphäre, mit der bodennahen Front landeinwärts. Die Wellenlänge beträgt ca. 50 km, die Phasengeschwindigkeit 10 m/s. Bei Erreichen des Tagant-Plateaus entkoppelt sich die Schwerewelle von der Bodenfront und schreitet weiter ostwärts voran. Die Front ist mit einer charakteristischen Frontalzirkulation verbunden: Vor der Front findet vom Erdboden bis ca. 800 hPa Aufsteigen statt. Oberhalb der Front schließt eine Region mit starkem Absinken in der mittleren Troposphäre an. Hinter der Front und in der mittleren und hohen Atmosphäre befindet sich eine Region mit schwachem Aufstieg (Abb. 5.22d, S. 85). Der „Atlantic Inflow“ zeigt sich weiter im Vertikalschnitt der horizontalen Temperaturadvektion und der Brunt-Väisälä-Frequenz (Abb. 5.22a, S. 85 und Abb. 5.25, S. 88): Advektion kühlerer Luft bis in ca. 850 hPa Höhe und ein Wechsel von neutraler zu stabiler Schichtung markiert die Küstenfront. Hinter der

Front strömt weiter kühlere und sehr stabil geschichtete Luft in die untersten Schichten ein.

Die Vertikalschnitte der potentiellen Temperatur, der horizontalen Temperaturadvektion und der Dichte machen auch deutlich, dass der „Atlantic Inflow“ den Charakter einer Dichteströmung in turbulenter Umgebung hat (vgl. Linden and Simpson (1986), Abb. 5.26, S. 88). Weiter ähnelt der „Atlantic Inflow“ Phänomenen, die in anderen Studien beschrieben und die mit Dichteströmungen verbunden werden (z.B. Haase and Smith (1989), Abb. 5.27, S. 89 oder Noonan and Smith (1986); Raymond and Rotunno (1989), Abb. 5.28, S. 90). Schließlich wurde gezeigt, dass die Propagationsgeschwindigkeit des „Atlantic Inflow“ mit der Geschwindigkeit übereinstimmt, die sich aus der Theorie von Dichteströmungen ergibt. Ein dem „Atlantic Inflow“ ähnliches Land-See-Wind-System beschreiben Kottmeier et al. (2000) in Spanien. Das „Morning Glory“-Phänomen in Australien hat ebenfalls Ähnlichkeiten mit der hier beschriebenen Seewind-Front. Einen guten Überblick über die zahlreichen Studien zu „Morning Glories“ geben Reeder and Smith (1999).

Der „Atlantic Inflow“ kann über das Gleichgewicht zwischen Horizontaladvektion und Turbulenz, verbunden mit den besonderen Gegebenheiten an der mauretanischen Küste, erklärt werden (Abb. 5.34, S. 99). Die differentielle Erwärmung der unteren Atmosphäre über See und Land am Tage führt zu einem starken Temperatur- und Dichtegradienten. Dieser ist Antrieb für ein landeinwärtiges Vordringen der kühleren und schwereren Luft über dem Ozean. Die starke turbulente Durchmischung in der konvektiven Grenzschicht über Land verhindert jedoch tagsüber eine horizontale Strömung. Eine Erwärmung aufgrund von turbulenter Diffusion balanciert und dominiert die horizontale Advektion kühlerer Luft (Abb. 5.33, S. 97). Dadurch maximiert sich der Temperatur- und Dichtegradient an der Küste, eine stationäre Front entsteht. Am späten Nachmittag wird der sensible Wärmestrom mit sinkendem Sonnenstand stetig schwächer. Schließlich verschwindet die Erwärmung aufgrund turbulenter Diffusion völlig und horizontale Advektion kühlerer Luft dominiert. Die Front wandert landeinwärts. Die nächtliche Stabilisierung und Abkühlung der untersten Luftschichten durch langwellige Ausstrahlung wird durch den „Atlantic Inflow“ verstärkt. Hinter der Küstenfront fließt kühlere und stabil geschichtete Luft ein. Die Front löst durch das vorderseitige Anheben der Isentropen in der leicht stabil geschichteten mittleren Atmosphäre Schwerewellen aus. Spätestens nach dem Erreichen des Tagant-Plateaus löst sich die Bodenfront auf. Die Höhe der Dichteströmung ist zu gering um das Gebirge zu überschreiten.

Abschließend wird der Einfluss des „Atlantic Inflow“ auf den Temperatur- und Feuchtehaushalt in der Küstenebene untersucht. Dazu werden die einzelnen Tendenzterme zeitlich über einen 48h-Zeitraum und räumlich über eine Sahara-Hitzetief-, eine Monsun- und eine „Atlantic Inflow“-Box gemittelt und als Profil aufgetragen. In der „Atlantic Inflow“-Box ähneln die Profile der Tendenzterme denen der Sahara-Hitzetief-Box (vgl. Abb. 6.2, S. 103 und Abb. 6.7, S. 108). Der „Atlantic Inflow“ macht sich jedoch in den bodennahen Schichten durch eine starke Advektion kühlerer Luft deutlich bemerkbar. Die Analyse des Wärme- und Feuchtehaushalts bestätigt die Balance zwischen Horizontaladvektion und Turbulenz als den steuernden Prozess für die Propagation des „Atlantic Inflow“.

Nach unserem Wissen ist die vorliegende Arbeit die erste detaillierte Beschreibung eines solchen Phänomens an der Westafrikanischen Küste.

1 Background

1.1 Introduction

The Saharan heat low is a prominent feature of the West African monsoon. Strong daytime insolation results in surface and low-level heating leading to a pressure minimum in the lower troposphere. The Saharan heat low affects the nocturnal advection of moisture in the Sahel from the south, controls the onset of the monsoon, and serves through its deep dry convection to maintain the African easterly jet, a zone of high wind speed in the midtroposphere over tropical North Africa. However, only few studies have focused on *mesoscale* interactions of the Saharan heat low and the West African monsoon. Mesoscale circulations are assumed to affect the uplift and layering of dust in the atmosphere.

The routine meteorological network in the Saharan region is sparse due to the harsh desert environment. Numerical weather models can provide an interesting alternate dataset to in situ measurements. However, less is known about the accuracy of numerical models in the Saharan heat low region. The research programme AMMA[1] tries to improve the understanding and thereby also the numerical modelling of the West African monsoon. In this context it is interesting to learn more about the representation of the Saharan heat low and related mesoscale features in numerical models. The COSMO[2] model of the Deutscher Wetterdienst (DWD) is a regional nonhydrostatic numerical weather prediction model designed to resolve mesoscale systems. Thus to analyse mesoscale interactions at the southern edge of the Saharan heat low it is interesting to run and test the COSMO model.

The GERBILS[3] campaign took place in June 2007. Six transects were conducted with the FAAM[4] BAe 146 aircraft across the south-western Sahara from bases at Niamey and Nouakchott. Airborne as well as dropsonde measurements provide a spatially high-resolved dataset along the flight track at 18°N. We performed an operational forecast during the campaign using the COSMO model. The data collected present a unique opportunity to validate the model at the edge of the Saharan heat low.

Model as well as observational data showed an interesting tilted baroclinic zone at the meridional transect along 18°N separating the deep well-mixed Saharan Planetary Boundary Layer (Saharan PBL) from a cooler atmosphere with moderately stable stratification influenced by the Atlantic Ocean in the west. This raised the question as to what extent low-level zonal advection from the Atlantic Ocean affects the regional heat and moisture budgets in North Africa. For this purpose the COSMO model code was adapted to provide additional output of temperature and humidity tendency terms. By analysing the model output we discovered a major mesoscale system at the Mauritanian

[1] African Monsoon Multidisciplinary Analysis
[2] Consortium for Small-scale Modeling
[3] GERB Intercomparison of Longwave and Shortwave radiation
[4] Facility for Airborne Atmospheric Measurements

coast which appeared every day during GERBILS: the Atlantic Inflow.

In this thesis we apply the COSMO model in the south-west Saharan region. The thermo-hydrodynamical structure of the troposphere is examined by a combined analysis of airborne measurements and model data. The COSMO model is validated against observations. Then we use model data to analyse the Atlantic Inflow.

The outline of this thesis is as follows: In chapter 1 the AMMA programme is introduced and the West African monsoon system is explained. In chapter 2 the basic equations for the description of the atmosphere and the numerical implementation in the COSMO model are presented. In addition the code adaption for calculating the heat and moisture budgets is explained. The chapter closes with the model setup of the runs performed for this thesis. In chapter 3 the GERBILS campaign is introduced, including the description of our operational COSMO forecast and a description of the large-scale weather conditions. In chapter 4 the model output is validated against airborne measurements. The Atlantic Inflow is analysed systematically in chapter 5. The general description of the Atlantic Inflow is followed by the presentation of different modes, depending on the synoptic situation. Close attention is payed to the detection of the Atlantic Inflow in various meteorological quantities and to the vertical structure, including gravity waves induced at the head of the coastal front. Gravity current characteristics of the Atlantic Inflow are studied, before ideas of how the Atlantic Inflow affects the observed baroclinic zone and about the observation of nocturnal jets are presented. Finally all findings are brought together to give a coherent mechanism, explaining the Atlantic Inflow. In chapter 6 the role of the Atlantic Inflow is analysed in the regional heat and moisture budget. Finally the major results are summarised and open questions are discussed in chapter 7.

1.2 The AMMA research programme

[5] The economies in West Africa are highly dependent on rain-fed agriculture. Although recently some wet years were observed in the Sahel, the continuing dramatic change towards much drier conditions in the 1970s marks one of the strongest trends in climate during the last century. An increase in population and the vulnerability of rainfall-dependent economies let West Africa be one of the most drought-threatened and food-insecure regions in the world. The absence of sufficient rainfall and the abrupt change in available water resources had devastating impacts on the environment, societies, and economies.

We lack a detailed understanding of the dynamics and variability of the West African monsoon system. However, reasonable weather and climate prediction is crucial for the adaptation of societies and economies to natural resources and global change. Therefore the African Monsoon Multidisciplinary Analyses (AMMA) project was launched. AMMA aims to help African decision makers to ensure food security, public health, and to adapt agriculture.

It is known that numerical weather prediction in West Africa is poor compared to other regions in the world. This is partly due to the lack of a routine meteorological network and to an inability to simulate key elements of the West African monsoon. Skills and techniques have to be developed to improve weather forecasting. Also climate forecasting lacks an understanding of the multiscale interactions in the West African monsoon system. Progress in both weather and climate forecasting is essential for the adaptation of the African populations to variable weather and climate conditions. Thus to prevent devastating impacts of rainfall variability in West Africa the knowledge of the West African monsoon has to be improved. Along with enhancing the geophysical understanding of the West African Monsoon, AMMA tries to improve the environmental monitoring and develops strategies to manage food security, water resources, and public health. The AMMA research strategy aims to help the African populations to reduce their vulnerability to weather and climate impacts by improving their environmental risk decision processes. To ensure a long-lasting benefit, knowledge has to be transferred to local people and the African science community has to be closely involved in the project.

Furthermore, AMMA needs to link the scales at which geophysical and human processes act, integrating various disciplines. Therefore a detailed data basis is collected through an integrated field campaign. The long term observing period (LOP) from 2002 to 2010 serves to study interannual to decadal variability of the West African monsoon. The objective of the enhanced observing period is to document the annual cycle of weather conditions over a short climate transect from 2005 to 2007, linking the LOP and the special observing period. The latter provides a detailed dataset of specific processes and weather systems during the rainy and dry season of 2006.

Based on a French initiative AMMA is embedded in a large community of international scientists from a big number of institutions. It is an important aim to integrate the African research community to form groups of local experts who can advise decision makers. This study contributes to AMMA working package 2.1 “Convection and atmospheric dynamics”.

[5] based on “An introduction to AMMA” at `http://www.amma-eu.org` (retrieved 20 February 2008)

1.3 The West African monsoon

The West African monsoon is the second largest monsoon system on the earth. Major parts of West Africa from the Guinean coast in the south to the southern edge of the Sahara at 20°N and from Cap Verde in the west to the Ethiopian highlands in the east rely on the seasonal precipitation linked to the monsoon. The annual rainfall decreases from 2000 mm/year at the mountainous Guinean coast to less than 200 mm/year in the northern Sahel (Fig. 1.1). Highest amounts appear where the south-westerly monsoon flow is maximally onshore and hits major mountain ranges, such as the Guinean mountains in in the west or the Cameroon mountains in the east (Fink 2006).

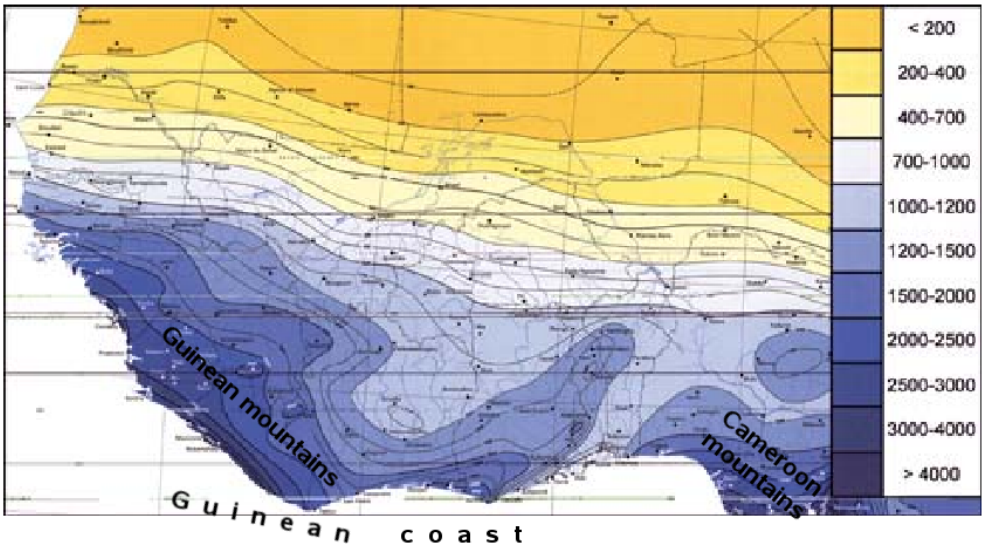

Figure 1.1: Fig. 2.3 from Fink (2006): mean annual rainfall [mm] for period 1951-1989, based on 890 stations in West Africa.

The West African monsoon results from the differential heating of the land and ocean surface in tropical North Africa. During the boreal summer the zone of maximal surface heating as well as the Inter Tropical Convergence Zone (ITCZ) is shifted northwards. As a consequence the rather cool and moist monsoon flow penetrates into West Africa. On a climatological view the ITCZ is the equatorial zone where strongest insolation occurs. This leads to a convective-driven circulation: in the ITCZ hot moist air ascends, resulting in a low-level equatorial trough. At the top of the troposphere the air moves polewards and partly subsides in the subtropics, forming the subtropical anticyclones. Here the air flows back in mid and low levels to the equatorial trough. The Coriolis force superposes the meridional flow with a zonal component. Poleward flow is linked with a westerly component, equatorward flow with an easterly component. Thus the low-level equatorward winds become the north-eastern and south-eastern so-called trade winds. In the ITCZ the northern and southern branch converges and deep moist convection occurs. These convective circulations are named Hadley cells[6]. However, the zenith of the sun migrates between the tropics of Cancer and Capricorn. The ITCZ follows the maximal insolation but lags around 4-6 weeks behind. Thus the latitudinal position of the Hadley cell shows

[6]after George Hadley who suggested their existence in 1735

a seasonal cycle. When the south-eastern trade winds overstep the equator in the boreal summer they turn into south-westerlies due to the the Coriolis force. This is the south-westerly monsoon flow which advects moisture inland on the tropical western coasts in the northern hemisphere and leads to the rainfall season (Holton 2004; Strahler and Strahler 2002; Schubert et al. 1991). In West Africa the north-eastern trade wind is also named Harmattan.

A characteristic of the West African monsoon is the sharp Inter Tropical Front (ITF), also referred to as Inter Tropical Discontinuity (ITD), which separates the dry Harmattan flow from the moist monsoon flow. The ITD marks the northernmost position of the monsoon layer. Here the latter is very shallow (partly less than 1000 m in vertical extent) and becomes deeper gradually towards the south. The ITD can easily be detected by low wind speed and approximated in low-level charts by the dew point difference $T - T_{dew} = 17\,K$. It is located at around 20°N in July/August. However, the actual ITCZ and deep moist convection occur approximately 10° further south. On a diurnal time scale the ITD shows a nocturnal northward progression of around 1°-2° latitude. The monsoon onset in West Africa is marked by an abrupt shift of the ITCZ from a quasi-stationary location at 5°N in May/June to 10°N in July/August, the so-called "monsoon jump". This is linked to the Saharan heat low (section 1.3.1), a shallow low-level pressure system over the Sahara desert (Sultan and Janicot 2003b,a; Ramel et al. 2006; Hagos and Cook 2007).

In the Sahelian part of West Africa (approximately 10°N-20°N) precipitation results predominantly from organised convection such as squall lines and mesoscale convective systems (MCS). Further south unorganised convection and synoptic-driven rainfall become more important (Fink 2006). Sultan et al. (2003) studied the intraseasonal variability of rainfall in the West African monsoon. Taylor et al. (2005, 2003) showed impacts of surface variability on precipitation in West Africa.

Another characteristic of the West African monsoon is the African easterly jet (AEJ) (section 1.3.3). The AEJ is a zone of strong easterly winds in the mid levels resulting from baroclinity between the rather cool monsoon air in the south and the hot desert air in the north. Instabilities in the AEJ lead to wave disturbances, the African Easterly Waves (AEW). It is well-known that major parts of severe hurricanes over the Atlantic Ocean originate from AEW and that AEW impact rainfall in West Africa. The dynamics of AEW have been investigated in many studies e.g. Thorncroft and Hoskins (1994a,b); Thorncroft (1995); Reed et al. (1977); Kiladis et al. (2006a,b); Thorncroft et al. (2003); Pytharoulis and Thorncroft (1999); Duvel (1990).

In this study we concentrate on interactions of atmosphere, land, and ocean in the south-western part of the Saharan heat low. Within this scope major components of the West African monsoon will be introduced in the following. These are: the Saharan heat low, the Saharan Planetary Boundary Layer, the African easterly jet and the diurnal cycle within the West African monsoon.

1.3.1 The Saharan heat low

The Saharan heat low is a shallow pressure system covering major parts of the Sahara desert. Vertically it extends from the surface up to approximately 700 hPa overlain by a strong subsidence due to the northern branch of the Hadley cell. The dry convective

heating and the descending vertical motion combined with adiabatic compression aloft are the major heat sources. Absorption of solar radiation through the presence of dust layers forms a secondary heat source. As a result a deep neutrally-stratified layer extends up to around 500 hPa in the Saharan heat low region (see section 1.3.2). General heat low dynamics are well-documented in the study of Racz and Smith (1999). The pressure minimum is the result of strong daytime insolation which heats the surface and low levels. A distinct diurnal cycle characterises the Saharan heat low: the pressure minimum occurs in the late afternoon following the maximum temperatures, the pressure maximum appears in the early morning. Nevertheless, the corresponding wind field lags around 9-12 hours behind, indicating that the system is not in geostrophic balance. The strong turbulent friction due to dry convection at daytime hinders horizontal flow. During the night turbulence vanishes and stable stratification becomes established in the low levels due to long wave radiation. The wind speed increases producing a low-level nocturnal jet and convergence into the heat low centre. At the southern edge of the Saharan heat low this nocturnal jet essentially contributes to the northward shift of the ITD and to moist advection from the south at nighttime. On the seasonal time scale the Saharan heat low was found to play a crucial role for the northward shift of the ITCZ at the time of the monsoon onset (Ramel et al. 2006; Sultan and Janicot 2003b,a). Furthermore, the Saharan heat low contributes to the maintenance of the AEJ (Thorncroft and Blackburn 1999).

1.3.2 The Saharan Planetary Boundary Layer

Extending from the surface up to 500 hPa the planetary boundary layer over the Sahara desert is one of the thickest in the world (Gamo 1996). We define the Saharan Planetary Boundary Layer (Saharan PBL) as this deep well-mixed layer above the Saharan desert. Two major internal layers are distinguishable. Whereas outgoing long wave radiation results in shallow stably-stratified low levels at nighttime, surface heating leads to turbulent mixing and dry convection at daytime. A well-mixed convective boundary layer (CBL) grows from the surface within the Saharan PBL, overlayed by the so-called Saharan residual layer (SRL) (Messager et al. 2007). At the edges of the Saharan heat low the Saharan PBL is elevated from the ground and can be transported over large distances. We name this elevated Saharan PBL the Saharan Air Layer (SAL). It is an important interface linking the Saharan surface to the atmosphere over the monsoon region and beyond. Figure 1.2 shows the vertical structure of the West African monsoon. Conserving the thermodynamic structure of the Saharan PBL, the SAL can be transported several thousands of kilometres over the Atlantic Ocean to South America and beyond. The boundaries of the SAL can be approximated as isentropic surfaces. In the upper SAL/Saharan PBL high amounts of relative humidity often result in shallow altocumulus. The top of the SAL/Saharan PBL is capped by a layer with strong stable stratification (Parker et al. 2005). Moreover the Saharan PBL often contains several fine layers characterised by distinct amounts of dust or humidity concentration (Messager et al. 2007). Despite the uplift due to synoptically forced strong low-level winds (Washington et al. 2006; Stanelle et al. 2007; Helmert et al. 2007), dust layers originate from various processes. As first results from the GERBILS campaign Marsham et al. (2007) found that mesoscale and boundary layer circulations affect dust uplift, layering, and transport.

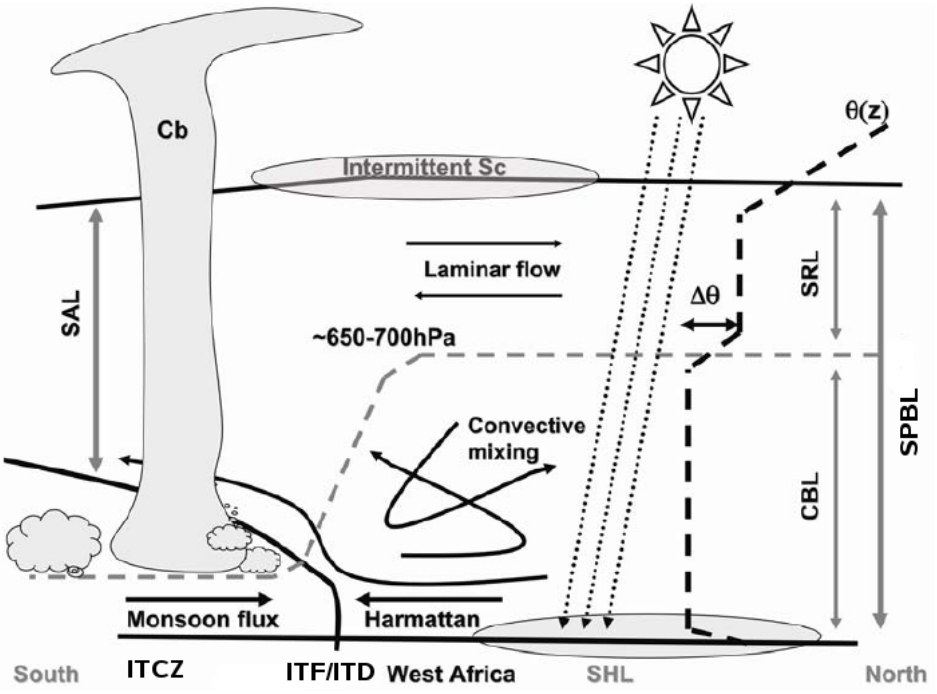

Figure 1.2: schematic latitude-height cross section of the West African monsoon from Messager et al. (2007). The grey dashed line marks the height of the convective boundary layer.

Moreover, Marsham et al. (2008) highlight the role of cold pools near the ITD. Dust uplift due to the gravity current characteristic of the monsoon head and due to downdraught of convective systems are subject of the studies from Flamant et al. (2007) and Bou Karam et al. (2008). Knippertz et al. (2007) highlight the impact of density currents originating from moist convection in the Atlas mountains on dust uplift. Following dust emission, mesoscale circulations within the Saharan PBL are responsible for the fine layering of the dust and the dust layers can be transported over long distances by the synoptic-scale flow.

In this thesis often a coarse classification of the troposphere is made by referring to the low levels ($p > 800\,\mathrm{hPa}$), mid levels ($800\,\mathrm{hPa} < p < 400\,\mathrm{hPa}$), and high levels ($p < 400\,\mathrm{hPa}$).

1.3.3 The African easterly jet

The African easterly jet (AEJ) is a midtropospheric wind speed maximum over Sahelian Africa during the boreal summer. Maximal easterly flow of around 10-15 m/s is reached at around 600 hPa and at 15°N (Fig. 1.3a) (Reed et al. 1977; Thorncroft and Blackburn 1999). Due to the vertical shear associated with the jet, it crucially affects the organisation of moist convection. A textbook explanation of the AEJ is given using the thermal wind relation. A baroclinic zone separates the rather cold, moist monsoon air in the Guinean zone (south of 5°N) from the hot, dry, and well-mixed air in the Saharan heat low region (17°N-30°N) (Fig. 1.3b,c). The temperature gradient weakens with height resulting in an easterly thermal wind. This is the AEJ. However, Thorncroft and Blackburn (1999) highlight that the maintenance of the AEJ cannot only be explained by

the baroclinity in the south. They suggest that both moist convection in the ITCZ and dry convection in the Saharan heat low region act to maintain the AEJ. This becomes evident when looking at the PV structure in the zonal-vertical cross section (Fig. 1.3d). The major features are a positive midtroposheric PV anomaly near 11°N associated with the ITCZ and a near-zero anomaly in the dry convective region of the Saharan heat low. The strong negative meridional PV gradient between these zones is consistent with the AEJ maximum. Only the combination of these two effects results in a realistic AEJ in the idealised model study of Thorncroft and Blackburn (1999). Parker et al. (2005) confirmed the presence and importance of the two convective regimes for the maintenance of the AEJ using JET2000 aircraft data. Furthermore, they emphasise the presence of three distinct layers in the AEJ region: the low-level monsoon layer, the SAL overlying it, and the free atmosphere above.

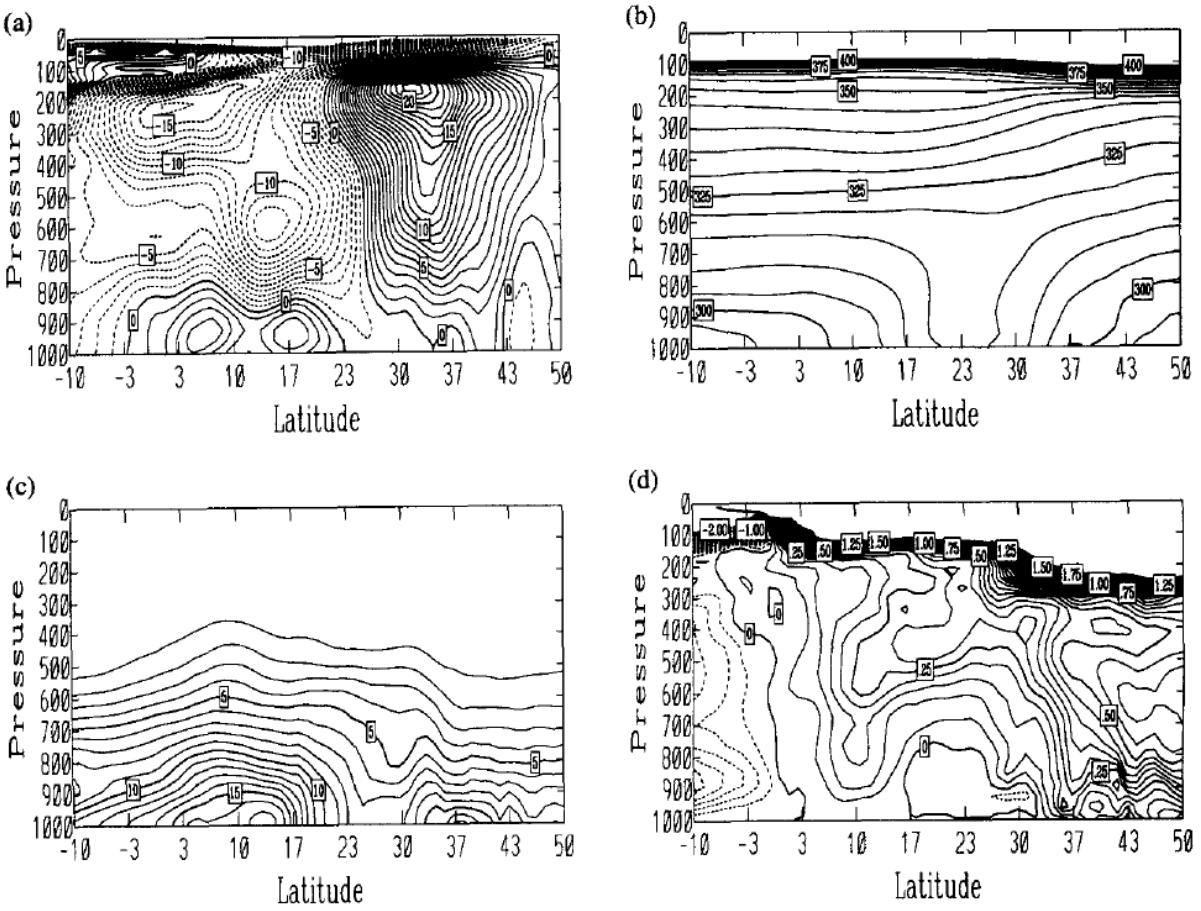

Figure 3. Latitude–pressure (mb) sections averaged between 10°W and 10°E over tropical north Africa, based on ECMWF analyses at 1200 UTC between 16 August and 31 August 1995. (a) Zonal wind, contour interval 1 m s^{-1} with dashed contours denoting easterlies; (b) potential temperature, contour interval 5 K; (c) specific humidity, contour interval 1 g kg^{-1}; (d) Ertel potential vorticity, contour interval 0.05 PV units (see Hoskins *et al.* 1985 for a discussion of PV units) with dashed contours denoting negative values.

Figure 1.3: Fig. 3 from Thorncroft and Blackburn (1999). latitude-height cross sections averaged from 10°W to 10°E. (a) zonal wind component [m/s], (b) potential temperature [K], (c) specific humidity [g/kg], and (d) Ertel potential vorticity [PVU]. Dashed contours denote negative values.

Finally, the AEJ is not a static system but mixed barotropically-baroclinically unstable (Thorncroft and Hoskins 1994a; Charney and Stern 1962). As a consequence, westwards wandering wave disturbances, the African Easterly Waves, evolve within the AEJ. These disturbances are the initial state of the major part of Atlantic and East Pacific hurricanes (Fink 2006).

1.3.4 Diurnal cycle in the West African monsoon

The diurnal cycle of the Saharan heat low and the diurnal cycle of the low-level convective boundary layer (CBL) impose a marked diurnal cycle on the West African monsoon (Parker et al. 2005). The CBL is not limited to the Saharan heat low region but also evolves as a shallower boundary layer south of the ITD within the monsoon layer at daytime. The monsoon flow is enhanced at nighttime in the absence of turbulent convection combined with low-level stable stratification. Horizontal advection of moist air towards the low pressure in the north increases. In contrast, at daytime the meridional flow is suppressed and vertical mixing of moist air in higher levels becomes more important. So the CBL helps to maintain the baroclinity between the monsoon and heat low region. Furthermore, the lifted air layers can be transported horizontally by isentropic upgliding during the night. This diurnal cycle has an important impact on the West African water budget.

2 The COSMO model

The Consortium for Small-scale Modeling (COSMO) model (Doms and Schättler 2002), formerly named Lokal-Modell (LM), is a non-hydrostatic regional weather prediction model. Initially designed at the Deutscher Wetterdienst (DWD) the model is enhanced and operationally run by the COSMO members and research institutions from various countries including Germany, Switzerland, Italy, Greece, Poland and Romania. The COSMO model together with the global model GME and corresponding assimilation schemes form the operational numerical weather prediction system at the DWD. The design of the COSMO model aims for resolving meso-β (5 km- 50 km) and meso-γ (500 m- 5 km) scales in both operational forecasts and scientific applications. The high resolution requires the implementation of the *non-hydrostatic* hydro-thermodynamical equations for compressible flow. The model equations are formulated in rotated geographical coordinates. A generalised terrain-following vertical coordinate is used. Various physical processes (e.g. sub-grid scale turbulence, moist convection, or radiation) are represented by parametrisation schemes.

2.1 Basic equations

The governing equations in the COSMO model start from the full Eulerian equations for a moist atmosphere. Turbulent motion is taken into account by Reynolds averaging. The application to small-scale meteorological systems requires the inclusion of vertical acceleration and thus a prognostic equation for vertical motion is used instead of a diagnostic relation. A set of non-hydrostatic fully compressible equations for the moist atmosphere is derived, including sound waves. The advantage of not filtering the acoustic waves is an independence from different scales and the adaptability to large model domains. Numerical efficiency is assured by a time-splitting scheme (see section 2.2). However, mass conservation is not guaranteed and depends on the numerical accuracy. Although no scale-dependent approximation is used, approximations of the thermodynamics are made for simplicity: molecular fluxes, except for diffusion of liquid and solid forms of water, are neglected as they are much smaller than turbulent fluxes. The molecular fluxes of liquid water and ice are approximated by sedimentation fluxes (precipitation). The specific heat of moist air is approximated with that of dry air. The effect of diffusion fluxes of water and phase changes on the pressure tendency equation are neglected. Also the buoyancy term in the heat equation and the mean dissipation rate due to viscous stress are neglected. This results in a set of tendency equations describing the evolution of the non-hydrostatic compressible mean flow. Prognostic variables are the three-dimensional wind components, pressure, temperature, and the water constituents:

$$\text{momentum} \qquad \rho\frac{d\vec{v}}{dt} = -\nabla p + \rho\vec{g} - 2\vec{\Omega}\times(\rho\vec{v}) - \nabla\cdot\mathbb{T} \tag{2.1}$$

$$\text{pressure} \qquad \frac{dp}{dt} = -\frac{c_{pd}}{c_{vd}}p\nabla\cdot\vec{v} + \left(\frac{c_{pd}}{c_{vd}} - 1\right)Q_h \tag{2.2}$$

$$\text{temperature} \qquad \rho c_{pd}\frac{dT}{dt} = \frac{dp}{dt} + Q_h \tag{2.3}$$

$$\text{specific humidity} \qquad \rho\frac{dq^v}{dt} = -\nabla\cdot\vec{F}^v - (I^l + I^f) \tag{2.4}$$

$$\text{cloud water} \qquad \rho\frac{dq^{l,f}}{dt} = -\nabla\cdot(\vec{P}^{l,f} + \vec{F}^{l,f}) + I^{l,f} \tag{2.5}$$

$$\text{equation of state} \qquad \rho = p\left[R_d(1 + q^v\left(\frac{R_v}{R_d} - 1\right) - q^l - q^f)T\right]^{-1} \tag{2.6}$$

$$\text{diabatic heating} \qquad Q_h = L_V I^l + L_S I^f - \nabla\cdot\left(\vec{H} + \vec{R}\right). \tag{2.7}$$

Here the variables stand for the following quantities:

$\rho = \sum_{x=d,v,l,f}\rho^x$	total density of air mixture
$x = d, v, l, f$	index for mixture constituent: dry air (d), water vapour (v), liquid (l), and frozen water (f)
ρ^x	partial density of mixture constituent x
$d../dt = \partial../\partial t + \vec{v}\cdot\nabla..$	total (Lagrangian) time derivative operator
$\partial../\partial t$	local (Eulerian) time derivative operator
$\vec{v} = (u, v, w)$	barycentric velocity relative to rotating earth
∇	gradient (Nabla) operator
p	pressure
$\vec{g}$	apparent acceleration due to gravity
$\vec{\Omega}$	constant angular velocity of earth rotation
$\mathbb{T} = \overline{\rho\vec{v}''\vec{v}''}$	Reynolds stress tensor (turbulent flux of momentum)
$\varphi = \overline{\varphi} + \varphi'$	Reynolds average where $\overline{\varphi}$ denotes the mean value and φ' the deviation
$\varphi = \widehat{\varphi} + \varphi''$	mass-weighted average where $\widehat{\varphi}$ denotes mass-weighted mean and φ'' the deviation from $\widehat{\varphi}$
c_{pd}, c_{vd}	specific heat of dry air at constant pressure, volume
Q_h	diabatic heating/cooling
T	temperature
$q^x = \rho^x/\rho$	mass fraction of constituent x
$\vec{F}^x = \overline{\rho\vec{v}''q^x}$	turbulent flux of water constituent x
$I^{l,f}$	phase transition rate for liquid water and ice

$\vec{P}^{l,f} = \rho q^{l,f} \vec{v}_T^{l,f}$	precipitation flux for liquid water and ice
$\vec{v}_T^{l,f}$	terminal velocity of constituent l, f
R_d, R_v	gas constants for dry air, water vapour
L_V, L_S	latent heat of vaporisation and sublimation
$\vec{H} = c_{pd}\overline{\rho \vec{v}'' T}$	turbulent flux of sensible heat
$\vec{R}$	flux of solar and thermal radiation

2.2 Model layout and implementation

The set of equations introduced in the previous section is valid for any coordinate system rotating with the earth. It is transformed into geographical coordinates and a generalised terrain following vertical coordinate. A model base state is introduced assuming horizontal homogeneity, stationarity, and hydrostatic balance. Thus a variable ψ at a specific location is described as the sum of its base state plus a deviation: $\psi(\lambda, \varphi, z, t) = \psi_0(z) + \psi'(\lambda, \varphi, z, t)$ where λ denotes geographical longitude, φ latitude, z height, and t time. Furthermore, the reference state is prescribed to be dry and at rest. It follows $u, v, w, q^x(\lambda, \varphi, z, t) = u', v', w', q'^x(\lambda, \varphi, z, t)$ and $T, p, \rho(\lambda, \varphi, z, t) = T_0(z), p_0(z), \rho_0(z) + T', p', \rho'(\lambda, \varphi, z, t)$. The profiles of reference temperature $T_0(z)$, pressure $p_0(z)$, and density $\rho_0(z)$ are prescribed, also.

The continuous equations (2.1)-(2.7) are transformed into a discretised form using finite differences of second order. This form is solved on a regular and rectangular computational grid. The COSMO model uses a box model with an Arakawa-C/Lorenz staggered grid in rotated geographical coordinates. Scalars are defined at the centre of a grid box and the velocity components normal to the corresponding box faces. The temporal integration is effected using a leapfrog method. The presence of meteorologically unimportant acoustic waves severely limits the time step of integration due to their fast propagation speed (CFL criterion $u\Delta t/\Delta x < 1$ must be fulfilled to ensure numeric stability, u propagation speed, Δt time step, Δx horizontal grid scale). To assure numeric efficiency a time-splitting scheme following Klemp and Wilhelmson (1978) is employed: the prognostic equations are separated into terms which are directly linked to fast sound waves and into comparatively slow modes of motion. The time step of the slow modes is divided into a number of small time steps, and fast terms are computed every small time step while slow terms are only computed every large time step. This makes the explicit time integration more efficient, as only a limited set of equations has to be solved on the small time step. Sound wave modes are related to the divergence term in the pressure tendency equation (Eqs. (2.2) and (2.3)), to the pressure gradient force in the horizontal equation of motion, to the buoyancy term due to p' in the equation for vertical motion (Eq. (2.1)), and to the vertical advection of p_0 in Eq. (2.2).

An important step of the numerical solution is to provide initial data fields and to adjust the model boundaries regularly. External datasets (from e.g. a lower-resolved global model or another COSMO run (nesting)) provide the initial data. The boundary conditions are either updated periodically or updated from an external data set. The external data are interpolated on the model grid using the preprocessor programme INT2LM. A

lateral boundary relaxation scheme after Davies (1976, 1983) is employed to avoid numerical noise at the boundaries. Linear fourth-order horizontal diffusion is used as a numerical filter. Rayleigh damping is applied at the upper model levels.

The numerical solution requires the representation of all physical processes. As a complete calculation of all processes is time-consumptive, parametrisation schemes are employed. The parametrisation of radiation and radiative absorption follows Ritter and Geleyn (1992). Eight spectral intervals are introduced, in which absorption in each is assumed to be constant.

Sub-grid scale turbulence links the resolvable to the nonresolvable fluctuations of motion. The turbulent fluxes represent the exchange of momentum, heat, and humidity between the surface and the free atmosphere thus being crucial for a correct numerical simulation. Horizontal components are neglected assuming horizontal homogeneity. The calculation of the vertical turbulent diffusion is based on a second-order K-closure (Mellor and Yamada 1974) and solved using a semi-implicit Crank-Nicolson scheme. This yields in a joint system of equations for vertical advection and turbulent diffusion.

Grid scale precipitation is treated using a Kessler-type bulk approach. The Tiedtke (1989) mass-flux scheme is employed to describe moist convection. Further processes e.g. cloud microphysics, soil model, and the surface fluxes are parametrised. Also surface properties e.g. surface height, vegetation, or land use are prescribed with an external constant data set. For more details we refer to the model documentation Doms and Schättler (2002) and references herein.

2.3 Code adaptation for heat and moisture budgets

Heat and moisture budgets enable a better understanding of physical processes. However, standard model output only represents a limited number of processes. We adapted the COSMO model code (version LM 3.19) to provide all individual terms of the temperature (T) and specific humidity (q^v) tendency equation. The equations are given in Doms and Schättler (2002) page 49 Eqs. 3.147 and 3.148. They are repeated in note form:

$$\begin{aligned}\frac{\partial T}{\partial t} =& HADV_T + VADV_T + FAST_T + MTD_T + RAD_T + MMC_T + SQ_T \\ &+ MCM_T + MLB_T + MRD_T\end{aligned} \tag{2.8}$$

$$\begin{aligned}\frac{\partial q^v}{\partial t} =& HADV_{q^v} + VADV_{q^v} + MTD_{q^v} + MMC_{q^v} + SQ_{q^v} \\ &+ MCM_{q^v} + MLB_{q^v} + MRD_{q^v}\end{aligned} \tag{2.9}$$

Here the expressions stand for tendencies due to physical processes ($i = T$, q^v):

$HADV_i$: horizontal advection
$VADV_i$: vertical advection
$FAST_i$: fast-waves (only $i = T$)
MTD_i : turbulent mixing
MMC_i : sub-grid scale moist convection
RAD_i : solar and thermal radiation (only $i = T$)
SQ_i : cloud condensation and evaporation

and for tendencies due to the numerical filters ($i = T$, q^v):

MCM_i : computational mixing (horizontal diffusion)
MLB_i : lateral boundary relaxation
MRD_i : Rayleigh damping scheme within upper boundary

Thus the physical processes contributing to the local temperature tendency are horizontal and vertical advection, the "fast wave" term, turbulent diffusion, radiation, grid scale cloud microphysics, sub-grid scale moist convection, and the numerical filters (cf. Eq. (2.3)). The fast wave term represents temperature changes due to pressure changes and thus due to the divergence of the wind field (cf. Eqs. (2.2) and (2.3)). The physical processes contributing to the local tendency of specific humidity are identical, except for the absence of a radiative and fast wave tendency (cf. Eq. (2.4)). A technical documentation of the code adaptations is available on request. In the following, we name the adapted COSMO version "COSMO_budget" while "COSMO" refers to the original unchanged model code. In the next section the temperature tendency equation is discussed in more detail and formulated for potential temperature, as the latter is more convenient for meteorological investigations.

2.3.1 Tendencies of potential temperature

In COSMO the heat equation is formulated as a temperature tendency equation which is derived from the first law of thermodynamics:

$$\frac{dT}{dt} = \frac{\partial T}{\partial t} + \vec{v} \cdot \nabla T = \frac{1}{\rho c_p} \left(\frac{dp}{dt} \right) + Q_T, \tag{2.10}$$

T denotes the temperature, $\vec{v}$ the three-dimensional wind vector, ρ the air density, c_p the specific heat, p the air pressure, and Q_T the diabatic heating term (Eqs. (3.65) and (3.134) from Doms and Schättler (2002)). Q_T includes the contributions of turbulent diffusion (sensible heat flux) (MTD_T), radiation (RAD), sub-grid scale moist convection (SQ_T), grid scale moist convection (MMC_T) and computational effects ($COMP_T = MCM_T + MLB_T + MRD_T$):

$$Q_T = MTD_T + RAD + SQ_T + MMC_T + COMP_T \tag{2.11}$$

The set of model equations contains sound waves as part of the solution. Because of their comparatively fast propagation these fast waves limit the time step of time integration. A mode-splitting scheme after Klemp and Wilhelmson (1978) is used to improve efficiency. In the temperature tendency equation the term $FAST = \frac{1}{\rho c_p} \frac{dp}{dt}$ is related to fast waves. We rewrite Eq. (2.10) using a note form:

$$\frac{\partial T}{\partial t} = \quad HADV_T + (VADV_T + FAST) + MTD_T + RAD + MMC_T + SQ_T + COMP_T, \tag{2.12}$$

where $HADV_T = -\vec{v_h} \cdot \nabla_{h,p} T$ stands for horizontal and $VADV_T = -\omega \frac{\partial T}{\partial p}$ for vertical advection in pressure coordinates, h denotes the horizontal components of a vector.

As it is more convenient to analyse the budget of potential temperature $\Theta = T\left(\frac{p_0}{p}\right)^{R/c_p}$ we transform Eq. (2.12) into a prognostic equation for Θ:

$$\frac{d\Theta}{dt} = \frac{\Theta}{T}\left[\frac{dT}{dt} - \frac{1}{\rho c_p}\frac{dp}{dt}\right] \overset{(2.10)}{=} \frac{\Theta}{T}Q_T \tag{2.13}$$

$$\Leftrightarrow \frac{\partial\Theta}{\partial t} = -\vec{v_h}\cdot\nabla_{h,p}\Theta - \omega\frac{\partial\Theta}{\partial p} + \frac{\Theta}{T}Q_T, \tag{2.14}$$

where $\omega = dp/dt$ is the vertical velocity in pressure coordinates.
With $HADV_\Theta = -\vec{v_h}\cdot\nabla_{h,p}\Theta = -\vec{v_h}\cdot\nabla_{h,p}\left[T\left(\frac{p_0}{p}\right)^{R/c_p}\right] = \frac{\Theta}{T}\left[-\vec{v_h}\cdot\nabla_{h,p}T\right] = \frac{\Theta}{T}HADV_T$ and $VADV_\Theta = -\omega\frac{\partial\Theta}{\partial p} = -\omega\frac{\Theta}{T}\left[\frac{\partial T}{\partial p} - \frac{1}{\rho c_p}\right] = \frac{\Theta}{T}\left[-\omega\frac{\partial T}{\partial p} + FAST\right] = \frac{\Theta}{T}\left[VADV_T + FAST\right]$ we can express horizontal advection of Θ with the help of horizontal temperature advection and vertical advection of Θ by the sum of vertical temperature advection and the FAST wave term in the temperature equation. In conclusion, the local tendency of potential temperature is given by:

$$\frac{\partial\Theta}{\partial t} = \frac{\Theta}{T}\left[HADV_T + (VADV_T + FAST) + MTD_T + RAD + MMC_T + SQ_T + COMP_T\right] \tag{2.15}$$

2.4 Model setup

Version LM 3.19 of the COSMO model was used in this thesis. Model runs were performed on the HP XC1 supercomputer of the Scientific Super Computing Center[1] at the University of Karlsruhe. In this section the external model specifications (model grid, initial and boundary conditions, temporal resolution) will be described as used for the different runs performed for this thesis. The model grid is restricted by computer resources, and horizontally limited to 50 000 grid points when using 35 levels vertically.

2.4.1 Operational forecast for GERBILS

From 18 June 2007 to 30 June 2007 we ran an operational COSMO forecast twice daily. The purpose of this was to provide a mesoscale forecast for West Africa as a support to GERBILS flight planning, to test the model performance in a desert environment, and to collect a set of model runs for further analysis.

The choice of the model domain was based on practical considerations e.g. covering the flight area and scientific considerations e.g. with respect to major meteorological systems and topography. The horizontal domain runs from 17°W to 2°E and from 13°N to 23°N (305x161 grid points) covering major parts of Mauritania, Senegal and Mali, thus most of the flight domain. Also the model domain covers an area in which interaction takes place between the Saharan heat low in the north, the monsoon flow in the south, and the atmosphere influenced by the Atlantic Ocean in the west. The horizontal grid spacing is 0.0625° (approximately 7 km). This is small enough to resolve major mesoscale systems while allowing a sufficient spatial extent. The model domain for GERBILS forecasts is indicated by the red box in Fig. 2.1.

[1] `http://www.rz.uni-karlsruhe.de/ssck/4141.php` (retrieved 15 February 2008)

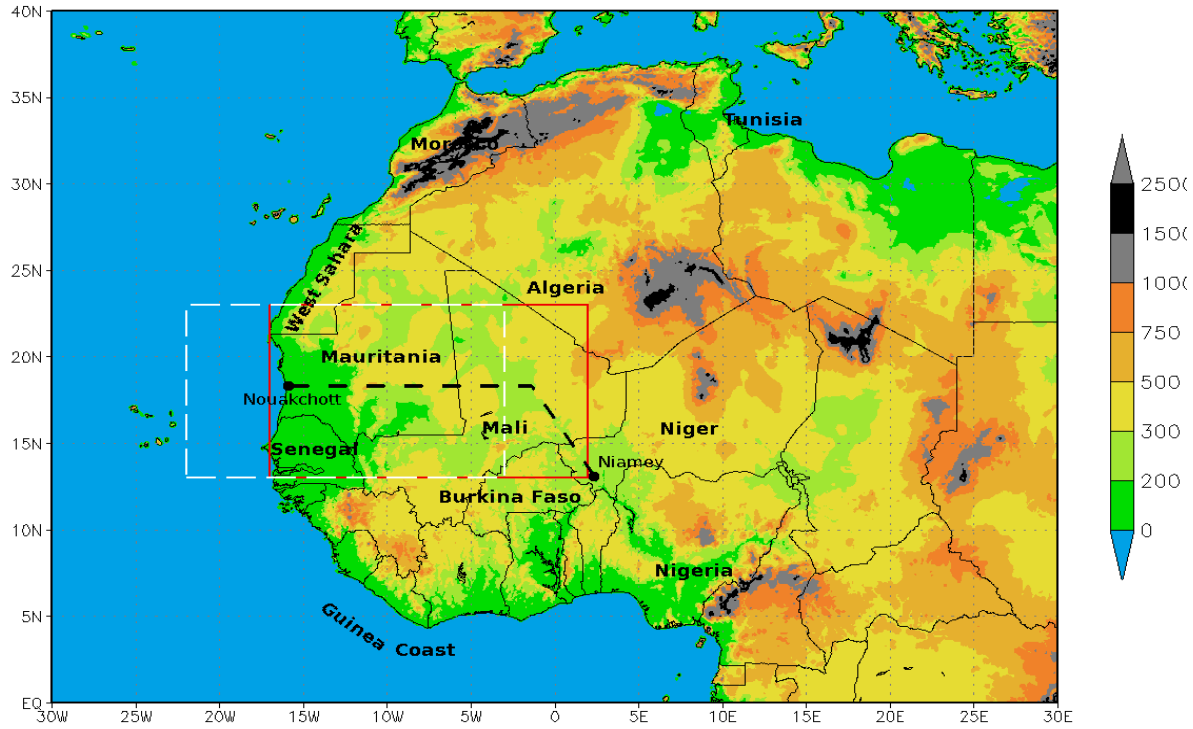

Figure 2.1: West Africa: political boundaries, COSMO orography [m above mean sea level] (0.0625° resolution), GERBILS flight track (black dashed line), COSMO model domain for GERBILS forecast (red) and shifted domain for analysis of 24 June 2007 (white).

The external constant data (surface height, land usage, etc.) on the 7 km grid was provided by the German Weather Service (DWD). A 69 hour COSMO forecast was computed for the domain specified above twice daily during GERBILS. Initial and boundary conditions were taken from the ECMWF[2] global forecast system with 0.25° horizontal resolution. COSMO was initialised with the ECMWF operational analysis at 00 UTC[3] and 12 UTC. Boundary conditions were updated every 3 hours using the ECMWF operational forecast. COSMO output was stored every full hour of the 69 hour forecast. The internal time step was 40 seconds.

The operational COSMO forecast for the GERBILS campaign was a challenging task. The whole process from the initial/boundary data retrieval to generating plots and to making them accessible on a website had to be automated. We could not count on manual intervention as it was not guaranteed that internet and remote access on-site in West Africa was available reliably. Furthermore, the process was time-critical as the most recent forecast had to be available before the flight planning meetings in the afternoon and morning. Data had to be transferred between and computed on computers in 3 different time zones. Each task was not only statically time controlled but also dynamically observing and waiting for the previous tasks on other machines to be completed. Finally computing resources had to be available on the supercomputer as soon as needed. Altogether, this made the forecast complex. Table 2.1 shows a simplified schedule of the automated operational forecast. Generally ECMWF data were available 8.5 hours after the specific initialisation time (00, 12 UTC). The COSMO run and the generation of

[2]European Centre for Medium-Range Weather Forecasts
[3]Coordinated Universal Time, see Table 3.1 for relation to solar time

weather forecast plots took a further 5.5 hours. Plots of the operational COSMO weather forecast were accessed via the internet[4]. Thus, model output was available at 14:00 UTC based on the 00 UTC initialisation time and 2:00 UTC based on the 12 UTC initialisation time.

This was just in time to analyse the most recent forecast before the flight planning meetings at 15:30 UTC and 8:00 UTC, respectively. The working group in Leeds met every day to discuss the COSMO forecasts and the weather situation in West Africa. In their summaries of the weather conditions they gave our group in Niamey crucial hints on interesting meteorological features. This teamwork enabled us to suggest modifications of the flight plans on-site in order to observe these features. For example, COSMO forecast essentially helped to adapt flight plans and dropsondes on 24 June 2007. Thus, a baroclinic zone which was predicted by the model could be captured well in the observations (see section 4.1).

Table 2.1: schedule of the operational COSMO forecast during GERBILS 00 UTC initialisation time. Comp.: computer name, location of the computer. Local time of computer in bold font.

UTC	**+1**	**+2**	**comp.**	**location**	**task**
8:30	9:30	10:30	MARS	Reading, UK	ECMWF data retrieval: copy from MARS to see-gw-01 (Leeds)
9:30	**10:30**	11:30	see-gw-01	Leeds, UK	data transfer: from see-gw-01 to imk-clyde (Karlsruhe)
9:35	10:35	**11:35**	imk-clyde	Karlsruhe, D	data transfer: from imk-clyde to xc1 (Karlsruhe)
9:40	10:40	**11:40**	xc1	Karlsruhe, D	preprocessing: wait for last input file
9:42	10:42	**11:42**	xc1	Karlsruhe, D	preproc.: generate input for int2lm
9:45	10:45	**11:45**	xc1	Karlsruhe, D	preprocessing: run int2lm
10:00	11:00	**12:00**	xc1	Karlsruhe, D	**start COSMO forecast**
13:50	14:50	**15:50**	xc1	Karlsruhe, D	finished copying model output to imk-tyne (Karlsruhe)
13:30	14:30	**15:30**	imk-tyne	Karlsruhe, D	post-proc.: prepare data for GrADS
13:40	14:40	**15:40**	imk-tyne	Karlsruhe, D	post-processing: generate plots using GrADS
14:00	15:00	**16:00**	imk-tyne	Karlsruhe, D	**plots published on website**
14:30	**15:30**	16:30	local PC	Niamey, RN Leeds, UK	analyse forecast/think about suggestions for flight track
15:30	16:30	17:30	local PC	Niamey, RN	**flight planning meeting**, specification of flight track

[4] `http://imk-tyne.physik.uni-karlsruhe.de/~christian/`

2.4.2 Analysis of the Atlantic Inflow

A tilted baroclinic zone combined with a sea-breeze phenomenon at the Mauritanian coast will be investigated in more detail in chapters 4 and 5. Therefore COSMO_budget (section 2.3) was run for 24 and 28 June 2007 in the same configuration (model domain, external, initial and boundary data, forecast times) as the COSMO forecast described in the previous section. This should assure consistency with the prior operational forecasts.

The western boundary of the GERBILS forecast domain is rather close to the coast. A sensitivity study was performed to ensure that the western model boundary does not affect meteorological fields at the Mauritanian coast. The model domain was shifted 5° westwards as indicated by the white dashed box in Fig. 2.1. The meteorological fields were compared where the domains overlap. Only very small differences in the fields could be found. This is illustrated in Fig. 2.2 showing the horizontal gradient of potential temperature and relative vorticity. The main features are a longitudinal band of increased potential temperature gradient approximately 1° in longitude onshore and a second almost zonal band along 16°-17°N, the latter linked with increased relative vorticity. These structures are detectable at nearly the same location in both model configurations.

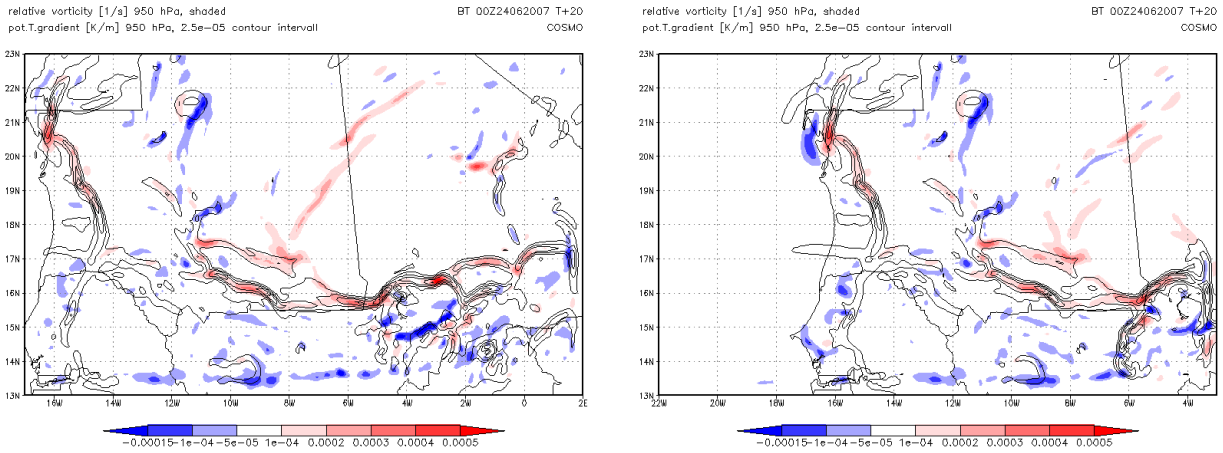

(a) original model domain (b) domain shifted 5° westwards

Figure 2.2: COSMO forecast 19 UTC 24/06/2007 for different domains initialised 00 UTC the same day. Horizontal potential temperature gradient [K/m] (2.5×10^{-5} contour interval), relative vorticity [1/s] (shaded). Both at 950 hPa.

This sensitivity study confirms that the western model boundary of the original model domain has an insignificant impact on the meteorological fields at the Mauritanian coast. Therefore the model data for either of the domains can be used to investigate the Atlantic Inflow. The model output of the COSMO_budget run initialised at 00 UTC 24/06/2007 for the shifted domain will be used to analyse the Atlantic Inflow in the first period. To avoid an extra model run the model output of the COSMO_budget run initialised at 00 UTC 28/06/2007 for the standard domain will be used to analyse the Atlantic Inflow in the second period.

3 The GERBILS campaign

The GERBILS[1] field campaign was organised by the United Kingdom Met Office from 18 to 29 June 2007. Eight transects over the south-western Sahara were conducted with the Facility for Airborne Atmospheric Measurements (FAAM) BAe 146-301 aircraft. The COSMO model was used to provide an operational forecast. In this chapter the campaign is presented including a description of the meteorological situation in West Africa during the campaign.

3.1 Overview

Haywood et al. (2005, 2007) found a discrepancy in clear sky top of atmosphere outgoing long wave radiation over the south-western Sahara desert when comparing data from the UK Met Office Unified Model to satellite data from the Meteosat-8 GERB (**G**eostationary **E**arth **R**adiation **B**udget Experiment) or Meteosat-7 instrumentation (Fig. 3.1). The discrepancy is largest from June to August. Haywood et al. (2007) assume that a lack of mineral dust in the model, errors in albedo and surface emissivity, and errors in model cloud fields contribute to this discrepancy. Airborne measurements of the physical and optical properties of mineral dust, radiation, and surface properties can be used to test and refine the model dust climatology and the model parametrisations. To this aim the GERBILS campaign took place in West Africa around the end of June 2007. At this time of year the monsoon is in its onset phase but the total cloud cover is still low compared to July or August. Clear sky conditions are essential for radiation measurements.

GERBILS exhibits a unique opportunity to obtain a dataset of in situ measurements for studying the Saharan heat low. The scientific flights took place over the southern part of the Saharan heat low where interaction with the monsoon flow takes place. In this region there is generally no in situ data available. Furthermore, GERBILS enabled us to test the COSMO model in a desert environment.

The measurements were effected with the FAAM BAe 146. The aircraft was equipped with instruments to observe the standard meteorological quantities, aerosol optical and physical properties, some air chemistry, terrestrial and solar radiances, and with dropsondes to obtain profiles of temperature, humidity, and wind. Dropsondes released from the aircraft were assimilated by the ECMWF assimilation system.

Three two-leg flights along 18°N, thus over the maximum of the discrepancy noted by Haywood et al. (2007), were conducted from an eastern base in Niamey, Niger, (2.06°E, 13.27°N) and a western base in Nouakchott, Mauritania, (15.95°W, 18.10°N) along 18°N (Figs. 2.1 and 3.2). Flight tracks and times were synchronised with satellite overpasses,

[1] **G**eostationary **E**arth **R**adiation **B**udget Experiment **I**ntercomparison of **L**ongwave and **S**hortwave radiation

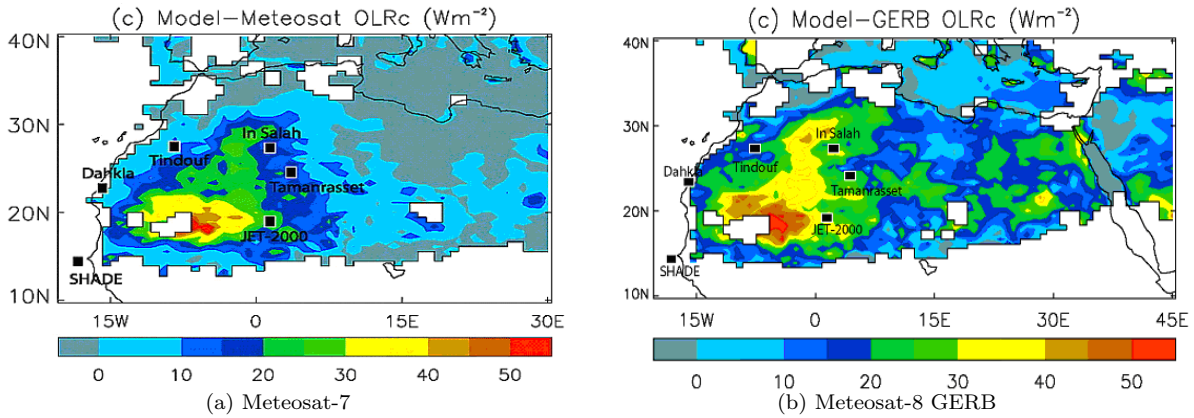

Figure 3.1: Fig. 1 from Haywood et al. (2007): discrepancy of clear sky top of atmosphere outgoing long wave radiation between Unified Model and satellite data.

whenever possible. Furthermore, two scientific transit flights over the Sahara desert were carried out. The meteorological data from aircraft and dropsondes are of primary interest in this thesis.

As described in section 2.4.1, a 69h COSMO forecast was computed twice daily during the GERBILS campaign. Figure 3.2 shows the orography in the model domain, which extends over the flight area. The usual flight track between Nouakchott and Niamey along 18°N is indicated by a black dashed line. The domain covers major parts of Mauritania (in the west of the domain), Senegal (in the south-west) and Mali (in the south and east). The vast coastal plain in western Mauritania and Senegal is one of the most striking geomorphological features. Its extent is from south of the southern model boundary at 13°N to 20°N in the north, and from the coast at around 16.5°W to approximately 12°W. The terrain is flat and ascends gradually to 200 m above sea level at the foot of the Tagant Mountains at 12°W. The Mauritanian part of the plain is almost entirely covered by bare soil. The land surface is characterised by sandy and stony desert environment.

The Tagant Mountains are located 400 km inland and form the first orographic barrier east of the Atlantic coast. At 12°W the terrain suddenly increases to 400-600 metres above mean sea level. The mountain range is oriented in a north-south direction from 15°N to 19°N. In the northern part (18-19°N) it extends eastwards to 10°W. A rather flat plateau of 300-400 m height follows east of the Tagant Mountains. North of 20°N, in West Sahara, the coastal plain is only a narrow band and the terrain becomes hilly a few kilometres inland. Other orographic features such as a mountain range north of the Tagant in Mauritania, the foothills of the Ahaggar Mountains in Mali and Algeria and mountain ranges in Mali are of less importance for this study. Table 3.1 gives an overview of the time (in GMT[2]) of sunrise and sunset at interesting points in the model domain. These points are highlighted by red dots in Fig. 3.2.

[2]Greenwich Mean Time, GMT≈UTC

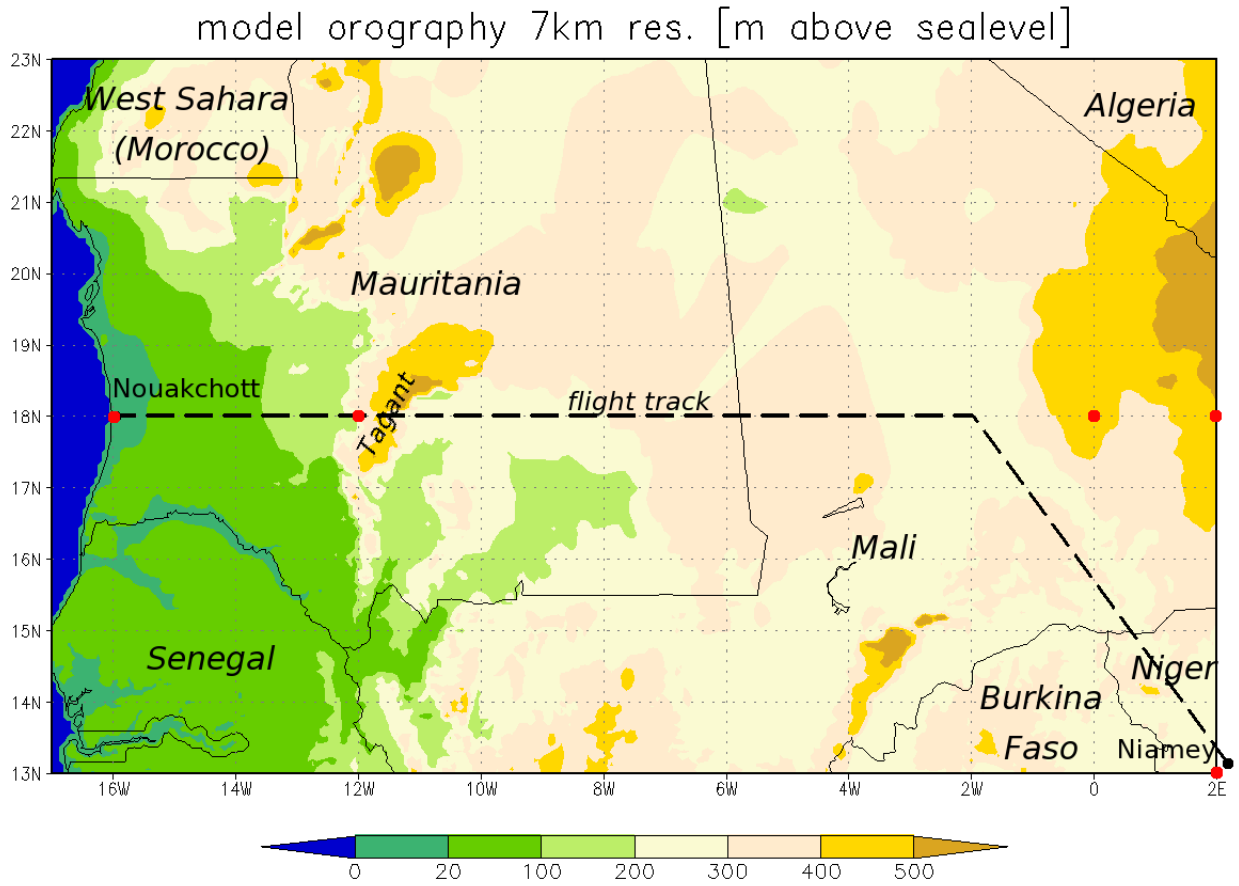

Figure 3.2: model domain COSMO forecast. Model orography, 7 km resolution (height in metres above mean sea level). Political boundaries in black thin lines. Black dashed line: flight track. Black dots: location of capitals. Red dots: points for which sunset/sunrise is given in Table 3.1.

Table 3.1: times of sunrise/sunset [hh:mm GMT] for 24/06/2007 at specific points (calculated at `http://www.met.reading.ac.uk/~ross/Astronomy/RiseSet.html` on 15 February 2008).

name	**LON [°E]**	**LAT [°N]**	**sunrise**	**sunset**
Nouakchott	-16.0	18.0	06:25	19:37
Tagant	-12.0	18.0	06:09	19:21
-	0.0	18.0	05:21	18:33
-	2.0	18.0	05:13	18:25
Niamey	2.0	13.0	05:22	18:16

3.2 Synoptic conditions during GERBILS

In this section the weather conditions will be described for 21-29 June 2007 which is the core period of the GERBILS campaign. Emphasis is placed on the large- and synoptic-scale as well as the diurnal cycle of major features.

3.2.1 Large-scale conditions

The description of the large and synoptic-scale weather situation is based on the ECMWF operational analysis at 18 UTC. Parker et al. (2005) showed that the analyses at 06 UTC and 18 UTC are better suited to describe the West African monsoon than that at 12 UTC. The use of morning and evening analysis respects the diurnal cycle of the West African monsoon (section 1.3.4). In the evening the Saharan heat low has its minimum pressure. This time of the day is sufficent for giving an overview of changes in the large-scale flow. The diurnal cycle will be illustrated in section 3.2.2 using analyses at 06 UTC and 18 UTC.

The geopotential and wind vectors at 700 hPa, the 2 m temperature and mean sea level pressure, and the specific humidity and wind vectors at 1000 hPa are given in Figs. 3.3 and 3.4. The section (5°N-40°N, 25°W-10°E) covers major parts of North and West Africa. The COSMO forecast domain is indicated in red outline.

A mid-latitude trough over Spain is an important feature in the mid levels during GERBILS (Figs. 3.3 and 3.4), as it affects parts of North Africa. On 21 June 2007 the trough causes a cyclogenesis in the lee of the Atlas Mountains (29°N, 5°W). This becomes evident in a cut-off low indicated by the 315 gpdm contour line at 700 hPa (Fig. 3.3a). The trough separates the Azores Anticyclone in the west from another mid-level high pressure system over Tunisia, Libya, and the western Mediterranean Sea. A ridge of the Azores Anticyclone extends across the northern part of the GERBILS domain with the ridge axis oriented west-eastwards at around 21°N. The 700 hPa geopotential height decreases towards the equator, associated with a zonal African easterly jet south of 18°N. The Saharan heat low centre lies over central Algeria (24°N-33°N, 4°W-8°E). Here the mean sea level pressure is less than 1004 hPa and the 2 m temperature exceeds 315 K (42°C) and reaches 318 K (45°C) locally (Fig. 3.3b). In the low-level fields a rather zonal band of high 2 m temperature ($T_{2m} > 312$ K) is striking from the Mauritanian coast over Mali to central Niger (16°N-20°N, 16°W-9°E). This is linked with a low surface pressure and can be seen as a heat trough. The closed 1004 hPa isobar in south-eastern Mauritania (15°N, 8°W) indicates a secondary heat low. The location of the ITD can be estimated roughly by the 0.008 kg/kg contour line of specific humidity which coincides with the change from blue to green shading and confluence of low-level winds. On 21 June the ITD lies far south at around 15°N (Fig. 3.3c).

One day later the lee cyclone became a strong cut-off low, dominating the 700 hPa flow in Northwest Africa (Fig. 3.3d). The ridge over the flight domain weakened dramatically. A weak African Easterly Wave (AEW) is evident in the geopotential and in the flow at 700 hPa. The trough is located at 10°W, indicated by south-easterly flow south of 15°N, east of 10°W, and north-easterly flow south of 15°N, west of 10°W. The secondary heat low ($T_{2m} > 312\,K$, $p_{min} < 1004\,hPa$) becomes the dominant low-level feature over south-west Mauritania and Senegal (Fig. 3.3e). The Saharan heat low extends over Algeria, Northern

Mali and Niger. Eastwards of the AEW cooler air ($T_{2m} = 309\,\mathrm{K}$ isotherm in Fig. 3.3e) is evident in the low levels as well as a northward penetration of the ITD ($q^v = 0.008\,\mathrm{kg/kg}$ isoline in Fig. 3.3f). This could be due to enhanced advection towards the secondary heat low.

On 23 June 2007 the cut-off low retreats westwards. A ridge from the Mediterranean anticyclone reintensifies and extends into the northern part of the GERBILS domain (Fig. 3.3g). The secondary heat low weakens but is still evident in a closed 1006 hPa isobar over western Mauritania (Fig. 3.3h). This seems to lead to a northward penetration of the monsoon flow between 13°W and 10°W. The 0.008 kg/kg contour line of specific humidity reaches 20°N at 12°W while the ITD slowly retreats to around 16°N in the eastern part of the GERBILS domain (Fig. 3.3i). The Saharan heat low wanders southwards and is seen over southern Algeria, Mali, and Niger.

Moist air up to 20°N in western Mauritania (from the coast to 12°W) is a prominent feature on 24 June 2007 (Fig. 3.3l). The moist layer reaches up to 700 hPa (see chapters 4 and 5) and is a remnant of the monsoon penetration from the south the day before. It is not advected from the Atlantic Ocean as might have been expected from Fig. 3.3l. East of 12°W the ITD is pushed back south to 16°N. At 700 hPa the ridge extends further to the south-west (Fig. 3.3j). The second heat low over Mauritania decayed. The pressure gradient over western Mauritania is rather homogenous and is directed from the coast towards the centre of the Saharan heat low over Mali (Fig. 3.3k). An ageostrophic onshore wind is prominent at the Mauritanian coast (Fig. 3.3l). This leads to an inland penetration of the 306 K isotherm in western Mauritania (Fig. 3.3k). The Saharan heat low centre wandered westwards into Mali and Mauritania. The 2 m temperature reached its maximum here, intensifying the meridional temperature gradient at 18°N.

The 2 m temperature at the Mauritanean and Northwest African coast is linked to the cold Canary current (see section 5.1, Fig. 5.2). As a result the 2 m temperature over the Atlantic Ocean and at the coast often does not exceed 297 K although insolation is strong at these low latitudes (e.g. Fig. 3.3b-k).

On 25 June a ridge at 700 hPa covers most of Northwest Africa (Fig. 3.4a), leading to a strong and zonal African easterly jet between 20°N and 12°N. On this and the following day the Saharan heat low is orientated southwest-northeastwards and extends from southern Mauritania over Mali into Algeria (Fig. 3.4b,e). The low pressure over Mauritania leads to a complicated low-level flow pattern in western Mauritania (Fig. 3.4c,f). Between 6°W and 6°E the ITD moves northwards to around 19°N, while the moist air in western Mauritania is pushed back to 15°N on 25 June (Fig. 3.4c). On 26 and 27 June the subtropical ridge at 700 hPa over the Sahara weakens and a mid-latitude trough over Spain strengthens (Fig. 3.4d,g). On 27 and 28 June the Saharan heat low wanders slightly eastwards. The centre and highest 2 m temperature lie over Mali and Algeria (Fig. 3.4h,k). This causes a strong northerly Harmattan between 10°W and 6°W, here the ITD is pushed south to 14°N on 28 June 2007 (Fig. 3.4l).

On 29 June 2007 the meteorological situation was rather similar to that on 24 June. A ridge at 700 hPa extends from Tunisia into northern and western Mauritania (Fig. 3.4m). The main difference to 24 June is the lack of moist air over western Mauritania (Fig. 3.4o) and a more uniform structure of the Saharan heat low, which now extends from southern Mauritania over northern Mali into central Algeria (Fig. 3.4n). Eastwards of 6°W there is a dramatic northward penetration of the monsoon flow pushing the ITD to 20°N.

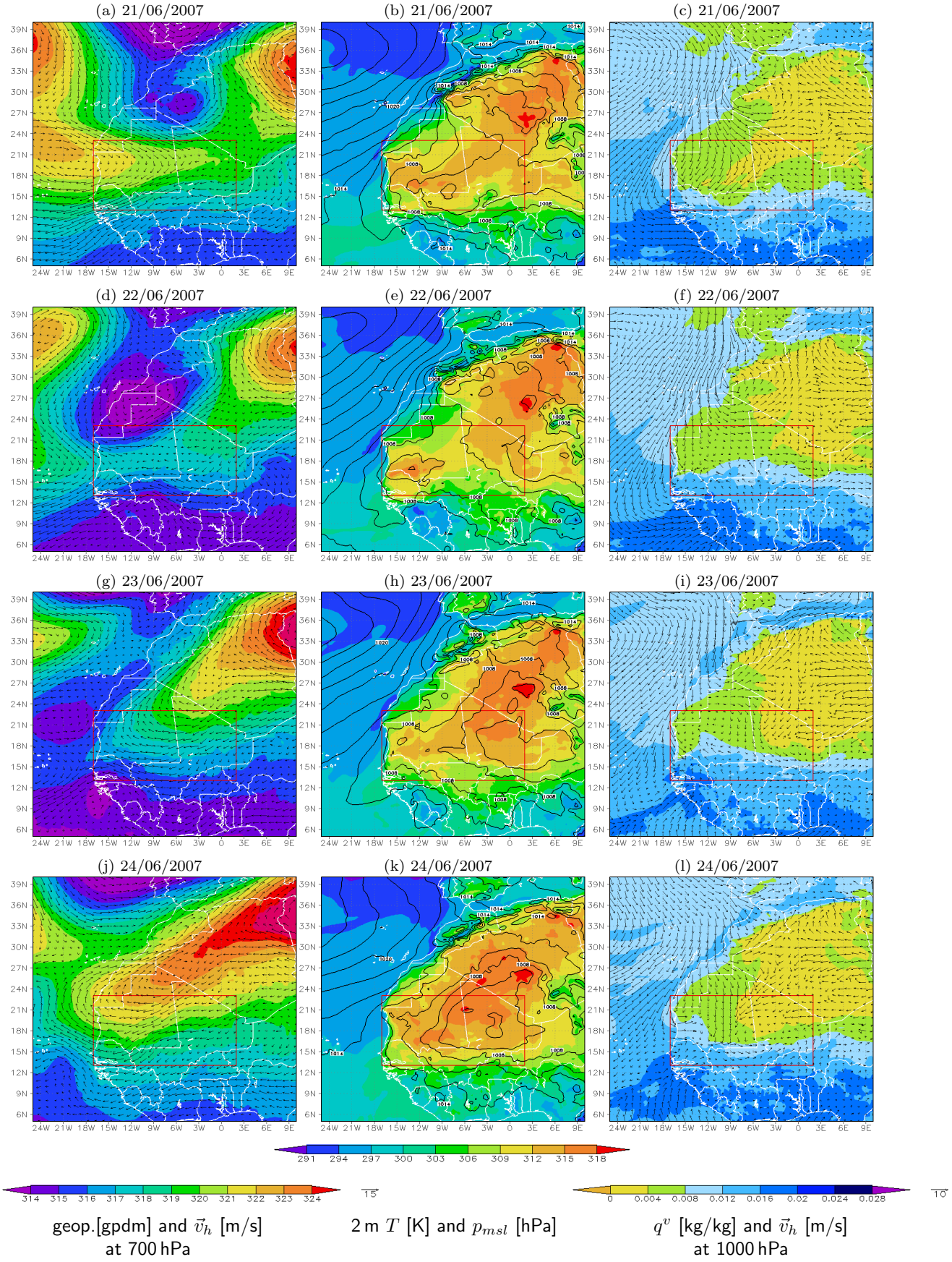

Figure 3.3: ECMWF analysis 18 UTC: Left: geopotential at 700 hPa [gpdm] (shaded), horizontal wind vectors $\vec{v}_h$ at 700 hPa [m/s] (black). Centre: 2 m temperature T [K] (shaded), mean sea level pressure p_{msl} [hPa] (black contours, 2 hPa interval). Right: specific humidity q^v at 1000 hPa [kg/kg] (shaded), horizontal wind vectors $\vec{v}_h$ at 1000 hPa [m/s] (black). All: Political boundaries (white). COSMO model domain (red).

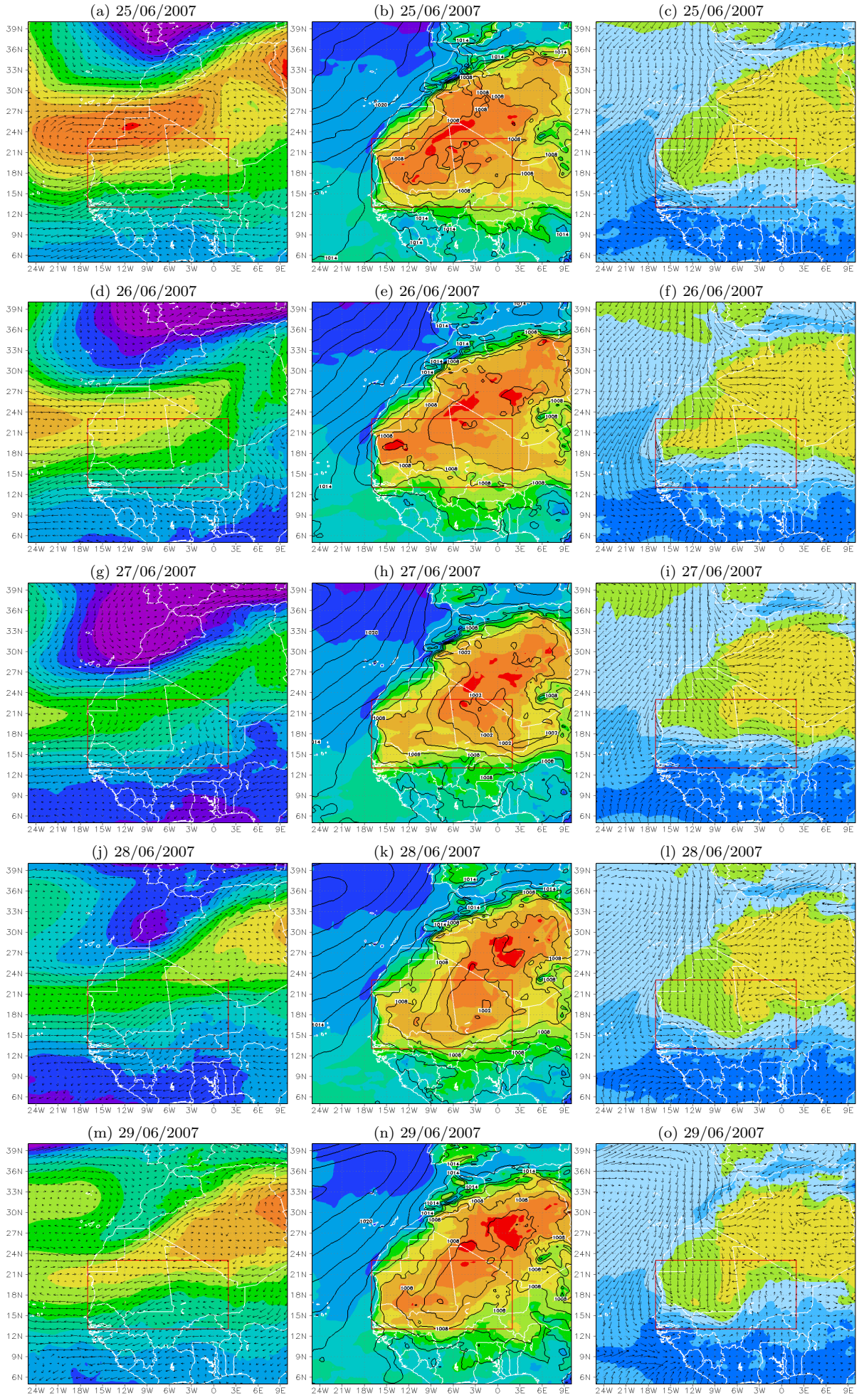

Figure 3.4: as Fig. 3.3 but for 25-29 June 2007.

3.2.2 Diurnal cycle in large-scale features

The large-scale diurnal cycle in the West African monsoon becomes evident when comparing ECMWF analyses at 18 UTC and 06 UTC. Figure 3.5 shows representatively for all nights the 2 m temperature and mean sea level pressure for the night of 24-25 June 2007. As Racz and Smith (1999) showed in idealised studies of a heat low, the mean sea level pressure in the Saharan heat low region has a diurnal amplitude of 2-4 hPa (Fig. 3.5). The pressure is minimum at 18 UTC ($p < 1004$ hPa at 21°N, 6°W and 17°N-21°N, 3°W-1°W) (Fig. 3.5a). In the morning the pressure in the centre of the heat low is much higher (Fig. 3.5b). The spatial extent of the diurnal cycle in mean sea level pressure is obvious when comparing the area covered by the 1008 hPa isobar in the evening and in the morning (Fig. 3.5). In the evening mean sea level pressure is less than 1008 hPa in a large area covering eastern Mauritania, the whole central and northern Mali, southern Algeria and large parts of Niger. Against that the mean sea level pressure is less than 1008 hPa in a much smaller area in the morning. The diurnal cycle of 2 m temperature is maximised in the Saharan heat low region (Fig. 3.5). Here the diurnal amplitude attains 20 K with evening maxima of 318 K (Fig. 3.5a) and morning minima of 297 K (Fig. 3.5b), whereas in the monsoon region south of 13°N the amplitude in 2 m temperature is at most 10 K. The mountainous regions of Atlas (27°N-35°N, 15°W-1°W), Ahaggar(23°N, 5°E) or the highlands at the Guinean coast show the coolest morning temperatures. The impact of the cold Canary current is seen in the cool morning temperatures over the West Saharan and Mauritanian coasts.

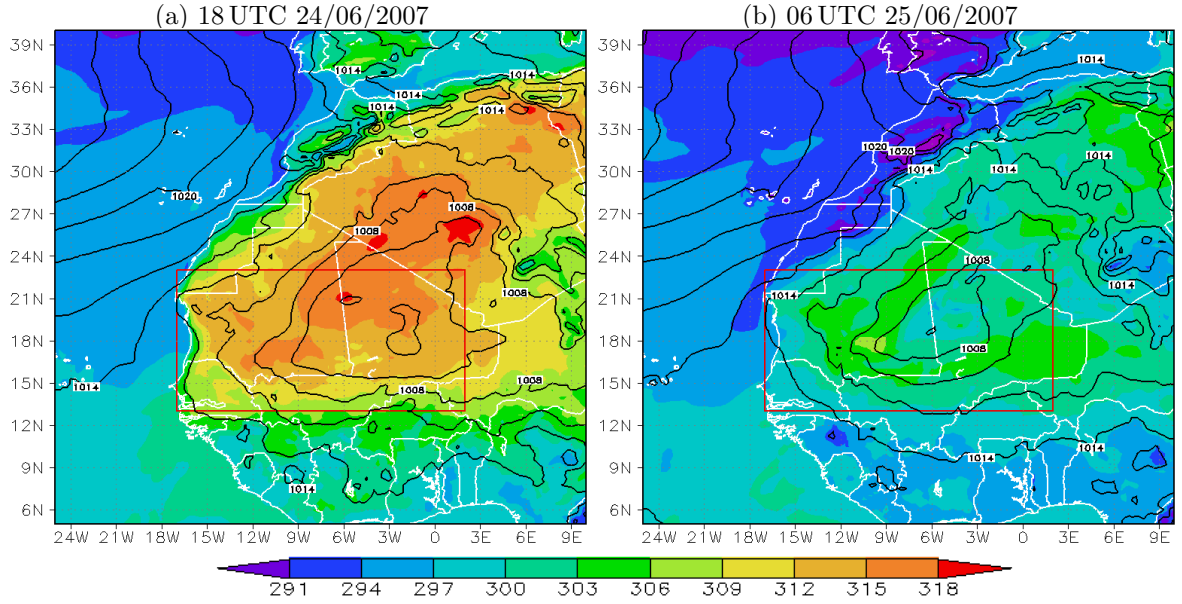

Figure 3.5: ECMWF analyses at 18 UTC 24/06/2007 and 06 UTC 25/06/2007: 2 m temperature T [K] (shaded), mean sea level pressure p_{msl} [hPa] (black contours, 2 hPa interval). Political boundaries (white). COSMO model domain (red).

Figure 3.6 shows the specific humidity and wind vectors for the same night. In the region east of 9°W, the 0.012 kg/kg contour line of specific humidity is at around 14-15°N in the evening (Fig. 3.6a). The next morning this contour line reaches 16.5°N-19°N (Fig. 3.6b) while it reatreats south to around 15°N as advection of humidity decays during the day (Fig. 3.4c). The low-level monsoon flow is much more homogenous and stronger in the morning (up to 10 m/s in a region south-east of a line from 15°N, 9°W to 18°N, 1°E (Fig. 3.6b)) compared to the evening hours (Figs. 3.6a and 3.4c).

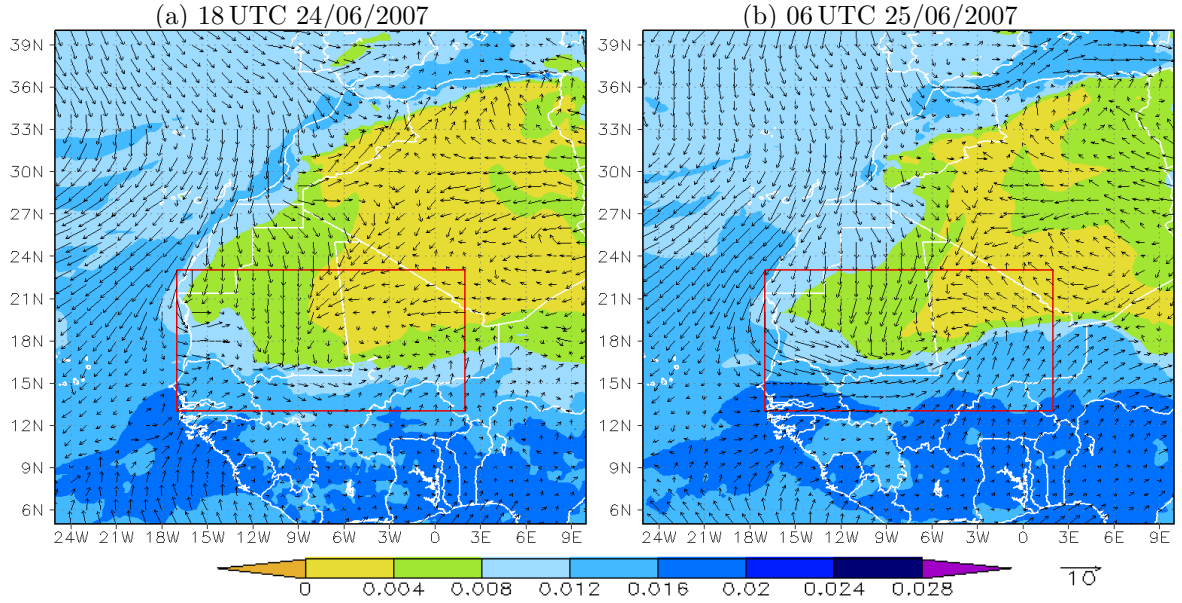

Figure 3.6: ECMWF analyses at 18 UTC 24/06/2007 and 06 UTC 25/06/2007: specific humidity q^v [kg/kg] at 1000 hPa (shaded), horizontal wind vectors $\vec{v}_h$ [m/s] at 1000 hPa (black). Political boundaries (white). COSMO model domain (red).

4 Model validation

The GERBILS campaign provides an excellent data set for validating the COSMO model. In this chapter two days will be highlighted: 24 and 28 June 2007. On both days scientific flights took place along the standard flight track at 18°N. Flight B299 on 24 June features several aircraft and dropsonde profiles of the cross section at 18°N as well as measurements at high levels ($\approx$ 400 hPa). Flight B302 on 28 June features data at a low-level leg along 18°N. The meteorological conditions were rather similar. The cross section at 18°N, 16°W-1°E showed three distinct layers in the low levels (Fig. 4.1) on both days:

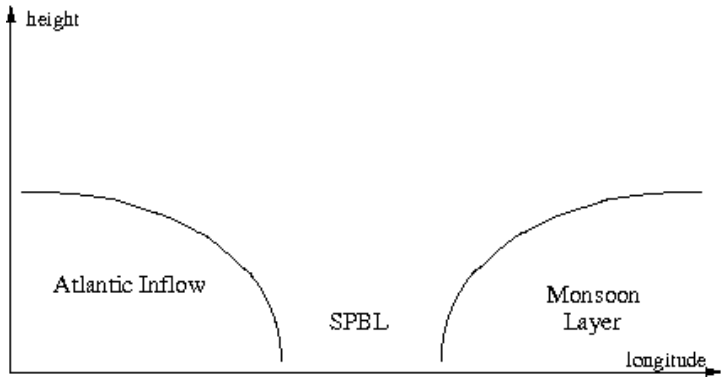

Figure 4.1: schematic longitude-height cross section at 18°N.

1) in the west a rather moist layer where westerly onshore wind dominates, 2) the Saharan PBL (Planetary Boundary Layer), mainly well-mixed from the surface up to mid levels (500 hPa) where northerly Harmattan winds dominate, and 3) in the east a rather shallow monsoon layer with dominant south-westerly winds. For both dates the mesoscale meteorological situation based on the COSMO model forecast and the flight pattern will be described. Then the model data will be validated against the aircraft and dropsonde data (FAAM 2007).

4.1 Flight B299 from Niamey to Nouakchott

On 24 June 2007, 12 UTC strong Harmattan winds (maximum velocity at 10 m up to 20 m/s) dominate the low-level flow in eastern Mauritania and the Mauritania/Mali border region (Fig. 4.2).

The position of the ITD can be estimated by the 0.008 kg/kg contour line of specific humidity at 1000 hPa as well as the convergence and rather low wind speed at 1000 hPa (Fig. 4.2). Between 10°W and 5°W the ITD retreats south to approximately 16°N. Eastwards it extends further north to around 18°N; westwards to around 19°N. Shallow vortices within the ITD zone are prominent features in the low-level flow (e.g. at 19.5°N, 15.5°W

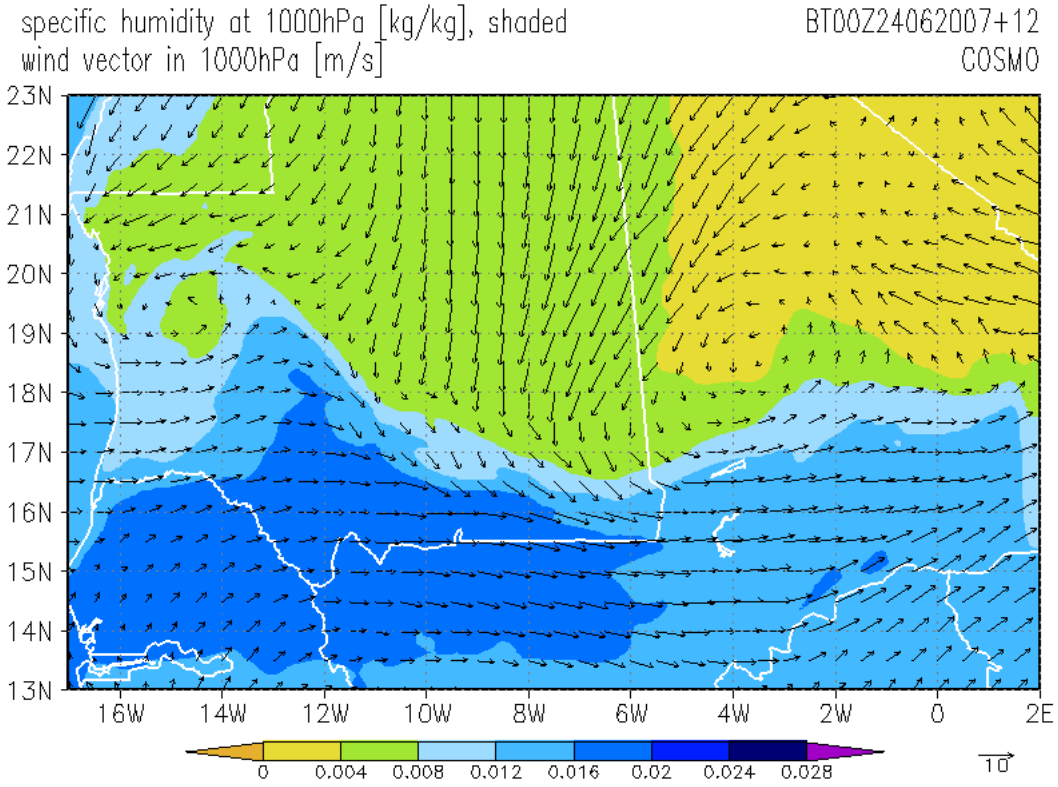

Figure 4.2: specific humidity and wind vectors at 1000 hPa in COSMO model domain. COSMO 24/06/2007 00UTC+12h.

and 18.5°N, 3.5°W). These are related to secondary heat low centres. The vortices extend up to 850 hPa vertically and are observable in high values of potential vorticity, also (not shown). At 18 UTC the western vortex disappeared. Above 700 hPa easterly flow dominates in the major part of the model domain (Fig. 3.3j).

A closer look along 18°N shows the three layers along the flight track. The specific humidity and the wind field near the surface show onshore low-level flow from the coast up to the Tagant Mountains at 12°W (Fig. 4.2). The cross section of specific humidity and virtual potential temperature along 18°N shows the top of this layer at approximately 700 hPa (Fig. 4.3). As shown in section 3.2.1 the thickness of this layer is due to a prior northward penetration of the monsoon flow and not due to moist air being advected from the Atlantic Ocean.

The layer between 11°W and 4°W can be characterised as the Saharan PBL within the Saharan heat low region. Here northerly Harmattan winds are the predominant feature of the low-level flow. The air is very dry and almost well-mixed in low and mid levels. The internal well-mixed convective boundary layer extends up to around 900 hPa indicated by stable stratification at this level. Above this shallow layer the top of the Saharan PBL, indicated by more stable stratification, reaches its maximal height (500 hPa, whereas east and west of this section the Saharan Air Layer (SAL) only extends up to 550 hPa). Eastwards of 3°W, a shallow south-westerly monsoon flow is observable at low levels. Its vertical extent is marked by a sharp decrease in specific humidity at around 900 hPa.

From 12°W to 6°W the cross section of virtual potential temperature shows a tilted baroclinic zone. This is the transition zone from the Atlantic influenced atmosphere into

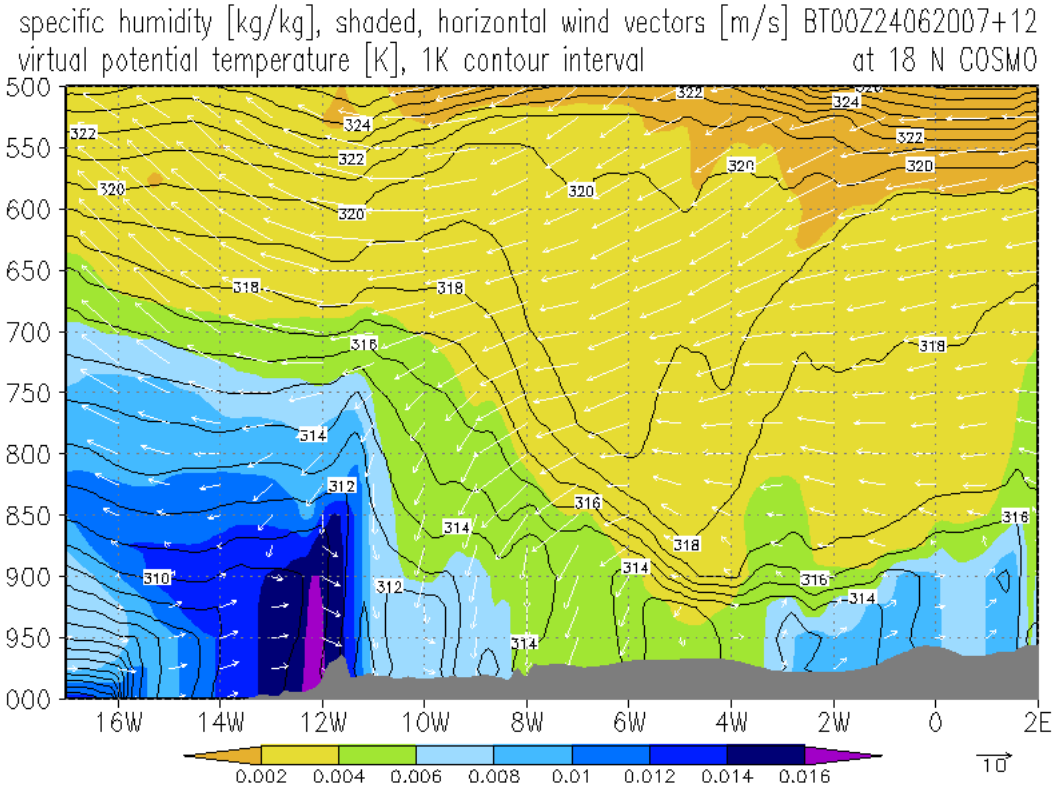

Figure 4.3: longitude-height cross section of specific humidity [kg/kg] (shaded), virtual potential temperature [K] (black, 1 K contour interval) and *horizontal* wind vectors [m/s] at 18°N. Vertical coordinate is pressure [hPa]. Grey shading indicates terrain by surface pressure. COSMO 24/06/2007 00 UTC+12h.

the Saharan PBL. A bulge in isentropes at 850 hPa extends from the eastern edge of the Atlantic impact at 12°W to the top of the SAL at around 550 hPa, 9°W (Fig. 4.3). This bulge marks the western edge of the baroclinic zone. Eastwards, isentropes decrease significantly in height and become more dense: at 9°W the 314 K isentrope is located at 830 hPa while the 318 K isentrope is located at 640 hPa. At 6°W the isentropes are very dense reaching from 314 K at 890 hPa to 318 K at 820 hPa. At 12 UTC the tilt of the baroclinic zone is weakening at the low levels due to the growing internal convective boundary layer in the Saharan heat low region. The baroclinic zone is much more pronounced earlier that day. The analysis of the Atlantic influenced atmopshere and of this baroclinic zone is the main focus of this thesis. These features will be investigated in more detail in chapter 5.

To complete the meteorological overview Fig. 4.4 shows the SEVIRI[1] dust product at 11:45 UTC on 24 June 2007. The satellite image shows decaying convective systems south of the flight track. A mid-level cloud field at the Atlantic coast of North Africa is evident as well. The flight track along 18°N is cloudless. Major dust layers are only detectable at the eastern leg of the flight domain (17°N, 1°W-1°E).

[1]Spinning Enhanced Visible and Infrared Imager on Meteosat Second Generation satellites

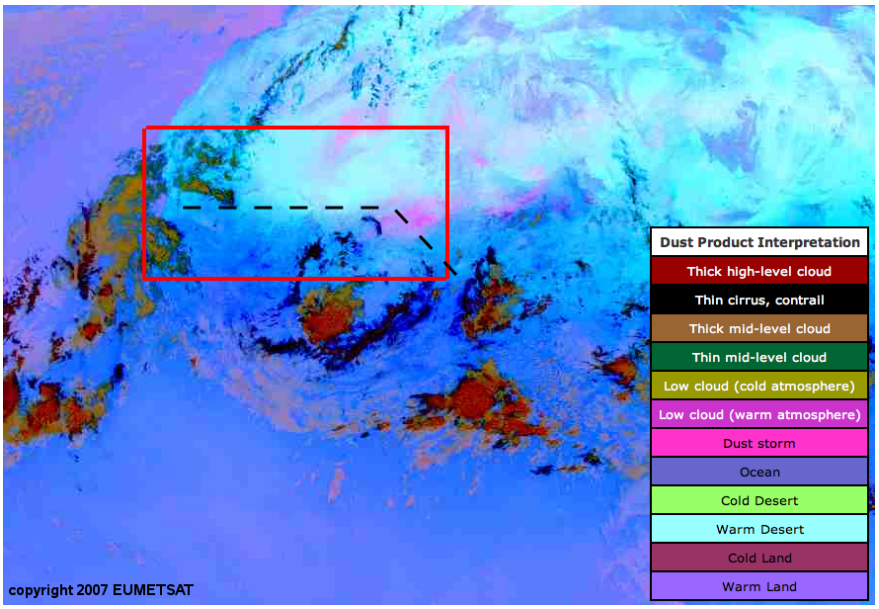

Figure 4.4: SEVIRI dust product for 11:45 UTC 24/06/2007. Retrieved from `http://radagast.nerc-essc.ac.uk`, data courtesy of Eumetsat. Approximate COSMO model domain (red). Approximate flight track (black dashed).

Flight B299 followed the standard flight track heading from Niamey (2.1°E, 13.3°N, 9:36 UTC) towards point (1.0°W, 18.0°N, 10:45 UTC), followed by a track along 18°N towards Nouakchott (16.0°W, 18.1°N, 14:26 UTC) (Fig. 4.5). From approximately 4.5°W to 10.4°W the aircraft headed towards the west at high level. During this leg sondes were dropped at 2.5°W, 5.7°W, 8.2°W, 8.6°W, and 10.0°W and aircraft profiles (steep ascent/descent in climb flight/dive at constant vertical aircraft speed) were performed from 3.5°W to 4.8°W and 10.3°W to 12.0°W at the begining and at the end of the leg. Thus the measurements capture the main features at 18°N, especially the observed baroclinic zone.

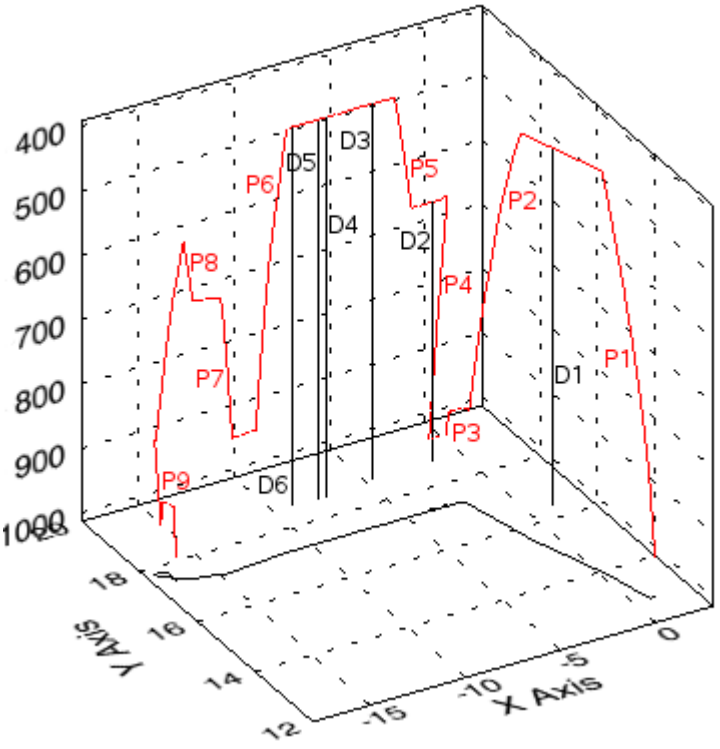

Figure 4.5: three-dimensional flight track for flight B299 24/06/2007 as function of longitude ([°E]: x-axis), latitude ([°N]: y-axis), and pressure ([hPa]: z-axis). Flight track indicated in red with profiles P1-P9 and dropsondes D1-D6 shown as vertical black lines. Projection of flight track onto surface shown in black.

In the following, profiles derived from dropsonde and aircraft data are compared to the corresponding model profiles. Then a cross section of potential temperature and humidity mixing ratio at 18°N is derived from combined dropsonde and aircraft data and compared to the model cross section at 18°N. Finally, model cloud cover is compared to satellite imagery.

Table 4.1: dropsondes from flight B299 24/06/2007: mean location (LON,LAT) and release time (UTC), location (LON,LAT) and forecast time of closest model grid points. The forecast initialisation time is 00 UTC 24/06/2007.

dropsonde				**model grid point**		
no.	**LON [°E]**	**LAT [°N]**	**t [hh:mm]**	**LON [°E]**	**LAT [°N]**	**fcst [hh]**
1	0.3285	15.7896	10:13	0.3125	15.8125	00Z+10h
2	-2.6264	18.0008	11:38	-2.6250	18.0000	00Z+12h
3	-5.7606	17.9989	12:12	-5.7500	18.0000	00Z+12h
4	-8.2527	17.9917	12:39	-8.2500	18.0000	00Z+13h
5	-8.6669	17.9857	12:43	-8.6875	18.0000	00Z+13h
6	-10.0500	17.9917	12:58	-10.0625	18.0000	00Z+13h

4.1.1 Dropsondes

The following figures show profiles of virtual potential temperature and humidity mixing ratio derived from dropsonde data and corresponding model data from the COSMO GERBILS forecast, initialised at 00 UTC 24/06/2007. Locations and release times of the dropsondes and closest model grid points/time steps are given in Table 4.1. The dropsonde data were assimilated by the ECMWF. However, this does not affect the COSMO forecasts as they are computed priorly to the measurements. Dropsonde data are presented in solid lines, model data in dashed lines. The standard deviation of data in a 0.5°x0.5° square on a constant pressure level around the closest grid point underlays, in grey shading, the model profile at the corresponding grid point. This gives an idea of spatial variability in the model data and allows for a realistic comparison of model data and observations in regions of sharp gradients. Model data are only available on pressure levels with vertical spacing of 25 hPa. The vertical resolution of the sondes is much higher. Dropsonde 4 was released over the model-predicted baroclinic zone. Unfortunately the sonde's parachute failed, so the vertical resolution is lower and the data has to be interpreted with reservation. The profiles are not discussed but shown in the appendix (Fig. A.1).

Sonde 1 gives a good example of a profile through the low-level monsoon layer (Fig. 4.6). The dropsonde profiles of both virtual potential temperature (Θ_v) and humidity mixing ratio (r) indicate the well-mixed monsoon layer with neutral stratification and almost constant mixing ratio from the ground up to approximately 870 hPa. A shallow stable layer follows up to approximately 820 hPa ($\partial\Theta_v/\partial p \approx 1\,\mathrm{K}/(10\,\mathrm{hPa})$), combined with a strong decrease of mixing ratio of about $\partial r/\partial p \approx (1.7\,\mathrm{g/kg})/(10\,\mathrm{hPa})$. This layer marks the bottom of the SAL which reaches from around 820 hPa to 580 hPa. The mixing ratio indicates fine layer structures within the SAL, probably related to dust layers. This hypothesis will be supported by the aircraft profiles, which provide dust concentrations.

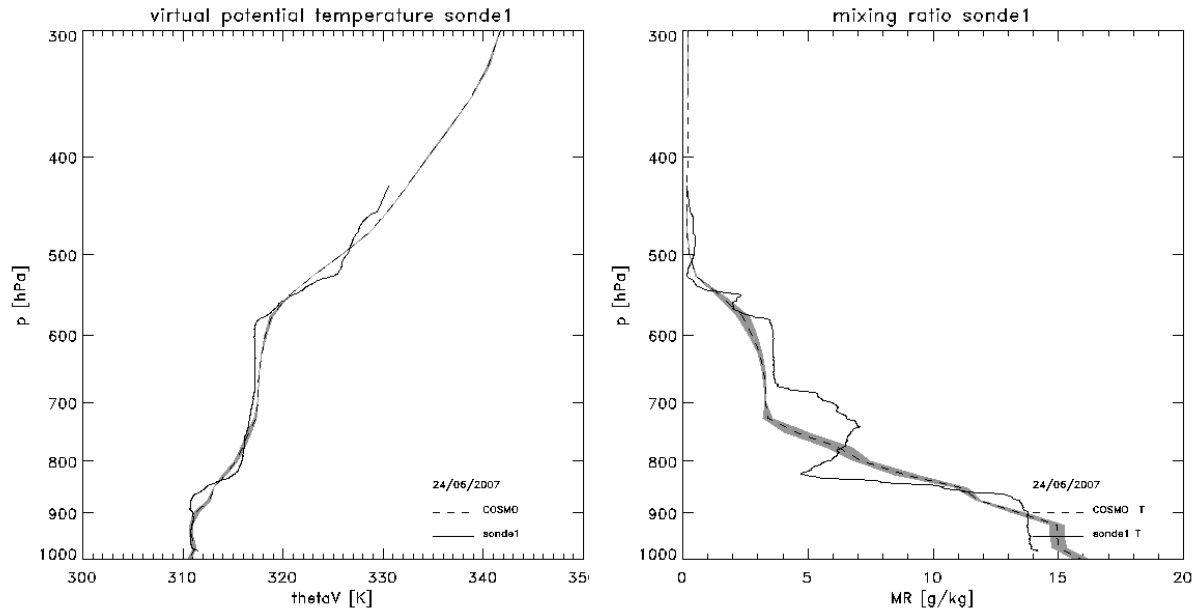

Figure 4.6: potential temperature and humidity mixing ratio from **sonde 1** (0.3°E, 15.8°N, 10:13 UTC) (solid) and COSMO model data at closest grid point (0.3125°E, 15.8125°, 24/06/2007 00 UTC+10h) (dashed). Grey shaded: standard deviation of model data on constant model level in a 0.5°x0.5° square centred around the closest grid point.

The top of the SAL is marked by strongly stable stratification from 580 hPa to 520 hPa ($\partial\Theta_v/\partial p \approx 1.5\text{K}/(10\,\text{hPa})$).

Generally the model profile fits the sonde profile well. Although the monsoon layer is 30 hPa shallower in the model and the stable layer on top of the monsoon layer ($\partial\Theta_v/\partial p|_{model} \approx 0.5\text{K}/(10\,\text{hPa})$) is not as strong as in the measurements, the model locates the top of the SAL at around 550 hPa, a similar height as in dropsonde data. The absolute value of potential temperature in the model is correct within the monsoon layer. Above this layer it differs by ±1-2 K from dropsonde data. The humidity mixing ratio is overestimated by 1 g/kg within the monsoon layer and underestimated by 1 g/kg where no layering within the SAL is detectable. Within the fine layering in the SAL humidity mixing ratio differs up to ±4 g/kg.

The rather smoothed character of the model temperature and humidity profile and the lack of fine layering within the SAL must be due to the relatively low vertical resolution of 25 hPa in the model data. The relatively sharp vertical gradients of the measured quantities are not resolved in the model data.

The underestimated height of the monsoon layer cannot be related to the low vertical resolution. The dropsonde was launched in a region where the model shows the south-westerly to westerly monsoon flow from the surface up to 900 hPa at 10 UTC. Above the monsoon layer the model predicts a cyclonic vortex structure at 17°N,0°W. This leads to a north-western flow and may induce entrainment of dryer air above 900 hPa. The measured fine layering of mixing ratio is probably related to dust layers, which the model does not include.

Sonde 2 was released just on top of the modelled "ITD vortex". As the location was still south of the ITD, the moist monsoon layer and the dry SAL above are still evident (Fig. 4.7). The model predicts a shallow neutral monsoon layer up to 950 hPa with a virtual potential temperature of 313 K and a mixing ratio of 8 g/kg. In the dropsonde

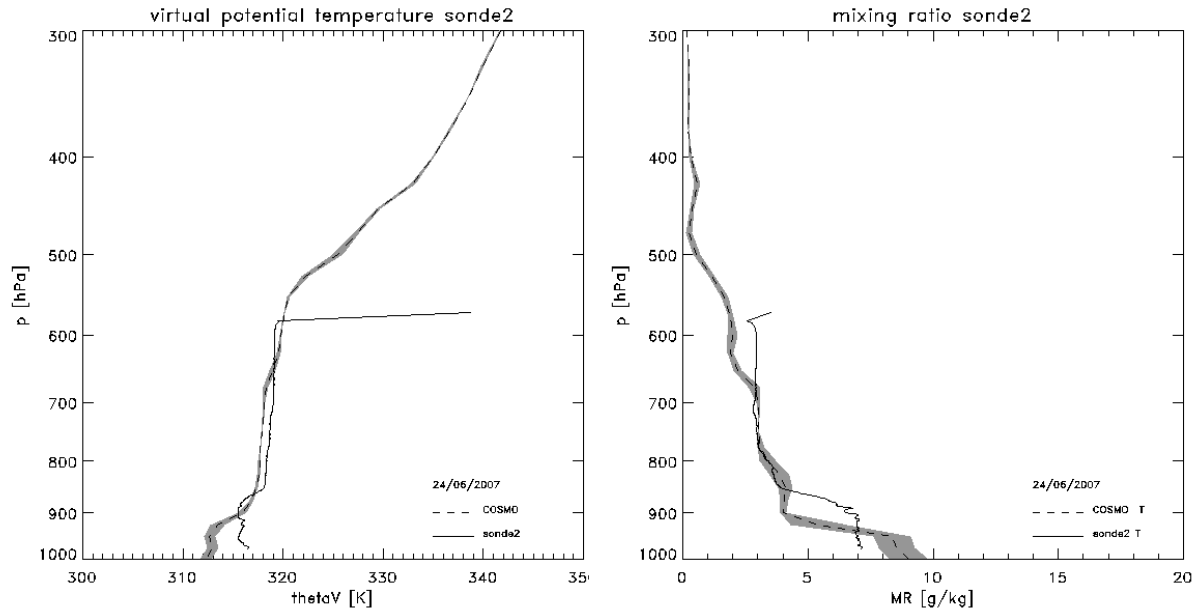

Figure 4.7: as Fig. 4.6 but for **sonde 2** (2.6°W, 18.0°N, 11:37 UTC) (solid) and COSMO model data (2.6250°W, 18.0000°N, 24/06/2007 00 UTC+12h) (dashed).

data the monsoon layer extends up to 880 hPa, the virtual potential temperature is 3-4 K higher and specific humidity is 1 g/kg lower. Within the SAL the model predicts the same mixing ratio as measured (decrease from 4 g/kg at 850 hPa to 3 g/kg at 770 hPa) but virtual potential temperature is 1 K lower than the measured value of 318 K. Above 660 hPa the model predicts a dryer, warmer (2 g/kg, 319 K) layer within the Saharan Air Layer, while the sonde data remains constant (3 g/kg, 318 K).

The data from sondes 1 and 2 show that the model is capable of predicting a shallow monsoon layer, locates the SAL at the right height, and - neglecting the errors combined with fine layer structures - predicts reasonable absolute values for potential temperature and humidity mixing ratio in a monsoon influenced environment.

The third sonde was released in the Saharan heat low region and in front of the model-predicted baroclinic zone. Both model and sonde data at the location of sonde 3 are a good example for a typical profile within the Saharan PBL (Fig. 4.8). The low level is characterised by a shallow well-mixed neutral layer up to 900 hPa, the internal convective boundary layer. A shallow stable layer marks the transition to the Saharan residual layer. The virtual potential temperature profile within the Saharan residual layer shows a well-mixed, neutrally-stratified layer up to 510 hPa. Although the mixing ratio indicates a well-mixed state as well, a rather fine-structured layer from the bottom of the Saharan Residual Layer to 700 hPa and a homogenous layer from 700 hPa to the top of the Saharan PBL are evident in sonde data. This fine structure in the lower Saharan residual layer is less evident in model data. Despite this, model and sonde data rather agree. While both model and sonde data show a mixed layer extending to 900 hPa, the virtual potential temperature in the model is 1 K lower than the measured value of 313 K. The humidity mixing ratio in the internal convective boundary layer is 1 g/kg higher in model data than the measured mixing ratio of 4 g/kg. Also the stable layer at the base of the Saharan residual layer is much shallower in dropsonde data (20 hPa, $\partial\Theta_v/\partial p \approx 2.5\text{K}/(10\,\text{hPa})$) than in the model (80 hPa, $\partial\Theta_v/\partial p \approx 0.8\text{K}/(10\,\text{hPa})$). Within the residual layer the model virtual potential temperature is 0.5-1 K higher and mixing

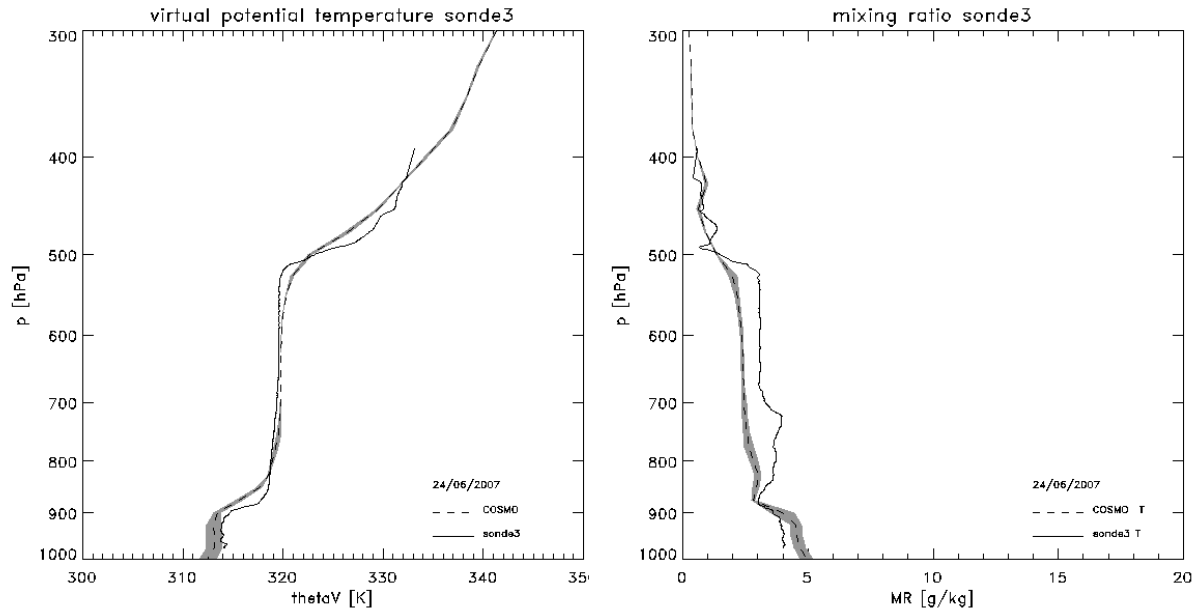

Figure 4.8: as Fig. 4.6 but for **sonde 3** (5.7°W, 18.0°N, 12:12 UTC) (solid) and COSMO model data (5.7500°W, 18.0000°N, 24/06/2007 00 UTC+12h) (dashed).

ratio around 1 g/kg lower than in the measurements. The transition from the residual layer to the free atmosphere also seems to be smoothed due to the vertical model resolution and the sharp gradients in reality. The COSMO model predicts the height of the internal convective boundary layer and of the Saharan residual layer accurately. There are only minor errors in the absolute values of temperature and humidity. Thus COSMO is a good tool for analysing the Saharan PBL within the Saharan heat low region.

Sonde 5 was released on top of the baroclinic zone in the model. The dropsonde profile of virtual potential temperature shows a well-mixed layer up to 800 hPa (Fig. 4.9). In the lower part of this layer a humidity mixing ratio of around 5 g/kg indicates the remnant monsoon layer (section 3.2.1). At 820 hPa a sharp decrease in mixing ratio of around 1 g/kg

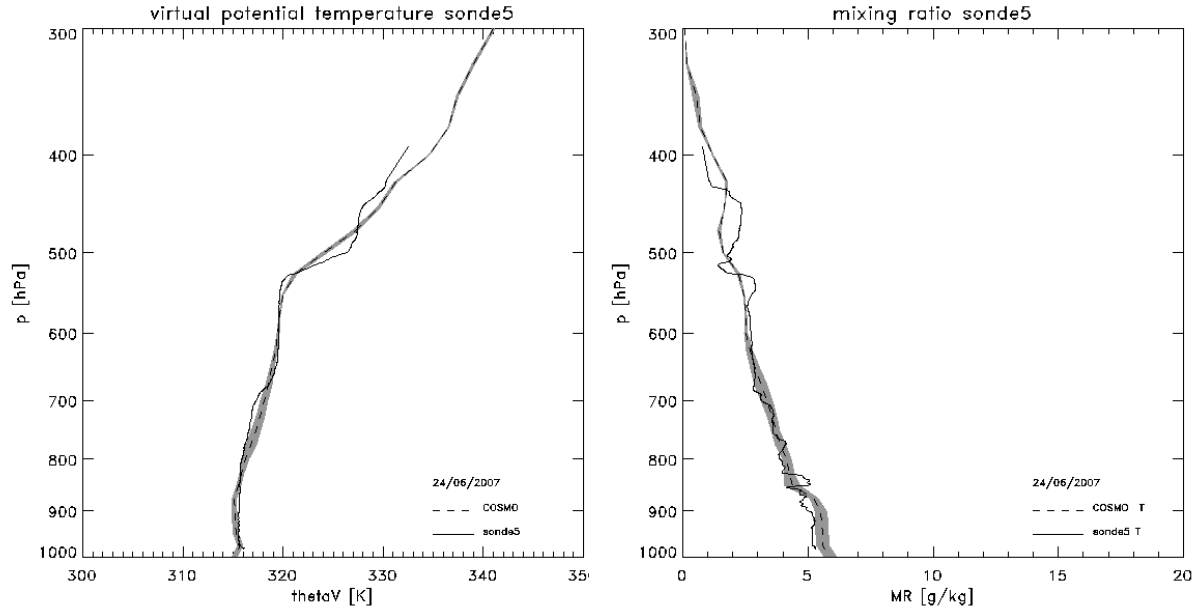

Figure 4.9: as Fig. 4.6 but for **sonde 5** (8.6°W, 18.0°N, 12:43 UTC) (solid) and COSMO model data (8.6875°W, 18.0000°N, 24/06/2007 00 UTC+13h) (dashed).

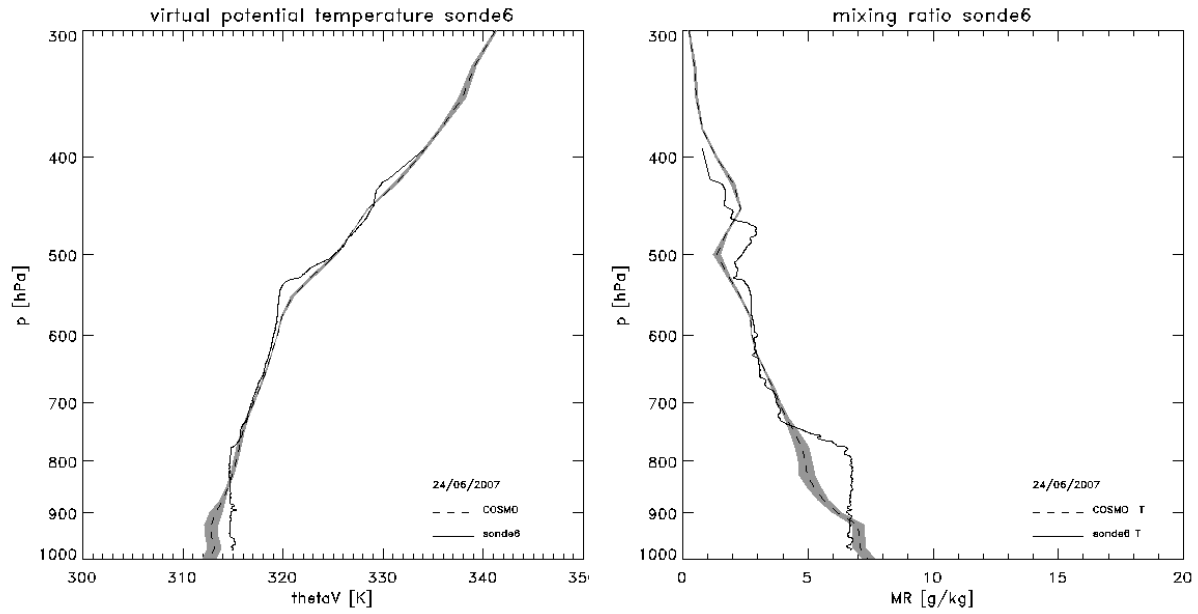

Figure 4.10: as Fig. 4.6 but for **sonde 6** (10.1°W, 18.0°N, 12:58 UTC) (solid) and COSMO model data (10.0625°W, 18.0000°N, 24/06/2007 00 UTC+13h) (dashed).

is evident. A moderately stable layer extends from 800 hPa up to 620 hPa. The profile of humidity mixing ratio indicates many fine structures here. However, humidity mixing ratio generally decreases from around 4 g/kg at 800 hPa to around 3 g/kg at 680 hPa. At 690 hPa there is evidence of stronger stable stratification. From 680 hPa to 620 hPa weakly stable stratification follows whereas humidity mixing ratio remains constant. From 620 hPa to 530 hPa the neutral stratification indicates the advected SAL. Fine layering of mixing ratio is obvious at the top of the SAL at 520 hPa, which is marked by a strongly stable layer in sonde data ($\partial\Theta_v/\partial p \approx 2K/(10\,hPa)$). Above the top of the SAL the profile of virtual potential temperature indicates shallow neutral and stable layers. Model data appears to be much more smoothed where strong gradients in sonde data exist and the model does not represent the fine structures in the profile of humidity. The overall agreement between model and sonde data is excellent. This shows that the predicted baroclinic zone is evident in reality as well.

Finally sonde 6 provides a profile of the western end of the baroclinic zone (Fig. 4.10). The profiles are rather similar to that of sonde 5, despite the fact that the influence of the deep moist layer in the west is evident below 780 hPa. Here the humidity mixing ratio is relatively high (7 g/kg) and the constant virtual potential temperature of 315 K indicates neutral stratification. The model fails to predict the depth of the moist layer in low levels. It is predicted further west, as will be seen in the cross section of humidity mixing ratio at 18°N (Fig. 4.18).

4.1.2 Aircraft profiles

Another approach to get vertical profiles of the atmosphere is the use of aircraft data from a climb flight or a dive (see Fig. 4.5, Table 4.2). These are special flight manoeuvres with a constant vertical aircraft speed. In this case profiles of every quantities which are measured by the aircraft instruments are available. However, flight patterns limit the location of measurements. Several profile ascents/descents were performed during flight B299 which give important additional information about the vertical structure of the

Table 4.2: flight B299 24/06/2007: starting/end (s/e) points (LON,LAT,pressure) and time (UTC) of aircraft profiles, location (LON,LAT) and forecast time of corresponding model grid points. Model initialisation time is 00 UTC 24/06/2007.

profile					**model grid point**		
no.	**LON [°E]**	**LAT[°N]**	**p[hPa]**	**t [hhmm]**	**LON [°E]**	**LAT [°N]**	**fcst [hh]**
1s	2.1575	13.4813	971	0936	2.0000	13.5000	00Z+10h
1e	1.2319	14.6969	427	0958	1.2500	14.6875	00Z+10h
2s	-0.1914	16.5391	428	1023	-0.1875	16.5625	00Z+11h
2e	-0.9222	17.8608	904	1042	-0.9375	17.8750	00Z+11h
3s	-1.8053	18.0035	903	1058	-1.8125	18.0000	00Z+11h
3e	-1.8889	18.0045	939	1059	-1.8750	18.0000	00Z+11h
4s	-2.7124	18.0570	936	1114	-2.6875	18.0625	00Z+11h
4e	-1.8293	18.0111	571	1128	-1.8125	18.0000	00Z+11h
5s	-3.7460	18.0012	569	1151	-3.7500	18.0000	00Z+12h
5e	-4.6536	18.0013	392	1201	-4.6250	18.0000	00Z+12h
6s	-10.2938	17.9996	393	1301	-10.3125	18.0000	00Z+13h
6e	-11.9912	17.9384	841	1321	-12.0000	17.9375	00Z+13h
7s	-13.2849	17.8871	843	1339	-13.3125	17.8750	00Z+14h
7e	-13.9652	17.8994	619	1348	-13.9375	17.8750	00Z+14h
8s	-15.1649	18.0363	618	1403	-15.1875	18.0625	00Z+14h
8e	-15.5504	18.0998	526	1407	-15.5625	18.1250	00Z+14h
9s	-15.5504	18.0998	526	1407	-15.5625	18.1250	00Z+14h
9e	-16.1506	18.4837	977	1426	-16.1250	18.5000	00Z+14h

atmosphere. Aircraft data include measurements of the aerosol. The aircraft profile starting/end points and times are indicated in Table 4.2. Aircraft data were not assimilated by the ECMWF assimilation system.

When analysing the aircraft profiles, one has to keep in mind that the profiles are not representative for a column of air over a distinct point above ground. Starting and end point of a profile often differ by 1° or more in longitude/latitude. In the following figures we account for this by giving the corresponding model profile at the starting (black dashed) and end point (grey dashed) of the profile. Aircraft data are shown in black solid lines. When profiles were interrupted or two profiles followed rather closely in time and space, the second profile is shown in the same plot in grey solid lines. Profiles of virtual potential temperature, humidity mixing ratio, and total scattering coefficient from nephelometer measurements are shown. Humidity mixing ratio is shown together with the nephelometer measurements in one plot to highlight the correlation of these datasets. The nephelometer measures the uncorrected total (i.e. up- and downward) scattering coefficient in the red, blue, and green spectrum. These data are plotted on an inverse x-axis at the top of the diagram.

Profile 1 was recorded through the monsoon layer northwest of Niamey (Fig. 4.11). As no direct measurement of mixing ratio below 550 hPa is available for profile 1, potential temperature is shown instead of virtual potential temperature. The vertical extent of the monsoon layer can be estimated using dew point measurements (not shown). It extends

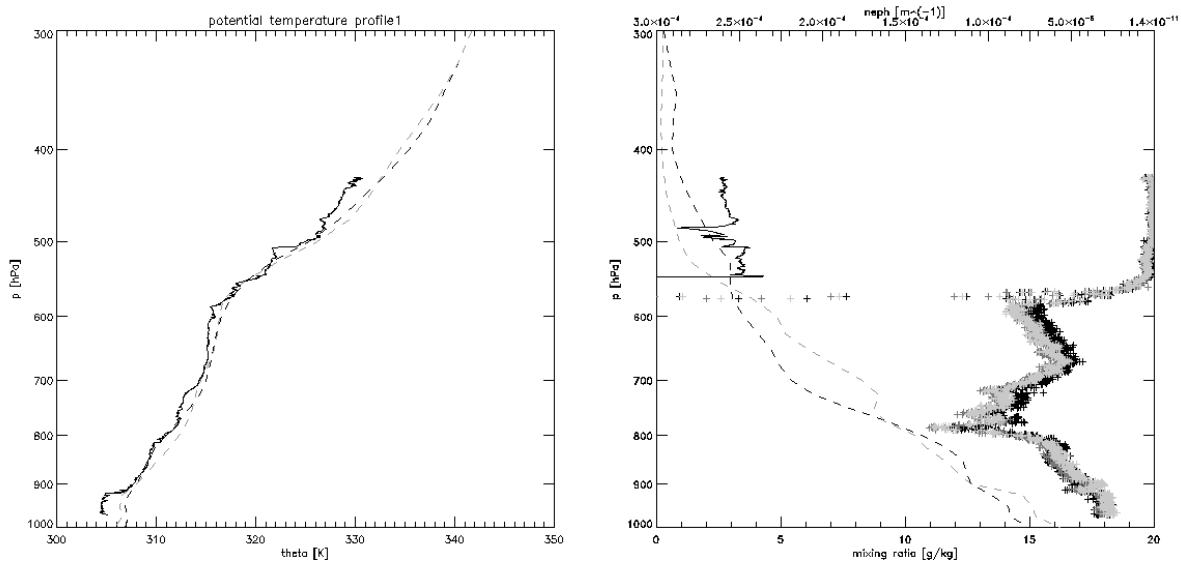

Figure 4.11: **profile 1**. Potential temperature (left) and mixing ratio (right) (black, solid: aircraft data of indicated profile (if two profiles in one plot: grey, solid: aircraft data of profile following in time); black, dashed: model profile at closest grid point to the profile starting point; grey, dashed: model profile at closest grid point to the profile end point). Uncorrected total scattering coefficient (right) (light grey, grey, black symbols stand for scattering in red, green, blue spectrum). For longitude and latitude of profile starting/end points and corresponding model grid points refer to Table 4.2.

up to approximately 720 hPa. From 720 hPa to 700 hPa a thin stable layer ($\partial\Theta/\partial p$ = 1 K/10 hPa) indicates the transition to the SAL above, which extends up to 590 hPa and is nearly neutrally-stratified (Θ = 315 K). Two thick dust layers are detectable: one reaching from 780 hPa to 720 hPa and a second one reaching from 650 hPa to 570 hPa. The top of the latter marks the top of the SAL. Here the dust concentration declines rapidly from high concentrations to zero. At 550 hPa the dew point depression is zero indicating shallow altocumulus clouds which were observed from the aircraft as well. The profile of potential temperature is rather typical for a monsoon-influenced atmosphere. The model and aircraft profile of potential temperature indicate the top of a shallow neutrally-stratified well-mixed layer at 900 hPa. In contrast, the model struggled to predict the correct height of the monsoon layer at the location of sondes 1 and 2 which were close to the ITD. Profile 1 was recorded far south of the ITD. This may imply that the model only struggles to predict the correct height of the monsoon layer close to the ITD. Overall the model slightly overestimates potential temperature (0 to 2 K) at the location of profile 1. Despite this and despite the smoothing due to the vertical resolution, the model profile of potential temperature fits very well to the measured profile.

Profiles 2&3 indicate the SAL from 880 hPa up to 550 hPa (Fig. 4.12) to be a well-mixed, neutrally-stratified layer with a constant virtual potential temperature of 317 K from 880 hPa to 630 hPa and with a weakly stable layer above ($\partial\Theta_v/\partial p$ = 0.1 K/10 hPa). Within the SAL the humidity mixing ratio gradually decreases from 4 g/kg at the bottom to 2 g/kg at the top. Also the dust concentration steadily decreases with height in the Saharan Air Layer. Due to the high vertical resolution of aircraft data a sharp increase in virtual potential temperature and a sharp decrease in mixing ratio/dust concentration at 880 hPa and 550 hPa are detectable. The strong vertical temperature, humidity, and

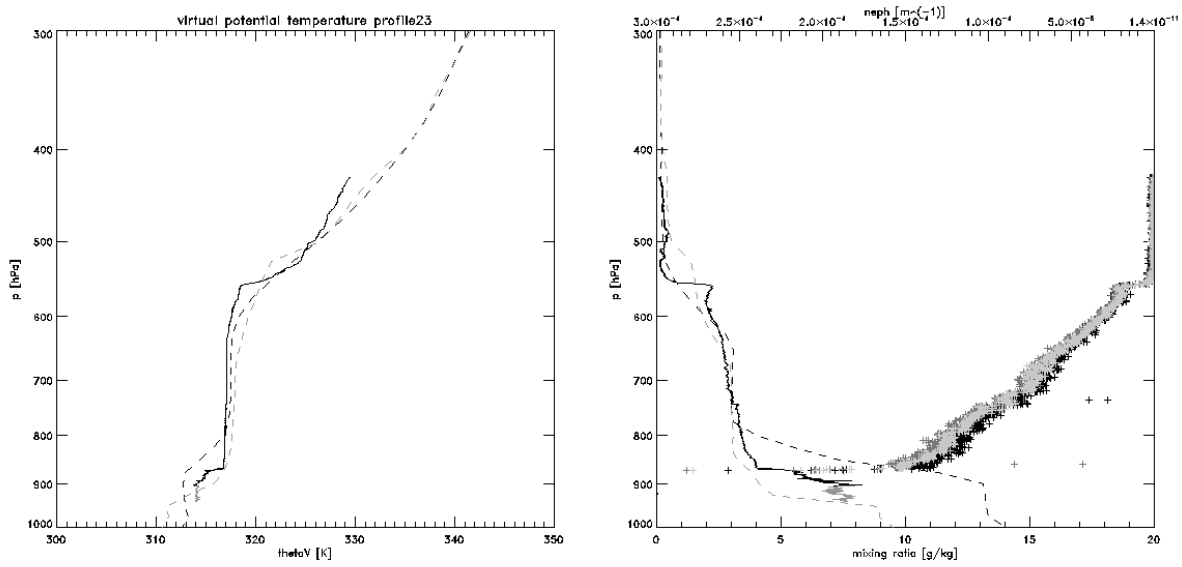

Figure 4.12: as Fig. 4.11 but for **profiles 2&3** and virtual potential temperature (left) instead of potential temperature.

dust gradients mark the bottom and the top of the SAL.

From the surface to 900 hPa the monsoon layer is observed. It is well-mixed and neutrally-stratified ($\Theta_v = 314\,\mathrm{K}$ and $r = 7.5\,\mathrm{g/kg}$). The free atmosphere above the SAL is dry and stably-stratified ($r = 0 - 0.5\,\mathrm{g/kg}$ and $\partial\Theta_v/\partial p \approx 0.7\,\mathrm{K}/10\,\mathrm{hPa}$). The strong "jumps" at the top and bottom of the SAL cannot be resolved by the model. Thus the model smooths the vertical gradients at the top and bottom of the SAL. Nevertheless, the absolute values of in-/decrease at the bottom and top of the SAL are similar. Within the monsoon layer, as for sonde 2, the model predicts a 2 K lower potential temperature and 1-2 g/kg higher humidity mixing ratio. Within and above the SAL the measured profile nearly fits within the range predicted by the model for the starting and end point.

The virtual potential temperature of profiles 4&5 (Fig. 4.13) is similar to profiles 2&3. The profile ascent started within a stable layer presumably at the top of the monsoon layer at 940 hPa ($\partial\Theta_v/\partial p = 0.5\,\mathrm{K}/10\,\mathrm{hPa}$). The nearly constant virtual potential temperature of 318 K from 860 hPa to 510 hPa indicates the SAL. The humidity mixing ratio within the SAL is constant in three internal layers (860-800 hPa, 800-680 hPa, 670-510 hPa). The dust profile shows several dust layers. Variations in mixing ratio correlate with the changes in dust concentration. The top of the SAL is marked by a sharp stable layer ($\partial\Theta_v/\partial p = 4\,\mathrm{K}/10\,\mathrm{hPa}$) from 510 hPa to 490 hPa. Humidity mixing ratio decreased from 3 g/kg at 510 hPa to 1 g/kg at 500 hPa. The free atmosphere above 490 hPa is dry and stably-stratified ($r = 1\,\mathrm{g/kg}$; $\partial\Theta_v/\partial p = 0.7\,\mathrm{K}/10\,\mathrm{hPa}$). The model profiles of potential temperature fit very well to the measured ones. The bottom of the SAL is predicted at around 880 hPa, only 20 hPa below the measured location. From 880 hPa to 780 hPa the measured profile lies within the range predicted by the model profiles at the starting and end point. Above this layer the model shows weakly stable stratification and therefore overestimates virtual potential temperature by around 1-2 K. A stable layer extending from 540 hPa to 490 hPa in model profiles shows that the top of the SAL is much more smoothed in the model compared to the aircraft data. Nevertheless, the model locates the top of the stable layer at the same height as observed. The potential temperature in the free atmosphere above is around 1 K lower than observed. Humidity mixing ratio in

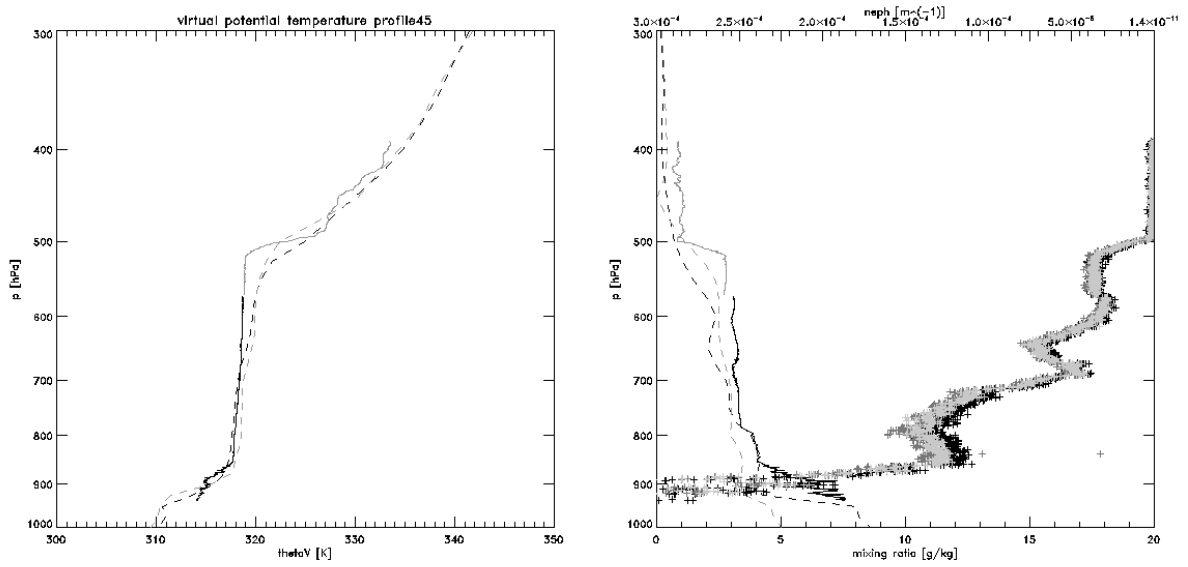

Figure 4.13: as Fig. 4.12 but data for **profiles 4&5**.

the model is around 0-1 g/kg lower than measured. Despite smoothed profiles at the top and bottom of the SAL, the model locates the internal layers of constant r within the SAL at the observed height.

Profile 6 was performed over the Tagant Mountains at 11.5°W. It is a very good example of the correlation of dust concentration, mixing ratio, and virtual potential temperature (Fig. 4.14). The lower atmosphere contains high amounts of dust up to a height of 710 hPa. The mixing ratio in this layer is rather high (around 10 g/kg at 800 hPa). This is the deep moist layer advected from the south the day before. The model profiles predict a wide range of humidity mixing ratio (5.5-15.5 g/kg at 850 hPa) which shows that the profile was flown in the transition zone from the Saharan Planetary Boundary Layer to a boundary layer influenced by maritime air and the remnant monsoon layer. The comparison of mixing ratio and virtual potential temperature profiles from model and aircraft data further shows that the measured data are closer to the western profile

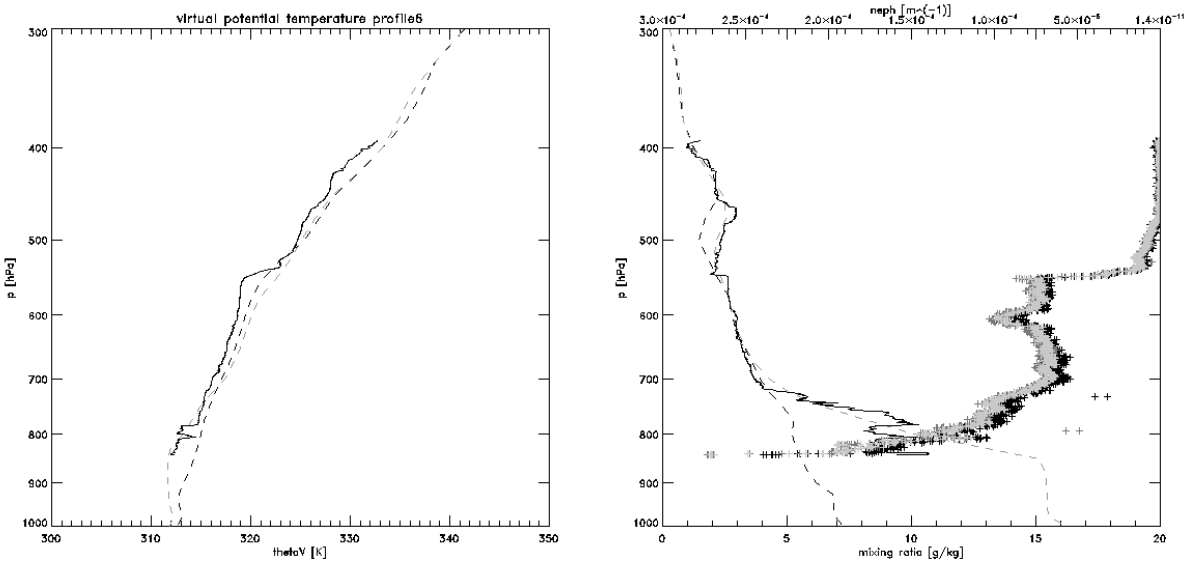

Figure 4.14: as Fig. 4.12 but data for **profile 6**.

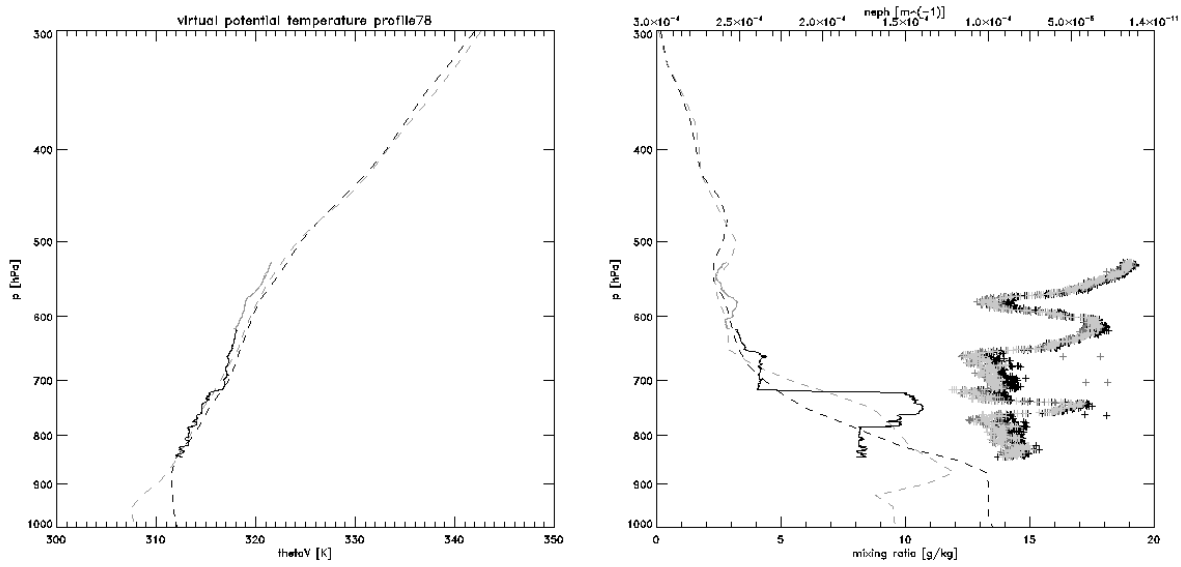

Figure 4.15: as Fig. 4.12 but for **profiles 7&8**.

(grey dashed). A strong decrease of humidity mixing ratio from 10 g/kg at 780 hPa to 4 g/kg at 710 hPa marks the top of the remnant monsoon layer and the top of the first dust layer. Above this transition zone the humidity mixing ratio further decreases to 2.5 g/kg at 540 hPa. The top of this first dust layer is less pronounced in the profile of virtual potential temperature. Nevertheless, a transition to less stable and more neutral stratification from 710 hPa to 540 hPa is detectable. A second dust layer extends from 710 hPa to 540 hPa. At its top there are remarkably sharp vertical gradients of the virtual potential temperature, of the mixing ratio, and of the dust concentration profiles. The model smooths the sharp gradients but a slight bend at 550 hPa is still detectable in the eastern profile of model virtual potential temperature (black dashed) and western profile of model humidity mixing ratio (grey dashed). A third layer in which dust concentration declines to zero extends from 530 hPa to 470 hPa. Here the mixing ratio is rather constant (around 2 g/kg) and the virtual potential temperature profile indicates a slightly stable profile ($\partial\Theta_v/\partial p = 0.5\,\mathrm{K}/10\,\mathrm{hPa}$). The top of this last layer is marked by a sharp gradient in both mixing ratio and potential temperature.

Profiles 7&8 and profile 9 are good examples for fine layers and their correlation with mixing ratio and other meteorological quantities (Figs. 4.15 and 4.16). The most striking feature in profiles 7&8 is the very sharp decrease in humidity mixing ratio from 11 g/kg to 4 g/kg at 710 hPa. This sudden decrease is not a measurement error, as it is evident also in the independent measurement of dew point temperature (not shown). The virtual potential temperature rises suddenly from 314 K to 317 K as well. The abrupt shift in humidity mixing ratio also corresponds to changes in the fine layer structure of dust concentration at this altitude. The model fails to predict these sharp layers. Nevertheless, model profiles of humidity mixing ratio for profiles 7&8 show the decrease from around 10 g/kg in low levels to 3 g/kg above 660 hPa. Above 690 hPa the model profiles for the endpoint show the closest agreement to the aircraft profiles. The potential temperature again is around 1 K higher in the model.

Below 720 hPa the model profile of virtual potential temperature generally fits profile 9 well (Fig. 4.16). Above 720 hPa the virtual potential temperature is underestimated by around 1-2 K. The profile of humidity mixing ratio from aircraft data shows a complicated

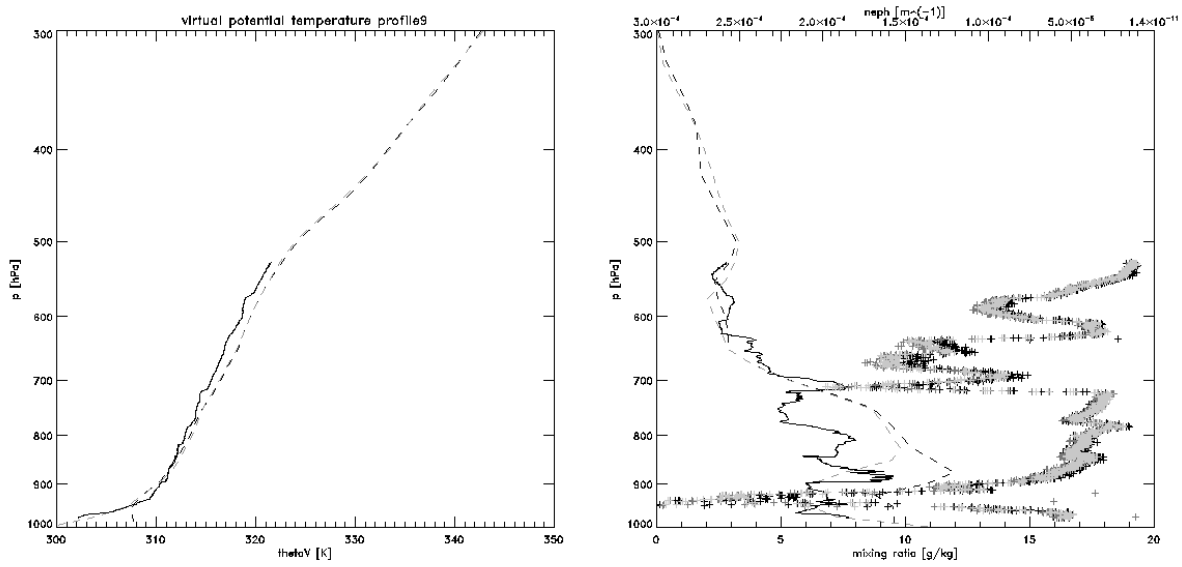

Figure 4.16: as Fig. 4.12 but for **profile 9**.

fine layering below 700 hPa. This highly correlates with dust concentrations. The model fails to predict these fine layers, but predicts the humidity mixing ratio above 700 hPa correctly.

4.1.3 Cross section

The dropsonde and aircraft profiles at 18°N are interpolated to give a vertical cross section along 18°N. The potential temperature cross section at 18°N from 2°E to 17°W is shown in Fig. 4.17 indicated by colour shading and black contours. The plot at the top shows data of the COSMO GERBILS forecast for 12 UTC 24 June 2007 (initialisation time 00 UTC 24/06/2007). The plot at the bottom shows the cross section of potential temperature at 18°N, interpolated from aircraft and dropsonde data. The location of sondes 2, 3, 5, and 6 are indicated from the east to the west by vertical red lines. These sondes were used for the interpolation, whereas sonde 4 was excluded as its parachute failed. Data along the flight track which is indicated by the black thick line are also used for the interpolation. The measured data are smoothed to avoid high-frequency perturbations. The location of the measurements was chosen (at least to some extent) to validate the model.

Measured data show the tilted baroclinic zone from 11°W to 8°W marked by the slope of 315 K to 318.5 K isotherms from 700 hPa to 550 hPa at 11°W to 900 hPa to 650 hPa at 8°W (Fig. 4.17). The inversion at the top of the SAL is detectable from 13°W to 4°W by tightly packed 320 K to 324 K isentropes. Both model and measurements show a higher inversion between 9°W and 4°W, the Saharan heat low region. At the eastern edge of the measurements the slope of isentropes in mid levels is indicated between the measurements of sonde 2 and profile 4. A closer look at the plots shows more interesting features. Although the high model potential temperatures of around 313.5 K below 900 hPa at 7°W are not evident in measured data, the local maximum at 8.7°W is evident in both. The measured data indicate the significant bulge in model potential temperature contours at 12°W, which reaches from 900 hPa to the top of the cross section. The 311, 315.5, 318.5, 319 and 325 to 331 K isentropes show a slight bulge at around 11°W. This could be linked to orography.

The extremely stable layer at 13.7°W, 710 hPa cannot be resolved by the model. Furthermore, the model seems to predict approximately 1 K higher potential temperature than measured. The only exception from this is the shallow monsoon layer in the east, where potential temperature is around 1-2 K lower than measured. Nevertheless, there is strong evidence in the sparse measured data that the predicted features really exist.

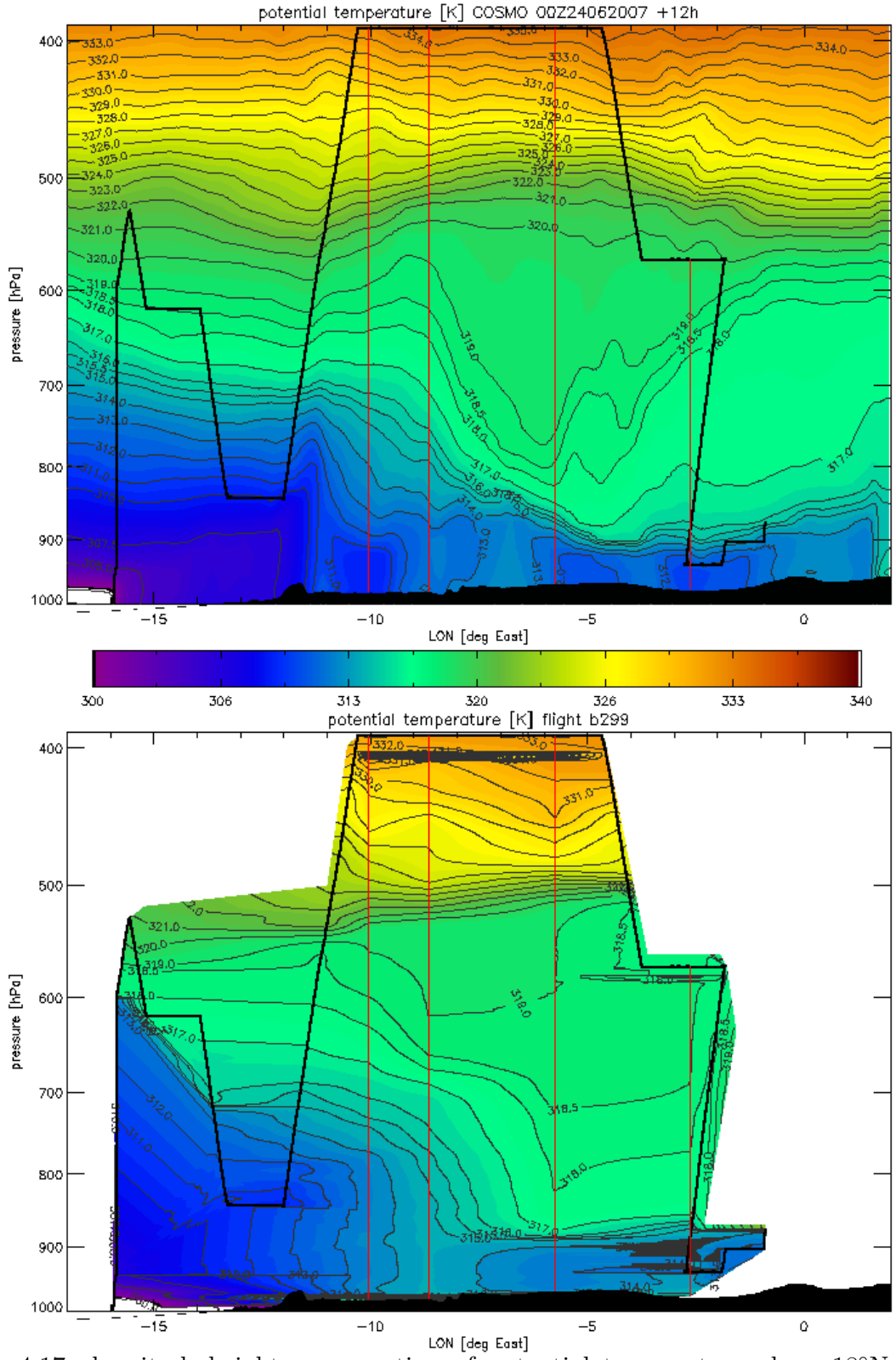

Figure 4.17: longitude-height cross section of potential temperature along 18°N. Top: model data. Bottom: interpolation from aircraft and dropsonde data. Same shading/contours used in both plots. Shading interval 0.5 K. Black contours: 295, 300, 305, 307.5, [310 to 335, 1 K interval], 315.5 and 318.5 K isentropes. Black shaded: orography. Black thick line indicates flight track. Red vertical lines show locations of dropsondes used for interpolation.

The corresponding vertical cross section of humidity mixing ratio at 18°N from 2°E to 17°W is shown in Fig. 4.18. Similar to Fig. 4.17 the plot at the top shows COSMO model data for 12 UTC 24 June 2007 (initialisation time 00 UTC 24/06/2007). The plot at the bottom shows the cross section of humidity mixing ratio at 18°N interpolated from aircraft data and dropsondes 2, 3, 5, and 6.

The measured data demonstrates the predicted classification of the lower levels into three distinct layers along 18°N (cf. Fig. 4.1): the Atlantic Inflow zone from 17°W to 9°W, the Saharan PBL from 9°W to 4°W, and the monsoon layer from 4°W to 2°E. Both model and measured data will predict the maximum vertical extent of the western moist air at around 700 hPa from 9°W to 14°W if $r > 5$ g/kg is taken as outer boundary of the moist air in the west. The model does not predict the sharp gradient of humidity mixing ratio at the top of this layer. Also, the model predicts a slight increase in depth of the moist layer to the west of 14°W. Measurements at 16°W show that the moist layer ($r > 5$ g/kg) extends up to 600 hPa whereas the model only predicts 2.5 g/kg at this height. The sharp gradient at the top of the moist layer in profiles 7&8 at around 700 hPa, 13.8°W produces errors in the interpolation towards profile 9 in the west. Also, it has to be kept in mind that the time over which the moist layer in the west was sampled ranges from 12:58 (sonde 6) to 14:26 (end of profile 9). Profile 9 shows very moist ($r = 10$ g/kg) and cold air near the ground ($p > 980$ hPa) in Nouakchott. This indicates the advection of maritime air from the Atlantic Ocean in the lowest levels at the Mauritanian coast.

Dry air from 15°W, 600 hPa to 6°W, 450 hPa in the model data are evident in measurements as well. Above this dry tongue a moister tongue spreads out from 15°W, 500 hPa to 8°W, 450 hPa in both model and observations. Between 9°W and 4°W both datasets predict a rather well-mixed Saharan PBL. The measured humidity mixing ratio is approximately 1 g/kg higher than that predicted, whereas in other regions it is generally 1 g/kg lower than that from model data. Furthermore, the position of the significant moisture gradient at both edges of the Saharan air mass differs in model and measured data. A comparison to cross sections at adjacent forecast times showed that this is not due to the relatively wide time range of data sampling. Thus the difference in the position of the moisture gradient at the edges of the Saharan PBL may be due to a lack of measured data, or point out a systematic error in COSMO. A closer look at the low-level cross section of flight B302 on 28 June 2007 will give more insight into this issue (see section 4.2 and Fig. 4.24).

Dropsondes 3, 5, and 6 sample a layer at 410 hPa where the potential temperature is less than 330 K and the mixing ratio higher than 1.5 g/kg. This is not evident in the aircraft profiles east of sonde 3 and west of sonde 6. It could be an effect of condensation right after launching the sonde.

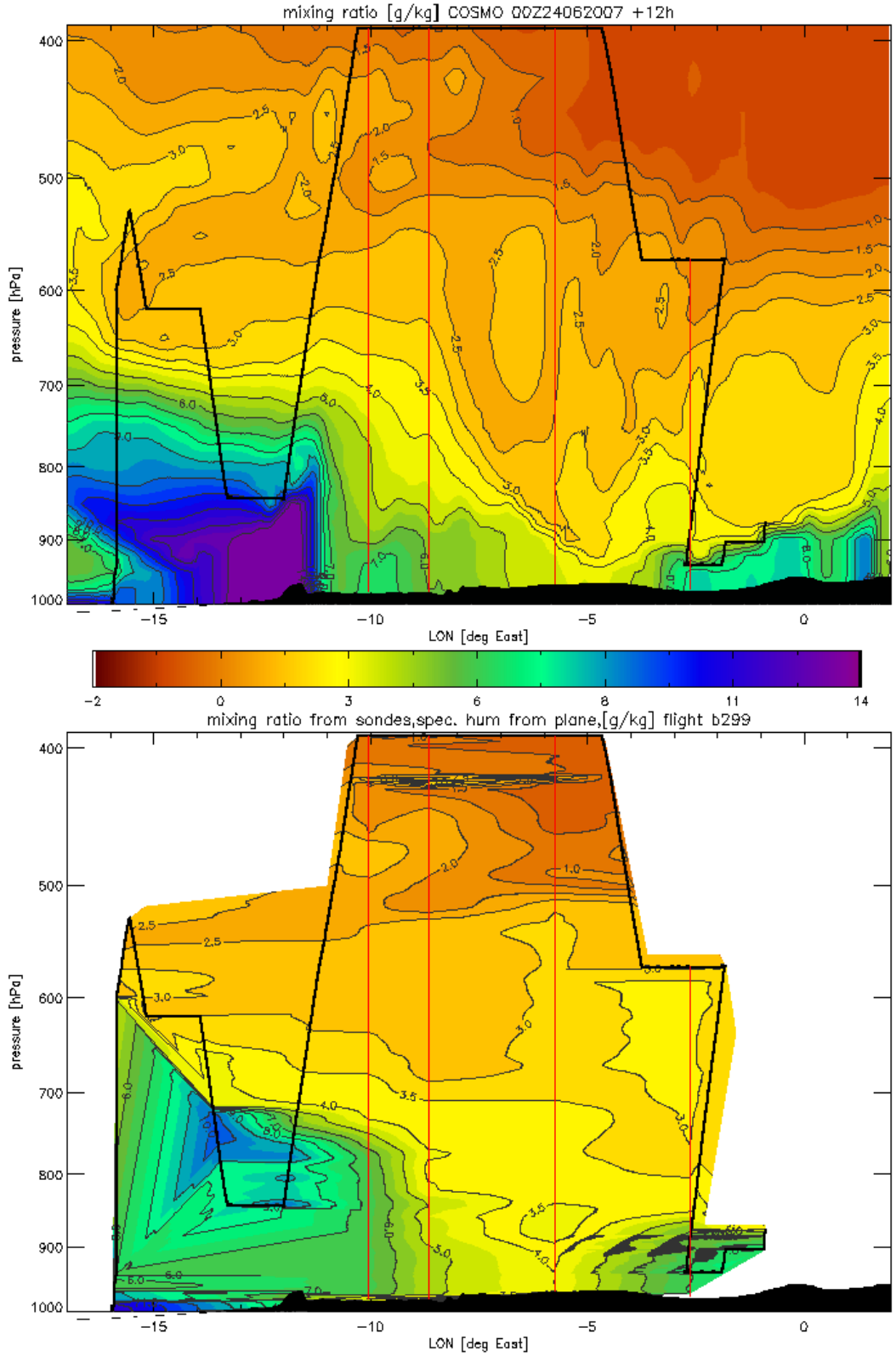

Figure 4.18: longitude-height cross section of humidity mixing ratio along 18°N. Top: model data. Bottom: interpolation from aircraft and dropsonde data. Same shading/contours used in both plots. Shading interbval 0.5 g/kg. Black contours: 0, 1, [1.5 to 4.0, 0.5 g/kg interval], [5 to 15, 1 g/kg interval] g/kg. Black shaded: orography. Black thick line indicates flight track. Red vertical lines show locations of dropsondes used for interpolation.

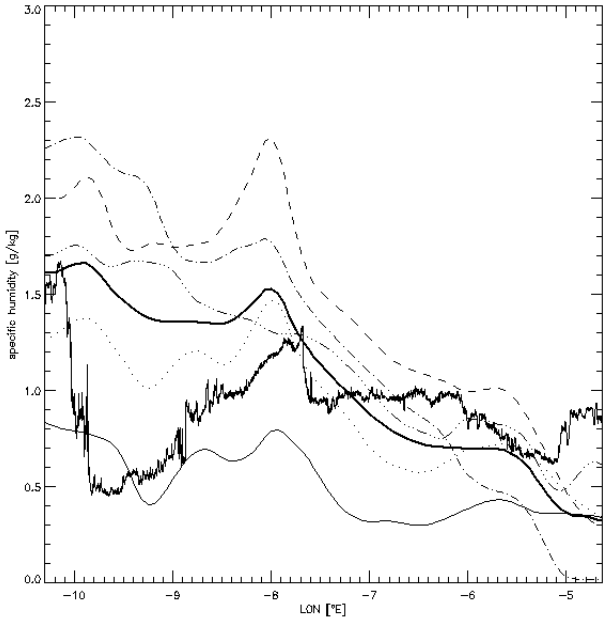

Figure 4.19: flight B299 24/06/2007: humidity mixing ratio from aircraft data during a high-level leg from 4.7°W to 10.4°W along 18°N at 392 hPa (solid, medium) and corresponding model data (00Z+12h) at levels 375 hPa (solid, thin), 400 hPa (dotted), 425 hPa (dashed, triple-dotted), 450 hPa (dashed-dotted), 475 hPa (dashed), and averaged from 375 hPa to 475 hPa (solid,thick).

Finally another interesting feature during the high-level leg at approximately 392 hPa from 4.7°W to 10.4°W is mentioned. At 9.8°W a sudden increase in humidity mixing ratio of 1 g/kg was observed in aircraft measurements (Fig. 4.19). This increase is evident in the model data as well, but more pronounced at 450 hPa.

In summary, the comparison of aircraft/dropsonde profiles and model profiles showed that COSMO is capable of reproducing reasonable profiles for the different elements of the West African monsoon along the flight track. Even if the predicted monsoon layer is generally up to 50 hPa shallower than observed, the model is capable of predicting the top and bottom of the Saharan PBL, Saharan residual layer, and SAL at the correct height ($\pm 20\,hPa$). Furthermore, the comparison showed that the model smooths vertical gradients in meteorological quantities when fine structured layers appear. The correlation between dust loading and meteorological quantities suggests that dust influences the local meteorological conditions. However, the absolute errors of potential temperature ($\pm$ 1 to 2 K) and humidity mixing ratio($\pm$ 1 to 2 g/kg) are minor for the purposes of our study of the Saharan PBL. Overall positive anomalies between model and observations of potential temperature appeared in the Saharan PBL and in the SAL, while negative anomalies appeared in the monsoon layer and in the free atmosphere. The model humidity mixing ratio within the monsoon layer is generally higher than that measured.

The vertical cross section along 18°N showed additional evidence for a systematic error of +1 K in model potential temperature and of +1 g/kg in model humidity mixing ratio (except for the Saharan PBL where model humidity mixing ratio is 1 g/kg smaller than the measured one). The interpolated cross sections also confirm the partitioning of the lower level atmosphere into the Atlantic Inflow, the Saharan PBL and the monsoon layer as predicted by the COSMO model on 24 June 2007.

4.1.4 Model validation in further quantities

So far the validation was limited to temperature and humidity profiles. In this subsection wind profiles and cloud cover will be validated. Therefore two examples of wind profiles from aircraft and dropsonde measurements, and an example of satellite imagery will be shown.

The wind profiles from sonde 6 and aircraft profile 6 were obtained rather close in time and space. At first sight it is obvious that the model data are much more smoothed compared to the measurements (Fig. 4.20). Nevertheless, COSMO profiles of zonal and meridional wind reproduce the shape of the measured profiles. From 700 to 500 hPa the African easterly jet is indicated by high values of zonal wind speed ($u > 10\,\mathrm{m/s}$) in both measured and COSMO data. COSMO fails to predict the lower zonal wind component at 600 hPa in the profile from sonde 6 and at 650 hPa in profile 6. Also, the winds from sonde 6 below 900 hPa differ stronlgy from modelled winds. It must be said that the difference in low-level winds is not as pronounced in other measured profiles.

Thus, COSMO struggles to reproduce thin layers in the wind fields and low-level winds which could be correlated with layering of dust and humidity. In spite of this, the basic shape of the wind profiles is reasonably reproduced. Profiles of wind components at other locations show similar patterns.

(a) sonde 6 (b) profile 6

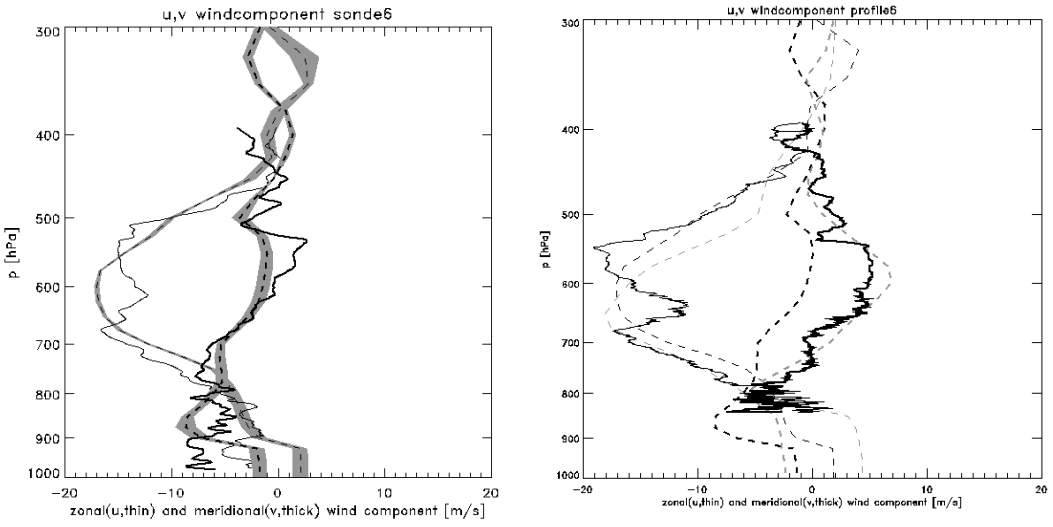

Figure 4.20: profiles of zonal (u-) (thin) and meridional (v-)(thick) wind components from sonde 6 (left) and aircraft profile 6 (right). Sonde/aircraft profiles are indicated with solid lines. Corresponding COSMO forecast data are indicated with dashed lines. Left grey shaded: standard deviation of model data on constant level in 0.5°x0.5° square centred around the closest grid point. Right: COSMO profile at starting point (black dashed), end point (grey dashed).

During the GERBILS campaign it became quickly clear that COSMO predicts mid-level clouds such as the altocumulus fields on top of the SAL very well. This was very helpful for the flight planning. Figure 4.21 shows the COSMO 33h total cloud cover forecast and the corresponding satellite image for 9 UTC 24 June 2007. The mid-level cloud fields over western Mauritania, the remnant of a convective system over Senegal, and some high and mid-level clouds over central Mali and Burkina Faso are well predicted by COSMO. They differ only a little in space and time from satellite measurements.

(a) COSMO 23/06/2007 00Z+33h

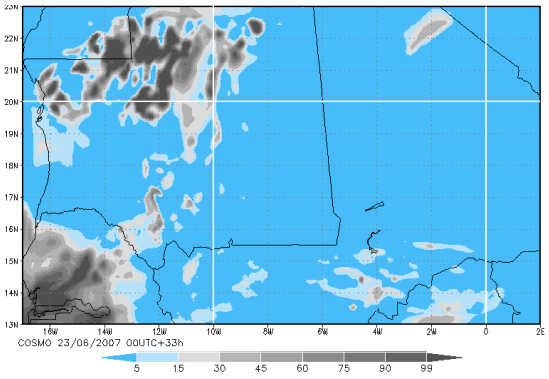

(b) Meteosat 9 10.8μm 24/06/2007 9 UTC

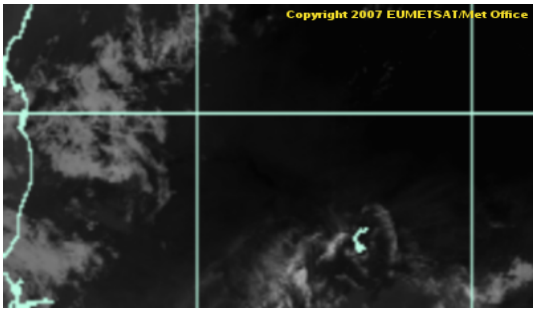

Figure 4.21: left: COSMO GERBILS forecast of total cloud cover [%] (shaded) for 9 UTC 24 June 2007, model initialisation time 00 UTC 23/06/2007. Right: Meteosat 9 10.8μm-channel, section of COSMO model domain, data courtesy of EUMETSAT.

4.2 Flight B302 from Nouakchott to Niamey

The meteorological conditions on 28 June 2007 were similar to those on 24 June 2007, except that the region west of the Tagant was not as strongly influenced by the monsoon flow as on 24 June (cf. Fig. 4.22 and Fig. 4.2). A secondary heat low vortex is only detectable over northern Mali at 20°N, 3°W, not over Mauritania.

Again the model separates the atmosphere along the flight track at 18°N into the three distinct layers (Figs. 4.23 and 4.22): from the Atlantic coast up to 12°W a moist layer indicates the Atlantic Inflow. It extends up to 850 hPa and is thus much shallower than the moist layer on 24 June which extended up to 700 hPa due to the monsoon. The eastern edge of the Atlantic Inflow is marked by a meridional gradient in virtual potential temperature ($\partial\Theta_v/\partial x = 3\,\mathrm{K}/(100\,\mathrm{km})$) and specific humidity ($q^v = 2.5\,\mathrm{g/kg}/(100\,\mathrm{km})$). The Saharan PBL is evident from 10°W to 5°W in the low levels and from 8°W to 2°W in the mid levels. A shallow monsoon layer can be detected in the east of the Saharan PBL. However, this layer is deeper than the one of 24 June. The flight track of flight B302 on 28 June 2007 followed a low-level leg at 18°N from 13°W to 4.5°W.

In this section aircraft data will be used to investigate the position of the horizontal gradients in potential temperature and humidity mixing ratio at the border of the Atlantic Inflow and the Saharan PBL. This adds a low-level view to the study of the longitudinal-vertical cross section at 18°N.

Aircraft measurements of potential temperature and humidity mixing ratio of the low-level leg at around 940 hPa from 13°W to 4.5°W during flight B302 on 28 June 2007

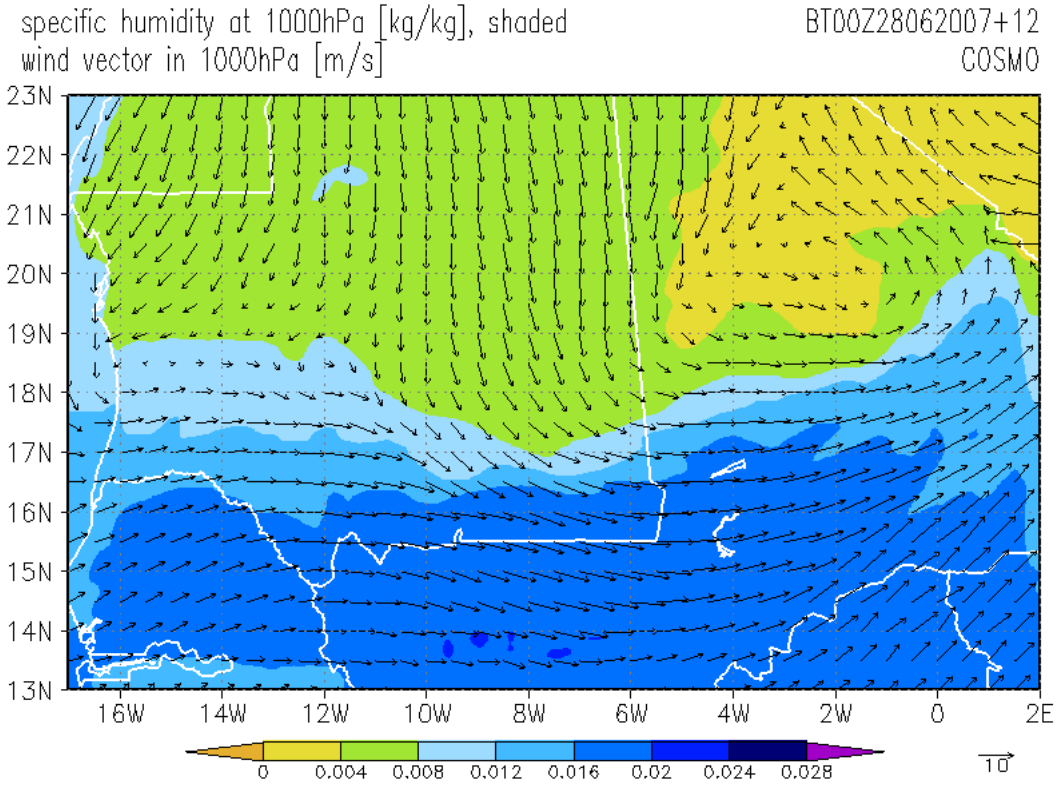

Figure 4.22: specific humidity and wind vectors at 1000 hPa in COSMO model domain. COSMO 28/06/2007 00UTC+12h.

are shown in Figure 4.24 together with corresponding model data. The leg started at around 11:45 UTC and ended at around 14:00 UTC. This is taken into account by giving model data for 12, 13, and 14 UTC. Additionally, measurements of wind components, equivalent potential temperature, ozone and dust are shown in Fig. 4.25. This enables us to characterise the dynamics and air masses in more detail.

As the aircraft enters the Saharan PBL potential temperature starts to increase from 306 K at 12°W to 310 K at 11°W. The humidity mixing ratio does not decrease before 10°W where aircraft data shows an abrupt decrease from 8 g/kg at 10.2°W to 6 g/kg at 10°W. The model at 12 UTC locates the increase in potential temperature between 12°W and 11°W at the right position and with the same absolute values, but it fails to predict the abrupt decrease of mixing ratio at the same location. In model data at 12, 13, and 14 UTC humidity mixing ratio decreases from 8 g/kg at 11.3°W to 5 g/kg at 10.5°W. Thus the humidity gradient in the model is much smoother and shifted by around 0.5°-1° westwards, but the absolute values agree. Marsham et al. (2008) made a similar observation for flight B301 on 27 June 2007 (cf. Fig. 4 in Marsham et al. (2008)). Also the incorrect position of the humidity gradient was indicated in the comparison of model cross section and interpolated cross section of flight B299 on 24 June 2007 (see Fig. 4.18). Looking at the air mass characteristics it becomes obvious that the moist air west of 10°W correlates with high amounts of dust (total backscattering of around $2 \times 10^{-4} m^{-1}$), low ozone concentrations (28ppbv) and high equivalent potential temperature (335 K). Thus the sharp gradient in various quantities at 10°W separates two different air masses. In contrast (virtual) potential temperature does not seem to be a tracer for air masses. The

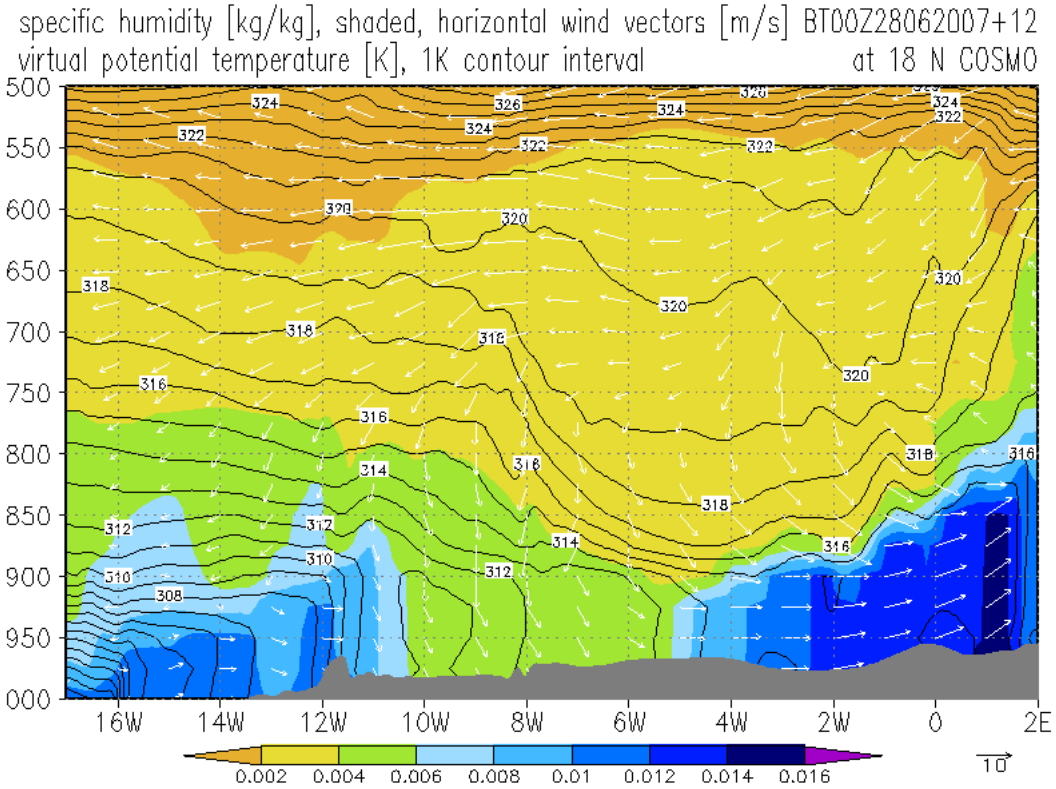

Figure 4.23: longitude-height cross section of specific humidity [kg/kg] (shaded), virtual potential temperature [K] (black, 1 K contour interval) and *horizontal* wind vectors [m/s] at 18°N. Vertical coordinate is pressure [hPa]. Grey shading indicates terrain by surface pressure. COSMO 28/06/2007 00 UTC+12h.

increase in (virtual) potential temperature from 12°W to 11°W agrees with the elevation of the terrain. At 12°W the coastal plain abruptly ascends towards the Tagant Plateau. The latter could form an elevated heat source. Surface pressure at the peaks of the Tagant is usually around 960 hPa. Thus the aircraft at 940 hPa was close to the ground.

Further east within the Saharan PBL the aircraft data shows a nearly constant humidity mixing ratio of around 5 g/kg (Fig. 4.24) which is also predicted by the model (13 UTC). Potential temperature increases steadily towards the east. The measured data fits within the range predicted by the model (12-14 UTC). At 8°W aircraft data shows a local maximum in potential temperature (313.5 K) correlated with a local minimum in humidity mixing ratio (4.5 g/kg). Both are evident in model data as well. Eastwards of the local extremum, the potential temperature decreases abruptly by about 1.5 K, and humidity mixing ratio increases to 5 g/kg, while in model data both remain constant. The feature is related to an abrupt change in surface properties, which are smoothed and possibly erroneous represented in the model. For example, at 8°W the albedo derived from MODIS data decreases from 0.50 to 0.25, whilst the model albedo only decreases from 0.40 to 0.35 (not shown). At 6.7°W the measurements indicate a second weaker anomaly (Fig. 4.24). Further east, the humidity mixing ratio decreases to around 4 g/kg, whereas in model data it remains constant. The model also predicts the western edge of the monsoon layer at around 5°W, whereas there is no sign of a monsoon layer in measured data. At 6.7°W the weaker anomaly is observed as an abrupt decrease of potential temperature

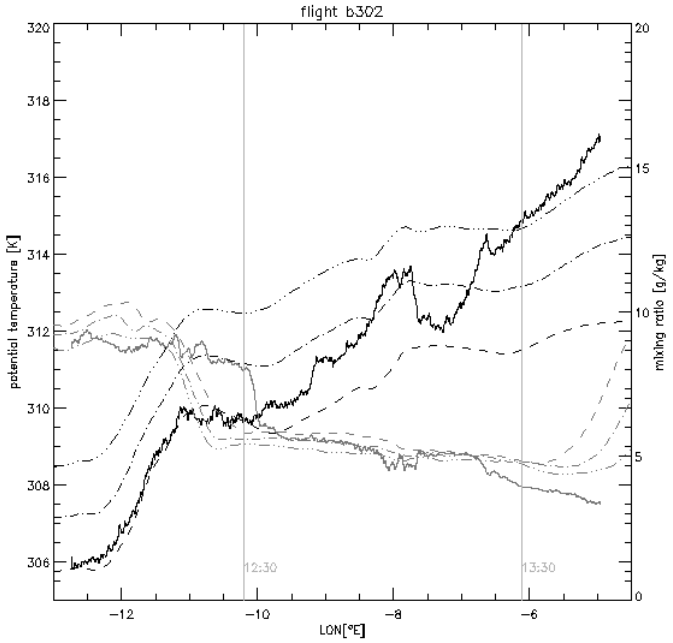

Figure 4.24: potential temperature (black) and mixing ratio (grey) from low-level leg of flight B302 28/06/2007. Thick solid lines: aircraft data. Dashed: model data at 12 UTC. Single dot-dashed: model data at 13 UTC. Triple dot-dashed: model data at 14 UTC. Model initialisation time is 00 UTC 28/06/2007. Grey vertical lines indicate time when aircraft passed.

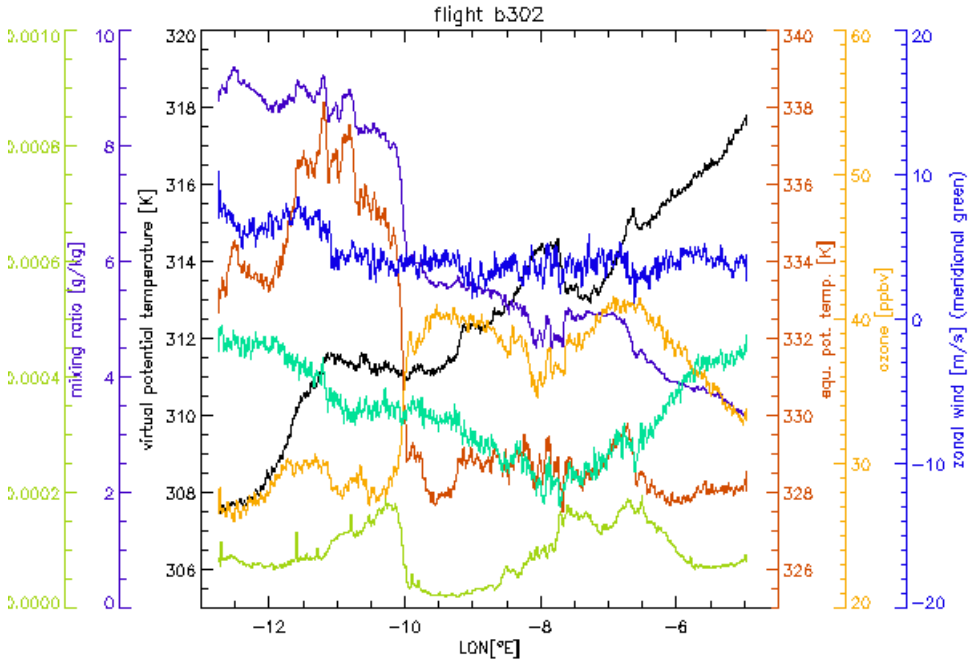

Figure 4.25: low-level leg flight B302, various quantities: virtual potential temperature [K] (black), humidity mixing ratio [g/kg] (violet), equivalent potential temperature [K] (orange), ozone [ppbv] (yellow), blue total scattering coefficient [1/m] (light green),zonal and meridional wind component [m/s] (blue and green, blue axis is valid for both).

by 0.5 K. Further east, the potential temperature increases again, which is also evident in model data. The low-level leg of flight B302 was also investigated by Marsham et al. (2007). He showed that the anomaly at 8°W is due to albedo variations.

In summary, the investigation of the low-level leg at 18°N showed that the model represents changes in potential temperature very well. It fails to take into account heterogenous small-scale surface properties and to predict gradients of humidity mixing ratio at the correct position. Nevertheless, absolute values within the Atlantic Inflow region and the Saharan PBL are predicted very well.

4.3 Conclusions

Aircraft and dropsonde data were used to validate the COSMO model in a desert environment. The character of the measurements determines an emphasis on the heat and moisture budget. The comparison showed that COSMO can represent the vertical structure of the atmosphere reasonably well. It locates the different features of the West African monsoon, such as the monsoon layer, the convective internal boundary layer, the Saharan residual layer, and the SAL at correct heights. The horizontal position of these features differs slightly from measurements. The height of the top of the SAL is remarkably well predicted. This leads amongst other things to good forecasts of mid-level altocumulus clouds at the top of the SAL. The potential temperature in the model seems to be generally around 1 K too high and humidity mixing ratio around 1 g/kg too low. As COSMO does not include dust it struggles with representing fine layers (observable in meteorological quantities as well) which are highly linked to dust loading. COSMO seems to struggle in predicting the flow within different layers at the correct height and with correct absolute values. This could be due to lack of data or erroneous aircraft measurements and needs more detailed analysis. The validation encouraged us to use COSMO for further investigations of the temporal and spatial evolution in the south-west Saharan region. In the following, the evolution of the observed baroclinic zone will be studied in more detail.

5 The Atlantic Inflow

A baroclinic zone separating the Saharan heat low from a region which is influenced by the Atlantic Ocean in the west was evident in the cross sections along 18°N. This raises the question which impact the Atlantic Ocean has on the atmosphere between the coast and the Saharan heat low region. A similar baroclinic zone has been observed in south-eastern Spain (Kottmeier et al. 2000). The numerical studies of Racz and Smith (1999) and Spengler et al. (2005) showed a baroclinic zone at the transition from the heat low to maritime air. The "morning glory" phenomenon in north-eastern Australia originates from a sea-breeze at the transition from maritime to continental air (Reeder and Smith 1999).

The COSMO model code was adapted to provide additional output of the individual tendency terms of the heat and humidity equation (section 2.3). In this chapter we use the additional model output to gain a more detailed insight into physical processes.

The analysis of model data showed that the atmosphere between the coast and the Saharan heat low is influenced by a major system which we call the "Atlantic Inflow". The Atlantic Inflow basically is a sea-breeze transforming into a sea-breeze front. This coastal front has characteristics of a gravity current. It affects the mid-level atmosphere through its frontal circulation and in the case of stably-stratified mid levels it induces internal gravity waves. The Atlantic Inflow seems to be a typical phenomenon at the Mauritanian coast. The spatial extent and depth of inland penetration is highly variable in time. Nevertheless, the Atlantic Inflow could be observed every day during GERBILS (at least as a small band at the coast). Three modes of the Atlantic Inflow were found depending on the location of synoptic-scale features such as the Saharan heat low, the monsoon flow, and the position of the Intertropical discontinuity (ITD).

In section 5.1 an overview of the Atlantic Inflow is given. The meteorological situation as well as the distinction in different modes is outlined in section 5.2. In section 5.3 methods for the detection of the Atlantic Inflow coastal front are presented and its inland penetration on several days is highlighted. The vertical structure as well as gravity waves induced in the mid-level atmosphere are shown in section 5.4, then the gravity current character of the Atlantic Inflow is discussed in section 5.5. Ideas about the effect of the Atlantic Inflow on the evolution of the baroclinic zone and about a nocturnal jet in the coastal region are presented in section 5.6 and section 5.7. Finally, the findings of these sections are discussed in section 5.8 and combined to give a coherent explanation of the physical mechanism which drives the Atlantic Inflow.

5.1 General description

During the GERBILS campaign we observed the diurnal formation of a coastal front at the Mauritanian coast. The front started moving eastwards in the late afternoon almost every day and penetrated up to 400 km inland. The front can be seen as a strong meridional gradient of virtual potential temperature. A series of longitudinal-vertical cross sections of virtual potential temperature at 18°N is given in Fig. 5.1. The plot shows the Atlantic Inflow on 24 June 2007.

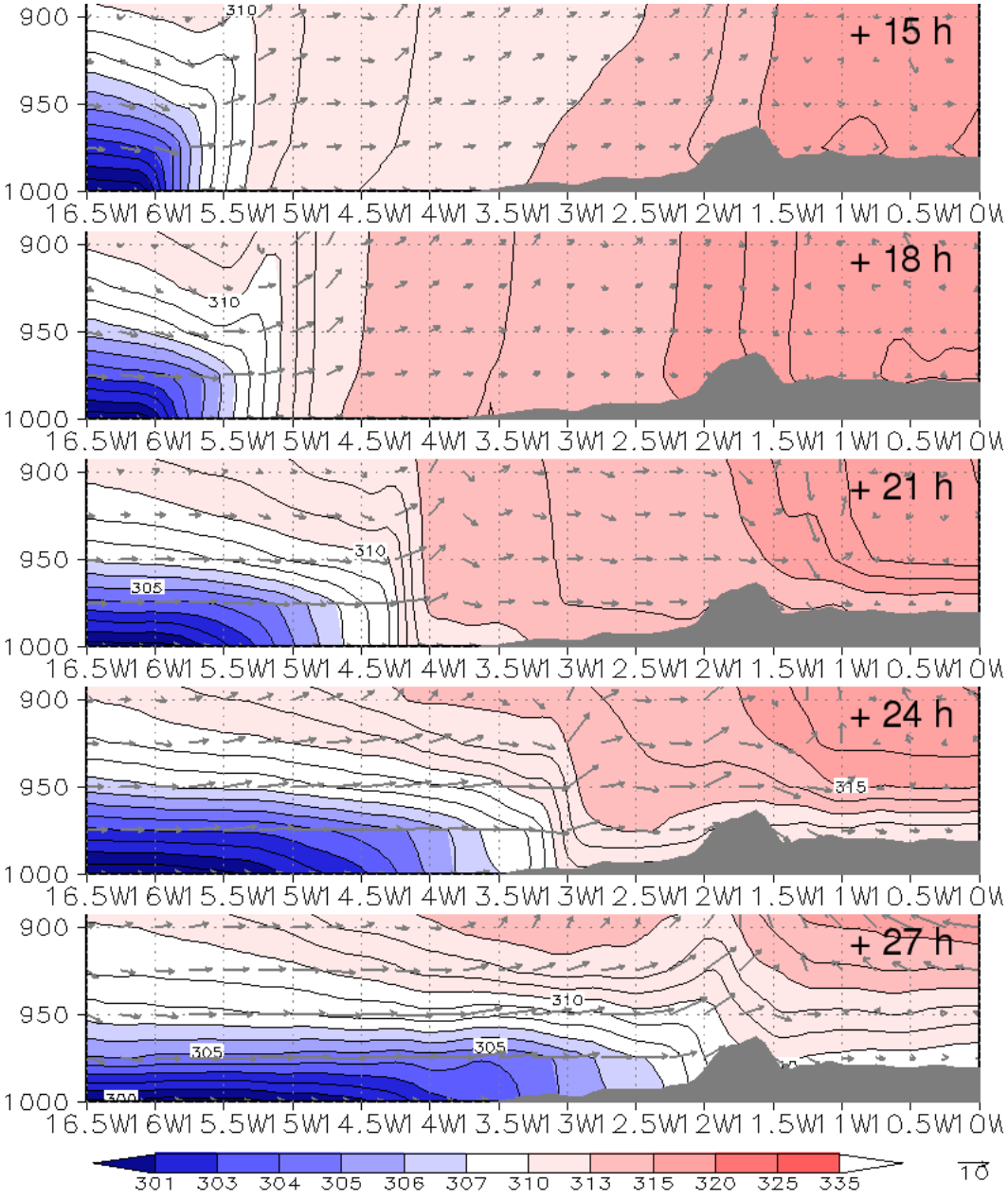

Figure 5.1: longitude-height cross section of virtual potential temperature [K] (shaded, 1 K contour lines) at 18°N on 24-25 June 2007 at 15, 18, 21, 00 and 03 UTC. Wind vector in plane of section (grey arrows). Orography (grey). Based on COSMO_budget run initialised 00 UTC 24/06/2007, shifted domain. Forecast hours in top right corner.

Cool, stably-stratified air from the coast penetrates inland with the coastal front up to the Tagant Mountains at 12°W. The low-level winds increase behind the front and are from the coast. Furthermore, in most cases this is linked to onshore advection of humidity. The system has characteristics of a sea-breeze transforming into a sea-breeze front and of a density current. As indicated by the bulge of isentropes at the head of the front in Fig. 5.1, the coastal front induces gravity waves (see section 5.4.2). The head of the Atlantic Inflow has the structure of a solitary wave and has parallels to the "morning glory" phenomena in Australia described by Reeder and Smith (1999). We call the whole of the phenomena described above the Atlantic Inflow. Its preferred region of occurence is the vast coastal plain in western Mauritania (longitude 16°W to 12°W, latitude 20°N to 16°N, Figs. 2.1 and 3.2). Deep inland penetration is especially notable between 17°N and 19°N. The Atlantic Inflow appears almost every day from the late afternoon to the first half of the night.

The West African coast between 15°N and 22°N is favourable for the development of sea-breezes and sea-breeze fronts penetrating far inland. In contrast to the case studied by Kottmeier et al. (2000) the terrain is flat and ascends gradually to 200 m above mean sea level at the foot of the Tagant Plateau at 12°W. The latter is located 400 km inland and forms the first orographic barrier east of the Atlantic coast (Fig. 3.2 and section 3.1). The peaks of the Tagant reach 400-600 m above mean sea level. Also, a strong temperature gradient between the coastal zone and the desert inland is formed by the rather cold surface waters of the Atlantic Ocean and by high insolation in the desert environment over land. This is illustrated with the soil temperature from the ECMWF analysis at 18 UTC 24/06/2007 (Fig. 5.2). Ocean temperatures of 22°C and below indicate the cold Canary current. In contrast, the surface temperature in western Mauritania reaches up to 45°C in the late afternoon.

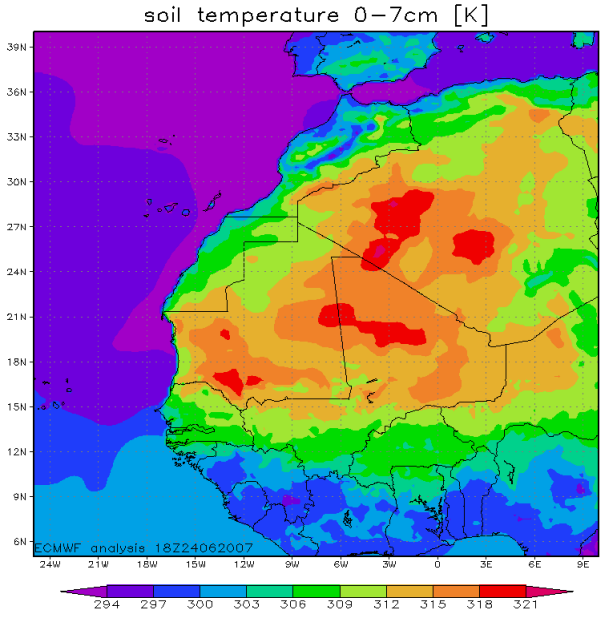

Figure 5.2: soil temperature [K] in the layer 0-7 cm from ECMWF analysis 18 UTC 24/06/2007.

The detection of the pure effect of the Atlantic Inflow is not straightforward. The Harmattan winds, Saharan heat low, ITD, and monsoon flow are important synoptic features which are highly variable in time and space at the time of the monsoon onset. The result is a superposition of different meteorological systems which makes it difficult

to detect the pure effect of the Atlantic Inflow at the Mauritanian coast. During the GERBILS campaign the Atlantic Inflow was best observable on one day: the 24 June 2007. On the other days the effect was detectable as well, but superimposed by other features. In the next section the Atlantic Inflow is studied based on two COSMO_budget 69h forecasts. The first one was initialised on 00 UTC 24/06/2007 with the shifted model domain. A second run was initialised on 00 UTC 28/06/2007 with the standard model domain. For details of the model setup refer to section 2.4.2.

5.2 Meteorological situation and modes

The synoptic situation in the Atlantic Inflow region (16°N-20°N, 16°W-12°W) is determined by the interaction of the Saharan heat low, the monsoon flow, and the position of the ITD. The latter separates the hot dry desert air from the cooler moist monsoon air.

A more detailed meteorological overview than in section 3.2 is given in this section for the two periods 24-26 June 2007 and 28-30 June 2007. The 2 m temperature, the mean sea level pressure, the horizontal wind field at 10 m and the 20 K contour of 2 m dew point difference are shown in the left columns of Figs. 5.3 and 5.4. The domain covers 13.5°N-22-5°N, 16.5°W-1.5°E. The right columns of Figs. 5.3 and 5.4 show longitudinal-vertical cross sections of virtual potential temperature and specific humidity at 18°N. The plots are shown at 18 UTC every day, a time when the Atlantic Inflow started the inland penetration.

On 24 June the Saharan heat low is located east of the Atlantic Inflow region (Fig. 5.3a). It covers major parts of northern Mali and eastern Mauritania. In the Atlantic Inflow region remnants of a heat low trough are indicated by the 1008 hPa contour. Despite this a rather homogenous meridional pressure gradient is dominant here. The ITD, as indicated by horizontal wind convergence and 20 K dew point difference contour, lies at around 17°N from 16°W to 12°W. The 2 m temperature shows a strong gradient at the Mauritanian coast. Due to the onshore flow on this day and due to the Atlantic Inflow a 50-100 km wide zone at the coast between 17°N and 20°N is already covered by cooler maritime air. The low-level flow in the Atlantic Inflow region seems highly ageostrophic, in particular west of 14.5°W behind the coastal front. The vertical cross section along 18°N shows the Saharan heat low extending from 11°W to 3°W (Fig. 5.3b). It is evident through the almost neutral stratification and specific humidity below 5 g/kg. The top of the Saharan PBL is marked by a strong vertical gradient of virtual potential temperature at around 500 hPa. At 12°W there is evidence of an orographically induced gravity wave. Nevertheless, east of the Tagant Plateau at 12°W the mid levels above 800 hPa are rather moderately stably-stratified. A baroclinic zone from 12°W, 500 hPa to 8°W, 750 hPa marks the transition between the Saharan PBL and the atmophere west of 12°W. However, daytime turbulent mixing destroyed the tilt of the baroclinic zone in the lower levels (cf. cross section at 12 UTC in Fig. 4.3 and discussion in section 4.1). In the Atlantic Inflow region the influence of turbulent mixing is evident up to around 800 hPa, whereas well-mixed layers reach 650-550 hPa in the Saharan heat low region. A strong meridional gradient of virtual potential temperature in the low levels at 15°W and an induced gravity wave in the mid levels marks the Atlantic Inflow. In the specific humidity we see a humid layer up to 700 hPa in the Atlantic Inflow region. This is a remnant of a

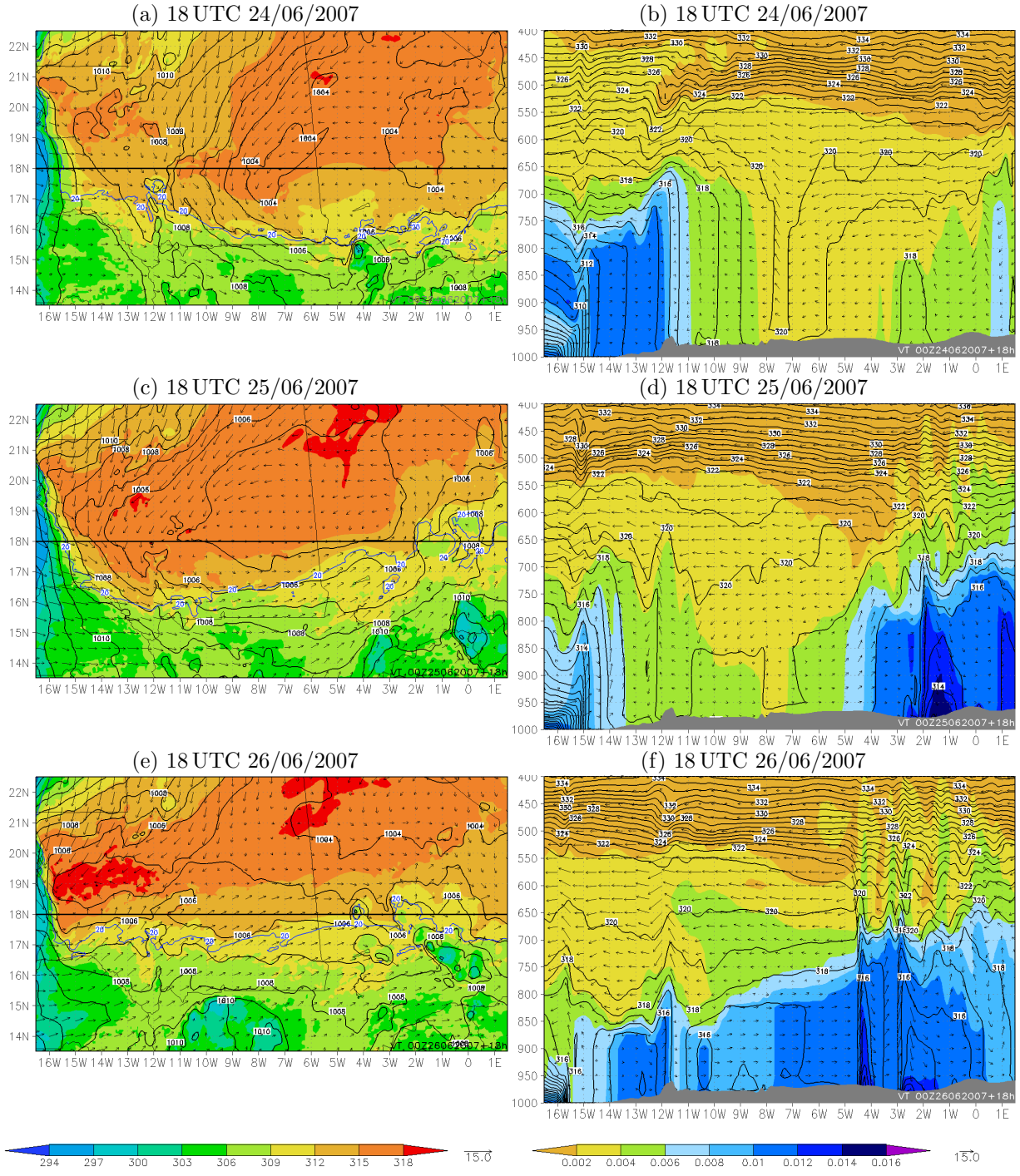

Figure 5.3: **period 1**: left column: 2 m temperature [K] (shaded), mean sea level pressure [hPa] (black, 1 hPa contour interval), dew point difference 20 K (blue contour), horizontal 10 m wind vectors [m/s] (black). From 00 UTC operational COSMO forecasts in standard domain. Black thick line: location of cross section at 18°N. Black thin line: political boundaries. Right column: longitude-height cross section at 18°N of virtual potential temperature [K] (black, 1 K contour interval), specific humidity [kg/kg] (shaded), wind vector in plane of section (black). From 00 UTC operational COSMO forecasts in standard domain.

northward monsoon penetration the day before. However, as mentioned previously, the ITD retreated south of 18°N (Fig. 5.3a) and weak Harmattan winds are dominant in the coastal plain.

On 25 June the Saharan heat low is located further to the west. A heat low trough extends into the Atlantic Inflow region (Fig. 5.3c). Hence the 2 m temperatures are higher than the day before and reach up to 318 K in the Atlantic Inflow region. A strong meridional temperature gradient marks the coastal zone. To the west of 11°W the ITD has retreated further south. To the west of 15°W the 20 K dew point difference contour indicates the Atlantic Inflow. In the eastern part of the model domain the monsoon flow shows a significant northward penetration. The westward position of the Saharan heat low is reflected in the cross section at 18°N (Fig. 5.3d). The rather well-mixed, neutrally-stratified Saharan PBL extends over the coastal plain from 15°W to 4°W. The top of the Saharan PBL moved westwards, too. It is evident from 15°W to 5°W at around 450-500 hPa. To the east of 4°W the northward penetration of the monsoon becomes evident through the high specific humidity. The Atlantic Inflow appears at around 15°W. It moves into the deep Saharan PBL resulting in a more pronounced bulge in isentropes at its leading edge. A steep baroclinic zone becomes established from the head of the Atlantic Inflow towards the Saharan PBL. This becomes easier to detect in the following hours (not shown).

High 2 m temperatures ($T_{2m} > 318$ K) and the almost closed 1005 hPa isobar at around 19°N indicate a secondary heat low in the northern part of the Atlantic Inflow region on 26 June 2007 (Fig. 5.3e). On this day, the ITD is detectable in the low-level wind field. The south-westerly flow south of 18.5°N indicates far northern penetration of the ITD. The low-level monsoon flow in the southern Atlantic Inflow region is highly ageostrophic. High values of specific humidity in the cross section at 18°N show the monsoon flow below 850 hPa in the west and below 650 hPa in the east (Fig. 5.3f). There is evidence of the remnant SAL from 15°W to 5°W in a layer from 750 to 550 hPa. The Atlantic Inflow appears at around 15.5°W.

On 28 June the synoptic situation is similar to 24 June. The Saharan heat low lies over northern Mali (Fig. 5.4a). A rather homogenous meridional pressure gradient extends over the Atlantic Inflow region. The 2 m temperature is around 3 K lower than on 24 June. The onshore flow is less pronounced and rather from the north-west. Again the flow is ageostrophic in the Atlantic Inflow region westwards of the low-level meridional temperature gradient. The ITD is located at around 17.5°N at 16°W and 17°N at 12°W. The cross section at 18°N shows a moderately stable layer above 800 hPa over the coastal plain (Fig. 5.4b). Below 850 hPa a rather well-mixed atmopshere indicates the daytime turbulent mixing. A tilted baroclinic zone from 12°W to 7°W marks the transition into the Saharan PBL. The latter extends from 8°W to 2°W. The top of the Saharan PBL is above 550 hPa. The Atlantic Inflow appears at 15°W. In contrast to 24 June it seems to advect more humid air onshore.

Although the Saharan heat low moved westwards on 29 June, the meteorological situation in the Atlantic Inflow region is similar to 24 and 28 June (Fig. 5.4c). The ITD retreated south of 17°N in the entire Atlantic Inflow region. A meridional temperature gradient is evident at the coast from 20°N to 17.5°N. Here the flow is not as strongly ageostrophic as on 24 or 28 June, indicated by a smaller cross-isobar angle. The cross section at 18°N shows the same structures as on 24 and 28 June (Fig. 5.4d) with a moderately stable layer at the mid levels over the coastal plain. East of 11°W there is the deep

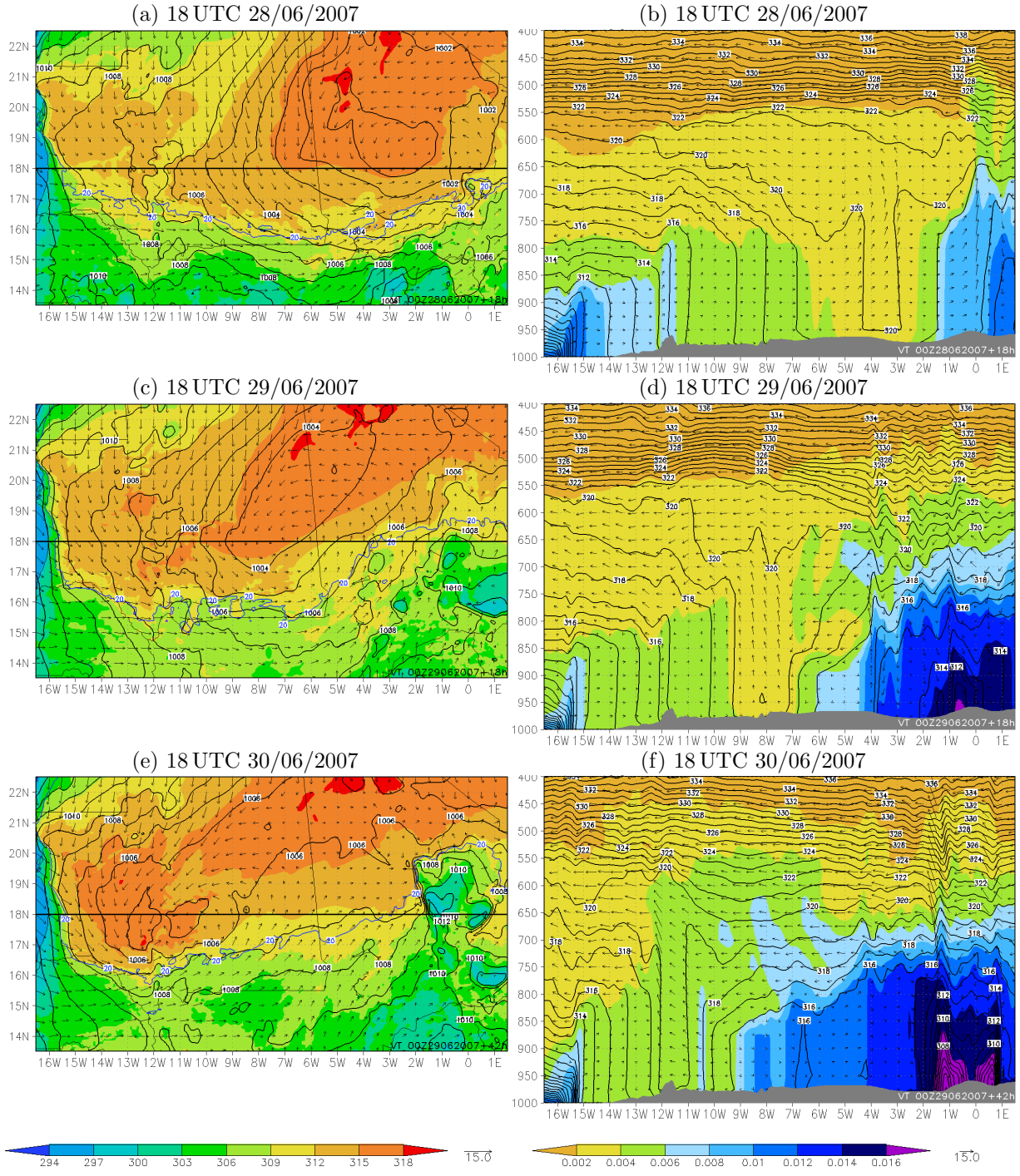

Figure 5.4: same as Fig. 5.3 but for **period 2**.

Saharan PBL. A weak baroclinic zone marks the transition between the two layers. The low levels above the coastal plain are rather well-mixed. The Atlantic Inflow appears at 15.5°W.

On 30 June 2007 the situation is similar to 25 June. A secondary heat low centred above the Tagant Plateau has become established over the whole Atlantic Inflow region (Fig. 5.4e). Here the ITD lies south of 16.5°N. The monsoon flow penetrates far north in the eastern part of the model domain. This is reflected also in the cross section of specific

humidity at 18°N (Fig. 5.4f). The cross section indicates the Saharan PBL from 15°W to 9°W and the Atlantic Inflow west of 15°N.

The discussion of the meteorological situation during the two periods showed three typical constellations of the Saharan heat low and the monsoon flow. Depending on the location of the synoptic-scale features relative to the Atlantic Inflow region three modes of the Atlantic Inflow can be defined. In mode 1 the Saharan heat low and its deep Saharan PBL (almost neutrally-stratified well-mixed atmosphere up to 450 hPa) is located east of the Tagant Plateau (Fig. 5.5a). In the Atlantic Inflow region daytime turbulent mixing leads to a convective, rather neutrally-stratified boundary layer up to 800 hPa while the mid levels above 800 hPa remain moderately stably-stratified. A strong baroclinic zone in the mid levels separates the two air masses. We will also refer to mode 1 as the "standard"- or the CBL-mode (convective boundary layer), as this seems to be the most typical synoptic situation at the Mauritanian coast. 24 June 2007 is a good example for this mode. It also occured on 28 and 29 June 2007. In mode 2 the Saharan heat low extends over the Atlantic Inflow region to the Mauritanian coast at 16°W (Fig. 5.5b). Thus, the Atlantic Inflow front penetrates into the deep neutrally-stratified Saharan PBL, leading to a strong updraft at the head of the coastal front. A very steep baroclinic zone evolves above and behind the front. We will also refer to mode 2 as the heat low-mode. Mode 2 was observed on 25 and 30 June 2007. In mode 3 the monsoon flow penetrates far north and covers major parts of the coastal plain (Fig. 5.5c). Thus the Atlantic Inflow penetrates into the monsoon flow. We will also refer to mode 3 as the monsoon-mode. Mode 3 was observed on 26 June 2007. In section 5.4 it will be shown that the three modes lead to different effects of the Atlantic Inflow in the vertical. The emphasis in this study lies on the standard-mode (mode 1).

(a) standard or CBL-mode: mode 1

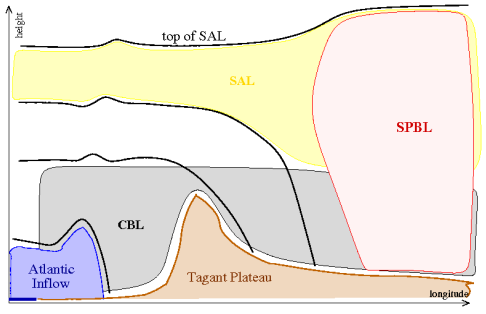

(b) heat low-mode: mode 2

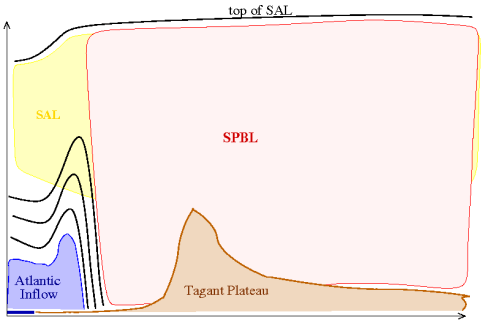

(c) monsoon-mode: mode 3

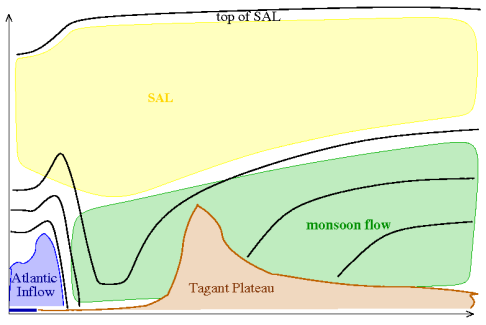

Figure 5.5: sketches of Atlantic Inflow modes. characteristic isentropes (black lines). Atlantic Inflow (blue), orography (brown), convective boundary layer (CBL) (grey), Saharan PBL (SPBL) (red), Saharan Air Layer (SAL) (yellow), and monsoon layer (green).

5.3 Detection of the Atlantic Inflow

In this section methods to detect the Atlantic Inflow are presented. Time-height plots are suitable for the determination of the time when the Atlantic Inflow appears at a specific location (subsection 5.3.1). The horizontal structure and extent of the Atlantic Inflow can be detected best in the horizontal gradient of virtual potential temperature in a longitudinal-latitudinal plot at low levels (subsection 5.3.2). Longitudinal-vertical cross sections are suitable for locating and investigating both the location and the vertical structure of the Atlantic Inflow at a specific latitude (section 5.4).

5.3.1 The Atlantic Inflow at a specific location

The passage of the Atlantic Inflow coastal front is linked with a sharp decrease of virtual potential temperature, a change in humidity, and an increase in zonal wind speed. This is illustrated using time-height plots at 18°N, 15°W and 18°N, 14°W for the second forecast period 28-30/06/2007 based on COSMO_budget forecast initialised 00 UTC 28/06/2007 for the standard domain.

In the night of 28-29 June 2007 the Atlantic Inflow appears at 15°W at around 22 UTC (Fig. 5.6). The specific humidity increases abruptly to values above 10 g/kg in the lowest levels ($p < 975$ hPa). At the same time the virtual potential temperature at 1000 hPa decreases by around 5 K in one hour. The zonal wind speed at 975 hPa increases from less than 2 m/s at 22 UTC to more than 10 m/s at 23 UTC. At 14°W the front passes at

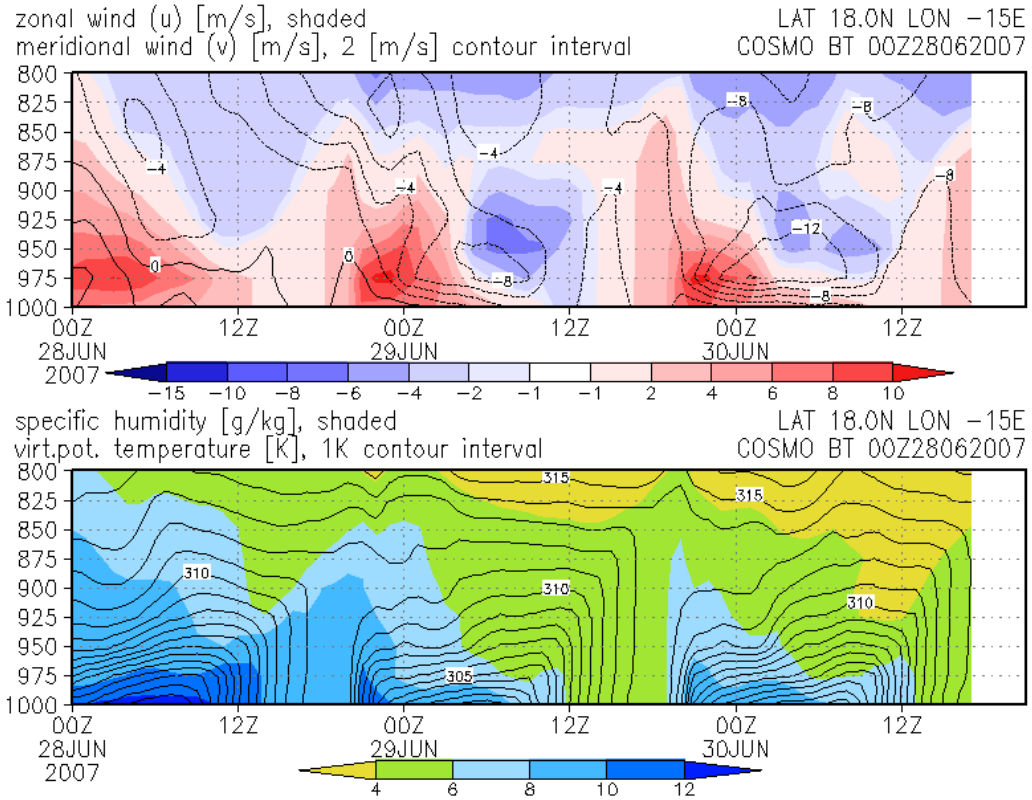

Figure 5.6: time-height plots of specific humidity (shaded), virtual potential temperature (1 K contour interval, both at bottom of the subfigures), zonal (shaded) and meridional wind speed (2 m/s contour interval, both at the top of the subfigures) at **18°N, 15°W**.

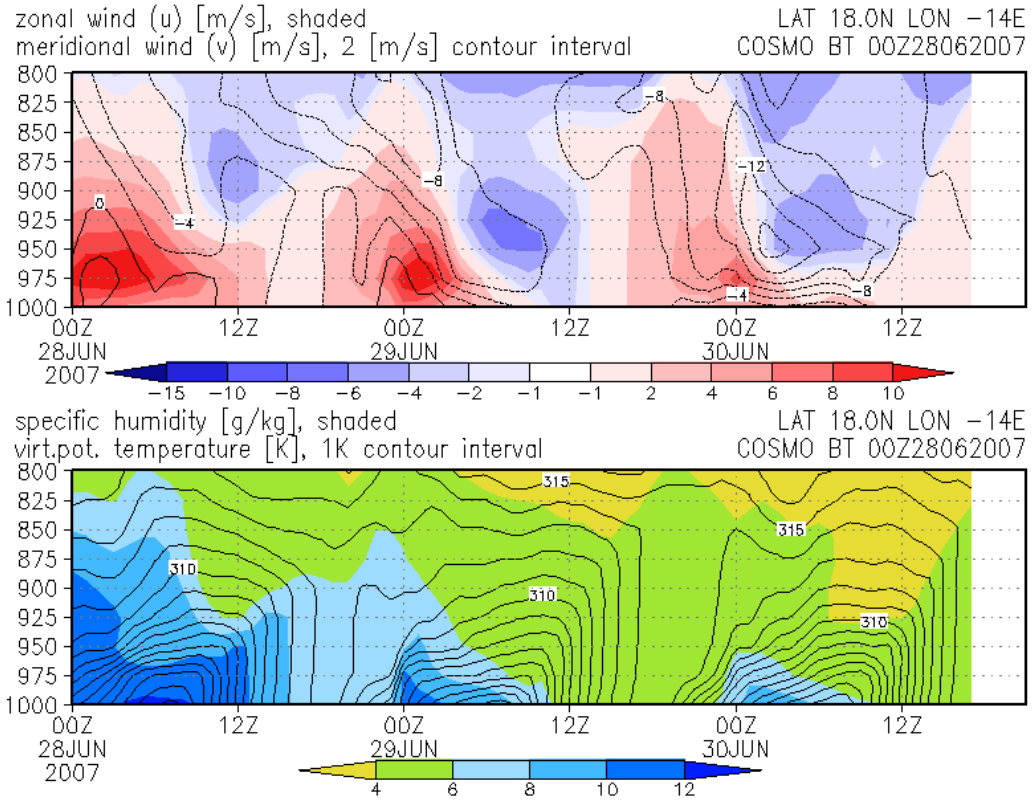

Figure 5.7: same as Fig. 5.6 but at **18°N, 14°W**.

around 00 UTC and leads to similar changes in the low-level meteorological fields (Fig. 5.7). At the lowest levels ($p < 950$ hPa) the virtual potential temperature starts to decrease from 22 UTC due to radiative cooling at the surface. The Atlantic Inflow superposes this radiative cooling effect by a stronger cooling up to 925 hPa from 00 UTC on. One day later in the night of 29-30 June 2007 the signal of the Atlantic Inflow in the meteorological fields is similar.

The occurrence of the Atlantic Inflow is also detectable in the Brunt-Väisälä-frequency N. Analogous to Fig. 5.6, Fig. 5.8 shows time-height plots of N^2, virtual potential temperature, temperature tendency due to sub-grid scale turbulence, and vertical velocity at 18°N, 15°W (Fig. 5.8) and 18°N, 14°W (Fig. 5.9).

On both nights the Atlantic Inflow becomes evident in a sharp increase of N^2 in the layers below 900 hPa. At 15°W and 14°W the low-level atmosphere is nearly neutrally-stratified ($N^2 \approx 0\ s^{-2}$) in the afternoon and early night before 21 UTC. With the passage of the coastal front at 15°W (22 UTC) the squared Brunt-Väisälä-frequency increases to more than $3.5 \times 10^{-4} s^{-2}$ indicating a dramatic stabilisation of the low levels in the rather maritime air behind the front (Fig. 5.8). At 14°W after 22 UTC radiative cooling leads first to a shallow stable layer ($N^2 \approx 2.0 \times 10^{-4} s^{-2}$, Fig. 5.9). At around 00 UTC the coastal front passes and leads to a deeper (up to 900 hPa) and more stable layer ($N^2 > 3.5 \times 10^{-4} s^{-2}$).

Figs. 5.8 and 5.9 also show the vertical velocity and the temperature tendency due to sub-grid scale vertical turbulent diffusion, which is linked to the sensible heat flux (cf. section 2.3). A distinct diurnal cycle in turbulent diffusion is striking. From around 10 UTC turbulent diffusion, which grows up to 850-800 hPa in the afternoon, leads to a warming from the ground into higher levels. At around 16-18 UTC there is a sudden

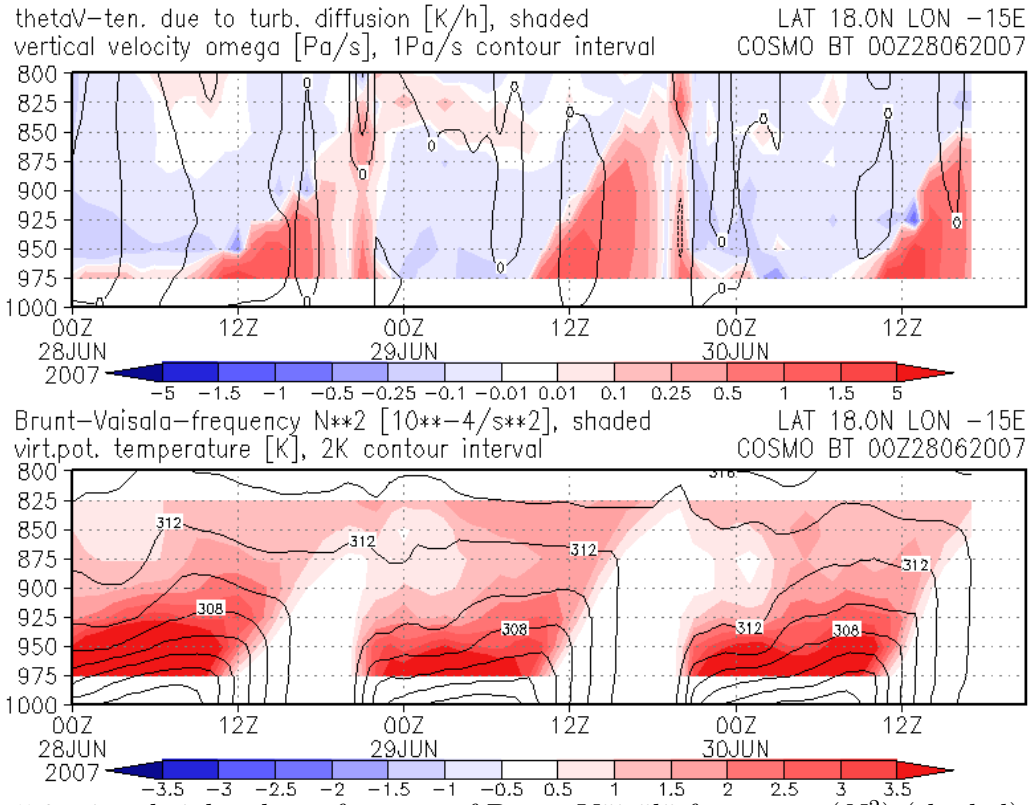

Figure 5.8: time-height plots of square of Brunt-Väisälä-frequency (N^2) (shaded), virtual potential temperature (2 K contour interval, both at bottom of the subfigures), temperature tendency due to sub-grid scale turbulence (shaded) and vertical velocity ω (1 Pa/s contour interval, both at the top of the subfigures) at **18°N, 15°W**.

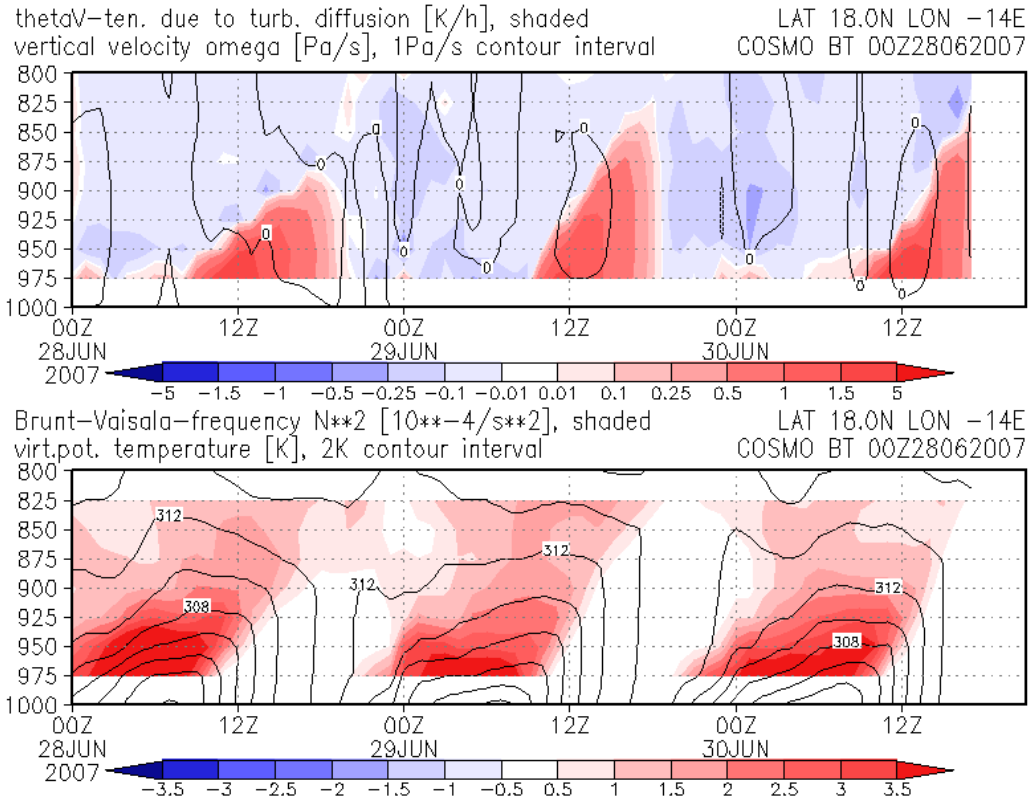

Figure 5.9: as Fig. 5.8 but at **18°N, 14°W**.

decrease in this tendency term which may indicate the gradual sunset. The sharp decrease may be due to the model parameterisation. At 15°W the passage of the coastal front at 22 UTC is evident as a positive temperature tendency due to turbulent diffusion, extending from 975 to 800 hPa. The passage can hardly be detected in the time-height plots of low-level vertical velocity. At 14°W there is no signal in turbulent diffusion or vertical velocity. This may indicate that the front passed between two of the hourly model output time steps. The signal in turbulent diffusion and vertical velocity is much easier to detect in the longitudinal-vertical cross sections, which will be presented in section 5.4.

The comparison of the structure of turbulent diffusion and the square of the Brunt-Väisälä-frequency in Figs. 5.8 and 5.9 shows that the turbulence leads to a well-mixed neutrally-stratified boundary layer up to 800 hPa. The signal of $N^2 \approx 0\ s^{-2}$ is identical in shape but lags around 2 h behind the signal of positive temperature tendency due to turbulent diffusion. In the evening the neutral stratification does not vanish suddenly as does the turbulent diffusion but is reduced gradually by the stabilisation from the ground and from the Atlantic Inflow. However, neutral and weakly stable stratification remains in a layer from 900-800 hPa in the first half of the night.

The corresponding plots in the undisturbed Saharan heat low region at 20°N, 10°W are shown in Figs. 5.10 and 5.11. The diurnal cycle of virtual potential temperature is similar to the one described in the numerical studies of Racz and Smith (1999). The variables show a much smoother diurnal cycle. Sharp gradients at nighttime as observed in the Atlantic Inflow region do not appear. The Brunt-Väisälä-frequency indicates a smooth transition to the stably-stratified low-level atmosphere at nighttime rather than the sharp gradients in the Atlantic Inflow region. The shape of the temperature tendency due to turbulent diffusion is slightly different in the Saharan heat low region.

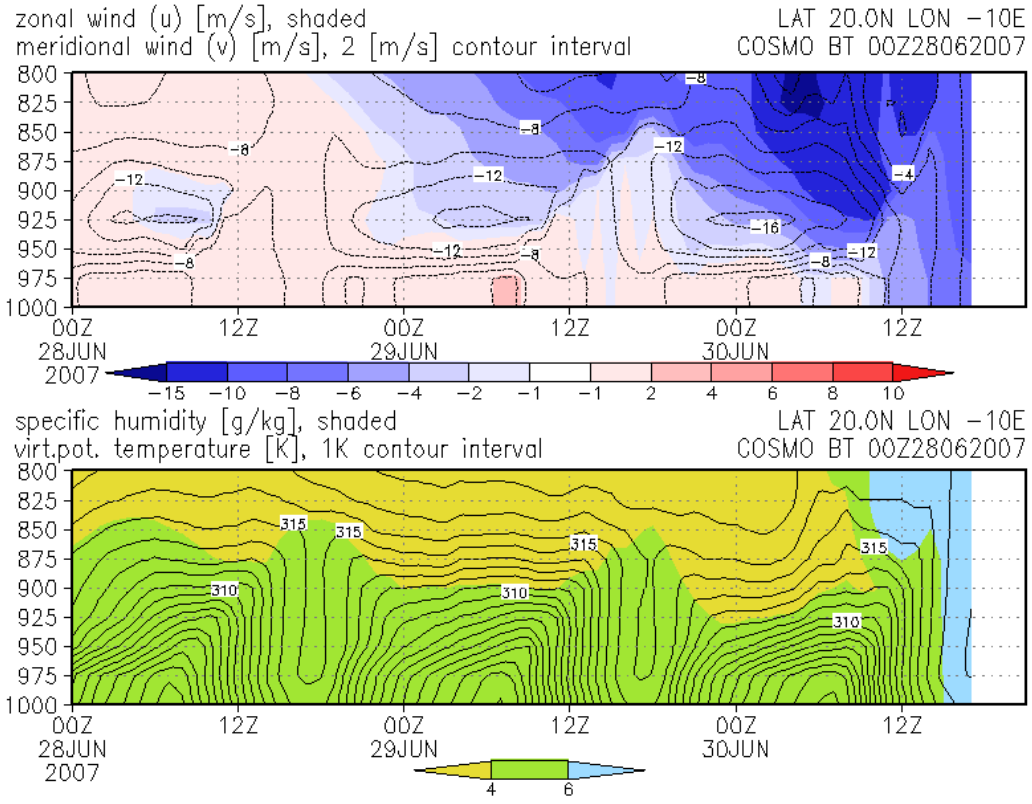

Figure 5.10: as Fig. 5.6 but at **20°N, 10°W**.

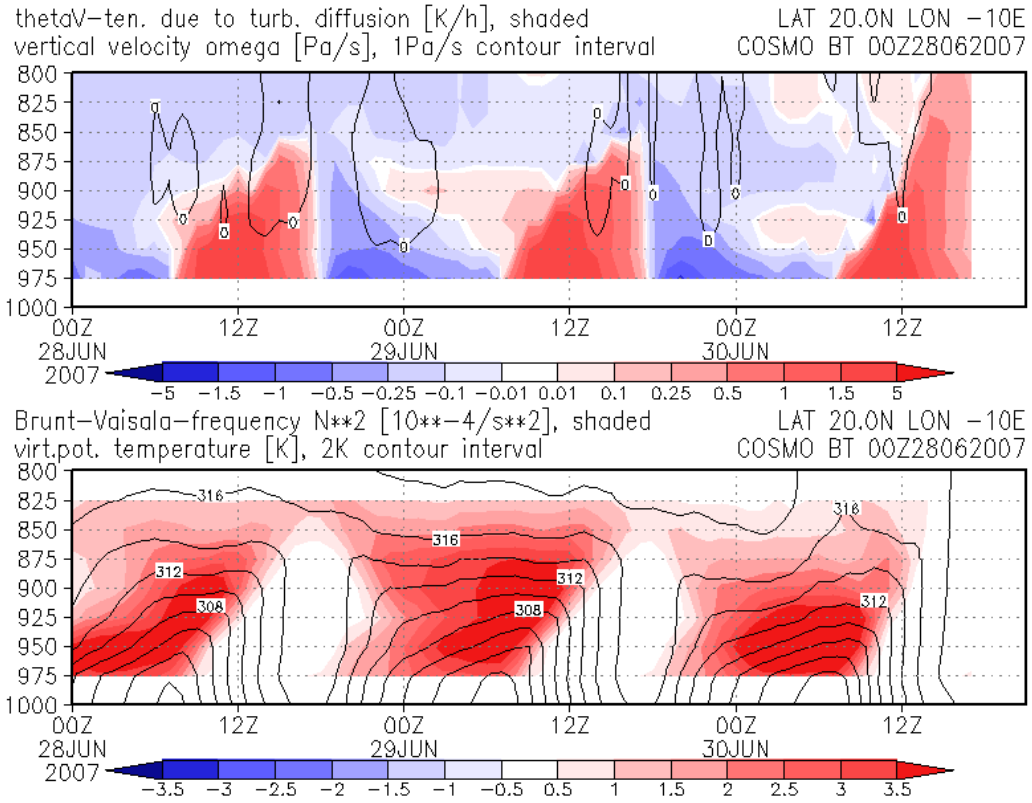

Figure 5.11: as Fig. 5.8 but at **20°N, 10°W**.

To complete the detection of the Atlantic Inflow in time-height plots, Fig. 5.12 shows the temperature tendencies due to horizontal and vertical advection at 18°N, 15°W for the second forecast period 28-30/06/2007. The Atlantic Inflow becomes evident by the sudden occurrence of a cooling due to horizontal advection of more than -1.5 K/h at low levels ($p > 900$ hPa) at around 22 UTC. The cooling remains close to the ground for a few hours. In the mid and high levels there is a signal of horizontal advection as well. The latter coincide remarkably with a signal of vertical advection. However, both have a rather complex structure and will be analysed in longitudinal-vertical cross sections (section 5.4). In time-height plots the Atlantic Inflow at a specific point may occur between two of the model output time steps. Horizontal advection of humidity shows a similar but weaker signal of moistening with the passage of the Atlantic Inflow front (not shown). The advective tendencies in the corresponding Saharan heat low location do not show a distinct diurnal cycle.

So far the emphasis of the Atlantic Inflow detection lies on temperature. To explain this we show a time-height plot of the meteorological quantities at 18°N, 14°W for the first period 24-26/06/2007 based on the COSMO_budget forecast initialised on 00 UTC 24/06/2007 for the shifted domain (Fig. 5.13). As mentioned in section 3.2 the monsoon flow penetrated far northwards over western Mauritania in the night of 23-24 June 2007. A remnant of the monsoon layer is evident in the high values of specific humidity ($q^v >$ 14 g/kg) at 18°N, 14°W on 24 June (Fig. 5.13, bottom). Nevertheless, the Atlantic Inflow does occur in the night of 24-25 June. The coastal front passes 14°W between 22 and 23 UTC, indicated by the decrease of the low-level virtual potential temperature around 7 K and by the increase of the low-level zonal wind from around 3 m/s to more than 10 m/s. However, there is a decrease in moisture with the passage of the front. The

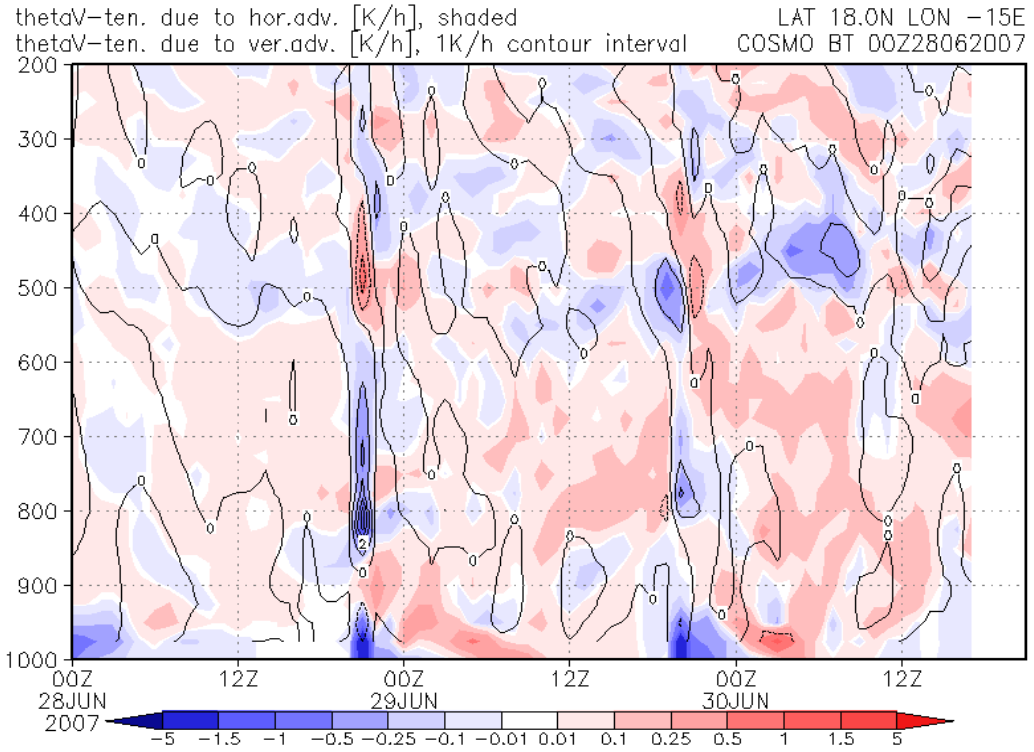

Figure 5.12: temperature tendency [K/h] due to horizontal (shaded) and vertical advection (1 K/h contour interval). 18°N, 15°W, 28-30/06/2007, based on COSMO_budget forecast initialised 00 UTC 28/06/2007 for the standard domain.

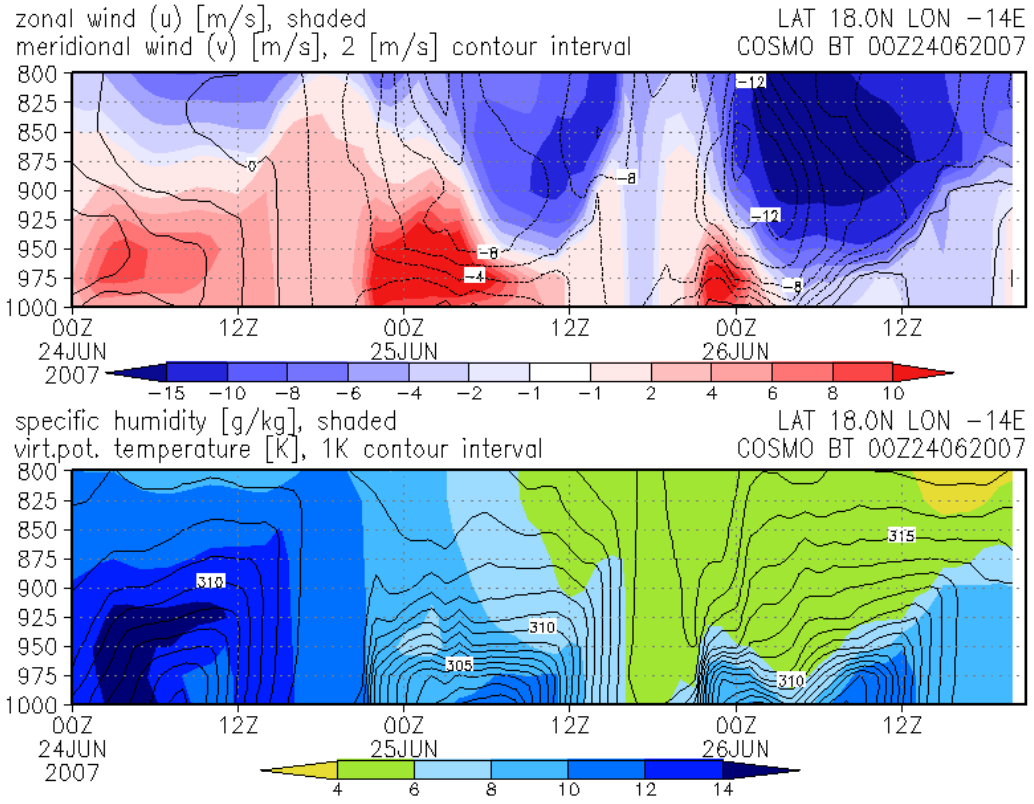

Figure 5.13: as Fig. 5.6 but for period 24-26/06/2007.

specific humidity does not increase before 3 UTC. Thus the Atlantic Inflow dried the low-level atmosphere and replaced the moist monsoon air with less moist maritime air. In the night of 25-26 June the expected moistening with the passage of the front can be observed at 18°N, 14°W.

In this subsection we showed that the Atlantic Inflow is easily detectable at a specific location using time-height plots. In the meteorological fields the Atlantic Inflow is best signalled by a sharp decrease of virtual potential temperature ($\partial\Theta_v/\partial t \approx -5\,\mathrm{K/h}$) and a strong increase in zonal wind speed ($\partial\Theta_v/\partial t \approx +7\,(\mathrm{m/s})/\mathrm{h}$) which extends from the surface to around 900 hPa. The specific humidity often shows a strong increase as well. However, the signal of the specific humidity depends on the synoptic situation. Another very useful variable is the Brunt-Väisälä-frequency or any other measure of stability. The Atlantic Inflow causes a sudden and strong stabilisation of the low-level atmosphere (up to around 900 hPa) behind its front. Standard mode 1 was dominant in the major part of the cases shown here. An effect of mode 2 on 25 June cannot be observed using time-height plots.

5.3.2 Horizontal view of the Atlantic Inflow

Spengler et al. (2005) and Racz and Smith (1999) stress the importance of sea-breezes in their model studies of a heat low over a landmass surrounded by sea. Spengler et al. (2005) uses the gradient of potential temperature and the relative vorticity at low levels to detect the fronts.

Figures 5.14-5.18 show the magnitude of the gradient of virtual potential temperature, the relative vorticity, the dew point difference $T - T_{dew} = 17\,\mathrm{K}$, and the horizontal wind vectors at 950 hPa. This level is above the surface except at the peaks of the Tagant mountains. The plots are shown at 3-hourly interval for 4 times starting at 15 UTC. This enables us to capture different stages of the Atlantic Inflow: the stationary coastal front at the coast, the Atlantic Inflow after starting to penetrate inland, the system in full propagation and the Atlantic Inflow when it begins to decay. This is a typical life cycle which can differ in time from day to day. The coastal front of the Atlantic Inflow can be identified in the plots through a strong gradient of potential temperature. The stationary front at the coast could be observed at 950 hPa on every day during GERBILS. The inland penetration often vanished at 950 hPa in the early night. In section 5.5 it will be shown that the front is more shallow in these cases but still penetrates inland. The 17 K dew point difference contour together with a convergence of the wind vectors approximately indicate the position of the ITD over land.

In the night of 24-25 June 2007 the Atlantic Inflow shows the clearest evolution and the deepest inland penetration during GERBILS (Fig. 5.14). At 15 UTC a virtual potential temperature gradient of up to 1 K/(10 km) is evident along the entire coast. Between 17°N and 19°N this gradient develops around 50 km inland. Here the low-level wind is onshore and advects the cool maritime boundary layer around 50 km inland (cf. Figs 3.3k and 5.3a). North of 19°N the virtual potential temperature gradient is linked with slightly increased relative vorticity of $1 \times 10^{-4} s^{-1}$ to $2 \times 10^{-4} s^{-1}$. The ITD is marked by a band of virtual potential temperature gradient of up to 0.6 K/(10 km) from 17°N, 12°W to 15.5°N, 6°W. Here relative vorticity reaches values of up to $2 \times 10^{-4} s^{-1}$. These features coincide remarkably well with the position of the 17 K dew point difference contour.

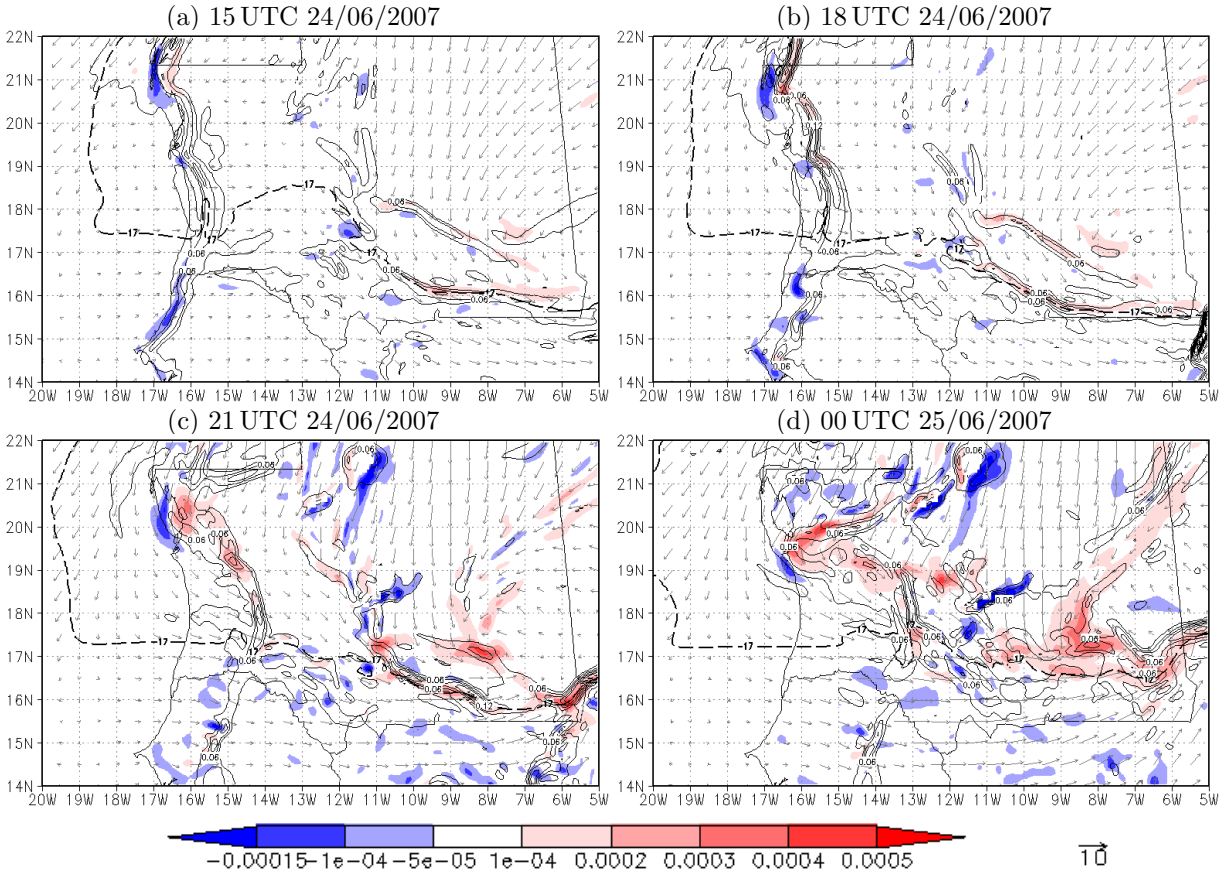

Figure 5.14: relative vorticity [1/s] (shaded), magnitude of potential temperature gradient [K/km] (0.03 K/km black thin contours), 17 K dew point difference contour (thick dashed line), and horizontal wind vectors [m/s] (grey) at 950 hPa and at 15, 18, 21, and 24 UTC 24/06/2007 calculated from COSMO_budget forecast initialised at 00 UTC 24/06/2007, for the shifted domain.

By 18 UTC the coastal front has moved around 0.5° inland (Fig. 5.14b). The virtual potential temperature gradient has increased up to 1.5 K/(10 km) at 15.5°W, 19° N. In the south-eastern corner of the plot a very strong virtual potential temperature gradient marks gust fronts due to convective systems within the model domain. The ITD changed only slightly its position. Three hours later the monsoon front is detectable as a band of virtual potential temperature gradient (up to 1.2 K/(10 km)) and positive relative vorticity (up to $3 \times 10^{-4} s^{-1}$) at around 16.3°N, reaching from 11°W towards the eastern edge of the plot domain (Fig. 5.14c). The coastal front is in full propagation, reaching 14°W from 17°N to 19°N. North of 20°N the Atlantic Inflow is superposed by synoptic activity and vanishes.

At midnight the Atlantic Inflow has reached 13°W between 17°N and 19°N which is nearly its farthest inland penetration (Fig. 5.14d). The virtual potential temperature gradient is still high (more than 0.9 K/(10 km)), north of 20°N synoptic activity dominates. South of 16.5°N there is only a remnant of the coastal front at 14°W, 14°N-16°N. At 17°N, 13°W-12°W the Atlantic Inflow merges with the monsoon front which has propagated further north (around 17°N). It is evident in both strong virtual potential temperature gradient (up to 1.2 K/(10 km) at 5°W, 17.6°N) and relative vorticity. A secondary front

appears north of the ITD from 9°W, 17.5°N to 5°W, 22°N.

It is striking that the horizontal flow at 950 hPa comes from the north-west behind the front where the Atlantic Inflow shows deepest inland propagation (17°N to 19°N) during the whole evening. The horizontal flow behind the front increases significantly at night when the front propagates.

The next day a strong gradient in virtual potential temperature (over 1.2 K/(10 km)) rebuilds directly at the coast between 16°N and 23°N (Fig. 5.15a). However, the Atlantic Inflow does not propagate as far inland as on the previous night. At 17°N it reaches 13°W while at 19°N the farthest inland penetration is 15°W (Fig. 5.15c). After 21 UTC the Atlantic Inflow can no longer be detected at 950 hPa. A complex structure of potential temperature gradient and relative vorticity appears in the centre of a secondary heat low vortex at 13°W, 18°N (Fig. 5.15d). The horizontal flow in the evening of 25 June 2007 is dominated by a secondary heat low/trough over the coastal plain. This is mode 2 of the Atlantic Inflow. The flow at 950 hPa is cyclonic around the centre of the low/trough at 13.5°W, 17.5°N. Again the Atlantic Inflow shows deepest inland penetration where the flow behind the front is from the north-west (from 18°N to 17°N). Here it wanders right into the centre of the vortex (Fig. 5.15c) before it disappears. When the Atlantic Inflow starts moving inland the southern part (around 17°N) seems to merge with the ITD (indicated by the dew point difference contour).

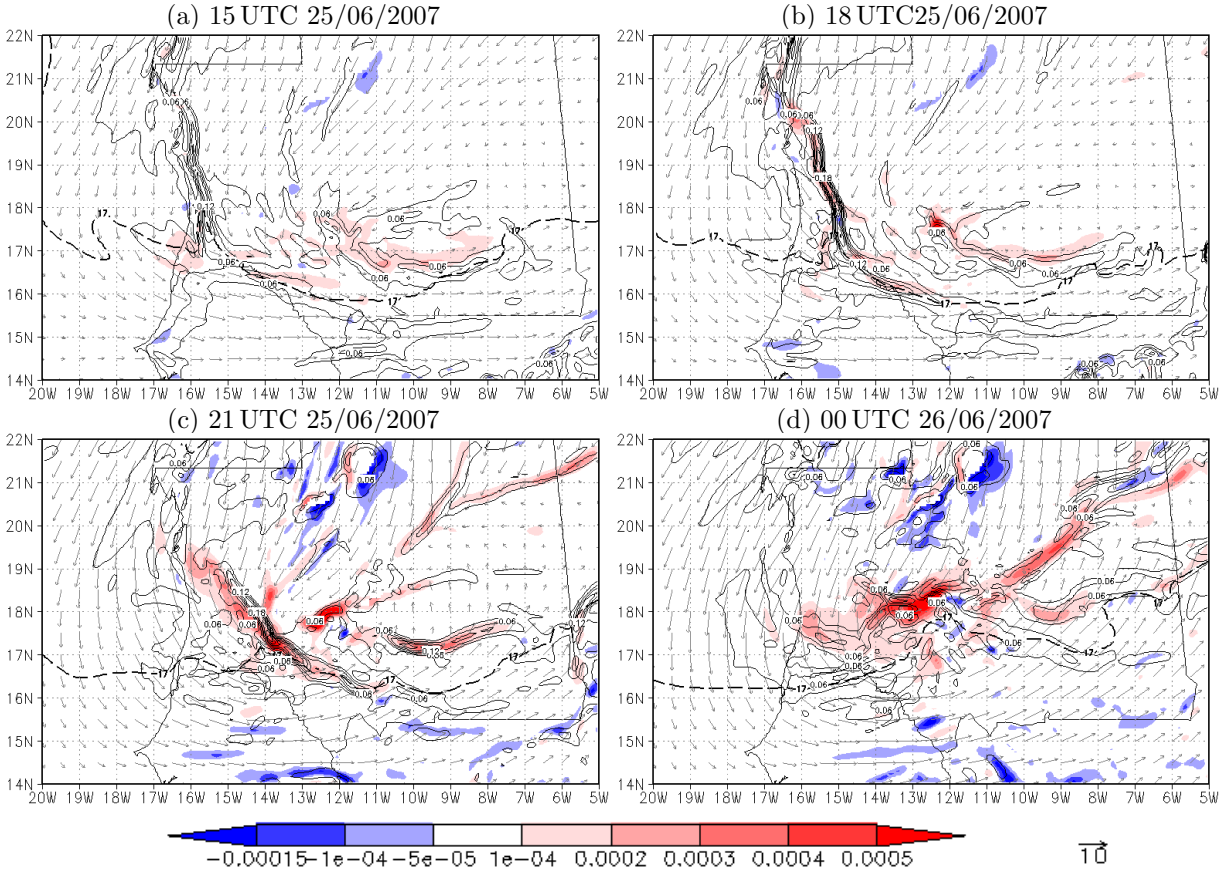

Figure 5.15: as 5.14 but for 25/06/2007.

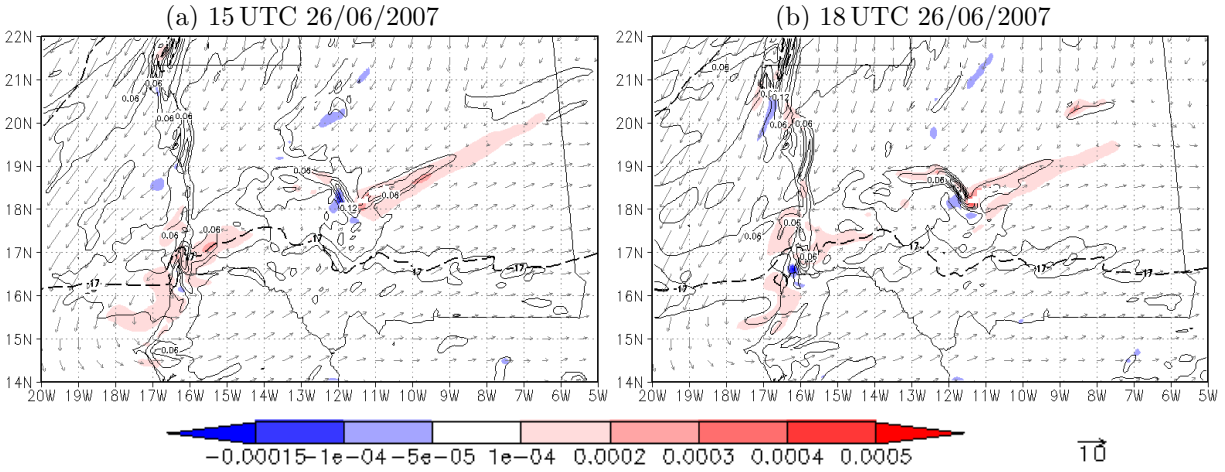

Figure 5.16: as 5.14 but for 26/06/2007 15, 18 UTC.

On 26 June 2007 a north-easterly offshore flow occurs at the Mauritanian coast. The Atlantic Inflow becomes established as a stationary front directly over the shore line (Fig. 5.16a). However, the front can barely be detected as a coherent band at 950 hPa after 18 UTC when it started moving inland (Fig. 5.16b).

28 June 2007 holds another example for a front which becomes barely detectable after

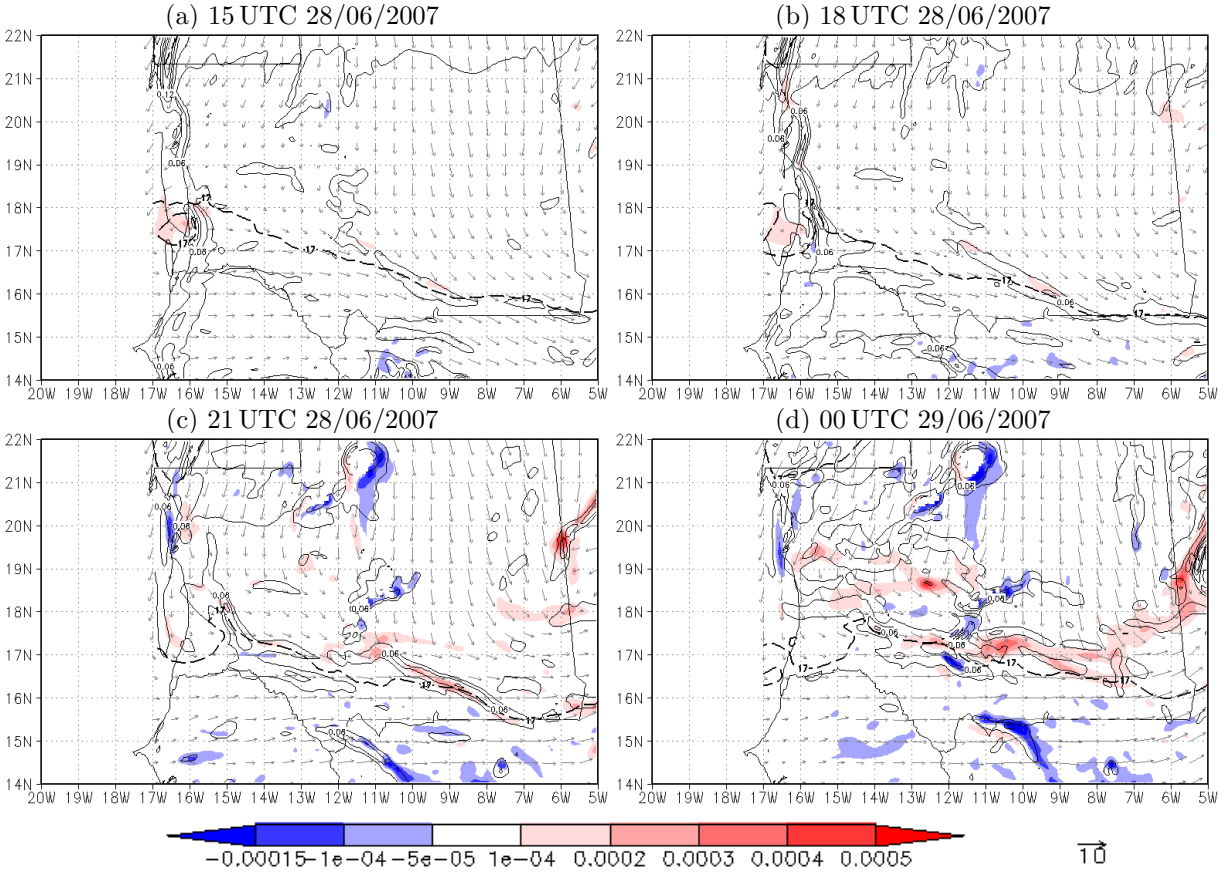

Figure 5.17: as 5.14 but for 28/06/2007 and based on COSMO_budget forecast initialised 00 UTC 28/06/2007, for the standard domain.

penetrating inland (Fig. 5.17). At 15 UTC a gradient in virtual potential temperature is seen along the entire coast (Fig. 5.17a). North of 18°N the flow is slightly offshore from the north to north-east, south of 18°N from the west. The ITD reaches around 18°N at the Mauritanian coast (16°W). The wind speed is lower than on 26 June. During the following three hours inland propagation is observed on the entire coast between 15°N and 20°N, maximised from 19°N to 20°N and from 17°N to 18°N (Fig. 5.17b). This is linked with a change of the wind direction to northerlies north of 18°N. At 21 UTC the Atlantic Inflow can only be detected at 950 hPa from 17°N and 18°N at 15.3°W, where a virtual potential temperature gradient of up to 0.9 K/(10km) marks the coastal front (Fig. 5.17c). Here the Atlantic Inflow seems to be linked to the ITD (17 K contour of dew point difference; wind turned to a westerly). At midnight the signature of the Atlantic Inflow vanishes (Fig. 5.17d).

On 29 June 2007 the Atlantic Inflow develops in a northerly flow (Fig. 5.18). The coastal front is evident in strong gradients of virtual potential temperature up to 0.9 K/(10km) along the entire Mauritanian coast (Fig. 5.18a). The ITD is far south at around 16°N. At 18 UTC the front wandered around 50 km inland and the virtual potential temperature gradient reaches up to 1.2 K/(10km). The inland propagation mainly occurs between 15°N and 19°N (Fig. 5.18b). At 21 UTC the front is barely detectable and lays at around 15.2°W from 16°N to 19.5°N. Behind the coastal front the horizontal flow turned to a northwesterly, and wind speed significantly increased (Fig. 5.18c). At midnight the Atlantic Inflow can be no longer detected at 950 hPa (Fig. 5.18d). Compared to 24 June the

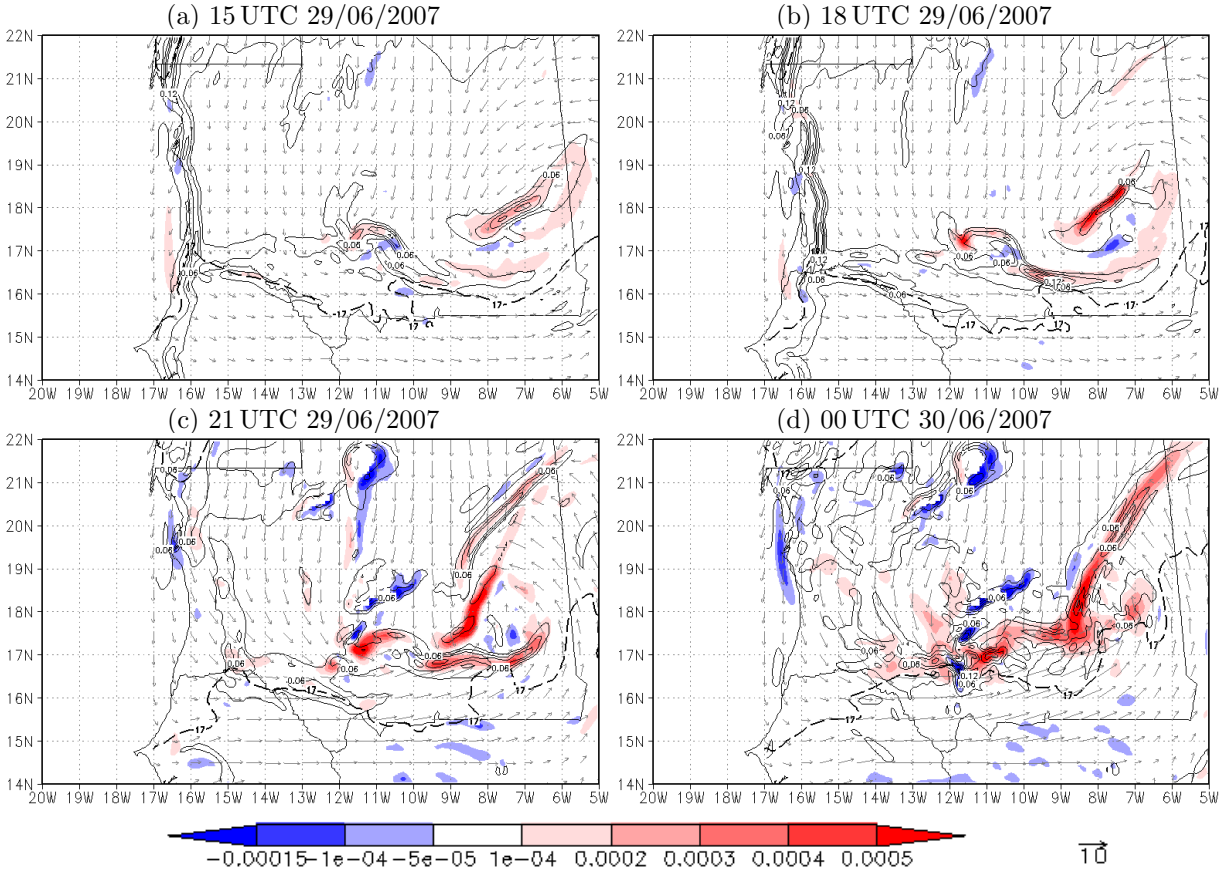

Figure 5.18: as 5.17 but for 29/06/2007.

Atlantic Inflow seems to have a lower propagation speed.

In this subsection the horizontal structure of the Atlantic Inflow was studied using model output at 950 hPa. The Atlantic Inflow evolves every day in the afternoon at the Mauritanian coast and becomes observable through its coastal front. This is independent of the distinct mode. However, the impact of the Atlantic Inflow on its surroundings depends on the specific mode. The horizontal flow seems to influence the position of the stationary front relative to the coast in the afternoon. When the coastal front moves inland, the wind behind the front turns to a more westerly flow. The coastal plain (16°W-12°W,16°N-19°N) in western Mauritania turns out to be very favourable for deep inland propagation. On 24 June 2007 the inland penetration of the Atlantic Inflow was clearly detectable in the figures at 950 hPa. On the other days the fronts became established at the coast, but vanished after starting to move inland. However, as shown in the previous subsection the Atlantic Inflow does exist on these days but the coastal front is shallower and penetrates inland at low levels. This becomes obvious by the examination of the variability of the Atlantic Inflow in section 5.5.

5.4 Gravity waves and the vertical structure

Although the coastal front of the Atlantic Inflow occurs at low levels ($p > 800$ hPa), the Atlantic Inflow affects the mid-level atmosphere (800 hPa $> p >$ 400 hPa). The major modifications occur in the temperature and wind field. In this section the vertical structure of the Atlantic Inflow will be discussed using longitude-height cross sections at 18°N and for 19 UTC a time when the Atlantic Inflow is propagating inland almost every day and not yet perturbed by synoptic-scale activity.

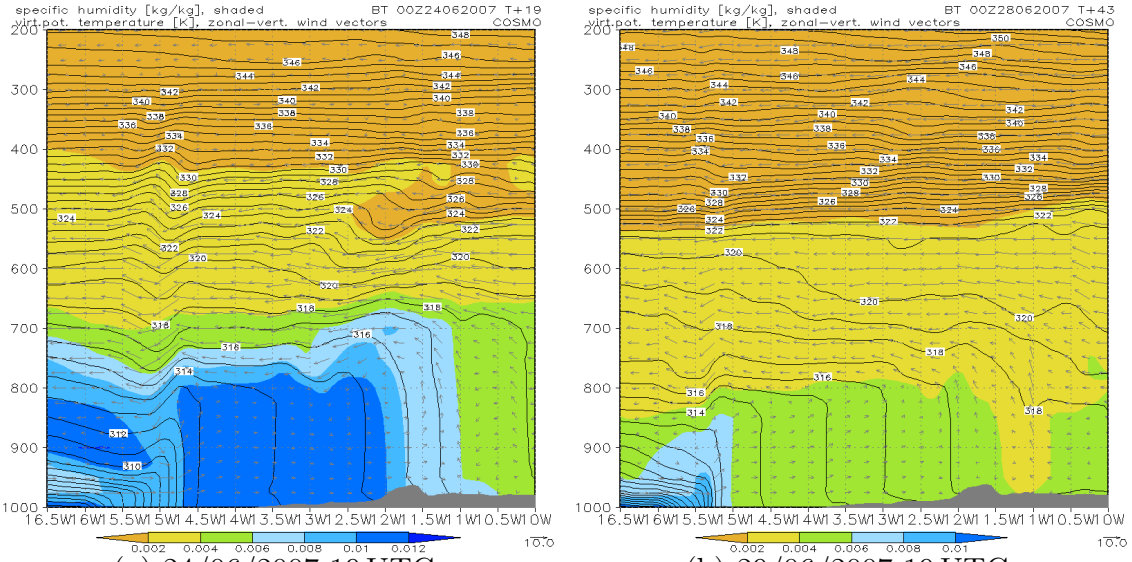

(a) 24/06/2007 19 UTC (b) 29/06/2007 19 UTC

Figure 5.19: longitudinal-vertical cross sections of virtual potential temperature [K] (1 K contour interval) and specific humidity [kg/kg] (shaded), wind in plane of section (grey arrows) for 19 UTC 24/06/2007 (a) and 19 UTC 29/06/2007 19 UTC (b) based on COSMO_budget forecast 00 UTC 24/06/2007, shifted domain (a) and 00 UTC 28/06/2007, standard domain (b).

The coastal front of the Atlantic Inflow is marked by a meridional gradient in virtual potential temperature (Fig. 5.19). A bulge of isentropes in mid levels and a modification in the vertical wind speed appears above the head of the coastal front. The wake of the Atlantic Inflow is detectable by a strong vertical gradient of potential temperature indicating stable stratification. The vertical structure of the Atlantic Inflow in various quantities will be described using COSMO_budget model output for 19 UTC 24 June 2007, initialised 00 UTC 24/06/2007 for the shifted domain. The 24 June is chosen as the pure effect and a deep inland penetration of the Atlantic Inflow was observed on this day. A comparison with other dates and times showed that the structures in the temperature, in the temperature tendency, and in the wind field on 24 June are characteristic for the Atlantic Inflow in standard mode 1. Modifications of the patterns in mode 2 will be shown at the end of this section.

5.4.1 Specific humidity

The Atlantic Inflow front is located at around 14.7°W on 24 June (Fig. 5.19a). It penetrates into a deep (up to 700 hPa) remnant moist layer. This layer was advected by a northward advancing monsoon flow due to the secondary heat low vortex the day before (cf. sections 3.2 and section 5.3.1). High values of specific humidity (8-12 g/kg) from 16.5°W to 11.7°W up to 700 hPa indicate the remnant moist layer (Fig. 5.19a). The Atlantic Inflow appears at low levels below 900 hPa as a rather dry layer west of 15°W. On 29 June 2007 the Atlantic Inflow front is located at around 15.2°W (Fig. 5.19a). In contrast to 24 June it is easily detectable in specific humidity. West of 15°W the Atlantic Inflow advects moist maritime air inland. The moist layer extends up to around 850 hPa

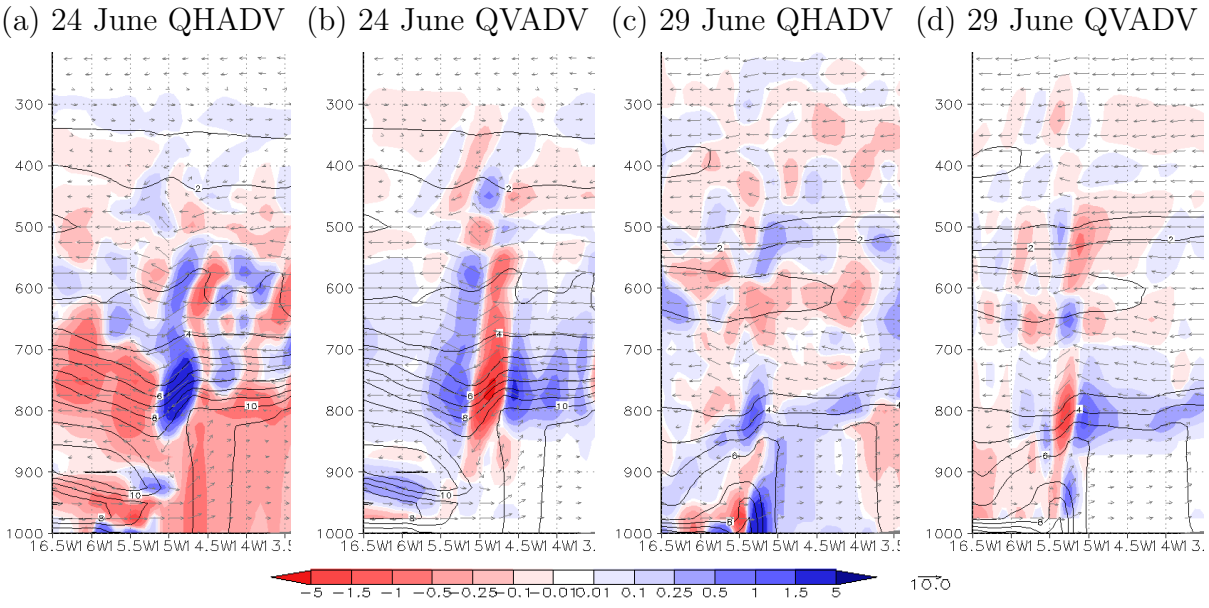

Figure 5.20: specific humidity tendencies [g/kg/h] due to horizontal advection (QHADV; (a),(c)) and vertical advection (QVADV; (b),(d)), specific humidity (black, 1 g/kg contour interval), and wind in plane of section (grey arrows) for 19 UTC 24/06/2007 ((a),(b)) and 19 UTC 29/06/2007 ((c),(d)) based on COSMO_budget forecast 00 UTC 24/06/2007, shifted domain ((a),(b)) and 00 UTC 28/06/2007, standard domain ((c),(d)).

at the head of the coastal front (15.2°W) and 950 hPa in the tail and over the Atlantic Ocean (16.5°W). The differences in the specific humidity fields are also reflected in the advection terms of humidity, which are given in Fig. 5.20.

On 24 June horizontal advection does not indicate the Atlantic Inflow at low levels (Fig. 5.20a). In contrast, on 29 June the coastal front of the Atlantic Inflow is detectable by high values of moistening tendency due to horizontal advection ($\partial q^v/\partial t > 1.5$ g/kg/h) below 900 hPa at around 15.2°W (Fig. 5.20c). The specific humidity tendencies due to advection indicate a signal of the Atlantic Inflow at mid levels on both days. A zone of moistening up to 5 g/kg/h due to horizontal advection from 800 hPa to 500 hPa above the coastal front at around 14.7°W is striking on 24 June (Fig. 5.20a). In contrast vertical advection shows a tripole structure of drying (up to -5 g/kg/h) slightly westwards above the coastal front at around 14.8°W and moistening up to 1.5 g/kg/h east- and westwards (Fig. 5.20b). A similar but less pronounced structure appears on 29 June (Figs. 5.20c and 5.20d). Above 700 hPa the signal of the Atlantic Inflow vanishes on this day.

The comparison of specific humidity and specific humidity tendencies on 24 and 29 June shows that the Atlantic Inflow indeed has an influence on this variable but the signal of humidity is ambiguous due to its synoptic-scale variability. Thus humidity is not suited to detect the Atlantic Inflow.

5.4.2 Induced gravity waves and wind field

The most striking feature in the longitudinal-vertical cross section of virtual potential temperature and vertical velocity for mode 1 is an induced gravity wave in the stably-stratified atmosphere above 800 hPa (Figs. 5.21 and 5.22d). The isentropes show a marked deflection above the low-level front. Vertical velocity indicates a frontal circulation. Similar structures were described for the "morning glory" in Australia by various studies of Smith. A good review on this phenomenon is given in Reeder and Smith (1999). In the following it will be shown without going into details that this feature has characteristics of an untrapped internal gravity wave.

The square of Brunt-Väisälä-frequency N^2 , virtual potential temperature Θ_v, and wind components for 19 UTC 24 June 2007 are shown in Fig. 5.21 in a vertical cross section at 18°N. The plot on the left-hand side extends from 16.5°W to 10°W, the plot on the right-hand side zooms into the front region and shows 15.5°W to 14.0°W.

At 19 UTC the rear of the coastal front lies at around 15.2°W. This is indicated by the strong meridional gradient of N^2 and Θ_v in the low levels. The maritime air behind the front is strongly stably-stratified ($N^2 > 3.5 \times 10^{-4} s^{-2}$) and cool ($\Theta_v < 308\,K$). The air inland over the desert (east of 14.5°W) is well-mixed ($N^2 \approx 0\ s^{-2}$) and much warmer ($\Theta_v > 313\,K$). Isentropes are elevated above the head of the front at around 14.7°W, and from 800 to 500 hPa a wave with a trough in the west and a crest to the east is evident. The phase lines tilt slightly eastwards. From around 600 to 400 hPa a crest-trough-crest structure is evident. The phase lines almost coincidence with a change of sign in vertical velocity. This upper-level gravity wave wanders as a singular (crest-)trough-crest wave eastwards against the mean flow. The phase speed of around 10 m/s is the same as the propagation speed of the low-level front. The (horizontal) wave length is around 50 km. The zoom into the frontal region shows a complex circulation at the front: a zone of ascending motion ahead of the front is maximised at 875 hPa and followed by a zone of

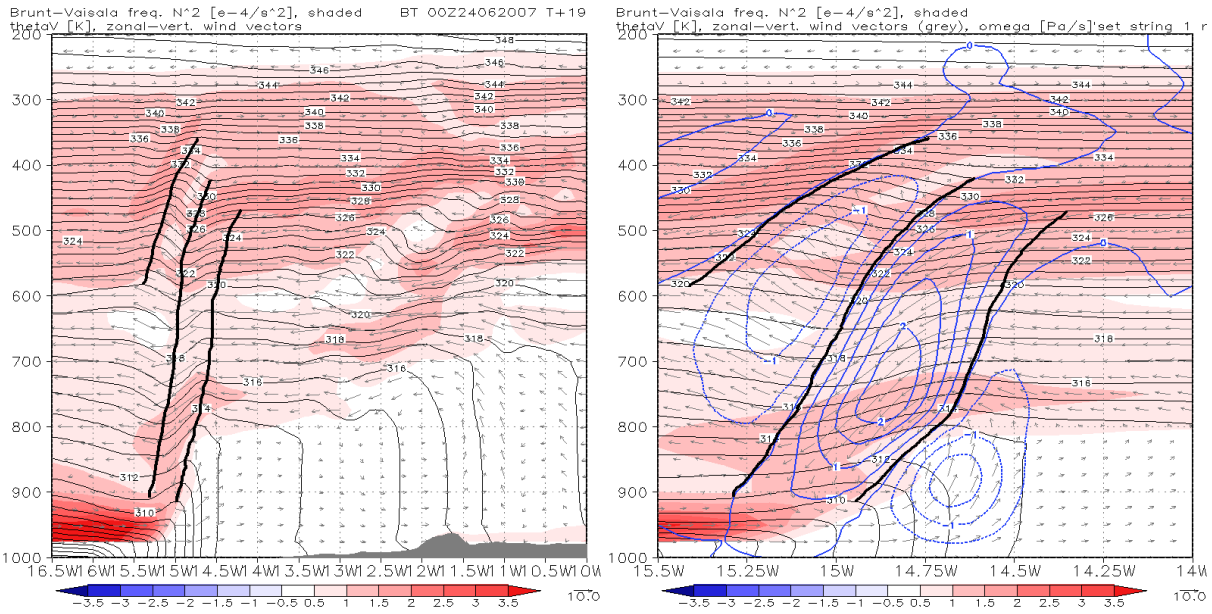

Figure 5.21: N^2 [$10^{-4}s^{-2}$] (shaded), Θ_v [K] (black, 1 K contour interval), wind vectors in plane of section (grey), and vertical velocity [Pa/s] (blue, 0.5 Pa/s contour interval only on the right-hand side) in a longitudinal-vertical cross section at 18°N. Left: 16.5°W to 10.0°W. Right: section of the coastal front: 15.5°W to 14.0°W. Both 19 UTC 24 June 2007. Thick black lines approximate phase lines of wave crests/troughs.

descending motion reaching from the surface front up to the top of the SAL. The strongest downdraft here is at 700 hPa. A second zone of updraft is maximised at 600 hPa. This higher level updraft is strongly evident at the top of the SAL at around 475 hPa. At 14.8°W the stably-stratified SAL ($N^2 = 1.5 - 2.0 \times 10^{-4}s^{-2}$) is interrupted and lifted to 350 hPa at the western edge of the break. The triplet of ascending/descending/ascending motion is tilted parallel to the phase lines and coincides with the perturbations in the Θ_v field. The flow in the plane of section is highly isentropic. Furthermore, it is notable that the wave in the mid levels decouples from the low-level front and oversteps the Tagant Mountains later in the night.

The horizontal wind field exhibits a remarkably shear (grey vectors in Fig. 5.22d): Below 800 hPa and ahead of the front, the wind comes from the north to north-west with wind speed below 5 m/s. Behind the front and below 900 hPa the horizontal wind comes from the north-west to west, wind speed reach more than 10 m/s. In a layer from 800 to 500 hPa ahead of the front the wind comes from the east with maxima of 15 m/s at 650 hPa. Behind the front this layer seems to have descended up to 900 hPa. This could indicate a counterflow due to the Atlantic Inflow front penetrating inland. From 400 to 300 hPa there is a layer of weak southerly winds turning into westerlies east of 14°W. Above this level there is weak easterly flow.

A brief review of internal gravity waves following Gill (1982) and Beheng (2006) shows that the observed structure has characteristics of internal untrapped gravity waves. Regarding the atmosphere as a fluid of continuously-stratified layers, Gill (1982) obtains

the simplified equation (6.4.12) chapter 6.4 page 130 for vertical motion:

$$\frac{\partial^2}{\partial t^2}\left[\frac{\partial^2}{\partial x^2}+\frac{\partial^2}{\partial y^2}+\frac{\partial^2}{\partial z^2}\right]w+N^2\left(\frac{\partial^2}{\partial x^2}+\frac{\partial^2}{\partial y^2}\right)w=0, \tag{5.1}$$

where $N^2=\frac{g}{\Theta_0}\frac{\partial\Theta_0}{\partial p}=-\frac{p_0 g^2}{RT_0\Theta_0}\frac{\partial\Theta_0}{\partial z}$ is the square of the Brunt-Väisälä frequency, assuming that hydrostatic approximation and equation of state is valid for the base state, ϕ_0 indicating base state variables. Gill (1982) furthermore investigates the evolution of waves in a horizontal flow over sinusoidal topography $h=h_0 sin[k(x+Ut)]$ where $-U$ is the phase speed of the topography relative to the air. Here the low-level front can be regarded as "moving topography". Thus U is the mean velocity of the flow relative to the low-level front, $k=2\Pi/L_x$, with L_x: the horizontal wavelength. Then $\omega=-Uk$ is the imposed frequency on the air flow. Assuming uniform stratification ($N=const.$ in each layer) the solution of Eq. (5.1) is $w=w_0 exp(i(kx+mz-\omega t))$. This yields to the dispersion relation $\omega^2=\frac{k^2N^2}{k^2+m^2}$, $m=2\Pi/L_z$ which can be rewritten as:

$$m^2=k^2(N^2-\omega^2)/\omega^2=(N/U)^2-k^2 \tag{5.2}$$

This solution is valid for $\omega^2<N^2\Leftrightarrow(kU)^2<N^2$. The horizontal wave length $L_x\approx 50\,km$ can be estimated from Fig. 5.21. The velocity $U\approx 20\,m/s$ relative to the ground is estimated from the mean velocity of 10 m/s of the mid-level flow which is from the east plus the propagating speed 10 m/s of the low-level front (section 5.5) which is from the west. Thus, with $k^2U^2\approx 6.32\cdot10^{-6}$ and $0.5\cdot10^{-4}\,s^-2<N^2<1.5\cdot10^{-4}\,s^{-2}$ the condition for untrapped waves $(kU)^2<N^2$ is fulfilled in the stable mid-level layer. If $(kU)^2>N^2$ the waves were damped with height and the solution were the so-called "trapped waves". The atmosphere experiences a drag exerted by the low-level front due to internal gravity waves. This explains the upstream (eastward) tilt of the phase lines (Holton 2004; Gill 1982).

5.4.3 Temperature

The temperature advection excites the gravity wave. Thus it is also reflected in longitudinal-vertical cross sections of these parameters (Fig. 5.22). The descending branch (15.0°W-14.6°W at 700 hPa) is marked by warming due to vertical advection. The bulge of lower virtual potential temperature east of the downdraft (14.6°W at 700 hPa) leads to a cooling tendency due to horizontal advection in the easterly flow. In contrast, the ascending branches in the mid-level atmosphere are marked by cooling due to vertical advection and warming due to horizontal advection.

At low levels horizontal advection reflects the gravity current characteristic of the Atlantic Inflow (Figs. 5.22a and 5.1). The head of the front can be observed by a bulge of high cooling due to horizontal advection ($\partial\Theta_v/\partial t>-1.5$ K/h) extending from the ground up to 875 hPa at 14.7°W. In the wake of the front the virtual potential temperature tendency due to horizontal advection remains negative but the cooling is located below 900 hPa and becomes gradually weaker. In particular, the low-level cooling due to horizontal advection has a much higher absolute value than the remnant low-level warming due to turbulent diffusion (0.1K/h$<\partial\Theta_v/\partial t<$ 0.25K/h) east of 14.5°W. At 19 UTC the turbulent diffusion decays as after sunset the sensible heat flux which depends on solar

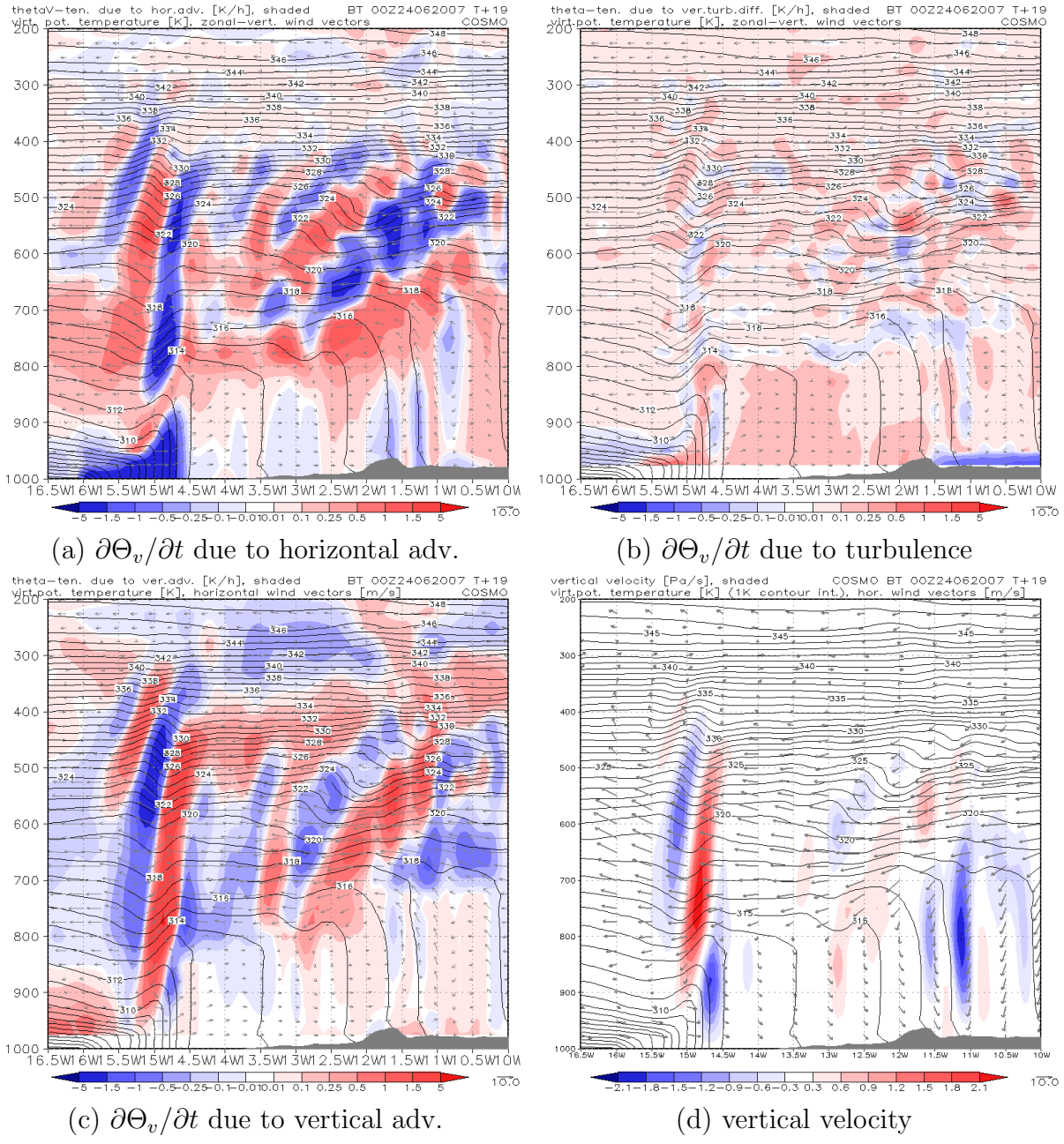

(a) $\partial\Theta_v/\partial t$ due to horizontal adv.

(b) $\partial\Theta_v/\partial t$ due to turbulence

(c) $\partial\Theta_v/\partial t$ due to vertical adv.

(d) vertical velocity

Figure 5.22: longitude-height cross sections of virtual potential temperature tendencies [K/h] due to horizontal advection (a), vertical turbulent diffusion (b), vertical advection (c), and the vertical velocity [Pa/s] (d) for 19 UTC 24/06/2007 based on COSMO_budget forecast 00 UTC 24/06/2007, shifted domain. Black contours: virtual potential temperature [K]. Grey vectors: wind vector in plane of section ((a),(b),(c)), horizontal wind (d).

heating of the surface is ceasing. As will be shown in section 5.8, the balance between low-level horizontal advection and low-level turbulent diffusion determines the frontal propagation.

A signal of the Atlantic Inflow front is also detectable in the temperature tendency due to turbulent diffusion (Fig. 5.22b). For example, the head of the low-level front is marked

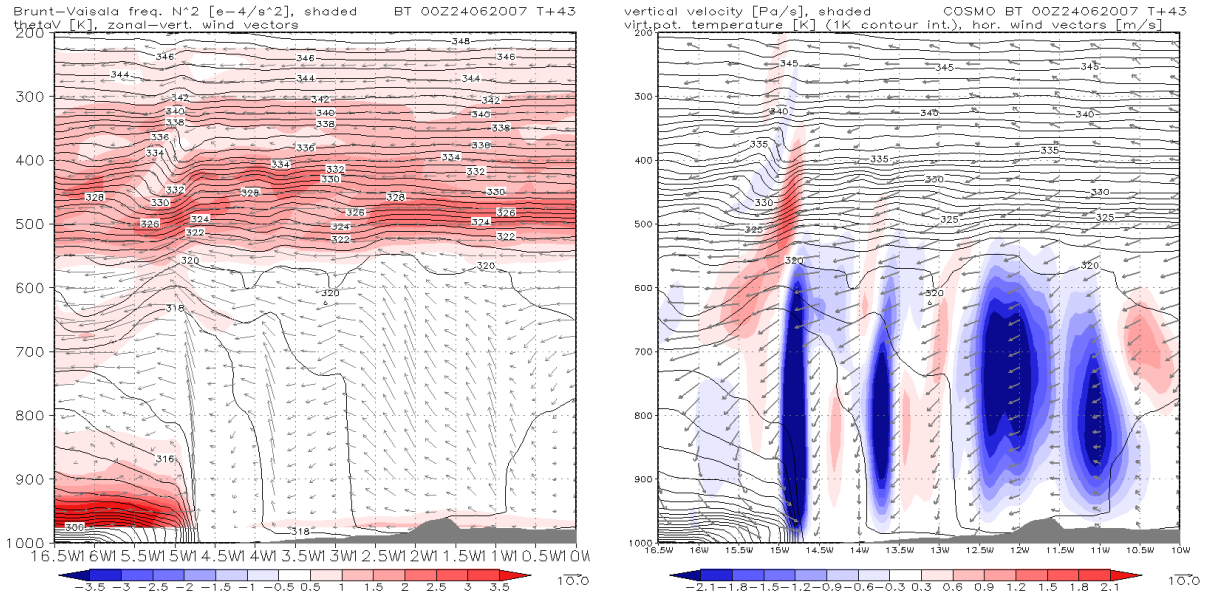

(a) Brunt-Väisälä-frequency (b) vertical velocity

Figure 5.23: as Figs. 5.21 and 5.22d but for mode 2, 19 UTC 25 June 2007.

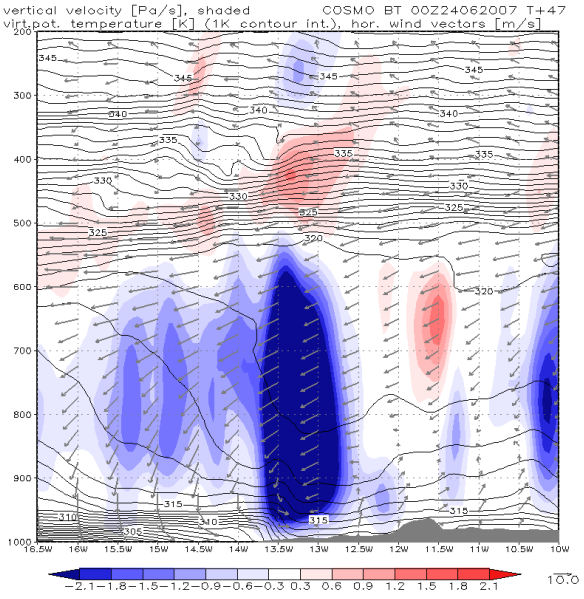

Figure 5.24: as Fig. 5.22d but for mode 2, 23 UTC 25 June 2007.

by a cooling-warming-cooling structure due to turbulent diffusion at 900 hPa, 15.0°W-14.5°W. Above 800 hPa this structure is less coherent, but a signal of turbulent diffusion is detectable up to 300 hPa. In the wake of the front turbulent diffusion contributes to a weak cooling of the layers below 900 hPa.

The pattern described above for mode 1 differs when the Atlantic Inflow penetrates into a deep rather neutrally-stratified atmosphere as in mode 2. To illustrate this, the square of the Brunt-Väisälä-frequency and the vertical velocity for 19 UTC 25 June 2007 are shown in Fig. 5.23. The westward shifted Saharan PBL is evident through the neutral stratification from the surface to 550 hPa east of 14.7°W (Fig. 5.23a). The Atlantic Inflow at 14.7°W has a very steep, strong baroclinic zone at its head. An induced gravity wave is not observable until above 600 hPa because of the neutral stratification aloft and ahead of the Atlantic Inflow. The ascent at the head of the front is much more pronounced than

in mode 1 and reaches up to 550 hPa (Fig. 5.23b). The mid-level descent is weaker and located much higher at 450 hPa within the upper part of the top of the SAL. The high-level ascent has almost vanished. Thus a gravity wave is excited where the ascent ahead of the Atlantic Inflow impinges on a stably-stratified layer. Fig. 5.23b also shows regions of orographically forced ascent in the neutral layer east of 14°W. These features propagate westwards embedded in the mean flow, whereas the ascent linked to the Atlantic Inflow front propagates eastwards. At 23 UTC the Atlantic Inflow ascent merges with one of the updrafts, forming a striking broad zone of ascending motion from 13.7°W to 12.7°W reaching from the ground to 550 hPa (Fig. 5.24).

At this time the gravity wave in the upper levels can no longer be detected. Instead, the isentropes above 500 hPa indicate a complex structure of crests and troughs. Later in the night the signal of the Atlantic Inflow vanishes. A detailed analysis of the variations within mode 2 and 3 goes beyond the scope of this thesis, and is therefore neglected. The emphasis lies on standard mode 1.

To get a complementary idea of the temporal evolution, longitudinal-vertical cross sections analoguous to Fig. 5.21 are shown at 3-hourly intervals for 24, 25, 28, and 29 June in the appendix.

5.5 Gravity current characteristics

Clarke (1955) was one of the first who highlighted that sea-breezes could be long-lived and propagate hundreds of kilometres inland at nighttime. The behaviour of propagating sea-breezes resembles gravity currents. The gravity current character of sea-breezes penetrating inland has been studied by various authors e.g. Simpson et al. (1977); Noonan and Smith (1986); Reible et al. (1993); Haase and Smith (1989).

According to Houze (1993) a gravity current "may be defined as a mass of high-density fluid flowing along a horizontal bottom and displacing ambient fluid of lesser density". The density difference in the Atlantic Inflow is established by the rather cold, stably-stratified, maritime air behind the coastal front and the hot desert air ahead of the front. As the atmosphere is a continuously-stratified fluid, the boundary between the gravity current and the ambient air is not marked by a jump in density or temperature. This makes an exact separation of both layers difficult. Nevertheless, there are several other indicators of the two fluids: the gravity current could be defined by a threshold for potential temperature which is below a value usually reached in the desert inland. Such a threshold for virtual potential temperature could be $\Theta_v = 310\,K$ on 24 June 2007. Another approach is to define the gravity current through its stable stratification. On 24 June a Brunt-Väisälä-frequency $N^2 > 2.0 \times 10^{-4} s^{-2}$ seems to characterise the denser layer (Figs 5.21, Fig. 5.25a). The head of the gravity current is best detectable in the temperature tendency due to horizontal advection (Fig. 5.25b). It is marked by a striking bulge of cooling tendency in the vertical and shows the maximum vertical extent of the gravity current.

In Fig. 5.1 a time series of potential temperature at low levels is given. White colours indicate virtual potential temperature less than 310 K, blue colours less than 307 K. These plots make the inflow of colder air from the Atlantic Ocean and its gravity current characteristic visible. At 15 UTC the coastal front is located at around 15.5°W. A bulge in the 310 K isentrope marks the head of the gravity current at around 15.3°W. The dense and

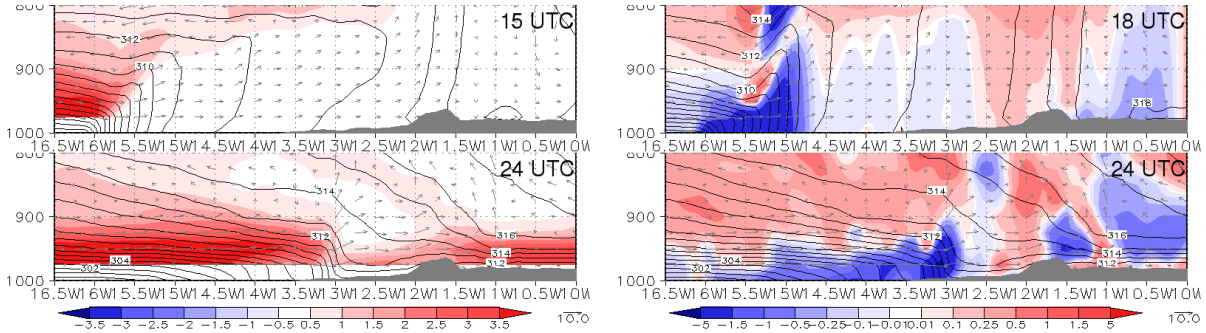

(a) Brunt-Väisälä-frequency (b) Θ_v tendency due to hor. advection

Figure 5.25: Atlantic Inflow on 24 June 2007: longitudinal-vertical cross section at 18°N, 16.5°W-10.0°W, 1000-800 hPa of virtual potential temperature Θ_v [K] (black contours 1 K contour interval), Brunt-Väisälä-frequency $[10^{-4}s^{-2}]$ (shaded (a) at 15 UTC and 24 UTC), and Θ_v tendency due to horizontal advection [K/h] (shaded (b) at 18 UTC and 24 UTC).

cold air with strong stable stratification lies east of 16°W over the Atlantic Ocean. Three hours later the gravity current has started penetrating inland. At 21 UTC the density current has reached its maximum propagation speed. The head is now evident at around 14.2°W. At 3 UTC the following day the cold air spreads out over the entire coastal plain up to the Tagant at 12°W.

The depth of the gravity current shrank around 10-20 hPa during its inland propagation. The relative change in depth can be derived from the height of the 307 K or 305 K isentrope at 16.5°W (Fig. 5.1 (15, 00 UTC)), from the $N^2 = 2.0 \times 10{-}4s^{-2}$ contour at 16.5°W (Fig. 5.25a) or from the maximum height of the cooling tendency due to horizontal advection (Fig. 5.25b).

The shape of the Atlantic Inflow has a remarkable resemblance to gravity currents from experimental studies. Linden and Simpson (1986) studied gravity currents in a turbulent environment using tank experiments. They observed the evolution of a homogenous

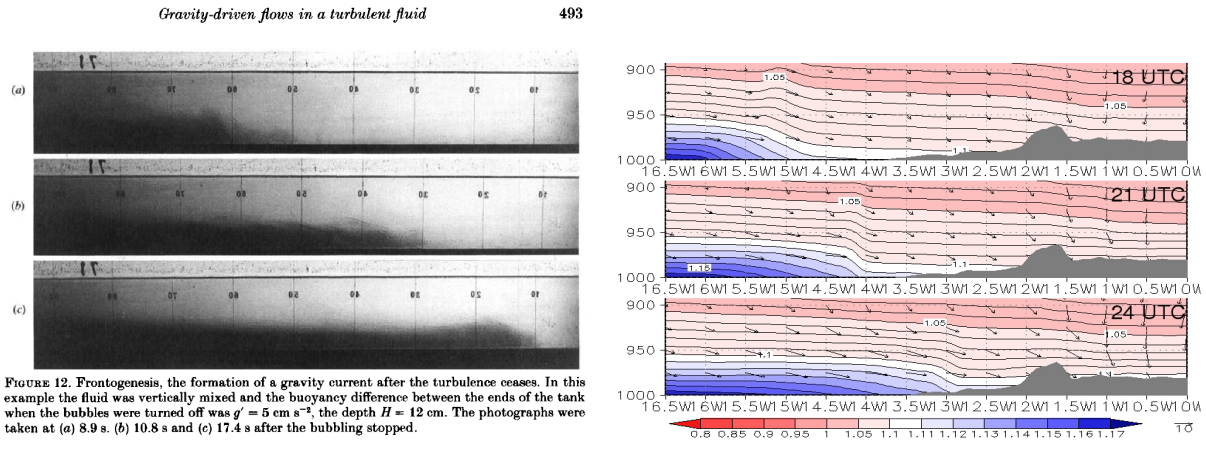

FIGURE 12. Frontogenesis, the formation of a gravity current after the turbulence ceases. In this example the fluid was vertically mixed and the buoyancy difference between the ends of the tank when the bubbles were turned off was $g' = 5$ cm s^{-2}, the depth $H = 12$ cm. The photographs were taken at (*a*) 8.9 s. (*b*) 10.8 s and (*c*) 17.4 s after the bubbling stopped.

(a) Linden and Simpson (1986) (b) density in COSMO 24/06/2007

Figure 5.26: left: gravity current in a tank experiment from Linden and Simpson (1986). Dark colours indicate the more dense fluid. Right: COSMO 24 June 2007: cross section at 18°N, 16.5°W-10.0°W, 1000-900 hPa, density [kg/m^3] (shaded, 0.01 kg/m^3 contour interval), horizontal wind vectors.

gravity current and frontogenesis at the head after the turbulence was switched off. A photo series of this experiment is given in Fig. 5.26a. Fig. 5.26b shows the corresponding series of density cross sections for 24 June 2007. In the evening when turbulence over the desert ceases, the cold, maritime air starts moving inland. While the density front is smoothed at 18 UTC, the frontal character is obvious at 21 UTC (Fig. 5.26b).

Looking at the depth of the gravity current also clarifies that the Atlantic Inflow must be limited to the coastal plain. The most dense and coldest air layer cannot flow over the mountain range as its vertical extent late at night is less than the height of the orographic barrier (Figs. 5.1 (03 UTC) and 5.26b (24 UTC)).

Haase and Smith (1989) carried out numerical simulations of atmospheric gravity currents moving into a homogeneously-stratified atmosphere. In the case of neutral stratification the head of the gravity current shows a strong vertical bulge, followed by a deep trough (Fig. 2(a) in Haase and Smith (1989), not shown). This is similar to the observations of the Atlantic Inflow (e.g. bulge of the isentropes in Fig. 5.19a). For a shallow weakly-stratified layer at the surface the shape of the isentropes in the experiment is nearly the same as for the Atlantic Inflow. This is illustrated in Fig. 5.27. In these first two cases the bulge is the head of the gravity current as it contains the dense air. A more stable layer leads to a bulge in isentropes moving ahead of the gravity current (Fig. 2(c) in Haase and Smith (1989), not shown). This maybe observed for the Atlantic Inflow as well: in the time series of Fig. 5.1 the horizontal distance between the bulge in isentropes and the coldest air in the wake of the Atlantic Inflow (e.g. $\Theta_v|_{1000\,hPa} < 303\,K$) increases. At 18 UTC the bulge and gravity wave aloft are located at around 15.1°W, while at 15.8°W the virtual potential temperature reaches 303 K at the surface. At midnight the bulge has moved inland by around 2.1° and is located at around 13.0°W, while virtual potential temperature reaches 303 K at 14.4°W, only 1.4° inland.

Experiments showed also that gravity currents produce a distinct circulation at the head, similar to the one described in section 5.4.2 for the Atlantic Inflow penetrating

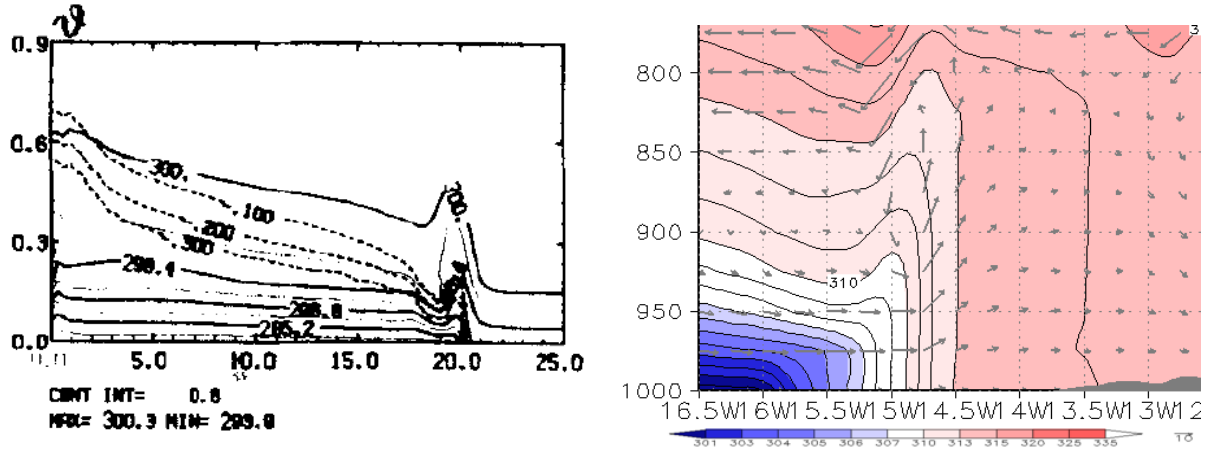

(a) Fig. 2b from Haase and Smith (1989)

(b) Θ_v in COSMO 19 UTC 24/06/2007

Figure 5.27: left: numerical experiment from Haase and Smith (1989): black solid line: potential temperature [K]. Dotted lines: concentration of a tracer, indicating the more dense air within the gravity current. Right: longitude-height cross section at 18°N, 16.5°W-10.0°W, 1000-775 hPa of virtual potential temperature [K] (shaded, 1 K contour interval), wind in plane of section.

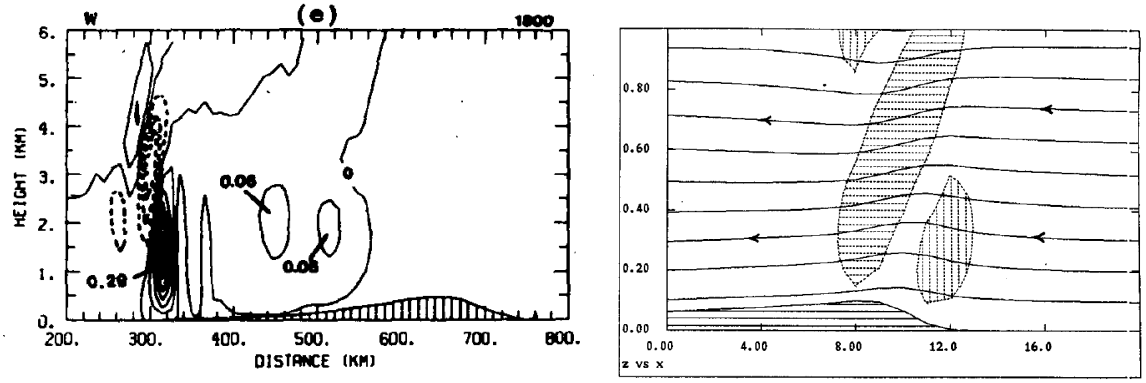

(a) Fig. 4(e) from Noonan and Smith (1986) (b) Fig. 4 from Raymond and Rotunno (1989)

Figure 5.28: longitudinal-vertical cross section of vertical velocity in two experiments: Left: Noonan and Smith (1986). Solid lines show updraft, dashed lines downdraft. Right: Raymond and Rotunno (1989): horizontal hatching: downdraft, vertical hatching: updraft, zonal-vertical streamlines, solid horizontal hatching: cold pool.

inland (Fig. 5.22d). In the experiments of Noonan and Smith (1986) or Raymond and Rotunno (1989) a gravity current propagates eastwards in an easterly flow. The vertical velocity for these simulations is shown in Fig. 5.28.

Noonan and Smith (1986) studied the sea-breezes over Cape York Peninsula, Australia, using a two-dimensional model. The sea-breezes are thought to initiate the so-called "morning glory", a cloud-line which appears occasionally in the Gulf of Carpentaria. Initially an easterly geostrophic wind is prescribed in all levels in their study. The vertical velocity for one time step is shown in Fig. 5.28a. The sea-breeze at the western coast is almost stationary at around kilometre 320. The vertical velocity shows a significant triplet of ascent in the low levels ($z < 2\,\mathrm{km}$), descent in the mid levels from 1.5 km to 4.5 km height and a weak ascent from 3.5 km to 5.5 km. This is quite similar to the vertical velocity field combined with the Atlantic Inflow in mode 1 (Fig. 5.22d).

Raymond and Rotunno (1989) investigated the behaviour of a cold pool in stably-stratified low levels. Various experiments were carried out. Here we show one case when the flow inhibits propagation of the gravity current against the mean flow and the propagation of gravity waves. In this case vertical velocity shows a triplet pattern, similar to that of the Atlantic Inflow.

Finally, the propagation speed of the Atlantic Inflow will be highlighted for four different days (Table 5.1). The propagation speed was derived from Fig. 5.29 in two different ways: firstly the position of the front is defined as the location x_i of a characteristic isentrope Θ_c on a level p_c. For an estimate of the propagation speed of the front, Θ_c and p_c are chosen to be located within the zone where the meridional virtual potential temperature is maximal during the whole night. For an estimate of the penetration speed of the cold air in the wake of the Atlantic Inflow, Θ_c and p_c are chosen to be located within the cold air mass and near to the ground during the whole night. The front must show inland penetration between two following time steps $t_1 < t_2$, which mark the time range when the front has reached its maximum propagation speed. Then the propagation speed is given by $U_f = \frac{|x_2(t_2) - x_1(t_1)|}{t_2 - t_1}$. At 18°N one degree in longitude equals around 106 km[1]. The

[1] calculation: $6378\,\mathrm{km} \cdot 1° \cdot \Pi/180° \cdot \cos(18°) \approx 106\,\mathrm{km}$

Table 5.1: propagation speed U_f [m/s] of the Atlantic Inflow (AI). Calculated based on Θ_c [K]: day of June 2007; f indicates the characteristic values taken at the front, l characteristic values for the cold layer behind the front. m refers to the mode of the AI. p_c [hPa] (sfc=surface), t_i time in hours [UTC] (in t_2 0h refers to following day), x_i =longitude[°W].

day	**m**	Θ_c	p_c	t_1	t_2	x_1	x_2	U_f
24f	1	310	sfc	18	00	15.1	13.1	**9.7**
24l	1	303	sfc	18	00	15.8	14.5	**6.4**
25f	2	316	950	18	22*	15.0	13.8	**8.8**
25l	2	305	sfc	18	22*	15.7	14.8	**6.6**
28f	1	311	sfc	20	01	15.2	13.3	**11.2**
28l	1	303	sfc	20	01	15.8	14.6	**7.1**
29f	1	311	975	18	22	15.5	14.4	**8.1**
29l	1	305	sfc	18	22	15.8	15.0	**5.9**

* before entering the very deep Saharan PBL

Table 5.2: as Table 5.1 but based on N_c^2. $[10^{-4}s^{-2}]$

day	**m**	N_c^2	p_c	t_1	t_2	x_1	x_2	U_f
24f	1	1.0	925	18	00	15.2	13.0	**10.8**
24l	1	3.5	975	18	00	15.8	14.3	**7.2**
25f	2	1.0	925	18	22*	15.1	13.8	**9.6**
25l	2	N_c^2 not definable						
28f	1	2.5	950	20	01	15.4	13.5	**11.2**
28l	1	3.5	975	20	01	15.6	14.2	**8.2**
29f	1	2.0	950	18	22	15.7	14.5	**8.8**
29l	1	N_c^2 not definable						

* before entering the very deep Saharan PBL

propagation speed can also be calculated based on the position of the stable layer, defined by a characteristic value of the square of the Brunt-Väisälä-frequency N_c^2 at a specific level p_c. The choice of N_c^2 and p_c is based on the same ideas as explained for Θ_c and p_c. It is obvious that this way of calculation is only a very rough estimate of the propagation speed. It depends highly on the choice of the characteristic values.

The rough estimate of the speed of the Atlantic Inflow shows that both methods are suitable. The differences are minor compared to the differences between the propagation speed of the head of the gravity current/of the coastal front and the propagation speed of the coldest air in the gravity current/behind the front. The head of the gravity current/the coastal front propagates with speeds of around 10 m/s. This is comparable with values quoted for the propagation of the "morning glories" of $U_f \approx 10$ m/s (Noonan and Smith 1986), and of $U_f \approx 10-15$ m/s (Reeder and Smith 1999). However, the speed of the coastal front varies slightly from day to day. Generally, the propagation speed is faster in mode 1 (24f, 28f in Tables 5.2 and 5.2), when the Atlantic Inflow moves into the moderately thick residual layer. Although 29 June is categorised as mode 1, the layer above the residual layer is less stable than on 24 or 28 June. On 28 June the head propagates with the

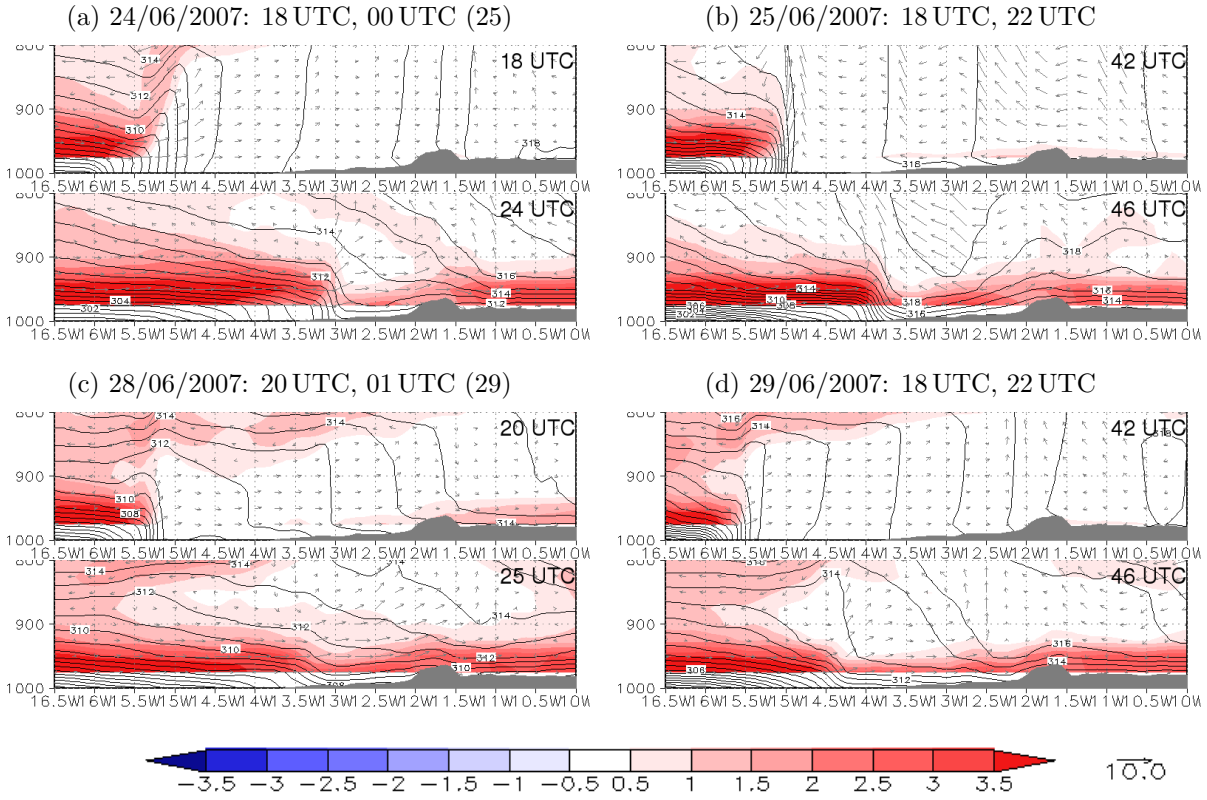

Figure 5.29: longitude-height cross sections at 18°N, 16.5°W-10.0°W, 1000-800 hPa: square of Brunt-Väisälä-frequency [$10^{-4}s^{-2}$] (shaded), virtual potential temperature [K] (black, 1 K contour interval), wind vectors in plane of section (grey). Forecast hour indicated in the upper right corner. Valid times in subcaption.

highest speed (11.2 m/s). On this day the Atlantic Inflow moves into a low-level stable layer ($p < 950$ hPa) which is not as pronounced on 24 or 29 June. Such a low-level stable layer can serve as a "wave guide" for induced gravity waves (Smith 1988). On 25 June the Atlantic Inflow moves into the rather neutrally-stratified thick Saharan PBL/SAL. The coldest air in the gravity current/behind the front seems to lag behind the head/front. The propagation speed of the Atlantic Inflow is $^2/_3$ $-^3/_4$ of the speed of the head, thus 2-4 m/s slower. Nevertheless, it shows the same day-to-day variablity as the head/front.

To conclude we calculate the theoretical propagation speed for a gravity current. It is derived from the x-component of the Boussinesq equation of motion neglecting friction and the Coriolis force (e.g. (Houze 1993)). The so-called densimetric speed is given by:

$$U_d = F\sqrt{g\frac{\Delta\rho}{\rho}H}, \tag{5.3}$$

F the nondimensional densimetric Froude number, g the apparant acceleration due to gravity, $\Delta\rho/\rho = (\rho - \rho_a)/\rho$ the nondimensional density difference between the gravity current (ρ) and the ambient air (ρ_a), and H the depth of the gravity current. F is of order 1 in calm surroundings. In the literature F covers a range from 0.4 to 1.4. The calculated densimetric speed U_d is given in Table 5.3 for the different days.

However, this is only a rough estimate as characteristic densities ρ and ρ_a for the

Table 5.3: densimetric propagation speed U_d in m/s, calculated from Eq. 5.3: day of June 2007, m: mode, ρ density of air in the gravity current [kg/m^3], ρ_a [kg/m^3] density in ambient air, for calculation of height H [m] refer to the text.

day	m	ρ	ρ_a	H [hpa]	T_0[K]	H_0 [m]	H [m]	$U_d/(F=1)$	$U_d/(F=1.2)$
24	1	1.14	1.10	950	300	8786	439	12.3	**10.3**
25	2	1.13	1.09	940	300	8786	527	13.5	**11.3**
28	1	1.14	1.11	940	301	8815	529	11.7	**9.8**
29	1	1.13	1.10	950	300	8786	439	10.7	**8.9**

two layers as well as the height H of the gravity current have to be defined subjectively. The height is estimated as the average height (in hPa) of the horizontal $N^2 > 3.5 \times 10^{-4} s^{-2}$ contour at 20 UTC and calculated from the equation for a homogeneous ($\rho =$ const.) atmosphere $z = H_0(1 - p(z)/p_0))$, where $H_0 = (R \cdot T_0)/g$ is the height of the homogeneous atmosphere. T_0 the temperature in K at the reference level $p_0 = 1000$ hPa, $R = 287.05 J/(kgK)$, $g = 9.8$ m/s^2. Assuming a Froude number of 1.2, the densimetric speed of around 10 m/s is of the same order as the propagation speed which was estimated from the position of the coastal front (Table 5.1). Thus, the propagation speed of the Atlantic Inflow can be derived from the theory of gravity currents, which together with the review of some experimental studies confirms the gravity current characteristics of the Atlantic Inflow.

5.6 The baroclinic zone

In longitudinal-vertical cross sections of virtual potential temperature at 18°N we observed a baroclinic zone separating the hot dry continental almost well-mixed Saharan air mass from a maritime air mass in the west (e.g. section 4.1.3, Figs. 4.3, 4.17, 4.23, 5.3 and 5.4). Its latitudinal extent was from around 16°N to the northern edge of the model domain (23°N). We found the Atlantic Inflow as a dominant feature west of this transition region. In this section we present ideas of how the Atlantic Inflow affects the evolution of the baroclinic zone.

In the central Saharan heat low region dry convection at daytime results in the deep almost neutrally-stratified Saharan PBL. Figures 5.3 and 5.4 (right column) show turbulent mixing extending up to around 550 hPa in the Saharan heat low region and up to 800 hPa over the continent at daytime. The mid levels west of the Saharan heat low region are moderately stably-stratified. The African easterly jet is a predominant feature in the mid-troposphere of the southern Saharan region. Easterly flow dominates from 750-500 hPa in the whole model domain. The longitudinal-vertical cross sections of virtual potential temperature shows that the tilt of the baroclinic zone dissipates and the baroclinic zone becomes vertically oriented at low levels due to dry convection at daytime (cp. Figs. 4.3 and 5.3b). However, a remnant baroclinic zone was evident west of the central Saharan heat low region from around 700 hPa to 550 hPa each day in mode 1 or 2 (Figs 5.3 and 5.4 (right column) except for 26 June). This may indicate that the baroclinic zone is a result of the westward advection of the Saharan PBL (becoming the SAL) through the African easterly jet . This is consistent with the position of the

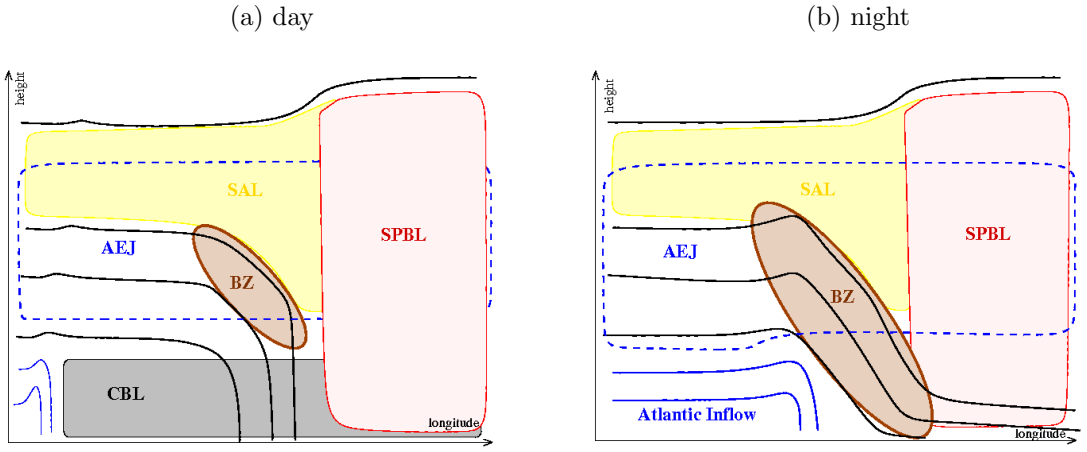

Figure 5.30: longitudinal-vertical sketches of the baroclinic zone at 18°N. Black lines indicate isentropes. Blue lines indicate isentropes related to the Atlantic Inflow. Blue dashed outline: AEJ=African easterly jet. Convective boundary layer (CBL) (grey), Saharan Air Layer (SAL) (yellow), Saharan PBL (SPBL) (red), and baroclinic zone (BZ) (brown).

baroclinic zone relative to the Saharan PBL which changes its longitudinal extent with the Saharan heat low. Fig. 5.30a shows a sketch of the daytime situation in mode 1 as described above.

During the night the baroclinic zone rebuilds at mid and low levels. Here the Atlantic Inflow may play an important role through two effects (cp. Fig. 5.30b): firstly, it advects cool air eastwards at low levels. This results in a reinforcment of the meridional temperature gradient and in an eastward tilting of the daytime vertical isentropes ahead of the front. Depending on the position of the Atlantic Inflow relative to the baroclinic zone, the Atlantic Inflow front itself becomes part of the baroclinic zone at low levels. Secondly, at mid levels the gravity wave at the head of the Atlantic Inflow causes a bulge in isentropes. Thus tilted isentropes move inland ahead of the Atlantic Inflow, which can contribute to a tilt of the baroclinic zone. This is indicated in Fig. 5.30b by the bulge of isentropes at the western point of the baroclinic zone. We observed that the bulge at the head of the Atlantic Inflow marks the westernmost point of the baroclinic zone (e.g. 03 UTC 25/06/2007, see appendix Fig. A.2e). In mode 2 and 3 the Atlantic Inflow itself seems to form a steep baroclinic zone through eastward advection of cooler air (e.g. 21 UTC 25/06/2007, see appendix Fig. A.3c).

5.7 Nocturnal jets

Kottmeier (1982) studied the evolution of low-level jet streams in a nocturnal planetary boundary layer with strong stable stratification. Although the desert environment of western Mauritania is very different to the midlatitude climate in northern Germany, a similar stable stratification is evident in the wake of the Atlantic Inflow. The passage of the Atlantic Inflow front is combined with an increase in zonal wind speed (section 5.3.1). Despite the coarse vertical resolution ($\Delta p = 25$ hPa) of the model output[2] the evolution of

[2]The vertical resolution of model levels is smaller but varies with height.

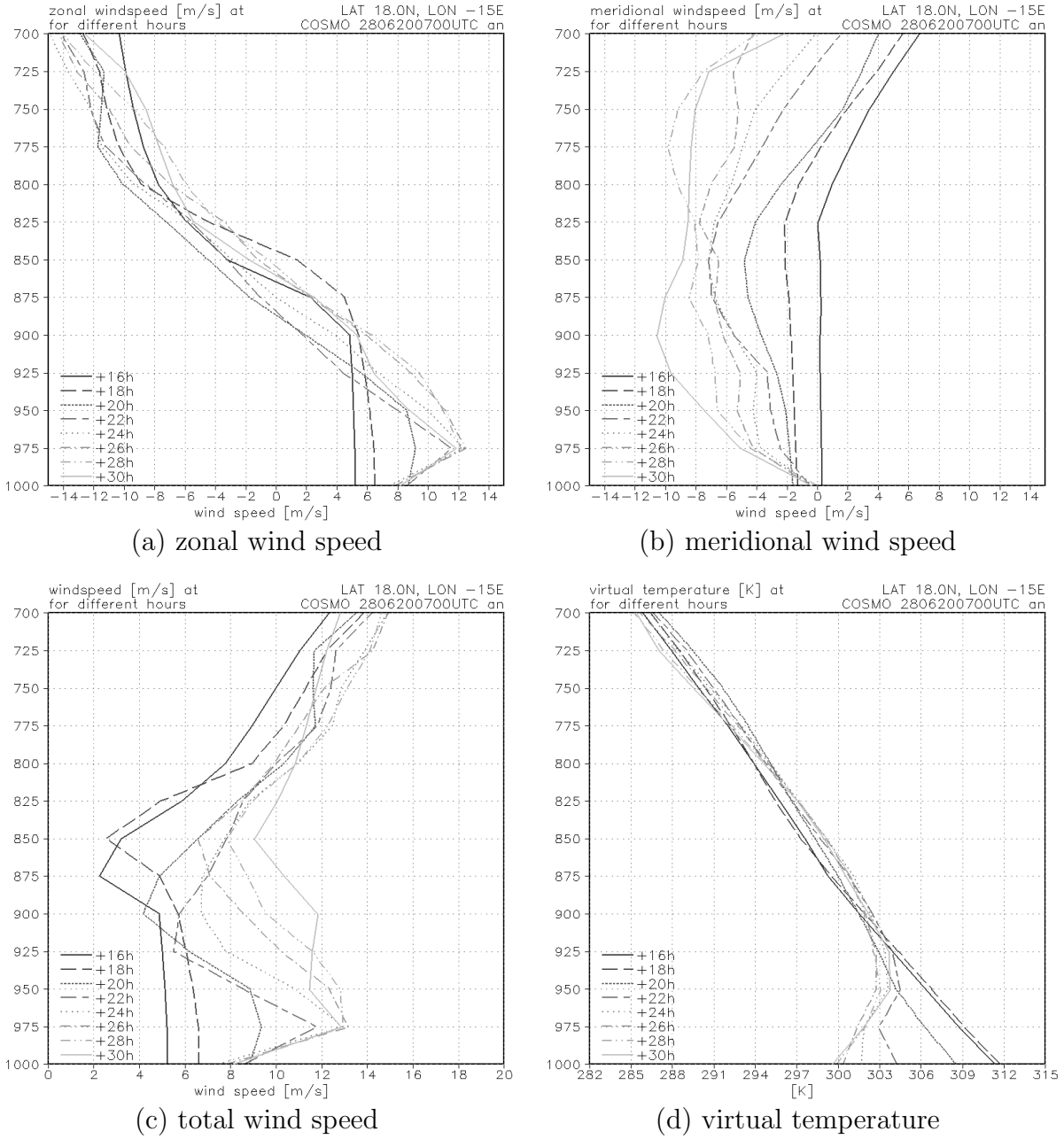

(a) zonal wind speed (b) meridional wind speed

(c) total wind speed (d) virtual temperature

Figure 5.31: profile of zonal, meridional, total wind speed, and temperature at 18°N, 15°W. Vertical axis: pressure [hPa]. The profiles are shown 2-hourly from 16 UTC 24/06/2007 to 6 UTC 25/06/2007. The Atlantic Inflow passed between 21 and 22 UTC.

a nocturnal low-level jet is observed in western Mauritania after the passage of the coastal front. Figure 5.31 shows profiles of the zonal and meridional wind component, the wind speed, and the temperature at 18.0°N, 15.0°W in a 2-hourly sequence during the night of 28-29 June 2007. The coastal front passed at around 22 UTC.

At 16 UTC (solid black lines) turbulent mixing is still strong. Hence the total wind speed is weak (5 m/s, Fig. 5.31c). Two hours later (long-dashed lines) the maximum temperature is reached at low levels (312 K, Fig. 5.31d). The convective boundary layer reaches its maximum vertical extent (indicated by the break at 850 hPa in Fig. 5.31d).

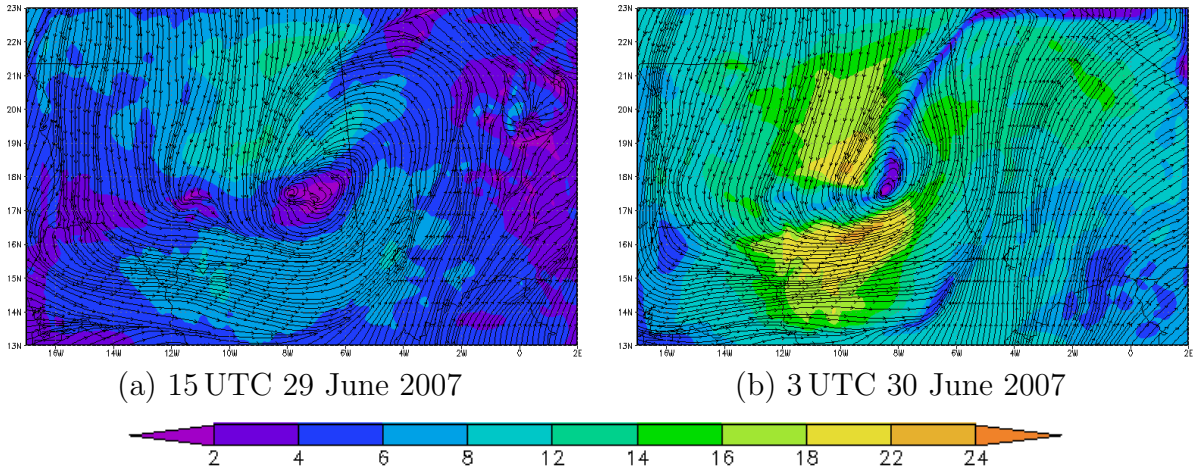

(a) 15 UTC 29 June 2007 (b) 3 UTC 30 June 2007

Figure 5.32: streamlines and wind speed [m/s] (shaded) at 925 hPa on 29 and 30 June 2007. The plots show the nocturnal intensification of the flow around a low-level heat low vortex. Based on COSMO forecast 00 UTC 28/06/2007, standard domain.

Turbulence had already decreased and thus the wind speed increased about 2 m/s below 850 hPa in the convective planetary boundary layer. At 20 UTC (short dashed lines) the wind speed further increased below 950 hPa. The temperature decreased by about 3 K, presumably due to radiative cooling. At 22 UTC the passage of the coastal front becomes evident in a further increase of total and zonal wind speed at 975 hPa and a cooling below 950 hPa to around 304 K. The Atlantic Inflow initiates the stabilisation of the low levels. In the following hours radiative cooling cools the levels below 925 hPa around further 2 K. Additionally, horizontal advection in the wake of the Atlantic Inflow leads to a cooling of 3 K near the ground. As a result the low levels show strongly stable stratification. The wind speed remains constant at around 13 m/s at 975 hPa marking the low-level jet. However, the vertical extent of high wind speed increases. At 4 UTC (dashed-double-dotted lines) the jet is evident from 975 to 925 hPa just on top of the stably-stratified air. The southerly meridional wind component increases also during the night, but this is maximised at around 900 hPa (Fig. 5.31b). The nocturnal increase of wind speed is in line with the theoretical mechansim of an inertial oscillation (Blackadar 1957).

The diurnal cycle of a heat low is also combined with the evolution of a nocturnal jet. This could be observed in the area of the secondary heat low vortex on 29 June 2007 (Fig. 5.32). In the afternoon the maximum mean wind speed at 925 hPa is around 12 m/s and occurs north-east and south of the heat low centre (Fig. 5.32a). In the absence of turbulent mixing, the maximum wind speed increased to more than 24 m/s twelve hours later (Fig. 5.32b). The location of the maxima relative to the vortex centre did not change. These plots highlight the diurnal cycle of wind velocity within heat low systems. The evolution of nocturnal jets in the south-western Saharan region is an interesting topic for further investigations. Higher vertical resolution at low levels would be helpful for this purpose.

5.8 The role of dry convection

The density contrast between the cold layer at the coast and the hot desert inland is the drive for inland penetration (section 5.5). The driving force is due to the meridional pressure gradient. However, the cold, denser air is prevented from moving more than a few kilometres inland at daytime by dry convection. The latter smooths and clears out the temperature contrast over land by heating the lower atmosphere from the hot surface. Thus, although the denser layer over the coast has a drive to move eastwards it is hindered as it is balanced by turbulent mixing. This becomes evident when looking at a Hovmöller plot of temperature tendencies due to horizontal advection and due to turbulence at low levels (Fig. 5.33). The Atlantic Inflow is marked by advection of cool air at low levels, while dry convection is reflected in a warming due to turbulent diffusion. In the following, we describe the situation on 24 June 2007. The process can similarily be described on the basis of other dates.

After sunrise the surface temperature over land increases steadily. Approximately one hour later the sensible heat flux starts warming the low-level atmosphere. This is seen as a steady increase of warming due to turbulent diffusion in the Saharan heat low region at 11°W after 7 UTC, in the Atlantic Inflow region at 14°W after 8 UTC and even later at the

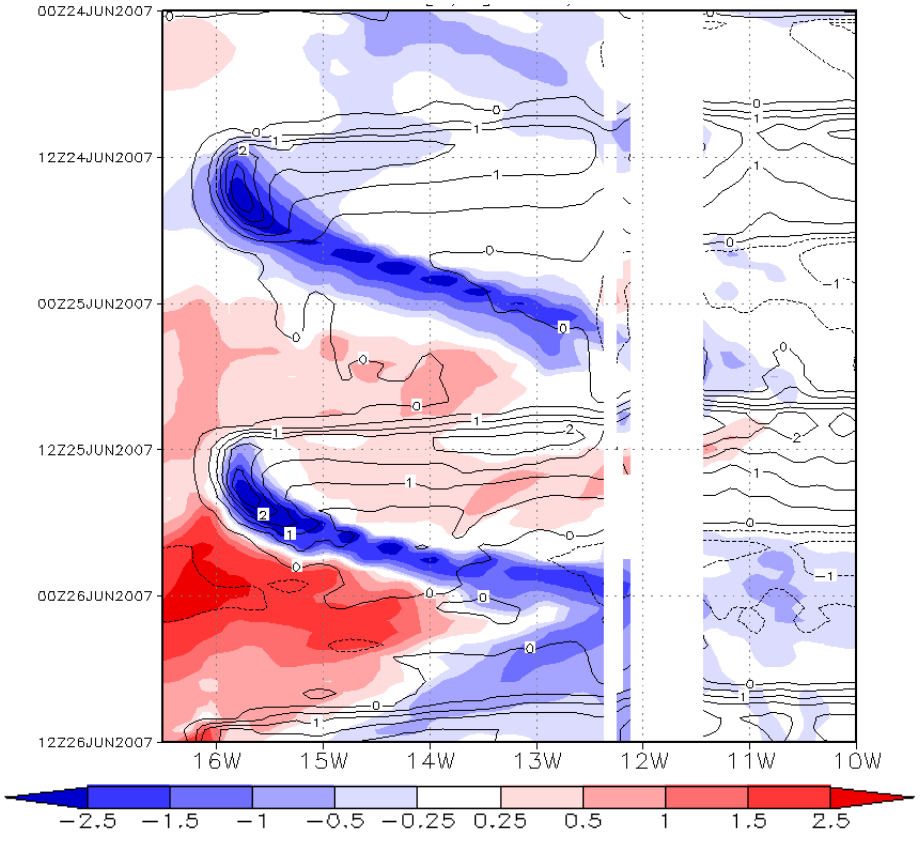

Figure 5.33: Hovmöller plots of temperature tendencies [K/h] due to horizontal advection (shaded) and turbulent diffusion (black 0.5 K/h contour interval). Averaged from 17.0°N to 19.0°N, at 975 hPa and 16.5°W-10.0°W. Hourly model output for a 60h forecast period. Areas where surface pressure is less than 950 hPa are masked out. Based on COSMO_budget initialised 00 UTC **24/06/2007**, shifted domain.

coast (16°W). The time lag from the east to the west reflects the different times of sunrise. At around midday the heating due to turbulent diffusion reaches its maximum. During the day turbulent mixing also extends into the low- and mid-level atmosphere (Figs. 5.8, 5.9 and 5.11). The rather uniform diurnal cycle is different east of 15.5°W near the coast. Here turbulent mixing does not warm the low-level atmopshere before 10 UTC. This is due to a more stably-stratified maritime boundary layer. At around 11 UTC the Atlantic Inflow becomes evident as a weak negative tendency due to horizontal advection. This cooling gradually increases up to more than -2.5 K/h at 15.8°W at 14 UTC. However, the warming due to turbulence increases at the same time and is much more pronounced than east of 15.5°W. Its absolute value is always higher than the absolute value of cooling due to horizontal advection Thus a meridional temperature gradient develops east of 15.8°W. This is the stationary coastal front.

As the diurnal cycle in low-level temperature over the desert inland is much stronger than in the coastal zone, the temperature, the pressure and the density gradients increase. Thus the driving force for inland penetration amplifies as well. However, the coastal front remains stationary as long as cooling due to horizontal advection is balanced by warming due to turbulent diffusion.

At around 15 UTC the front, defined by maximum advective cooling tendency, is located at 15.8°W and starts penetrating inland. This is evident in the weak eastward bending of the tendency contours. Cooling due to horizontal advection seems to dominate over warming due to turbulence (magnitude of both more than 2.5 K/h). At around 16 UTC the dominance of advective cooling becomes evident: the front is located at around 15.7°W. Here the temperature tendency due to turbulent diffusion falls below 2.0 K/h while the tendency due to horizontal cooling remains below -2.5 K/h. In the following hours the turbulent diffusion decays rapidly due to sunset. At the same time the Atlantic Inflow accelerates. After 19 UTC turbulent diffusion is negligible. At 19 UTC the Atlantic Inflow, located at around 15°W, has reached its final propagation speed. This is indicated by the rather linear progression up to 12.5°W at 02 UTC 25 June. The interaction of horizontal advection and turbulent diffusion becomes evident also, when looking at the time-height plots at a specific location (Figs. 5.8, Fig. 5.12). The Hovmöller plot Fig. 5.33 of horizontal advection does also show that the Atlantic Inflow front does not overstep the Tagant Plateau at 12°-11.5°W. When reaching the foot of the mountain range the Atlantic Inflow becomes diffusive to the east of 13°W every day.

In this section the balance between horizontal advection and turbulent diffusion was found to play a key role for the propagation of the Atlantic Inflow. The analysis of heat and moisture budgets in chapter 6 will additionally confirm this mechanism.

5.9 Discussion

The Atlantic Inflow is a phenomenon which was observed at the West African coast during the GERBILS campaign at the end of June 2007. It consists of a low-level ($p >$ 800 hPa) eastwards moving front penetrating inland from the coast at 16°W up to the foot of the Tagant Plateau at 12°W at nighttime. It is most distinct between 17°N and 19°N. In the following we refer to this region as the "Atlantic Inflow region". In the wake of the front cold, stably-stratified, and occasionally more humid air moves inland, combined with a strengthening and turning of the wind to a more westerly flow. This

inflow can be described as a gravity current. The coastal front forms the head of the gravity current. Above this leading edge a gravity wave can be induced if the mid-level atmosphere (800 hPa> p > 400 hPa) is stably-stratified (mode 1). This leads to a complex triplet structure in the vertical wind field with ascent at low levels, descent at mid levels and further ascent at high levels (p > 400 hPa). This pattern reflects the gravity wave crests and troughs. The phase lines are tilted eastwards upstream of the predominant easterly flow in the mid levels. In mode 2, when the atmosphere above the coastal front is neutrally-stratified, the prefrontal updraft is dominant and can lead to a very strong ascent up to 500 hPa (Fig. 5.23b).

In Fig. 5.34 a schematic overview of elements determining the Atlantic Inflow is given. The most striking feature of the Atlantic Inflow is its coastal front. The front is defined by the sharp meridional temperature gradient. The temperature gradient is also linked with a gradient in density and pressure. The Atlantic Inflow region lies at the south-western edge of the Sahara desert which is climatologically below the subsiding branch of the northern Hadley cell. This results in almost cloudless conditions and strong insolation which heats the surface over the continent at daytime. The 2 m maximum temperature often reaches more than 45°C (318 K) in the afternoon. In contrast, the low-level atmosphere over a small land zone at the coast and over the Atlantic Ocean is rather cool ($T_{max} \approx$ 27°C (300 K)) and strongly stably-stratified ($\partial\Theta/\partial p \approx$ 1K/(10 hPa)). At the end of June the ocean temperature at the Mauritanian coast is around 22°C (Fig. 5.2). The relatively cool sea surface is due to the cold Canary current and weak up-welling of cold deep waters at the West African coast. This explains the temperature contrast between the coastal zone and the desert inland. However, it does not explain why this contrast is concentrated in a coastal front.

The hot surface inland leads to a strong sensible heat flux which results in strong turbulent mixing due to dry convection. This leads to a rather well-mixed neutrally-stratified convective boundary layer which extends up to 800 hPa (mode 1) in the Atlantic Inflow region and up to 500 hPa in the Saharan heat low region (east of 12°W in mode 1, east of 16°W in mode 2). The dry convection balances cooling due to horizontal advection

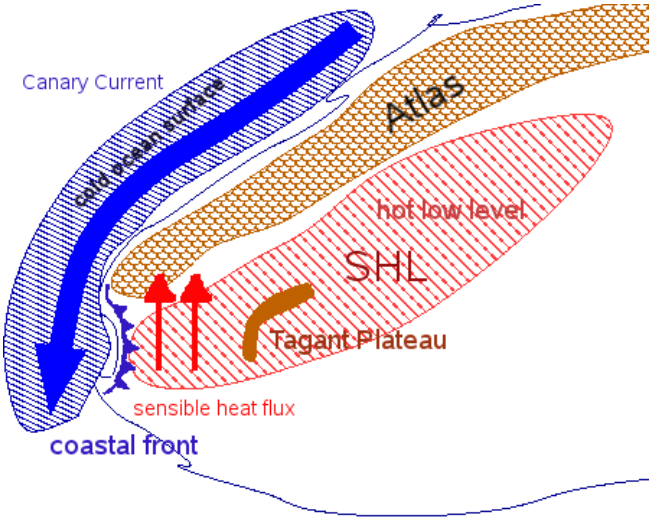

Figure 5.34: schematic sketch of the Atlantic Inflow.

from the Atlantic Ocean at daytime and thus prevents inland penetration of the cool and more dense maritime air. The temperature gradient is maximised near the coast and a front is formed. As soon as turbulence decays in the evening the Atlantic Inflow penetrates inland.

Once penetrating inland, the Atlantic Inflow behaves like a gravity current in the low levels (section 5.5) and leads to a cooler stably-stratified low-level atmopshere in its wake (section 5.4). The gravity current character determines the propagation speed of the Atlantic Inflow. In case of a weakly stably-stratified atmosphere aloft the Atlantic Inflow affects the mid levels by inducing a gravity wave and a distinct circulation at the front (section 5.4.2).

Orography in Western Mauritania favours the inland penetration. At the coast of Mauritania and Senegal a fast coastal plain extends 400 km inland. The terrain ascends only gradually towards the foot of the Tagant Plateau (Fig. 3.2) at 12°W, 16°N-20°N where it ascends steeply up to 600 m. This plateau forms the first orographic barrier east of the coast. North of 20°N the coastal plain is narrow and the hilly terrain dominates a few kilometres inland. Here fronts penetrating inland were not observed.

6 Heat and moisture budgets

Several studies, e.g. Cadet and Nnoli (1987) and Long et al. (2000), highlight the importance of humidity advection in the low levels from the south to the Sahelian region due to the monsoon flow, and of humidity export in the mid-troposphere to the Atlantic Ocean due to the African easterly jet. Recently Peyrillé et al. (2007) and Peyrillé and Lafore (2007) stressed the importance of low-level advection for the balance of the heat and moisture budgets in the West African monsoon system using a two-dimensional model. In this context it is interesting to examine the effect of the Atlantic Inflow on the heat and moisture budgets in western Mauritania and adjacent regions. Therefore we use tendency terms from COSMO_budget and calculate heat and moisture budgets in a Saharan heat low (SHL), monsoon (M), and Atlantic Inflow (AI) box.

COSMO_budget provides the individual terms of the temperature and humidity tendency equations. They are repeated in slightly modified form for potential temperature and specific humidity as described in sections 2.3 and 2.3.1 (Eqs. 2.15 and 2.9):

$$\frac{\partial \Theta}{\partial t} = HADV_{\Theta} + VADV_{\Theta} + MTD_{\Theta} + RAD + MMC_{\Theta} + SQ_{\Theta} + COMP_{\Theta}$$
$$\frac{\partial q^v}{\partial t} = HADV_{q^v} + VADV_{q^v} + MTD_{q^v} + MMC_{q^v} + SQ_{q^v} + COMP_{q^v}.$$

The contributions to the local tendency are from horizontal advection (HADV), vertical advection (VADV), turbulence (MTD), radiation (RAD), grid scale moist processes (SQ), sub-grid scale moist convection (MMC) and computational effects (COMP).

In section 6.1 we present profiles of the tendency terms averaged over boxes and over the two-day period 28-29 June 2007. In section 6.2 the diurnal cycle of the tendency terms is investigated using time-height plots. For both investigations we use model output of COSMO_budget, initialised at 00 UTC 28/06/2007 for the standard domain. The areal average is taken over the horizontal box area in each level. The temporal average is taken over the two-day period 00 UTC 28 June to 00 UTC 30 June 2007 in the SHL- and AI-box using the hourly model output. In the M-box we neglect the first 9 hours as a mid-level cloud perturbs the tendencies in the morning of 28 June and we do not consider this to be typical for the monsoon box. The boxes are chosen so that the meteorological conditions are typical for the different regions. For the SHL-box the ITD is always south and Harmattan winds dominate the low-level flow. For the M-box the ITD is always north and the monsoon flow dominates the low-level flow. The nocturnal coastal front passes through the entire AI-box. We assume these boxes to be representative for general characteristics of the temperature and humidity budget in the distinct regions. The horizontal locations of the boxes are shown in Table 6.1 and Fig. 6.1. All profiles will be described on pressure levels. For the SHL- and M-box, level $p = 975$ hPa is closest to the ground, for the AI-box level $p = 1000$ hPa. We neglect data in the upper levels ($p < 200$ hPa) as the effects of the upper boundary become dominant from 200 hPa upwards.

Table 6.1: minimal/maximal longitude [°E] and latitude [°N] of the boxes.

box	min.[°E]	max.[°E]	min.[°N]	max.[°N]
SHL	-10.0	-8.0	20.0	22.0
M	-2.0	-1.0	14.0	15.0
AI	-15.5	-14.5	17.5	18.5

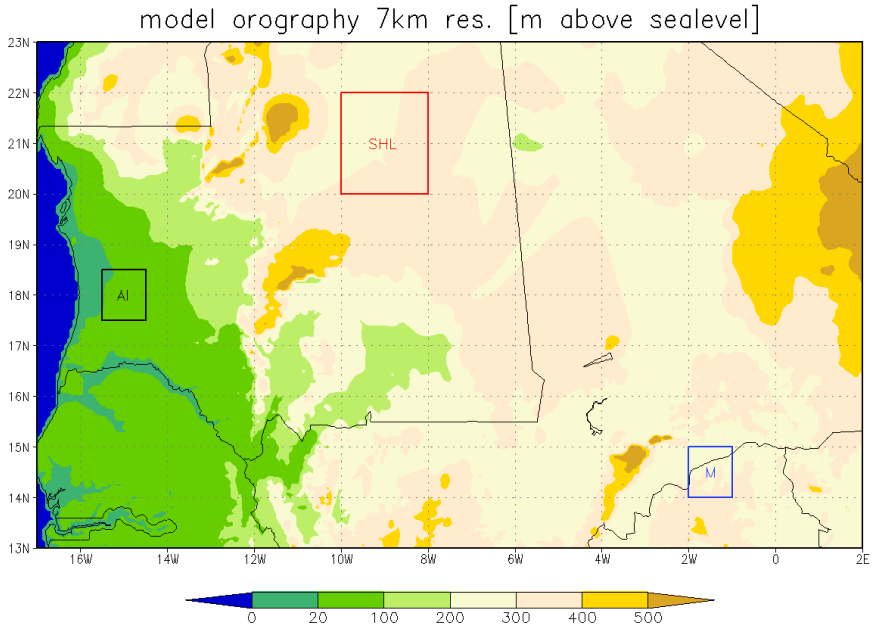

Figure 6.1: location of the Saharan heat low (SHL, red), monsoon (M, blue) and Atlantic Inflow (AI, black) boxes within the model domain. The background shows the orography (height in metres above mean sea level).

6.1 Profiles of the tendency terms

In the following profiles of potential temperature and specific humidity tendency terms are shown for the different boxes.

6.1.1 Saharan heat low region

The profiles of potential temperature tendencies in the Saharan heat low region show three distinct layers (Fig. 6.2a). Below 800 hPa there is a net warming of up to 0.05 K/h, except near the surface. This layer corresponds to the daytime internal convective boundary layer and nocturnal stable layer indicated by the mean moderately stable stratification ($\partial\Theta/\partial p \approx 0.5\,\mathrm{K}/(10\,\mathrm{hPa})$) and decrease of specific humidity ($\partial q^v/\partial p \approx 0.14\,\mathrm{g/kg}/(10\,\mathrm{hPa})$) from the ground upwards (Fig. 6.3a). From 800 hPa to 600 hPa the sum of tendencies is almost zero. This is the neutrally-stratified Saharan residual layer (Fig. 6.3a). Above 600 hPa there is a transition layer from the Saharan PBL into the free atmosphere (from 450 hPa upwards). Here the local temperature budget shows a complex pattern of warming and cooling.

Although the sum of tendencies is small, the individual tendency terms show a signifi-

(a) Θ-tendencies in SHL-box (b) q^v-tendencies in SHL-box

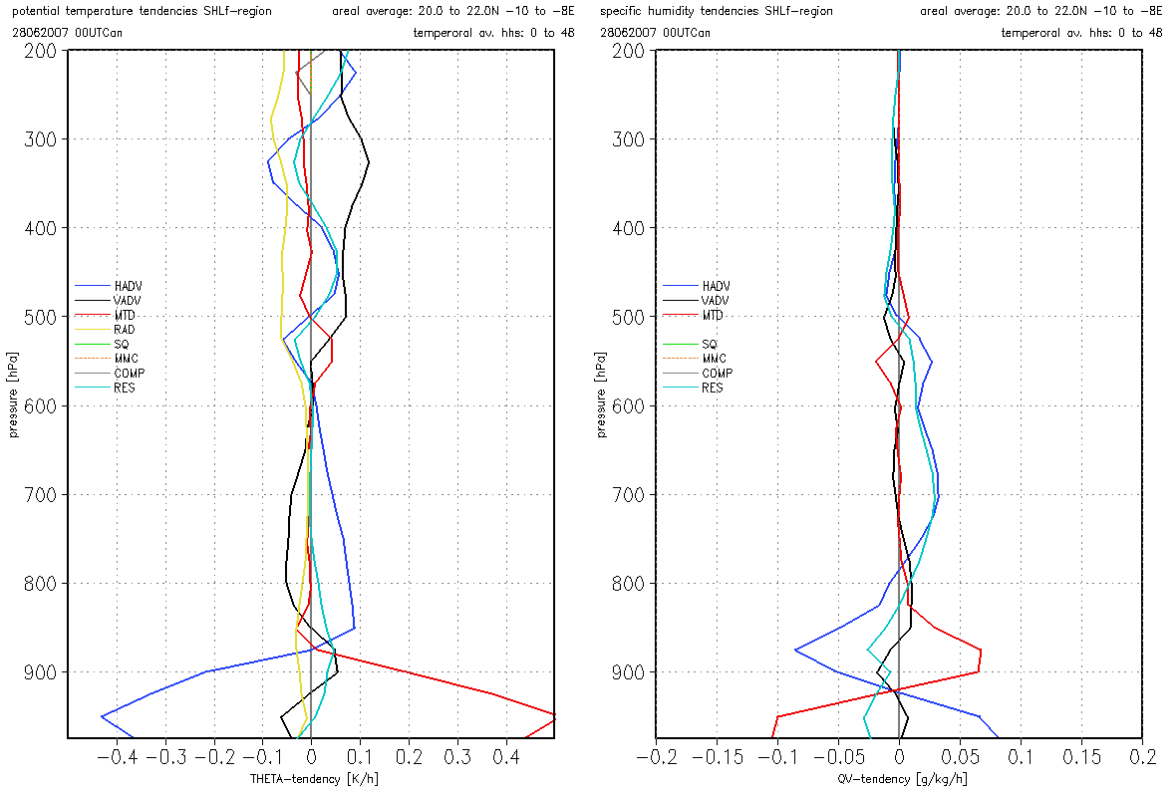

Figure 6.2: averaged profiles of potential temperature (Θ) tendencies [K/h] (left) and specific humidity (q^v) tendencies [g/kg/h] (right) in **SHL-box**. Temporal average over 48h COSMO_budget forecast initialised at 00 UTC 28/06/2007, standard domain. Colours and abbreviations stand for: horizontal advection (HADV) dark blue, vertical advection (VADV) black, turbulence (MTD) red, radiation (RAD) yellow, grid scale moist processes (SQ) green, sub-grid scale moist convection (MMC) orange dashed, computational effects (COMP) grey, and sum of tendencies (RES) (local tendency) cyan.

cant amplitude. At low levels, cooling due to horizontal advection (-0.4 K/h) is almost balanced by warming due to turbulent diffusion (0.5 K/h). Vertical advection (+/-0.05 K/h) and radiative cooling (-0.03 K/h) play a minor role. Northerly flow dominates in this layer (Fig. 6.3e). The balance in the mid levels is achieved by moderate cooling (up to -0.06 K/h) due to VADV, which is consistent with the mean ascending motion (Fig. 6.3a), and warming due to HADV (up to 0.08 K/h). At the top of the Saharan PBL (at around 500 hPa) the tendency terms show a complex pattern. Radiative cooling increases to -0.07 K/h and remains one of the dominant terms in the higher levels (-0.08 to -0.04 K/h). However, VADV becomes the most important tendency term (warming up to 0.12 K/h due to descending motion (Fig. 6.3a)). This is consistent with the mean descending motion in the subsiding branch of the Hadley cell. While MTD is dominant just below the top of the Saharan PBL (warming up to 0.04 K/h from 550 to 525 hPa) it only plays a minor role above in the free atmosphere (cooling of around -0.01 K/h). As the other terms are almost in balance, the rather complex pattern of HADV determines the sum of tendencies in higher levels. It shows a range from -0.04 to 0.08 K/h.

The profiles are consistent with a similar profile of temperature tendencies from

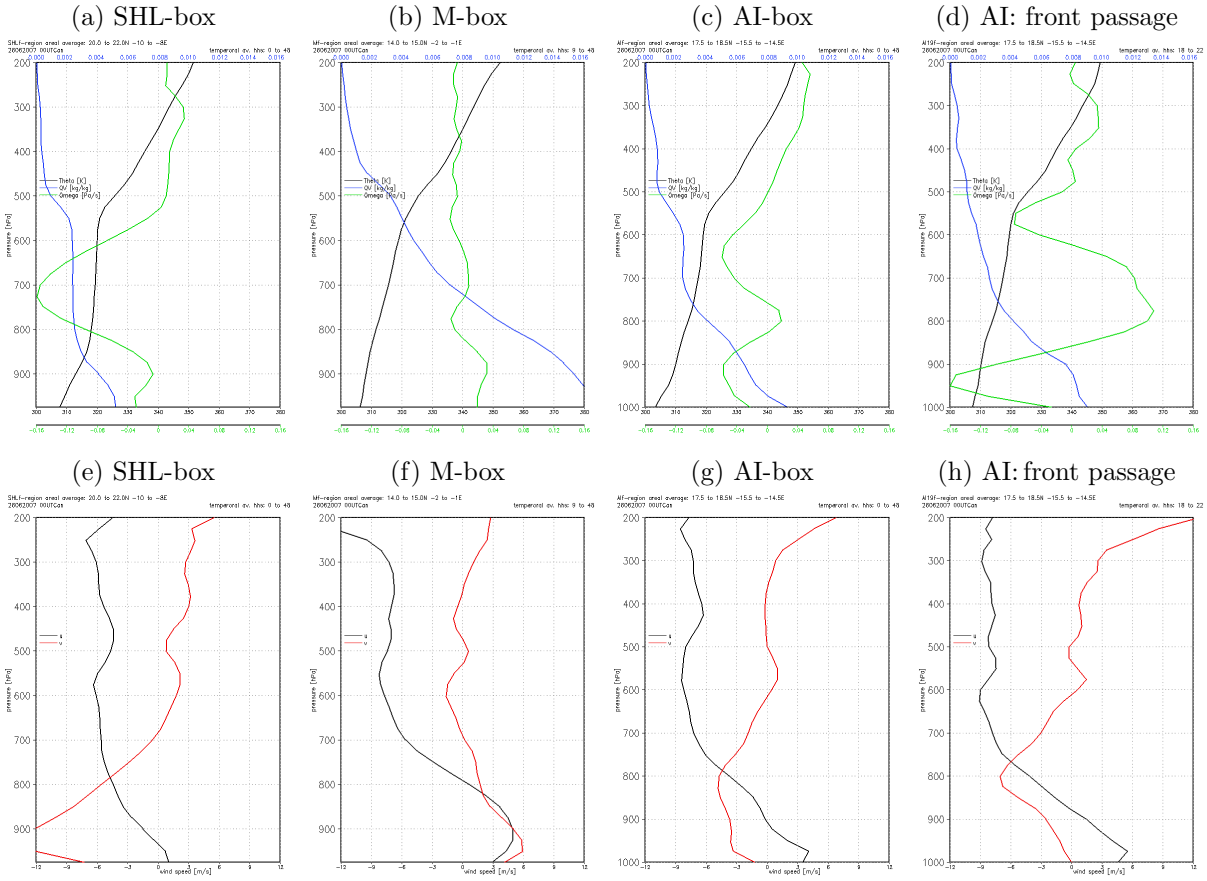

Figure 6.3: profiles of potential temperature [K] (black), specific humidity [kg/kg] (blue), vertical velocity [Pa/s] (green) (top). Profiles of zonal ((a)-(d)) and meridional wind component [m/s] (red) ((e)-(h)). The interval on the x-axis is 10 K, 0.002 kg/kg, 0.04 Pa/s, and 3 m/s starting at 300 K, 0.000 kg/kg, -0.16 Pa/s, and -12 m/s. Averages over area and time indicated as in Fig. 6.2.

Peyrillé and Lafore (2007) averaged over a 20-day period. However, their net temperature budget in a SHL-box is balanced (Fig. 6.4a). At low levels the balance is achieved by zonal forcing (which represents zonal advection) and turbulence. In the free atmosphere radiative cooling is balanced by advective warming (which is mainly vertical advection).

The three layers are not as clearly reflected in the budget profiles of specific humidity (Fig. 6.2b). The atmosphere below 825 hPa is marked by a net drying of around -0.03 g/kg/h. Below 925 hPa this tendency results from moistening due to HADV and VADV on the one hand, and drying due to MTD on the other. From 925 hPa to 800 hPa this pattern reverses sign and the tendency results from a drying due to HADV and moistening due to MTD. The absolute values of the tendency terms reach up to 0.1 g/kg/h. Thus the rather strong northerly flow (Fig. 6.3e) advects humidity in the lowest levels which is mixed into the levels above by turbulent diffusion. This is consistent with the smooth decrease of humidity with height below 800 hPa (Fig. 6.3a). Horizontal advection (up to 0.03 g/kg/h) dominates the net tendency within the Saharan PBL. At the top of this layer the tendency terms show a structure corresponding to the temperature ten-

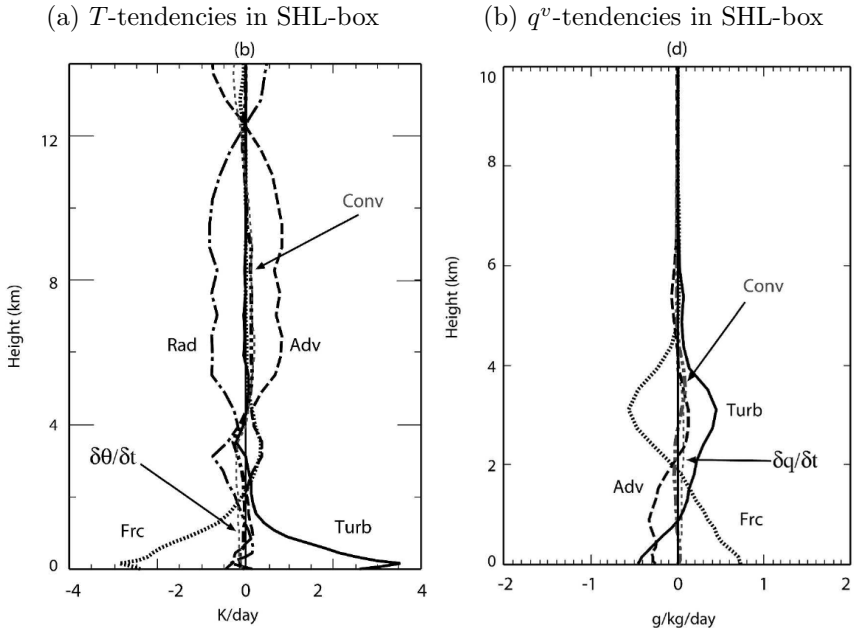

Figure 6.4: Figures 9 (b) and (d) from Peyrillé and Lafore (2007): profiles of temperature [K/day] (left) and specific humidity [g/kg/day] (right) tendencies in the **SHL-box**. The tendencies are from: Adv: vertical and meridional advection; Conv: convection; Frc: forcing term≙zonal advection; Rad: radiation; Turb: turbulence.

dencies. The cooling/warming just below 500 hPa due to HADV/MTD is combined with a moistening/drying. At around 500 hPa these tendencies reverse sign. From 500 hPa the sum of tendencies is negative but becomes almost zero above 450 hPa. The reversal of sign of turbulence and horizontal advection in the lower troposphere is also evident in the profiles of specific humidity tendencies of Peyrillé and Lafore (2007) (Fig. 6.4b). However, this structure extends up to 4 km and is not limited to the low levels as in our data (Fig. 6.2b).

6.1.2 Monsoon region

As deep moist convection within the ITCZ evolves only at the southern edge of the GERBILS model domain, the M-box is limitedly representative of the monsoon region. There is hardly any precipitation within the box during the two-day period but moist convection does occur on both days.

In the M-box the sum of potential temperature tendencies is not balanced. Below 900 hPa the net tendency is positive (up to 0.06 K/h) (Fig. 6.5a). This is the result of strong warming due to MTD (up to 0.4 K/h) and cooling due to HADV (-0.18 K/h), subgrid scale moist convection MMC (-0.07 K/h), and radiation (-0.03 K/h). Low-level winds show strong south-westerly monsoon flow in this layer (Fig. 6.3f). From 900 to 600 hPa HADV is the dominant cooling and VADV the dominant warming tendency. From 900 to 750 hPa RAD and from 900 to 825 hPa MMC is negative (up to -0.1 K/h at 800 hPa). The effect from MTD vanishes resulting in a negative sum of tendencies (-0.08 K/h) up to 725 hPa. Radiative cooling strongly increases at 550 hPa above the monsoon layer, becoming the dominant term (-0.1 K/h) in high levels. Also MMC indicates warming

(a) Θ-tendencies in M-box

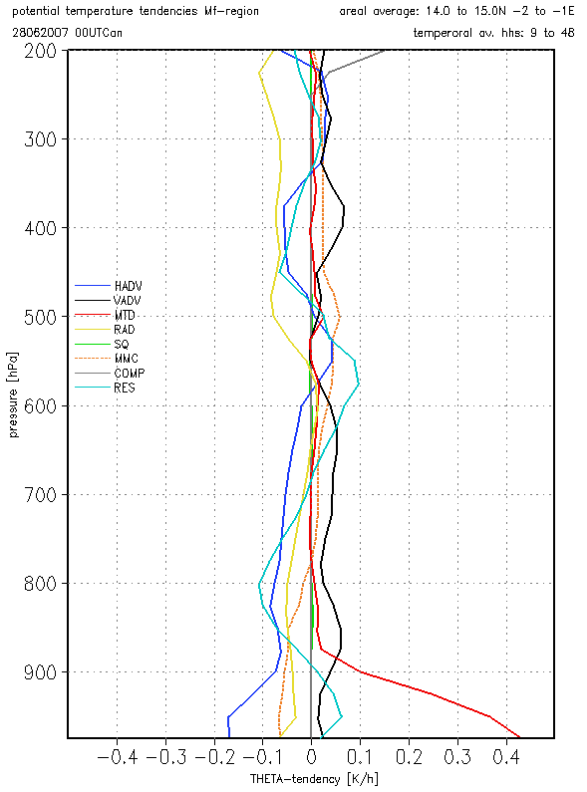

(b) q^v-tendencies in M-box

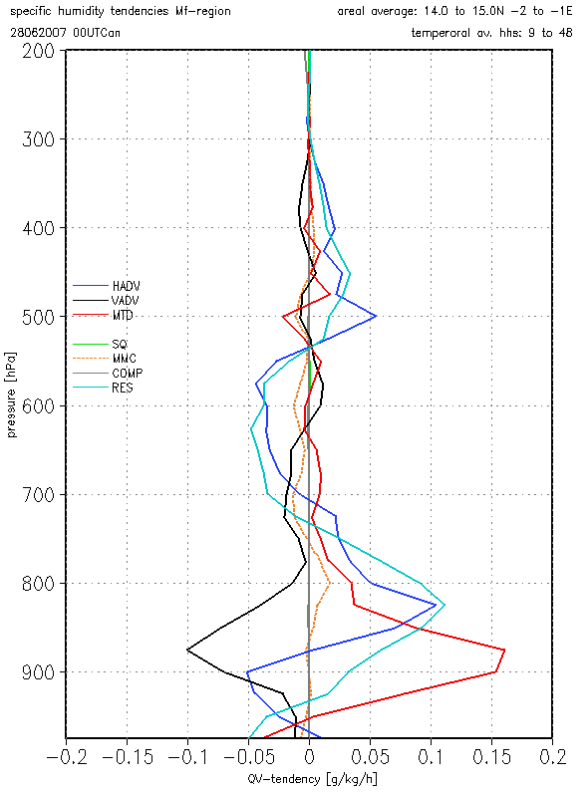

Figure 6.5: as Fig. 6.2 but for the **M-box**. Temporal average: 00 UTC 28/06/2007 forecast hours 9-48.

due to convection from 750 hPa onwards. It is maximised in a layer from 600 to 400 hPa (0.05 K/h). Again HADV seems to determine the sum of tendencies as the other terms are more or less balanced. Despite the limited representativeness of the M-box there are some similarities to the ITCZ profiles of Peyrillé and Lafore (2007) (Fig. 6.6a). Their profile of temperature tendencies also shows advection and turbulence as the dominant terms in the low and mid levels. An increase in radiative cooling caps the monsoon layer. Warming due to convection plays the dominant role in mid and high levels and is much higher compared to our data.

HADV, VADV and MTD dominate the water budget in the low and mid levels (Fig. 6.5b). Below 700 hPa the sum of tendencies of specific humidity is positive (up to 1.1 g/kg/h) except for near the ground. Turbulence seems to mix the moist monsoon air from the lowest levels (Fig. 6.3b) into higher levels. This is consistent with Peyrillé and Lafore (2007) (Fig. 6.6b), where turbulent moistening is maximum at low levels also. From 700 to 550 hPa net drying due to HADV (-0.05 g/kg/h) indicates the export of moisture through the African easterly jet (Fig. 6.3f). Here a weak drying tendency (-0.01 g/kg/h) due to MMC is evident as well. However, the humidity budget in our M-box does not show the balance between turbulence, advection, and convection as proposed by Peyrillé and Lafore (2007).

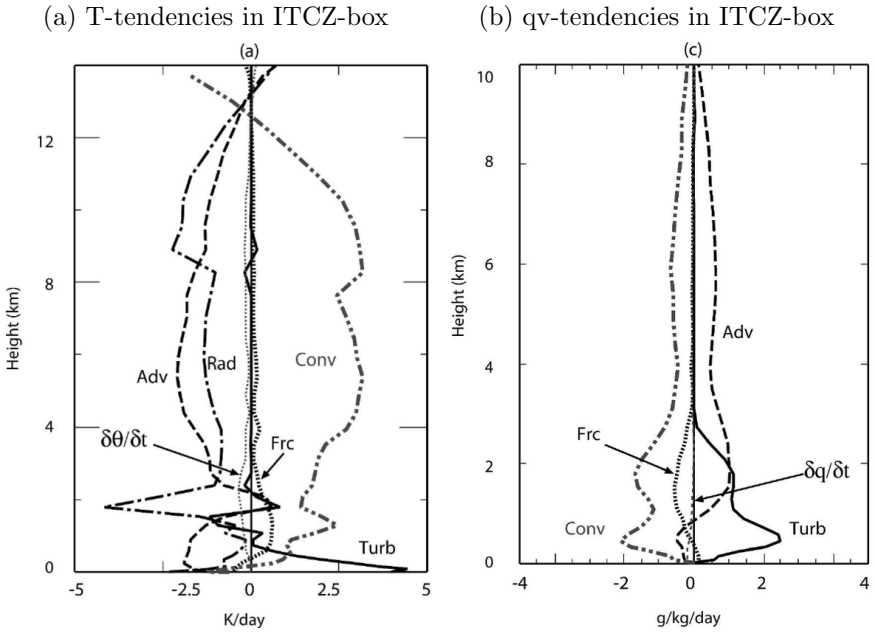

Figure 6.6: Figures 9 (a) and (c) from Peyrillé and Lafore (2007): as Fig. 6.4 but for a box in the **monsoon** region.

Summary of main characteristics in SHL- and M-box In the SHL-box potential temperature and specific humidity budgets are almost in balance. In contrast, net tendencies in the M-box cover a wide range of temperature and humidity changes. In the low levels of the SHL region the temperature balance results from cooling due to horizontal advection and warming due to the sensible heat flux. In the monsoon region the low-level warming due to turbulence is opposed by horizontal advection, radiation, and moist convection. At high levels, horizontal advection determines more or less the sum of potential temperature tendencies whereas the other terms are almost balanced.

Radiative cooling is important in the low and high levels. Its absolute value is nearly doubled in the monsoon region compared to the Saharan region. The top of the Saharan PBL and of the monsoon layer is marked by a strong increase in radiative cooling. Moist convection plays a role only in the M-box. Here it moderately cools the low levels and slightly warms and dries the mid levels. Turbulence seems to be responsible for a mixing of humidity from the lowest into higher levels.

6.1.3 Atlantic Inflow region

The sum of potential temperature tendencies in the AI-box is positive and almost constant (0.04 K/h) in the whole atmosphere except for a layer from 575 to 400 hPa (Fig. 6.7a). At the top of the Saharan PBL around 500 hPa an increase in cooling from RAD and a layer of horizontal advection of colder air leads to a net cooling of around -0.1 K/h. This is reflected in the profile of potential temperature which shows weakly stable stratification up to 575 hPa ($\partial\Theta/\partial p \approx 0.04\,\mathrm{K}/(10\,\mathrm{hPa})$) and a more strongly stable layer above ($\partial\Theta/\partial p \approx 0.08\,\mathrm{K}/(10\,\mathrm{hPa})$).

Below 900 hPa there is evidence of the Atlantic Inflow. Here the temperature tendency due to HADV dramatically changes from a warming of 0.05 K/h at 900 hPa to a

(a) theta-tendencies in AI-box

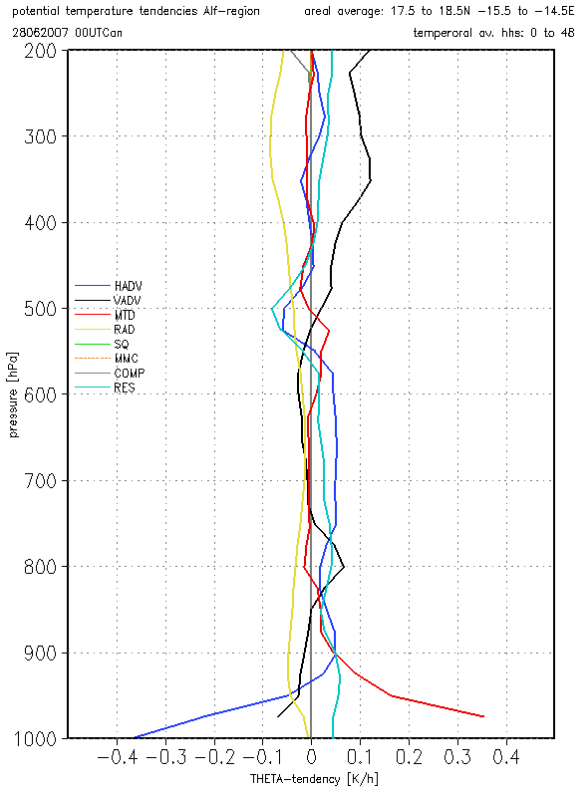

(b) qv-tendencies in AI-box

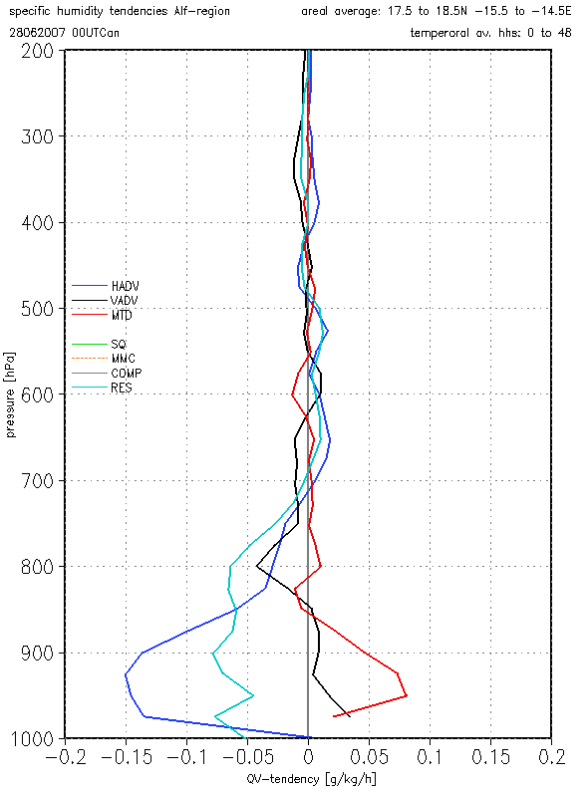

Figure 6.7: as Fig. 6.2 but for the **AI-box**. Temporal average: 00 UTC 28/06/2007 forecast hours 0-48.

cooling of -0.37 K/h at 1000 hPa and westerly onshore flow dominates (Fig. 6.3g). However, the cooling is balanced by a warming due to MTD of up to 0.35 K/h at 975 hPa. In the layer from 900 to 500 hPa HADV is almost constant ($\approx$ 0.05 K/h). An effect of the top of the Saharan PBL comparable to the one observed in the SHL-box is evident at around 500 hPa. At high levels warming due to vertical advection (up to 0.12 K/h) is linked to descending motion (Fig. 6.3c). Furthermore, cooling from RAD (up to -0.09 K/h) reaches similar values as in the monsoon region.

The moisture budget is only close to balance above 650 hPa (Fig. 6.7b). Below 700 hPa the sum of tendencies indicates drying of up to -0.08 g/kg/h in the low levels. HADV is dominant and reaches -0.15 g/kg/h at 925 hPa. MTD (0.08 g/kg/h) and VADV (0.03 g/kg/h) slightly reduce the drying due to HADV. Nevertheless, there is evidence of the Atlantic Inflow. The specific humidity tendency due to HADV dramatically increases to a very weak moistening of 0.01 g/kg/h at 1000 hPa. Above 700 hPa the absolute values of all tendency terms are below 0.02 g/kg/h. Three features are striking: At around 600 hPa there is a drying tendency due to MTD, this is not colocated with a warming due to MTD as it is observed in the SHL-box. However, the temperature tendency due to MTD becomes positive at 600 hPa, too. From 700 to 600 hPa there is a weak moistening tendency due to HADV. This is a layer where the African easterly jet is strongest (Fig. 6.3g). At around 525 hPa the moistening tendency due to HADV dominates. This correlates with the cooling due to HADV at the top of the Saharan PBL (Fig. 6.7a).

Strong vertical wind shear marks the lowest levels in the Atlantic Inflow region

(Fig. 6.3g). Below 900 hPa the wind comes from the north to northwest and is onshore. This is reflected by a slightly stronger stable stratification and higher values of specific humidity (Fig. 6.3c). From 900 to 700 hPa the wind turns into the African easterly jet.

Although the Atlantic Inflow passes through the box during few hours each day, a weak effect was detectable in the 48-hour averaged profiles. We finally show profiles of the tendency terms temporally averaged over the passage of the Atlantic Inflow on 28 June 2007 (18-22 UTC) (Fig. 6.8). Here the effect of the Atlantic Inflow on the temperature and humidity budgets in the AI-box becomes obvious. At 1000 hPa the Atlantic Inflow is evident by a net cooling tendency of -1.47 K/h (Fig. 6.8a). The contribution of horizontal advection to this cooling is -1.05 K/h. Turbulence (0.15 K/h) hardly contributes to the low level temperature tendency. The frontal circulation at the head of the Atlantic Inflow is reflected in the profile of vertical velocity (Fig. 6.3d). From 1000 hPa to 850 hPa there is ascending motion, while vertical velocity indicates descent in the layer from 850 hPa to 625 hPa. From 625 hPa to 475 hPa the high-level ascent can be detected. This pattern is also reproduced in the temperature tendency due to vertical advection (Fig. 6.8a) and weaklier in the tendency due to horizontal advection (section 5.4). The horizontal wind components indicate a stronger wind from the west during the frontal passage than in the two-day average (cf. Figs. 6.3g and 6.3h). The humidity budget shows moistening in the lowest levels due to the Atlantic Inflow (Fig. 6.8b). The sum of tendencies is 0.35 g/kg/h, the contribution due to horizontal advection 0.2 g/kg/h. The profiles of humidity tendency

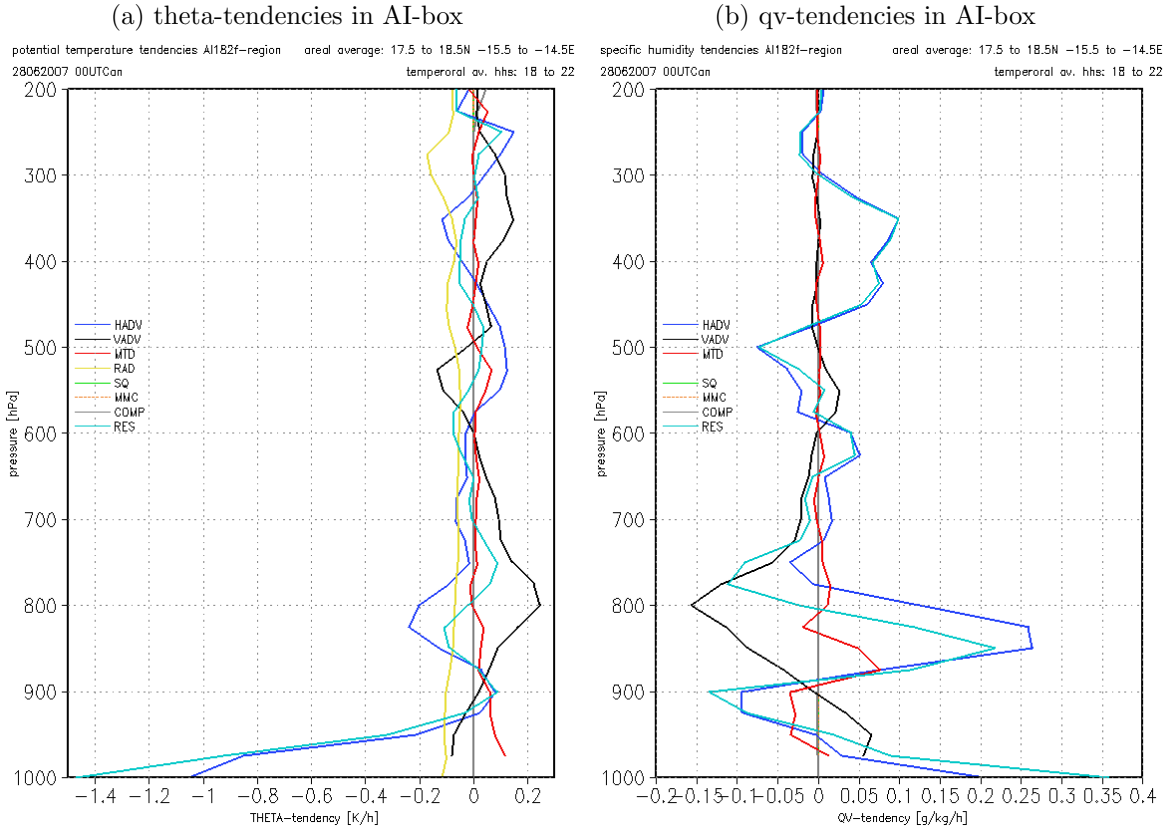

Figure 6.8: as Fig. 6.2 but for **AI-box and front** passage. Temporal average: 00 UTC 28/06/2007 forecast hours 18-22. Note the different scaling of the x-axis compared to Fig. 6.7.

terms show a rather complex pattern in mid and high levels.

The profiles of temperature tendencies in the Atlantic Inflow region support the mechanism for the propagation of the front which we proposed in section 5.8. Whereas in the two-day mean profiles cooling due to horizontal advection is more than balanced by turbulent warming, the front passes in the evening when turbulence only plays a minor role. Cooling due to horizontal advection dominates by far during the passage of the Atlantic Inflow front. The absolute value of temperature tendency due to horizontal advection exceeds the effect of turbulence by more than a factor of five.

6.2 Diurnal cycle of the tendency terms

In the previous section we analysed temporally averaged profiles of the temperature and humidity budget spatially averaged over a SHL-, M-, and AI-box. However, meteorological elements such as the Saharan heat low, the monsoon flow, or the Atlantic Inflow have a distinct diurnal cycle. In this section we investigate the diurnal cycle of the tendency terms using time-height plots spatially averaged over the box area at each level.

6.2.1 Saharan heat low region

In the SHL-box the time averaged sum of potential temperature tendencies was weak. However, in time-height plots it shows a strong diurnal cycle at low levels, which reflects the daytime insolation (Fig. 6.9a). As a result, the potential temperature shows a diurnal cycle of around 15 K with its minimum at around 6-9 UTC and its maximum from 17 to 19 UTC. After sunrise insolation starts warming the low levels and the surface (Fig. 6.9f). This leads to a strong sensible heat flux resulting in strong turbulent mixing which grows in the vertical during the day (Fig. 6.9b). The temperature tendency due to turbulent mixing reaches values of more than 1.5 K/h and is mainly responsible for the net warming in the low levels at daytime. Turbulent cooling (-0.5 K/h) at nighttime is limited to a shallow layer near the surface. Thus the daytime warming dominates the mean profile of MTD (Fig. 6.2a). However, the net potential temperature tendency shows moderate cooling in the low levels at nighttime (-1.5 to -1.0 K/h, Fig. 6.9a), which balances the daytime warming resulting in a near-zero sum of tendencies in temporal average (Fig. 6.2a). This cooling is mainly due to horizontal advection, but also due to radiation and near the ground due to MTD. The temperature tendency due to HADV is negative below 900 hPa during the whole period, but maximised during the early evening and in the morning at around 6 UTC (Fig. 6.9c). The second maximum correlates with the highest wind speed (Fig. 6.10f). In mid and high levels HADV does not show a diurnal cycle. Also, the weak warming due to MTD just below the top of the Saharan PBL is evident during the whole period. So the pattern of warming due to MTD and cooling due to HADV at around 525 hPa does not show a diurnal cycle. The tendendcies due to moist convection are close to zero in the SHL region (Figs. 6.9e and 6.10e). Vertical advection only indicates a diurnal cycle in a layer from 900 to 700 hPa (Fig. 6.9d). Here a cooling tendency appears in the late morning, which may indicate ascent due to insolation. The corresponding time-height plots of temperature tendencies from Peyrillé and Lafore (2007) show similar structures (Fig. 16 from Peyrillé and Lafore (2007)).

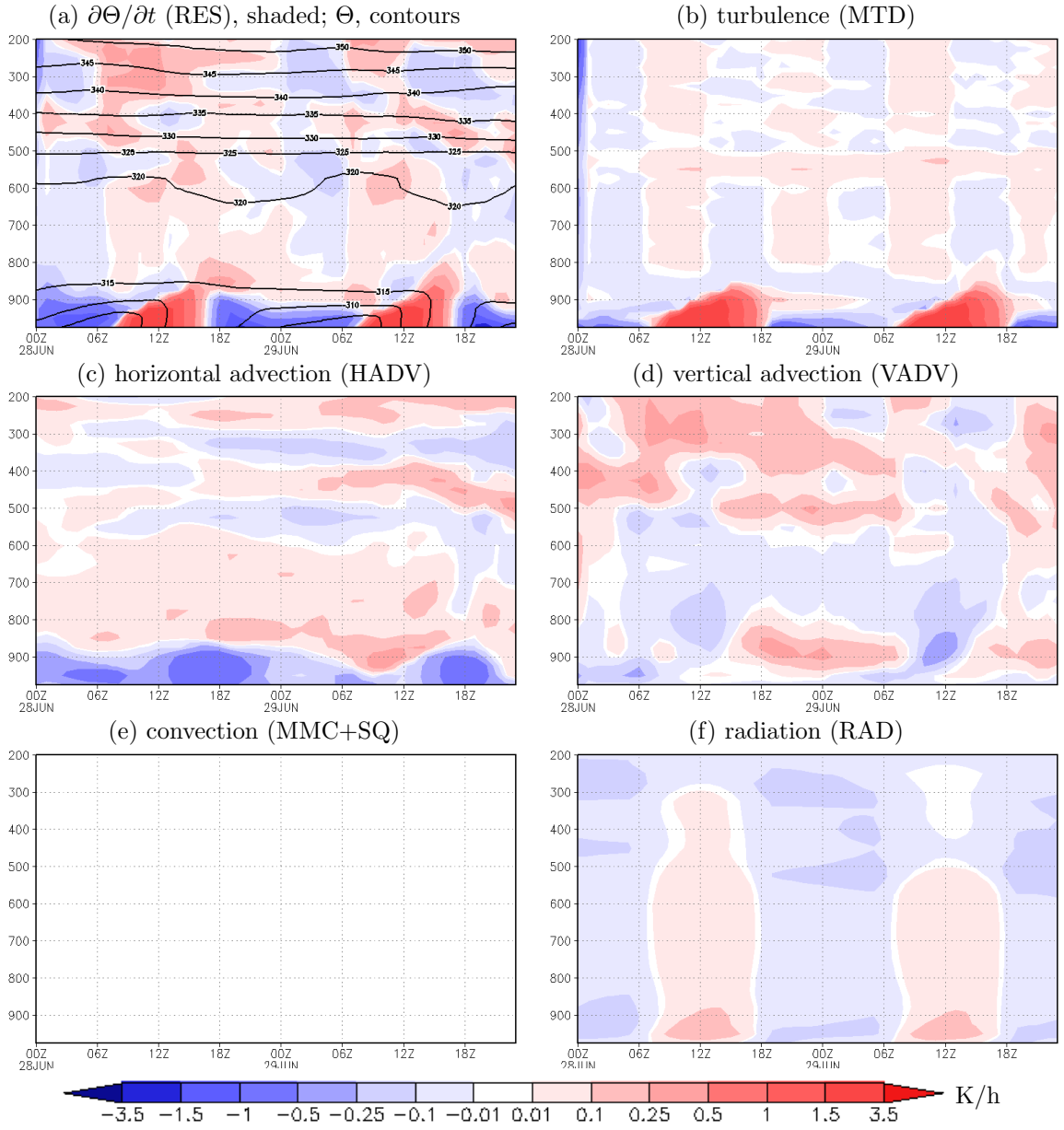

Figure 6.9: time-height plots of areal averaged potential temperature tendencies [K/h] (a)-(f) and potential temperature [K] (a) in **SHL-box** from 00 UTC 28/06/2007 to 00 UTC 30/06/2007.

The tendencies of specific humidity show a pattern as described for potential temperature tendencies. The maximum in specific humidity appears in the low levels in the morning (more than 6 g/kg from 6-9 UTC), the minimum in the early evening. (Fig. 6.10a). The maximum results from a strong moistening due to horizontal advection (>0.15 g/kg/h) in the morning (Fig. 6.10c) correlating with the strongest low-level flow (Fig. 6.10f). The low-level wind in the Saharan heat low region is consistent with theoretical studies such as Racz and Smith (1999) (cp. section 1.3.1). The highest wind speed occurs in the early morning (3-6 UTC) several hours delayed after the pressure minimum and highest low-level temperatures (17-19 UTC). After sunrise the humidity tendency due to MTD shows drying which grows into higher levels (Fig. 6.10b). However, humidity seems to

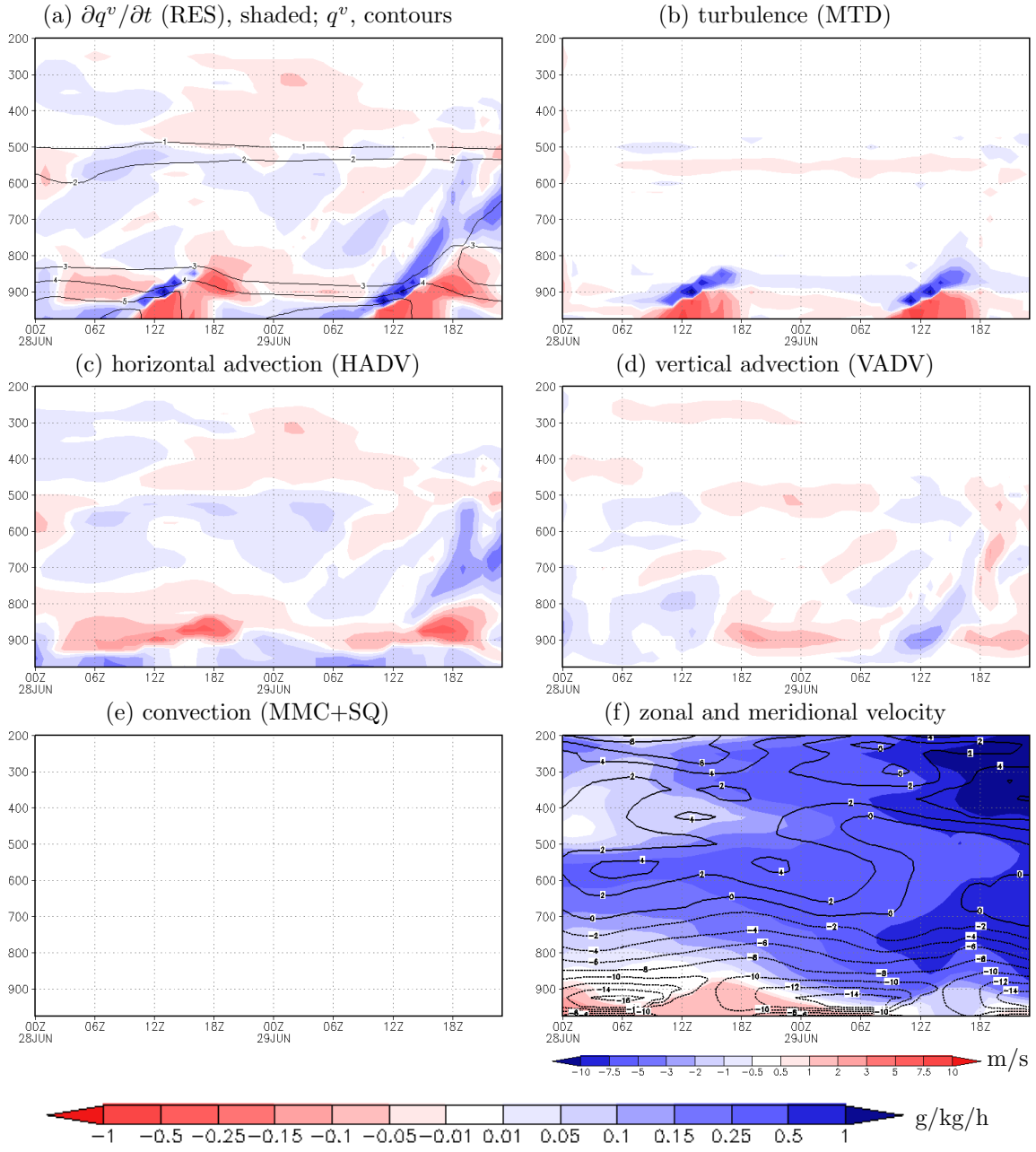

Figure 6.10: time-height plots of areal averaged specific humidity tendencies [g/kg/h] (a)-(e), specific humidity [g/kg] (a), and zonal (shaded) and meridional (contour) wind components [m/s] (f) in the **SHL-box** from 00 UTC 28/06/2007 to 00 UTC 30/06/2007.

be transported into higher levels by turbulent mixing just above the drying tendency as strong moistening is evident in a shallow layer above the drying due to MTD. This dipole of low-level drying and moistening just aloft was reflected in the mean profile (Fig. 6.2a) and is consistent with Fig. 18 in Peyrillé and Lafore (2007). The corresponding dipole of low-level moistening and drying due to HADV hardly shows a diurnal cycle (Fig. 6.10c). At the top of the Saharan PBL at 550 hPa the pattern of moistening due to HADV and drying due to MTD seems to be almost constant during the whole period. Vertical advection shows a diurnal cycle in the layer from 900 to 700 hPa (Fig. 6.10d). Moderate

moistening characterises the hours from 6 to 15 UTC (up to 0.05 g/kg/h). These patterns, in particular the dipole of drying in the low-levels and moistening just above due to MTD, are consistent with the tendencies of Peyrillé and Lafore (2007).

6.2.2 Monsoon region

The time-height plots of tendency terms in the M-box (Figs. 6.11 and 6.12) indicate perturbations due to a mid-level cloud in a layer from 650 to 450 hPa on 28 June. That is why we neglected the first 9 hours in the time averaged profiles in Fig. 6.5. In the monsoon region the sum of tendencies of potential temperature shows a diurnal cycle in almost all layers (Fig. 6.11a). The amplitude of potential temperature in the low levels is around 10 K. The effect of turbulent mixing is similar to that in the Saharan heat low region

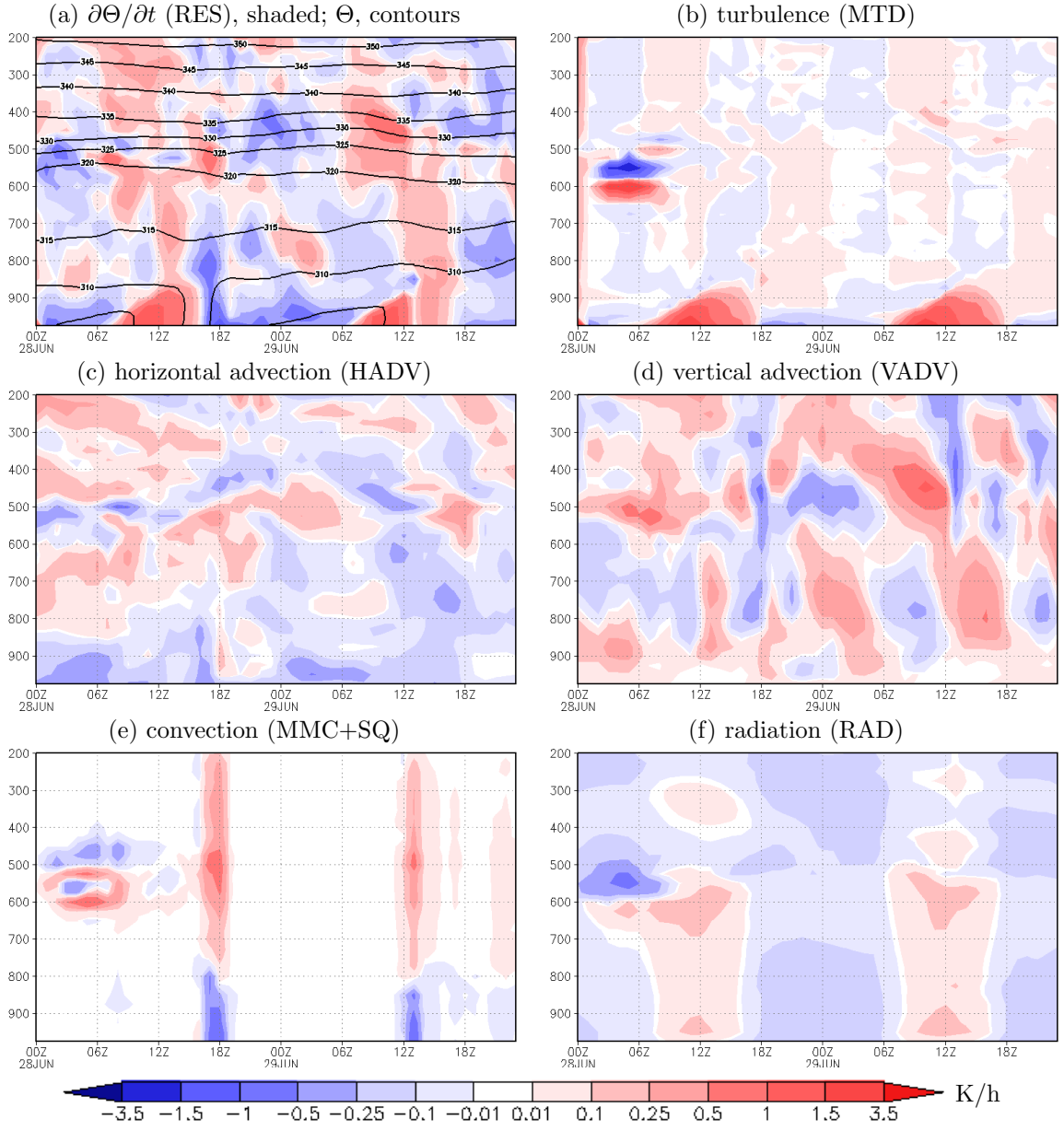

Figure 6.11: as Fig. 6.9 but for the **M-box**.

(Fig. 6.11b). In contrast, temperature tendencies due to HADV, VADV, and convection differ strongly from the SHL-box. The absolute value of low-level cooling due to HADV is smaller but the layer of cooling is thicker (Fig. 6.11c). Maximum cooling occurs with the strongest south-westerly monsoon flow in the early morning (Fig. 6.12f). Figure 6.12f also indicates a strong African easterly jet from 700 to 400 hPa. In the mid-troposphere HADV shows cooling in a layer from 900 to 700 hPa in the afternoon. Despite this there is no distinct diurnal cycle observable. Moist convection is evident by a typical pattern in the temperature tendency (Fig. 6.11e). Below 800 hPa convection causes a cooling of more than -0.5 K/h. From 800 to 200 hPa a warming of up to 0.5 K/h indicates latent heat release due to condensation. Moist convection occurs at 18 UTC on 28 June and at 13 UTC

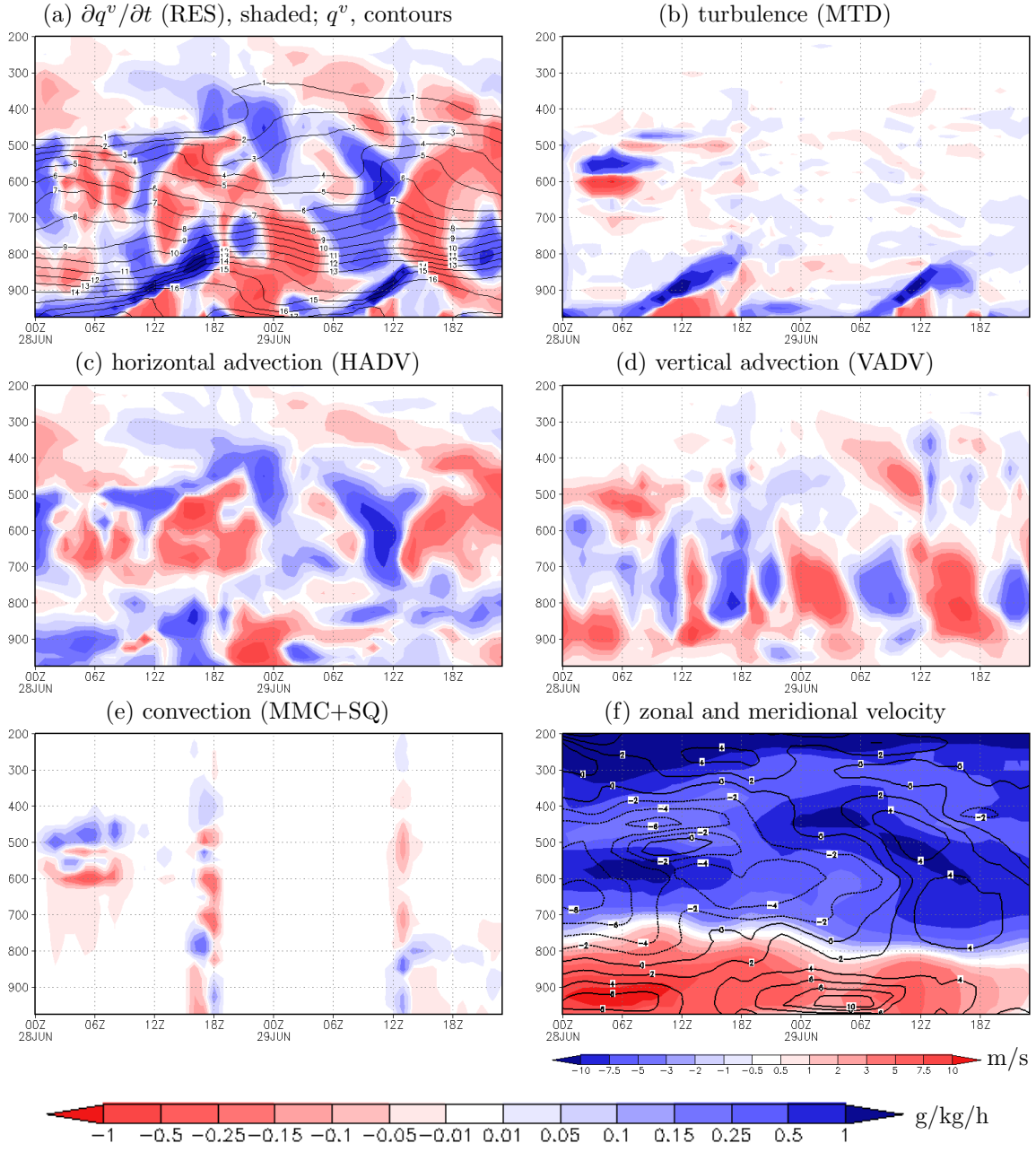

Figure 6.12: as Fig. 6.10 but for the **M-box**.

on 29 June. The convection also seems to be reflected in the temperature tendency due to vertical advection (Fig. 6.11d). At the time when convection occurs VADV shows warming in the low and cooling in the mid and high levels. The latter is consistent with the updraft in a convective cloud. Peyrillé and Lafore (2007) suggest a slightly different structure of the convective temperature tendency (Fig. 13(c) from Peyrillé and Lafore (2007)). Here warming in low levels due to convection is evident from the early morning on. A layer of cooling in the afternoon is shallower. Convection does not seem to be sharply limited to few hours in the afternoon as in our data. However, the other temperature tendencies show rather similar structures.

It is difficult to recognise a diurnal cycle in the sum of tendencies of specific humidity in the monsoon region (Fig. 6.12a). The most striking diurnal cycle is evident in MTD. Here a similar structure to Peyrillé and Lafore (2007) during the day, drying near the ground with moistening just above growing into the vertical, is evident (Fig. 6.12b). However, the drying is less and the moistening above much more pronounced. This is consistent with Peyrillé and Lafore (2007). Furthermore, diurnal cycles in HADV seem to influence the sum of tendencies as well (Fig. 6.12c). A strong low-level moistening is evident in the early morning when the monsoon flow is strongest. This pattern of moistening due to HADV in the night and mixing up in the vertical due to MTD reflects the mechanism proposed by Parker et al. (2005). In a layer from 700 to 500 hPa there is a strong drying due to HADV in the afternoon and first half of the night. Both structures are consistent with Fig. 15(d) from Peyrillé and Lafore (2007). The tendency due to moist convection rather indicates moistening below 800 hPa and drying above (Fig. 6.12e). The humidity tendencies due to vertical advection do not show a distinct diurnal cycle (Fig. 6.12d).

6.2.3 Atlantic Inflow box

The diurnal cycle of the Atlantic Inflow is clearly evident in time-height plots of the tendency terms averaged over the AI-box (Figs. 6.13 and Fig. 6.14). The sum of potential temperature tendencies shows a strong diurnal cycle (Fig. 6.13a). Daytime warming of more than 1.5 K/h is linked to MTD and radiation (Fig. 6.13b) as described for the SHL- and M-box. However, the Atlantic Inflow causes a strong cooling of more than -1.5 K/h due to HADV after 18 UTC each day (Fig. 6.13c). This strong diurnal cycle is reflected in the low-level potential temperature which ranges from 300 K in the morning (6 UTC) to more than 310 K in the afternoon. In the mid levels the Atlantic Inflow is also evident by temperature tendencies of HADV and VADV. Between 18 and 23 UTC there is a cooling due to HADV in a layer from 900 to 700 hPa (600 hPa on 28 June) and a more shallow layer of warming above. VADV indicates cooling below 900 hPa and warming up to 600 hPa followed by a shallow layer with cooling tendency above (Fig. 6.13d) (the latter does not appear before 23 UTC on 29 June). Moist convection does not play a role in the AI-box (Fig. 6.13e). The structure in the tendencies of HADV and MTD at the top of the Saharan PBL (500 hPa) is similar to that observed in the SHL-box. The time-height plots also support the mechanism proposed for the frontal propagation: the coastal front, indicated by strong cooling due to horizontal advection in the low levels, does not pass the AI-box before the strong warming due to turbulence decayed in the evening.

Horizontal advection in the moisture budget also shows the influence of the Atlantic

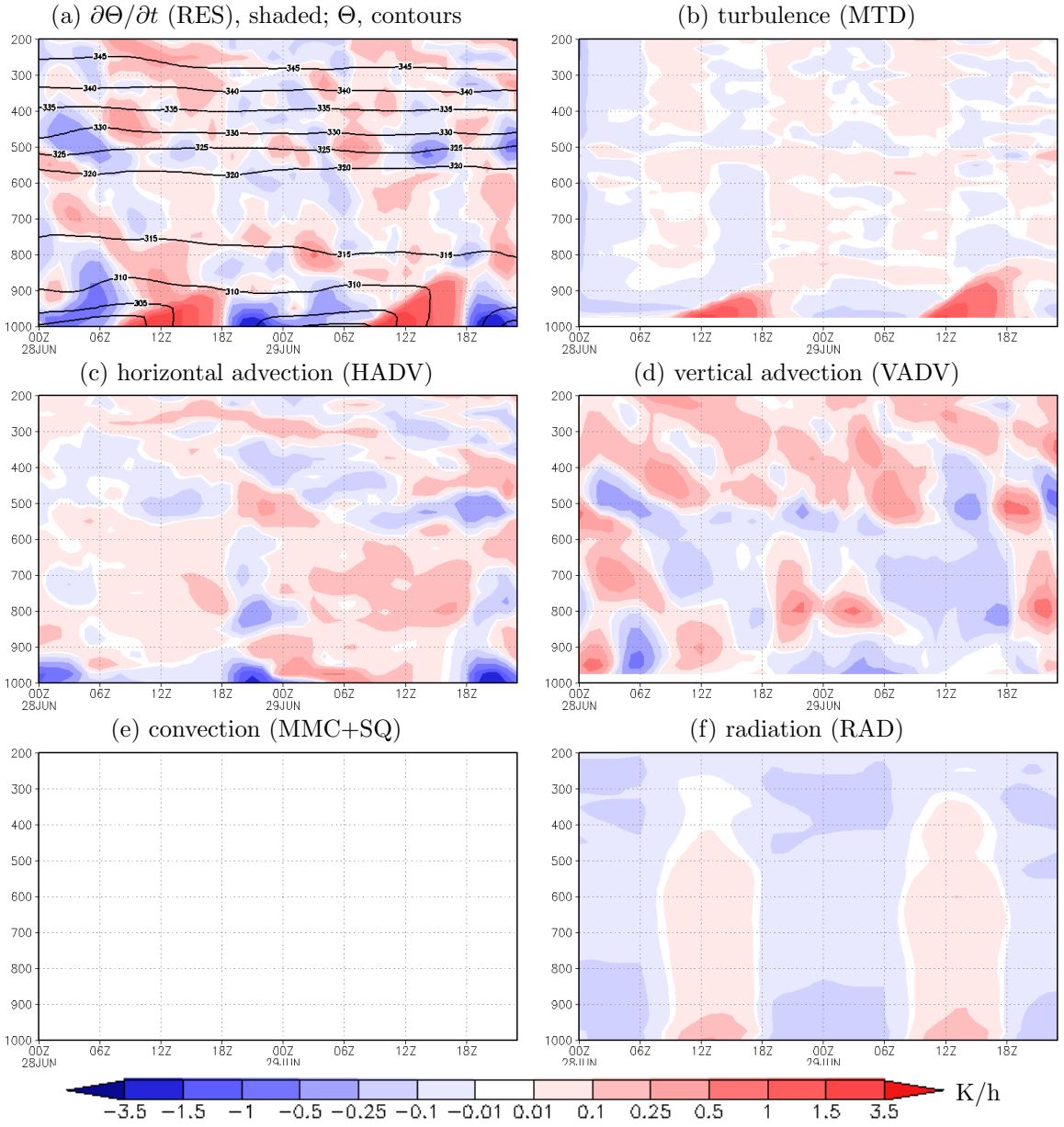

Figure 6.13: as Fig. 6.9 but for the **AI-box**.

Inflow. A strong moistening tendency due to HADV of more than 0.5 g/kg/h is evident in a layer from 1000 hPa to 800 hPa after 18 UTC on both days (Fig. 6.14c). The humidity tendency due to VADV also reflects the passage of the coastal front indicated by a low-level moistening after 18 UTC and a mid-level drying after 20 UTC (Fig. 6.14d). However, the Atlantic Inflow must not always be linked to a moistening, as explained in section 5.4. The turbulent humidity tendency shows the mixed Saharan heat low and monsoon character of the Atlantic Inflow (Fig. 6.14b): the moistening above the near-surface drying due to MTD at daytime is less pronounced than in the monsoon region but more than in the Saharan heat low region. Thus, turbulent mixing seems to be an important process for mixing up humidity from lowest levels to higher levels.

The wind components in the AI-box also indicate the Atlantic Inflow. After 18 UTC the zonal wind increases to more than 7.5 m/s indicating a strong component from the

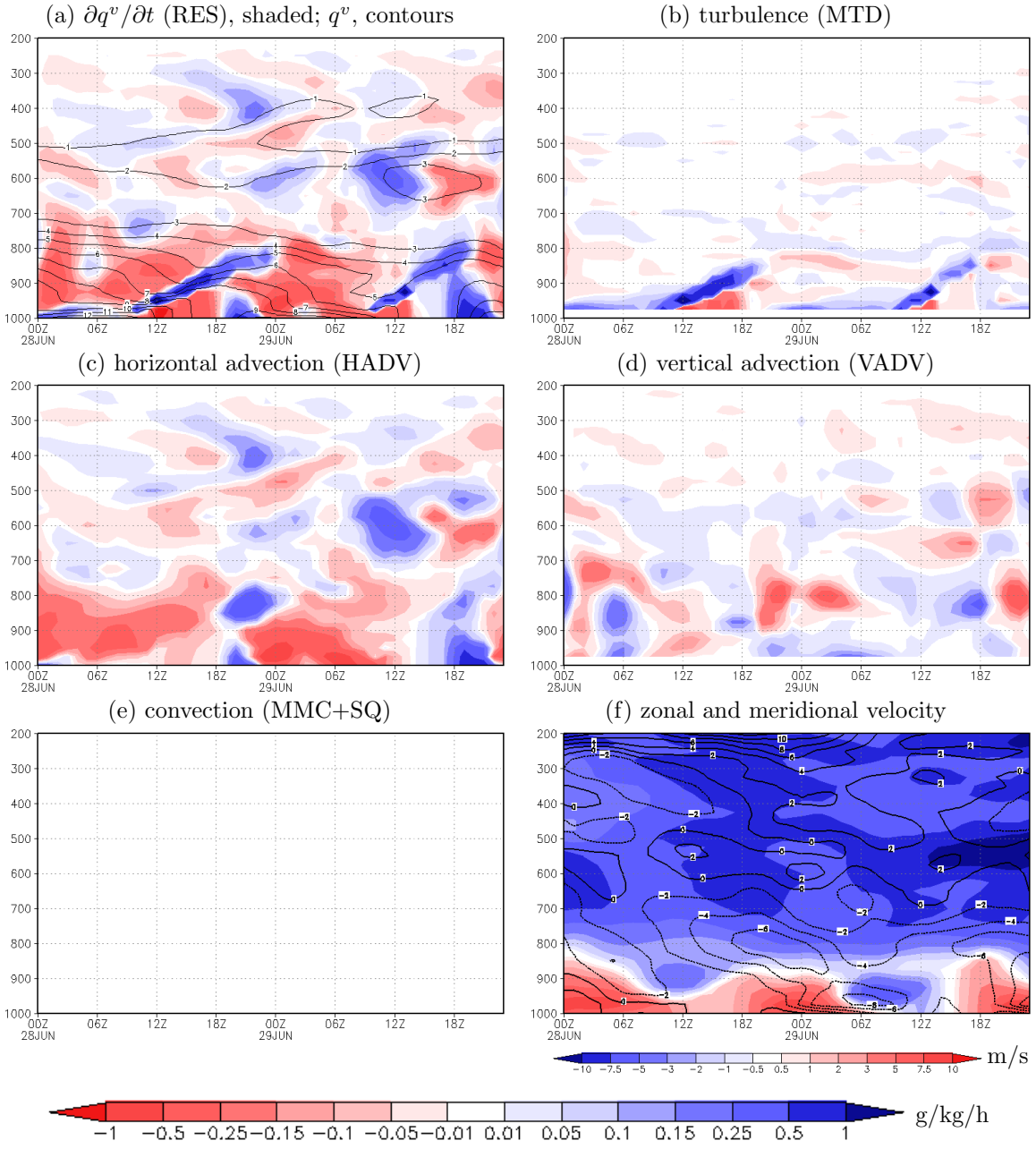

Figure 6.14: as Fig. 6.10 but for the **AI-box**.

west (Fig. 6.14f). In the morning strong north-easterly flow seems to indicate the enforced heat low circulation.

6.3 Effect of the Atlantic Inflow on the heat and moisture budgets

The analysis of heat and moisture budgets in a SHL-, M-, and AI-box showed that the budgets in the Atlantic Inflow region have characteristics of both the Saharan heat low and the monsoon region. While the temperature budget is rather comparable to that in the heat low region, the moisture budget has characteristics of that in the monsoon region. The lack of moist convection in the Atlantic Inflow region indicates the predominant heat low character of this region.

This becomes obvious when comparing the time averaged profiles of the tendency terms in Figs. 6.2a and 6.7a. Cooling due to horizontal advection is balanced by warming due to turbulence in the low level of both Saharan heat low and Atlantic Inflow region. Also the perturbation at the top of the Saharan PBL is evident in both. In the time-height plots of the tendency terms the similarities in the turbulence term are striking, although turbulence reaches higher values in the SHL-box. The time-height plots of horizontal and vertical advection would also strongly be similar in mid and high levels if one neglected the passage of the coastal front (cp. Figs. 6.9 and 6.13).

The monsoon character is mainly indicated in the humidity budget. In the Atlantic Inflow region a moister layer is present than in the Saharan heat low region. Furthermore, the Atlantic Inflow often advects moist humid air into the low levels of western Mauritania. Thus there is more humidity available which daytime turbulence can mix up into higher levels. As a result the humidity tendencies due to turbulence in the M- and AI-box are similar (cf. Figs. 6.12b and 6.14b, Figs. 6.5b and 6.7b). In this regard the Atlantic Inflow could be considered as a weak West African monsoon front. However, there is no moist convection in the Atlantic Inflow region. Advective humidity tendencies in the AI-box differ from the M- and SHL-box.

The dramatic effect of the coastal front becomes obvious when the analysis is limited to a few hours in the evening. A mean net cooling of almost -1.5 K/h and a mean net moistening of 0.35 g/kg/h was observed, when the Atlantic Inflow passed the AI-box on 28 June (18-22 UTC) (Fig. 6.8).

7 Discussion

In this study the COSMO model was applied in the desert environment of the south-western Sahara. We have shown that COSMO represents the thermodynamical structure of the atmosphere in this region very well. Furthermore, we discovered a major mesoscale system: the Atlantic Inflow.

The Saharan heat low is known to play a key role in the West African monsoon system (Parker et al. 2005; Ramel et al. 2006; Sultan and Janicot 2003a,b) as well as for lifting and layering dust in the atmosphere (Marsham et al. 2007; Messager et al. 2007). Thus the correct representation of the Saharan heat low dynamics in numerical models is crucial for modelling the West African monsoon.

The GERBILS field campaign in West Africa at the end of June 2007 provided a unique opportunity to validate the COSMO model against observational data. During GERBILS we performed an operational forecast running COSMO twice-daily. The combined analysis of model data and airborne measurements showed that COSMO represents the thermodynamical structure of the Saharan PBL and of the boundary layer in adjacent regions very well. The absence of moist convection and precipitation may favour the model results.

Furthermore, aircraft profiles showed distinct fine dust layers within the Saharan PBL which the model did not resolve due to a too coarse vertical resolution and due to the lack of actual dust in the model. A good correlation between temperature, humidity, and dust concentration characterised these layers. Marsham et al. (2007) found mesoscale circulations which result from anomalies in surface albedo. These circulations affect dust uplift and the generation of dust layers.

Also during GERBILS a major dust outbreak was observed and captured by scientific flights. The dust was lifted in two steps due to very high low-level wind speed in the Saharan heat low region on 20 and 21 June. The COSMO forecast for these days shows an amazingly good correlation between the areas of maximum velocity and the generation of dust layers in SEVIRI satellite imagery. The dust plume covered an area as big as Spain and was advected westwards over the Atlantic Ocean. As COSMO modelled the high surface wind speed which produced the high dust loadings and airborne measurements are available, this event is interesting for further case studies using a model which includes dust. The "COSMO-ART" model developed at the IMK (Vogel et al. 2006; Stanelle et al. 2007; Vogel 2007) includes dust and is based on the COSMO model. However, analysing the impact of dust was beyond the scope of this thesis.

The cross section of potential temperature along the flight track at 18°N showed an interesting baroclinic zone separating the Saharan PBL from an Atlantic influenced atmosphere in the west. The good overall agreement of this feature in model and measured data gave us confidence to use COSMO for further investigations.

By analysing the temporal and spatial evolution of the baroclinic zone we discovered the Atlantic Inflow - a mesoscale system at the Mauritanian coast. The Atlantic Inflow basically is a sea-breeze transforming into a sea-breeze front and penetrating far inland

in the low levels. This results in an advection of cool, moist air and in a significant stabilisation of the low levels. The low-level inflow has characteristics of a gravity current. Three modes were defined depending on the synoptic situation which affects the impact of the Atlantic Inflow on the mid and high levels. In the standard mode the atmosphere has moderately stable stratification. In this case the Atlantic Inflow induces a gravity wave, which is evident up to 300 hPa and moves eastwards against the mean flow. Furthermore, the head of the Atlantic Inflow is marked by a distinct frontal circulation with a strong ascent in the low levels ahead of the front, a descent in the mid levels above the front, and a weaker ascent in the mid and high levels behind the front. When the Atlantic Inflow penetrated into a neutrally-stratified layer the prefrontal ascent became dominant and strong uplift was evident in the low and mid levels.

The COSMO model code was adapted to provide the individual tendency terms of the heat and humidity equation (COSMO_budget). Thus terms describing the contribution of the physical processes to the heat and moisture budget are available. This enabled us to find a physical explanation of the Atlantic Inflow. Low levels over the Atlantic Ocean and in a small band at the coast are relatively cool due to the cold Canary current at the West African coast. The differential heating of the ocean and land surface results in strong meridional temperature and density gradients between the coastal zone and the desert inland. In terms of gravity current theory, the strong density gradient is a drive for inland penetration. However, at daytime turbulence over land opposes horizontal flow and thereby inland penetration of the cool dense air layer. A front evolves at the coast. As soon as turbulence decays in the evening the coastal front starts penetrating inland. Thus the balance between horizontal advection and turbulence is the steering mechanism for the propagation of the Atlantic Inflow. The wide coastal plain in western Mauritania favours deep inland propagation. At low levels, the propagation halts 400 km inland at the foot of the Tagant Plateau, while the induced gravity wave is able to overstep the mountain range. The propagation speed of the Atlantic Inflow is in accord with the theory for gravity currents. The Atlantic Inflow is a proper system which is meridionally orientated along the Mauritanian coast. Although interaction takes place at its southern end, the Atlantic Inflow is not directly linked to the zonally orientated classical monsoon front originating from the Guinean coast. During GERBILS the Atlantic Inflow did not affect moist convection. However, we assume that the strong frontal circulation contributes to dust uplift in western Mauritania.

Although low-level winds in the coastal plain were not studied in detail, we observed a striking low-level nocturnal jet in the stably-stratified wake of the Atlantic Inflow. The maximum wind speeds occurred at 975 hPa. Here the mean wind speed gradually increased from around 5 m/s before the passage of the Atlantic Inflow to around 12 m/s in the next morning (Fig. 5.31). Furthermore the Atlantic Inflow seems to influence the nocturnal reestablishment of the baroclinic zone. A nocturnal increase of the low-level wind speed was also pronounced at the baroclinic zone as well as in the area of the small heat low vortices on 29 June 2007 (Fig. 5.32).

Finally, the impact of the Atlantic Inflow on the regional heat and moisture budgets was analysed using spatially and time averaged profiles of the tendency terms in a Saharan heat low box, a monsoon box, and an Atlantic Inflow box. The profiles showed a striking cooling due to horizontal advection when the Atlantic Inflow occurred. The proposed balance between horizontal advection and turbulence as driving mechanism for

the Atlantic Inflow was confirmed.

Although this study was limited to the GERBILS period the Atlantic Inflow is evident in other datasets and at other dates as well. The phenomenon was observed in the coarser ECMWF input data. Furthermore, the Atlantic Inflow at the Mauritanian coast was also detected in the data of Juliane Schwendike (IMK), who is studying the genesis of Hurricane "Helene" in September 2006. The Atlantic Inflow has similarities to other heat low driven sea-breezes e.g. in Spain or Australia (Kottmeier et al. 2000; Reeder and Smith 1999; Racz and Smith 1999; Spengler et al. 2005; Noonan and Smith 1986). However, to our knowledge this is the first detailed analysis of such a phenomenon at the West African coast. We presented a set of tools how to detect the Atlantic Inflow. In addition to the dust studies proposed earlier, future investigations could involve the detection of the Atlantic Inflow in observational data from surface station as well as from radio soundings. Unfortunately we could not find a suitable dataset from the operational meteorological network. Also, the role of the Atlantic Inflow for dust uplift in western Mauritania needs further investigation. This should involve a detailed study of low-level winds and especially emphasise the evolution of a nocturnal jet in the Atlantic Inflow region. For both aspects simulations with a model including dust and with higher spatial resolution would be suited.

Appendix

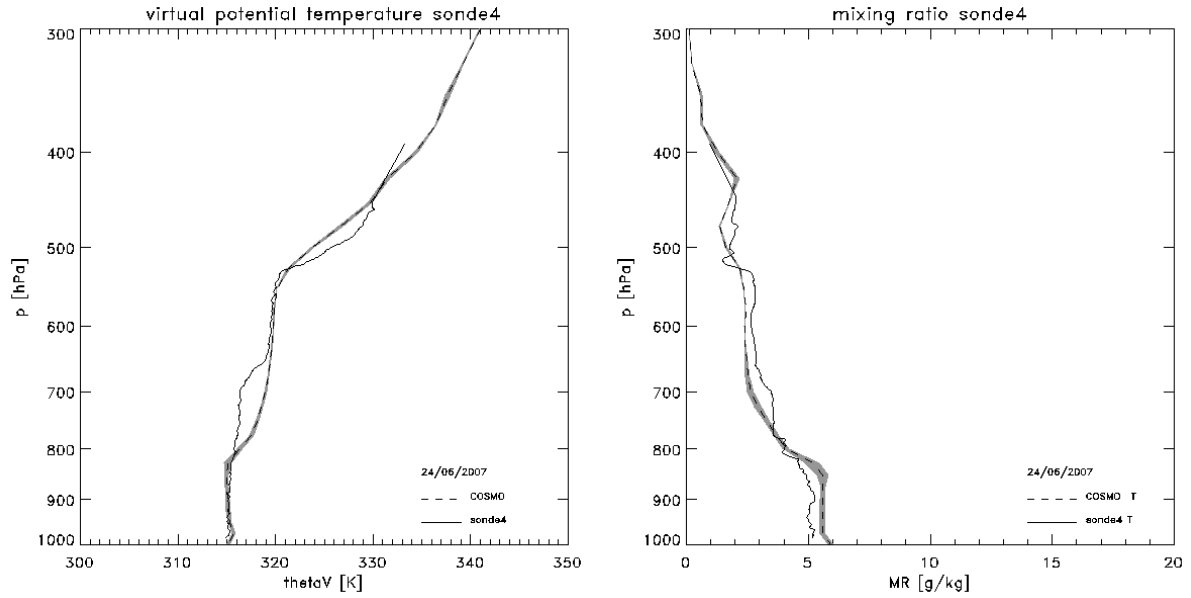

Figure A.1: potential temperature and humidity mixing ratio from **sonde 4** (8.2°W, 15.8°N, 12:39 UTC) (solid) and COSMO model data at (8.2500°W, 18.0000°N, 24/06/2007 00 UTC+13h) (dashed), grey shaded: standard deviation of model data on constant model level in a 0.5°x0.5° square centred around the closest grid point. The parachute of the dropsonde failed. Thus vertical resolution is lower and data has to be interpreted with reservation.

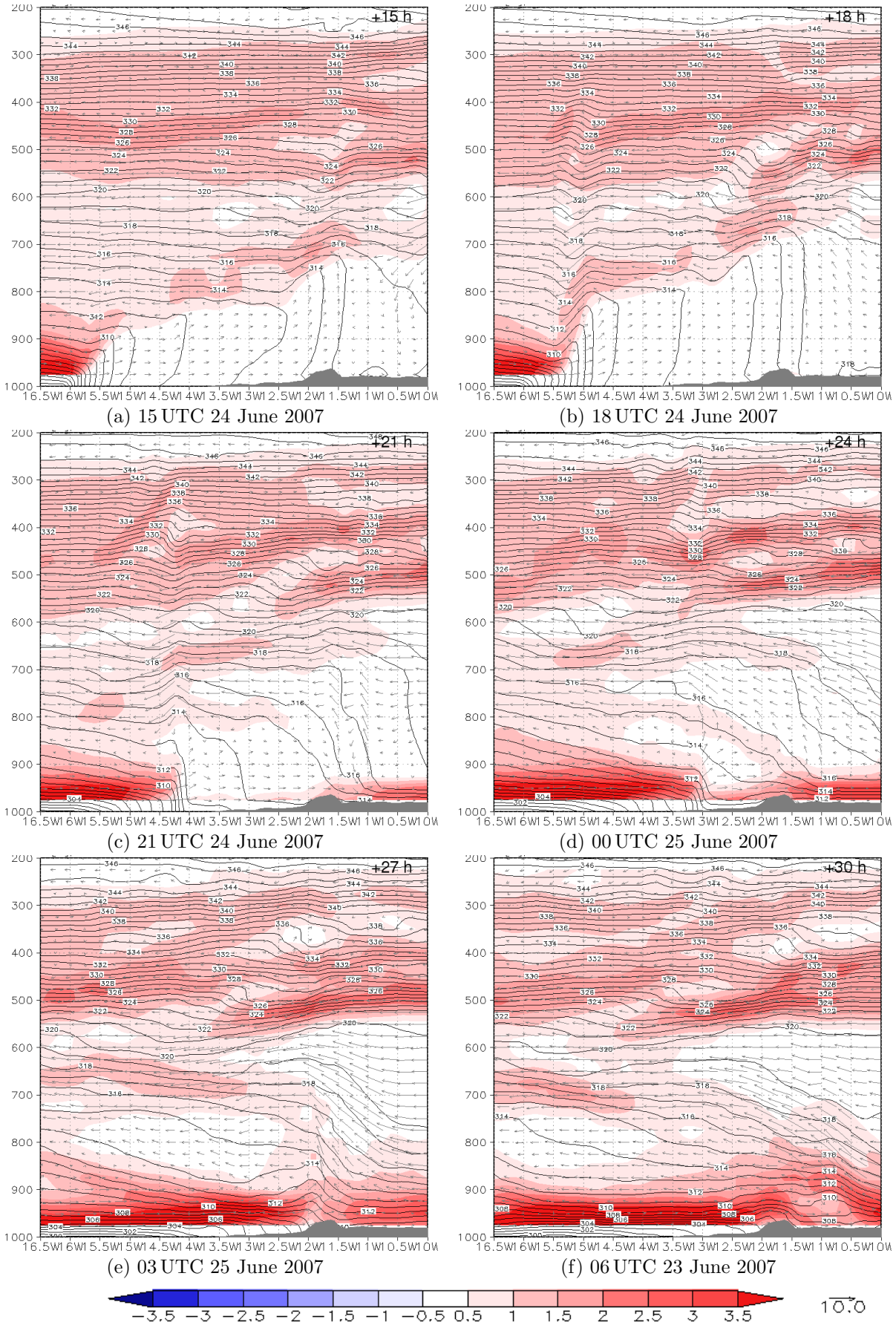

(a) 15 UTC 24 June 2007 (b) 18 UTC 24 June 2007

(c) 21 UTC 24 June 2007 (d) 00 UTC 25 June 2007

(e) 03 UTC 25 June 2007 (f) 06 UTC 23 June 2007

Figure A.2: square of Brunt-Väisälä-frequency $[10^{-4}s^{-2}]$ (shaded), virtual potential temperature [K] (1 K contour interval), wind vector in plane of section (grey). Orography grey shaded. 3-hourly, starting at 15 UTC 24/06/2007.

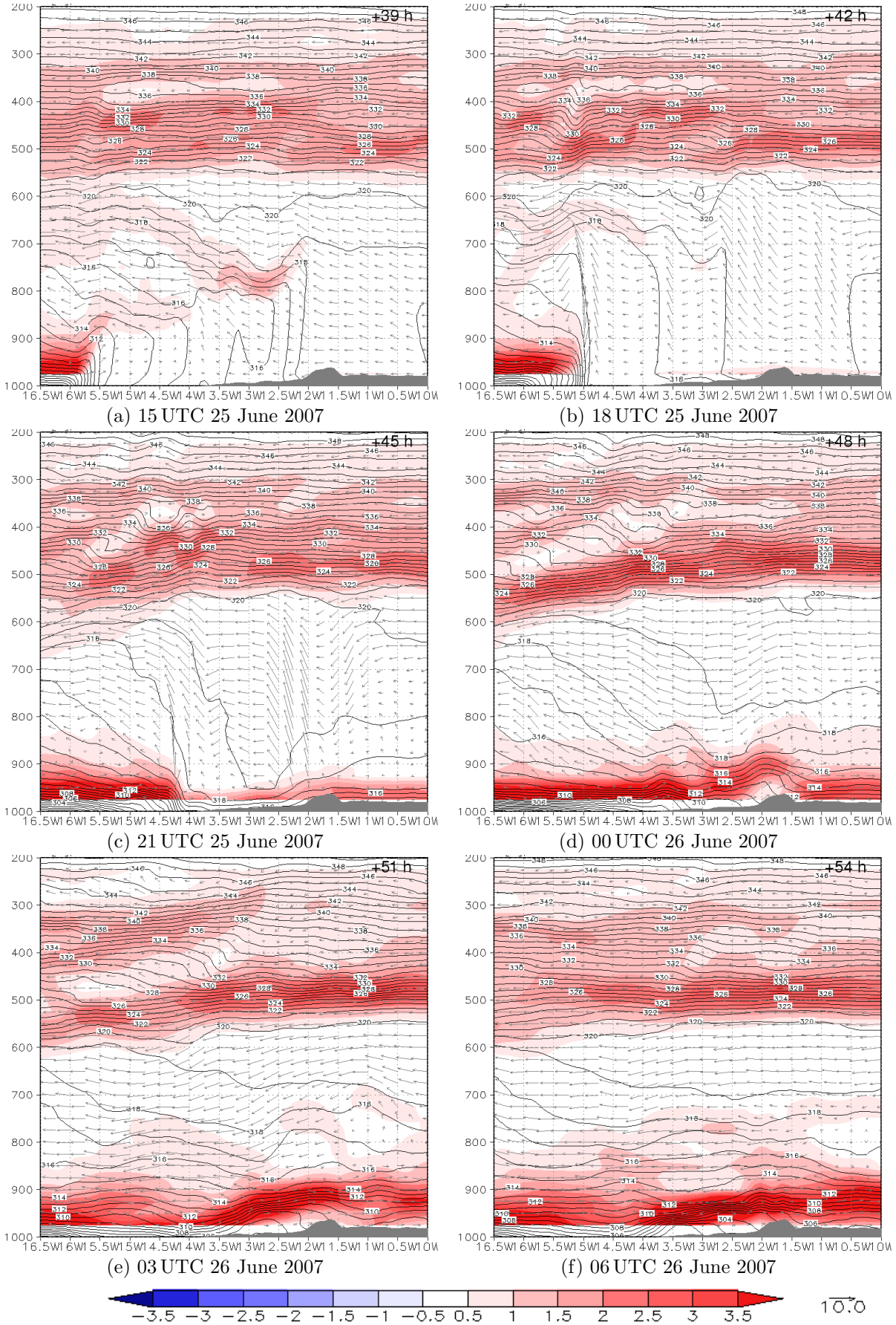

(a) 15 UTC 25 June 2007

(b) 18 UTC 25 June 2007

(c) 21 UTC 25 June 2007

(d) 00 UTC 26 June 2007

(e) 03 UTC 26 June 2007

(f) 06 UTC 26 June 2007

Figure A.3: as Fig. A.2 but starting at 15 UTC 25/06/2007.

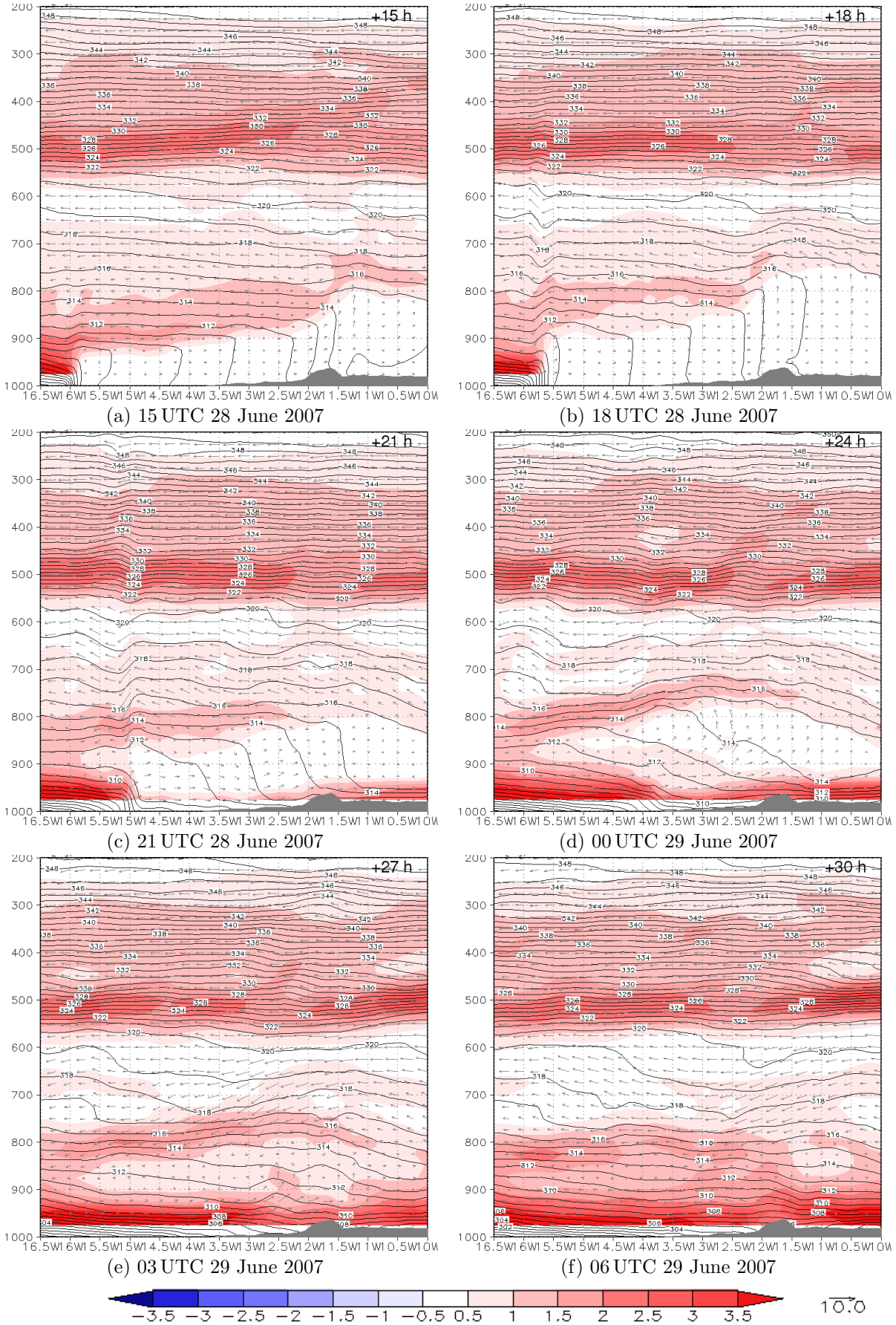

(a) 15 UTC 28 June 2007

(b) 18 UTC 28 June 2007

(c) 21 UTC 28 June 2007

(d) 00 UTC 29 June 2007

(e) 03 UTC 29 June 2007

(f) 06 UTC 29 June 2007

Figure A.4: as Fig. A.2 but starting at 15 UTC 28/06/2007.

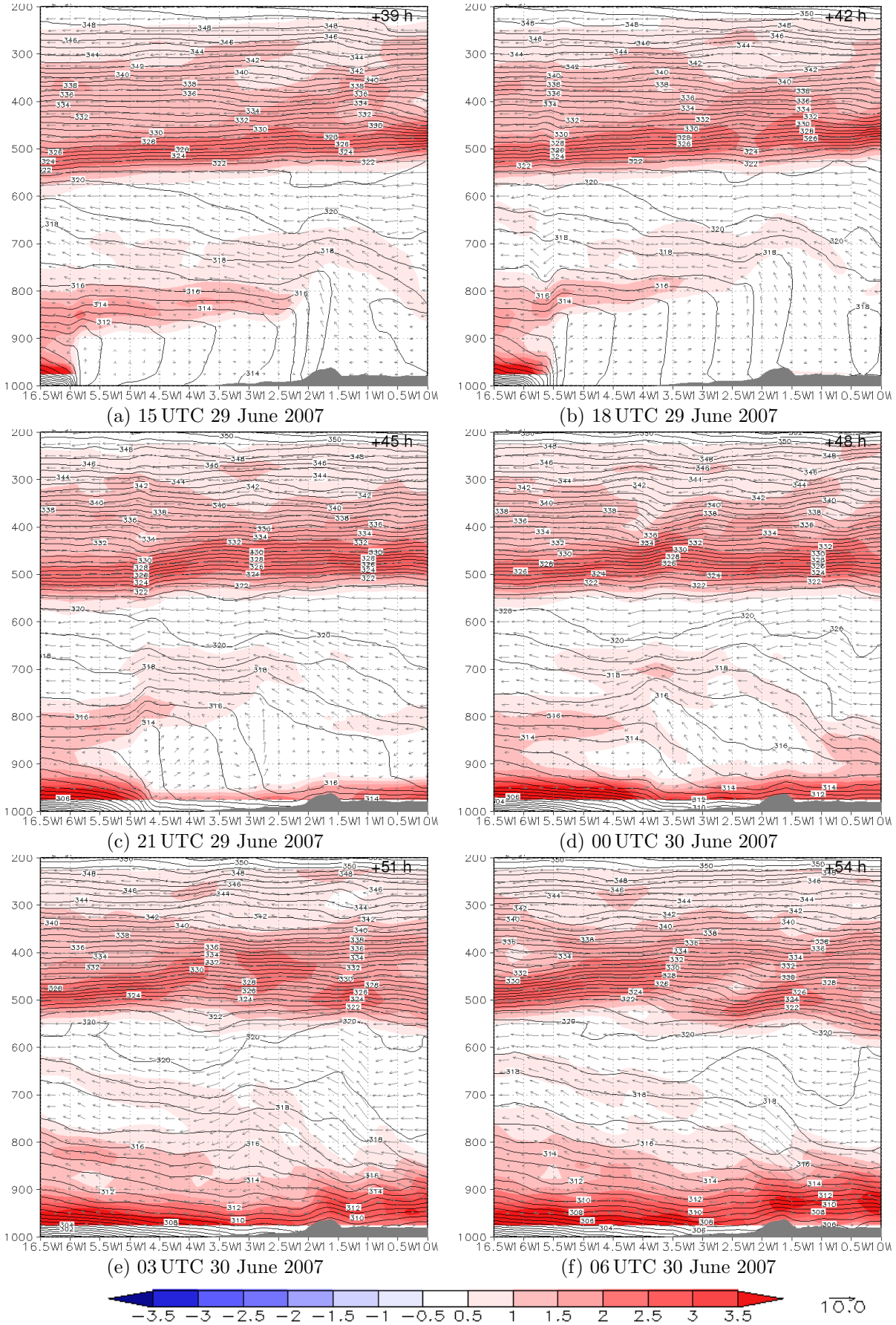

(a) 15 UTC 29 June 2007

(b) 18 UTC 29 June 2007

(c) 21 UTC 29 June 2007

(d) 00 UTC 30 June 2007

(e) 03 UTC 30 June 2007

(f) 06 UTC 30 June 2007

Figure A.5: as Fig. A.2 but starting at 15 UTC 29/06/2007.

Bibliography

Beheng, K. D., 2006. Skript zu Dynamik II. unveröffentlichtes Skript zur Vorlesung Dynamik II, SS 06, Universität Karlsruhe (TH).

Bou Karam, D., C. Flamant, P. Knippertz, O. Reitebusch, J. Pelon, M. Chong and A. Dabas, 2008. Dust emissions over the Sahel associated with the West African Monsoon inter-tropical discontinuity region: a representative case study. *unpublished draft for Quarterly Journal of the Royal Meteorological Society*.

Cadet, D. L. and N. O. Nnoli, 1987, Apr.. Water vapour transport over Africa and the Atlantic Ocean during summer 1979. *Quarterly Journal of the Royal Meteorological Society 113*, 581–602.

Charney, J. G. and M. E. Stern, 1962, Mar.. On the Stability of Internal Baroclinic Jets in a Rotating Atmosphere. *Journal of Atmospheric Sciences 19*, 159–172.

Clarke, R. H., 1955. Some observations and comments on the sea breeze. *Aust. Meteor. Mag.*.

Davies, H. C., 1976, Apr.. A lateral boundary formulation for multi-level prediction models. *Quarterly Journal of the Royal Meteorological Society 102*, 405–418.

Davies, H. C., 1983. Limitations of some common lateral boundary schemes used in regional NWP. *Monthly Weather Review 111*, 1002–1012.

Doms, G. and U. Schättler, 2002, Nov.. A description of the nonhydrostatic Regional Model LM. Part I: Dynamics and Numerics. download at http://www.cosmo-model.org.

Duvel, J. P., 1990. Convection over tropical africa and the atlantic ocean during northern summer. part ii: Modulation by easterly waves. *Monthly Weather Review 118*, 1855–1868.

FAAM, 2007. FAAM, UK Meteorological Office, Natural Environment Research Council, [Wells, B.;Perry, A.; Ball, S.]. Facility for Airborne Atmospheric Measurements (FAAM), [Internet]. British Atmospheric Data Centre, 2004-2008. Available from http://badc.nerc.ac.uk/data/faam/.

Fink, A. H., 2006. The West African monsoon system. *promet 32*(3/4).

Flamant, C., J.-P. Chaboureau, D. J. Parker, C. M. Taylor, J.-P. Cammas, O. Bock, F. Timouk and J. Pelon, 2007, Jul.. Airborne observations of the impact of a convective system on the planetary boundary layer thermodynamics and aerosol distribution in the inter-tropical discontinuity region of the West African Monsoon. *Quarterly Journal of the Royal Meteorological Society 133*, 1175–1189.

Gamo, M., 1996, May. Thickness of the dry convection and large-scale subsidence above deserts. *Boundary-Layer Meteorology 79*, 265–278.

Gill, A. E., 1982. *Atmosphere-Ocean Dynamics*, volume 30 of *International Geophysics Series*. Academic Press, London.

Grams, C. M., 2007, Aug.. Im Tiefflug über die Sahara - Rechenzentrum ermöglicht Wettervorhersage für Forschungsexperiment. *RZ-news Universität Karlsruhe (TH) 3*.

Haase, S. and R. Smith, 1989, Jun.. The numerical simulation of atmospheric gravity currents. Part II. Environments with stable layers. *Geophysical and Astrophysical Fluid Dynamics 46*, 35–51.

Hagos, S. M. and K. H. Cook, 2007, Mar.. Dynamics of the West African Monsoon Jump. *Journal of Climate 20*, 5264–5284.

Haywood, J., J. Taylor, S. Milton, O. Boucher, M. Boucher, M. Harrison, T. Slingo, R. Allan, E. Highwood, H. Brindley, D. J. Parker, R. Washington, M. Todd, A. Tompkins, P. Formenti and C. Flament, 2007, Mar.. GERBILS (GERB Intercomparison of Longwave and Shortwave radiation. *unpublished draft*.

Haywood, J. M., R. P. Allan, I. Culverwell, T. Slingo, S. Milton, J. Edwards and N. Clerbaux, 2005, Mar.. Can desert dust explain the outgoing longwave radiation anomaly over the Sahara during July 2003? *Journal of Geophysical Research (Atmospheres) 110*(D9), 5105–+.

Haywood, J. M., G. Greed, S. Milton, A. Keil, C. Sundar, P. Gupta and E. Highwood, 2007, Mar.. Aerosol optical thickness over North Africa. Part 2: modelling and model validation. *unpublished draft*.

Heinold, B., J. Helmert, O. Hellmuth, R. Wolke, A. Ansmann, B. Marticorena, B. Laurent and I. Tegen, 2007, Jun.. Regional modeling of Saharan dust events using LM-MUSCAT: Model description and case studies. *Journal of Geophysical Research (Atmospheres) 112*(D11), 11204–+.

Helmert, J., B. Heinold, I. Tegen, O. Hellmuth and M. Wendisch, 2007, Jul.. On the direct and semidirect effects of Saharan dust over Europe: A modeling study. *Journal of Geophysical Research (Atmospheres) 112*(D11), 13208–+.

Holton, J. R., 2004. *An Introduction to Dynamic Meteorology Fourth Edition*, volume 88 of *International Geophysics Series*. Elsevier Academic Press, Burlington, San Diego, London.

Hoskins, B. J., M. E. McIntyre and A. W. Robertson, 1985, Oct.. On the use and significance of isentropic potential vorticity maps. *Quarterly Journal of the Royal Meteorological Society 111*, 877–946.

Houze, Robert A., J., 1993. *Cloud Dynamics*, volume 53 of *International Geophysics Series*. Academic Press, Inc., San Diego.

Kiladis, G. N., C. D. Thorncroft and N. M. J. Hall, 2006a. Three-dimensional structure and dynamics of african easterly waves. part i: Observations. *Journal of the Atmospheric Sciences 63*, 2212–2230.

Kiladis, G. N., C. D. Thorncroft and N. M. J. Hall, 2006b. Three-dimensional structure and dynamics of african easterly waves. part ii: Dynamical modes. *Journal of the Atmospheric Sciences 63*, 2231–2245.

Klemp, J. B. and R. B. Wilhelmson, 1978, Jun.. The Simulation of Three-Dimensional Convective Storm Dynamics. *Journal of Atmospheric Sciences 35*, 1070–1096.

Knippertz, P., C. Deutscher, K. Kandler, T. Müller, O. Schulz and L. Schütz, 2007, Nov.. Dust mobilization due to density currents in the Atlas region: Observations from the Saharan Mineral Dust Experiment 2006 field campaign. *Journal of Geophysical Research (Atmospheres) 112*(D11), 21109–+.

Kottmeier, C., 1982. *Die Vertikalstrukture nächtlicher Grenzschichtstrahlströme*. Dissertation, Berichte des Instituts für Meteorologie und Klimatologie der Universität Hannover.

Kottmeier, C., P. Palacio-Sese, N. Kalthoff, U. Corsmeier and F. Fiedler, 2000, Nov.. Sea breezes and coastal jets in southeastern Spain. *International Journal of Climatology 20*, 1791–1808.

Linden, P. F. and J. E. Simpson, 1986. Gravity-driven flows in a turbulent fluid. *Journal of Fluid Mechanics 172*, 481–497.

Long, M., D. Entekhabi and S. E. Nicholson, 2000, Nov.. Interannual Variability in Rainfall, Water Vapor Flux, and Vertical Motion over West Africa. *Journal of Climate 13*, 3827–3841.

Marsham, J. H., D. J. Parker, C. M. Grams and B. Johnson, 2007, Nov.. Observations of mesoscale and boundary-layer circulations affectin dust uplift and transport in the Saharan boundary layer. *draft for Atmospheric Chemistry and Physics*. submitted to ACP on 7 November 2007.

Marsham, J. H., D. J. Parker, C. M. Grams, C. Taylor and J. M. Haywood, 2008, Jan.. Uplift of Saharan Dust at the inter-tropical discontinuity (ITD): the role of cold pools. *draft for Journal of Geophysical Research*. submitted to JGR on 21 January 2008.

Mellor, G. L. and T. Yamada, 1974. A hierarchy of turbulence closure models for planetary boundary layers. *Journal of Atmospheric Sciences 31*, 1791–1806.

Messager, C. J., D. J. Parker, O. Reitebuch, A. Agusti-Panareda and C. M. Taylor, 2007. Structure and dynamics of the saharan heat low during the west african monsoon 2006 onset: Observations and analyses. *unpublished draft*.

Noonan, J. A. and R. K. Smith, 1986, Aug.. Sea-Breeze Circulations over Cape York Peninsula and the Generation of Gulf of Carpentaria Cloud Line Disturbances. *Journal of Atmospheric Sciences 43*, 1679–1693.

Parker, D., R. Burton, A. Diongue-Niang, R. Ellis, M. Felton, C. Taylor, T. C.D., P. Bessemoulin and A. Tompkins, 2005. The diurnal cycle of the west african monsoon circulation. *Quarterly Journal of the Royal Meteorological Society 131*, 2839–2860.

Parker, D. J., C. D. Thorncroft, R. R. Burton and A. Diongue-Niang, 2005. Analysis of the african easterly jet, using aircraft observations from the jet2000 experiment. *Quarterly Journal of the Royal Meteorological Society 131*, 1461–1482.

Peyrillé, P. and J.-P. Lafore, 2007, Aug.. An Idealized Two-Dimensional Framework to Study the West African Monsoon. Part II: Large-Scale Advection and the Diurnal Cycle. *Journal of the Atmospheric Sciences 64*, 2783–2803.

Peyrillé, P., J.-P. Lafore and J.-L. Redelsperger, 2007, Aug.. An Idealized Two-Dimensional Framework to Study the West African Monsoon. Part I: Validation and Key Controlling Factors. *Journal of the Atmospheric Sciences 64*, 2765–2782.

Pytharoulis, I. and C. Thorncroft, 1999. The low-level structure of african easterly waves in 1995. *Monthly Weather Review 127*, 2266–2280.

Racz, Z. and R. K. Smith, 1999. The dynamics of heat lows. *Quaterly journal of the Royal Meteorological Society 125*, 225–252.

Ramel, R., H. Gallée and C. Messager, 2006, Mar.. On the northward shift of the West African monsoon. *Climate Dynamics 26*, 429–440.

Raymond, D. J. and R. Rotunno, 1989, Sep.. Response of a Stably Stratified Flow to Cooling. *Journal of Atmospheric Sciences 46*, 2830–2837.

Reed, R. J., D. C. Norquist and E. E. Recker, 1977. The structure and properties of african wave disturbances as observed during phase iii of gate. *Monthly Weather Review 105*, 317–333.

Reeder, M. J., R. Grimshaw, D. R. Christie and R. K. Smith, 1995, Jul.. Interacting "Morning Glories" over Northern Australia. *Bulletin of the American Meteorological Society, vol. 76, Issue 7, pp.1165-1172 76*, 1165–1172.

Reeder, M. J. and R. K. Smith, 1999. Meteorology of the Southern hemisphere. *Meteorological Monographs 27*(49), 211–223.

Reible, D. D., J. E. Simpson and P. F. Linden, 1993, Jan.. The sea breeze and gravity-current frontogenesis. *Quarterly Journal of the Royal Meteorological Society 119*, 1–16.

Ritter, B. and J. F. Geleyn, 1992, Feb.. A comprehensive radiation scheme for numerical weather prediction models with potential applications in climate simulations. *Monthly Weather Review 120*, 303–325.

Schubert, W. H., P. E. Ciesielski, D. E. Stevens and H.-C. Kuo, 1991, Jun.. Potential Vorticity Modeling of the ITCZ and the Hadley Circulation. *Journal of Atmospheric Sciences 48*, 1493–1509.

Simpson, J. E., D. A. Mansfield and J. R. Milford, 1977, Jan.. Inland penetration of sea-breeze fronts. *Quarterly Journal of the Royal Meteorological Society 103*, 47–76.

Smith, R. K., 1988. Travelling Waves and Bores in the Lower Atmosphere: The 'Morning Glory' and Related Phenomena. *Earth-Science Reviews 25*, 267–290.

Smith, R. K. and M. J. Reeder, 1988, Oct.. On the Movement and Low-Level Structure of Cold Fronts. *Monthly Weather Review 116*, 1927–1944.

Smith, R. K., M. J. Reeder, N. J. Tapper and D. R. Christie, 1995. Central Australian Cold Fronts. *Monthly Weather Review 123*, 16–38.

Spengler, T., M. J. Reeder and R. K. Smith, 2005, Oct.. The dynamics of heat lows in simple background flows. *Quarterly Journal of the Royal Meteorological Society 131*, 3147–3165.

Stanelle, T., B. Vogel, H. Vogel, D. Bäumer and C. Kottmeier, 2007. A dust outbreak over West Africa and its impact on the state of the atmosphere: A model study with LM-ART. *European Geosciences Union, Geophysical Research Abstracts 9*. http://cosis.net/abstracts/EGU2007/08594/EGU2007-J-08594.pdf.

Strahler, A. and A. Strahler, 2002. *Physical Geography: Science and Systems of the Human Environment 2e*. John Wiley & Sons, Inc., New York.

Sultan, B. and S. Janicot, 2003a, Apr.. The onset of the summer monsoon in West Africa : a role of the heat low dynamics? *EGS - AGU - EUG Joint Assembly, Abstracts from the meeting held in Nice, France, 6 - 11 April 2003, abstract #3610*, 3610–+.

Sultan, B. and S. Janicot, 2003b, Nov.. The West African Monsoon Dynamics. Part II: The „Preonset“and „Onset“of the Summer Monsoon. *Journal of Climate 16*, 3407–3427.

Sultan, B., S. Janicot and A. Diedhiou, 2003, Nov.. The West African Monsoon Dynamics. Part I: Documentation of Intraseasonal Variability. *Journal of Climate 16*, 3389–3406.

Taylor, C. M., R. J. Ellis, D. J. Parker, R. R. Burton and C. D. Thorncroft, 2003. Linking boundary-layer variability with convection: A case-study from jet2000. *Quarterly Journal of the Royal Meteorological Society 129*, 2233–2254.

Taylor, C. M., D. J. Parker, C. R. Lloyd and C. D. Thorncroft, 2005. Observations of synoptic-scale land surface variability and its coupling with the atmosphere. *Quarterly Journal of the Royal Meteorological Society 131*, 913–937.

Thorncroft, C. D., 1995, Oct.. An idealized study of African easterly waves. III: More realistic basic states. *Quarterly Journal of the Royal Meteorological Society 121*, 1589–1614.

Thorncroft, C. D. and M. Blackburn, 1999. Maintenance of the african easterly jet. *Quarterly Journal of the Royal Meteorological Society 125*, 763–786.

Thorncroft, C. D. and B. J. Hoskins, 1994a, Jul.. An idealized study of African easterly waves. I: A linear view. *Quarterly Journal of the Royal Meteorological Society 120*, 953–982.

Thorncroft, C. D. and B. J. Hoskins, 1994b, Jul.. An idealized study of African easterly waves. II: A nonlinear view. *Quarterly Journal of the Royal Meteorological Society 120*, 983–1015.

Thorncroft, C. D., D. J. Parker, R. R. Burton, M. Diop, J. H. Ayers, H. Barjat, S. Devereau, A. Diongue, R. Dumelow, D. R. Kindred, N. M. Price, M. Saloum, C. M. Tayor and A. M. Tompkins, 2003, Mar.. The jet2000 project: Aircraft observations of the african easterly jet and african easterly waves. *Bulletin of the American Meteorological Society 84*, 337–351.

Tompkins, A. M., A. Diongue-Niang, D. J. Parker and C. D. Thorncroft, 2005, Oct.. The African easterly jet in the ECMWF Integrated Forecast System: 4D-Var analysis. *Quarterly Journal of the Royal Meteorological Society 131*, 2861–2885.

Vogel, B., 2007. A new Online Coupled Regional Scale Model System to treat the Dispersion of Aerosols and Reactive Trace Gases. downloaded at http://www.imk.uni-karlsruhe.de/3613.php (24 april 2007).

Vogel, B., C. Hoose, H. Vogel and C. Kottmeier, 2006, Dec.. A model of dust transport applied to the Dead Sea Area. *Meteorologische Zeitschrift 15*(6), 611–624.

Washington, R., M. C. Todd, S. Engelstaedter, S. Mbainayel and F. Mitchell, 2006, Feb.. Dust and the low-level circulation over the Bodélé Depression, Chad: Observations from BoDEx 2005. *Journal of Geophysical Research (Atmospheres) 111*(D10), 3201–+.

Acknowledgements

I am deeply grateful to Prof. Dr. Sarah Jones and Dr. Doug Parker for the promising topic, the extensive mentoring, for the participation in GERBILS, numerous contacts, and uncounted enlightening discussions.

I thank Prof. Dr. Beheng for helpful conversations, excellent advice and the kind willingness to do the proofreading.

My thanks also apply to Prof. Dr. Kottmeier for the supply with good literature and for useful tips.

Thanks to Dr. Jim Haywood and to the entire GERBILS- and FAAM-Team for allowing me to participate in GERBILS. I also thank the Scientific Computing Center at the Univerity of Karlsruhe, particularly Prof. Dr. Heuveline and Horst Gernert for enabling the COSMO-forecasts.

I am very grateful to Dr. John Marsham for the great time in Africa and England, and for the unlimited helpfulness with topical and technical issues. Special thanks goes to Dr. Conny Schwierz for data provision. Furthermore I thank the Phds, computer administrators, and all the members of the IAS for professional and technical help, fruitful talks, and the pleasant working atmosphere. Thanks to Hui, Jenny, Sam, Sam, Ben, and Laety for the lovely home in Leeds.

Many thanks to Juliane, Leo, Bele, Tanja, Bernhard, and Heike for the support with COSMO and inspiring discussions, to Doris for the data provision and GrADS help, and to Mr. Brückel for always quick and friendly help with computer problems. Thanks to Ms. Birnmeier and Ms. Schönbein for their nice assistance with various administrative problems, and to all the colleagues of the IMK who supported me throughout my studies. I thank Julia S. for convincing me to go to Africa. Thanks go to my fellow students, in particular Julia K., Tobias, Daniel and Max; Meike, Peggy, Simon L., Heike, Sana and Lisa; Christian E. and Kiki. I also thank Simon Z. for corrections.

I owe gratitude to the German Merit Foundation, notably Prof. Dr. Reimert, Ms. Hensgen, Prof. Dr. Pfingsten, Dr. Happ, and Dr. Weingärtner, for the ideal and finacial sponsorship during my studies.

Last but not least I deeply thank my parents and my brother Anting, whose absolute support and understanding have made my studies possible.

Danksagung

Mein besonderer Dank gebührt Prof. Dr. Sarah Jones und Dr. Doug Parker für die großartige Aufgabenstellung, eine umfassende Betreuung, die Teilnahme an GERBILS, viele Kontakte und unzählige aufschlussreiche Diskussionen.

Prof. Dr. Beheng danke ich für hilfreiche Gespräche, gute Ratschläge und die freundliche Übernahme des Korreferats.

Prof. Dr. Kottmeier danke ich für nützliche Literatur und gute Hinweise.

Dem Rechenzentrum der Universität Karlsruhe, insbesondere Prof. Dr. Heuveline und Horst Gernert, danke ich für das Ermöglichen der COSMO-Wettervorhersagen. Dr. Jim Haywood und dem gesamten GERBILS- und FAAM-Team danke ich dafür, dass ich an GERBILS teilnehmen durfte.

Vielen Dank an Juliane, Leo, Bele, Tanja, Bernhard und Heike für die Hilfe mit COSMO und interessante Diskussionen, an Doris für die Datenbeschaffung und GrADS Hilfe und an Herrn Brückel für stets prompte und freundliche Hilfe bei Computerproblemen. Frau Birnmeier und Frau Schönbein sei für die nette Hilfe bei allerlei verwaltungstechnischen Dingen gedankt sowie allen Mitarbeitern des IMK, die mich im Laufe meines Studiums immer wieder unterstützt haben. Danke Julia S., dass du mich überredet hast nach Afrika zu gehen! Meinen Kommilitonen besonders Julia K., Tobias, Daniel und Max; Meike, Peggy, Simon L., Heike, Sana und Lisa; Christian E. und Kiki möchte ich für das gemeinsame Stützen im Studium danken. Danke auch an Simon Z. fürs Korrekturlesen.

Mein herzlicher Dank gilt Dr. John Marsham für die tolle Zeit in Afrika und England und die uneingeschränkte Hilfsbereitschaft bei thematischen und technischen Fragen. Dr. Conny Schwierz gilt mein besonderer Dank für Datenbeschaffung und allerlei Hilfe. Weiter sei den Phds, Computeradministratoren und allen Mitarbeitern des IAS für fachliche und technische Hilfe, nette Diskussionen und die angenehme Arbeitsatmosphäre gedankt. Danke Hui, Jenny, Sam, Sam, Ben und Laety für das schöne Zuhause in Leeds.

Der Studienstiftung des deutschen Volkes, namentlich Prof. Dr. Reimert, Frau Hensgen, Prof. Dr. Pfingsten, Dr. Happ und Dr. Weingärtner, danke ich herzlich für die ideele und finanzielle Unterstützung meines Studiums.

Nicht zuletzt danke ich von tiefem Herzen meinen Eltern und meinem Bruder Anting, ohne deren unbedingte Unterstützung und deren Verständnis mein Studium nicht möglich gewesen wäre.

Erklärung

Hiermit erkläre ich, dass ich die vorliegende Arbeit selbst verfasst und nur die angegebenen Hilfsmittel verwendet habe.

Ich bin damit einverstanden, dass die Arbeit in die Bibliothek eingestellt wird und vervielfältigt werden darf.

Karlsruhe, den 18. März 2008